

**HIGH-POWER SINGLE-PASS RAMAN CELLS  
IN THE ULTRAVIOLET: NUMERICAL AND EXPERIMENTAL  
STUDY, WITH APPLICATIONS IN THE DIFFERENTIAL  
ABSORPTION LIDAR MEASUREMENT  
OF TROPOSPHERIC OZONE**

THÈSE N° 1561 (1996)

PRÉSENTÉE AU DÉPARTEMENT DE GÉNIE RURAL

ÉCOLE POLYTECHNIQUE FÉDÉRALE DE LAUSANNE

POUR L'OBTENTION DU GRADE DE DOCTEUR ÈS SCIENCES

PAR

**Laurent DE SCHOULEPNIKOFF**

Ingénieur physicien diplômé EPF  
originaire de Lausanne (VD)

acceptée sur proposition du jury:

Prof. H. van den Bergh, directeur de thèse  
Dr B. Calpini, corapporteur  
Dr M.J.T. Milton, corapporteur  
Dr V. Mitev, corapporteur  
Prof. A. Quattropiani, corapporteur

Lausanne, EPFL  
1997

## Abstract

High gain single-pass (HG-SP) Raman cells consist of a tube containing the Raman active gas, in which the pump laser beam is focused. In the UV spectral region, a number of frequency down-converted (Stokes) and up-converted (anti-Stokes) beams are generated with excimer or quadrupled Nd:YAG pump lasers in a single pass. Raman cells used as wavelength-shifting devices have number of applications, such as the differential absorption lidar (DIAL) measurement of ozone, or laser ranging. Two numerical and two experimental studies were conducted on the UV Raman cells characterization and their configuration in an ozone DIAL instrument. The pump beam propagation and conversion in the Raman cell is numerically modelled, which helps the interpretation of the HG-SP stimulated Raman scattering physics, and to compare the results obtained with different Raman cell experimental setups. An experimental investigation of the Raman cells is carried out in view to complement former works. In particular, a more complete parametric study is conducted, the quality of the shifted beams is characterized, and the feasibility of a mixture of two Raman-active gases is investigated. The experimental work also aimed at the optimization of the Raman cells performance (conversion efficiency and beam quality) in view of their implementation in the ozone DIAL. The best configurations of the Raman cell in terms of pump energy, lens focal length and gas partial pressures, are determined for the particular laser used. A computer code has been developed which simulates the lidar (transmitter, receiver) together with the propagation of the laser beams in the atmosphere and the interaction with its constituents. This simulation is used to study which wavelengths of the Raman-shifted spectrum are to be used in the ozone tropospheric DIAL. The best compromises in relation with the needs of photochemical airshed pollution modellings (as undertaken at LPAS) have been determined.

## Résumé

une cellule Raman est composée d'un tube qui contient le gaz Raman-actif, dans lequel un faisceau laser de pompe est focalisé. Dans l'ultraviolet, un certain nombre de faisceaux sont générés, dont la fréquence est soit additionnée (faisceaux anti-Stokes) ou soustraite (faisceaux Stokes) de l'énergie de la transition Raman. L'excimer KrF et le Nd:YAG quadruplé sont les lasers de pompe généralement utilisés pour cette application dans l'UV, et permettent de hautes efficacités de conversion en un unique passage dans la cellule. Les cellules Raman, utilisées comme instrument pour changer la longueur d'onde d'un laser, ont un certain nombre de domaines d'application, dont la mesure lidar par absorption différentielle (DIAL) de l'ozone. Deux études numériques et deux études expérimentales ont été conduites dans ce travail, pour soit caractériser la cellule Raman ou déterminer sa configuration optimale au sein d'un DIAL ozone. la propagation et la conversion du faisceau de pompe dans la cellule Raman est simulée numériquement. Cette simulation permet de mieux expliquer la physique du processus Raman stimulé à haut gain, et de pouvoir interpréter des mesures effectuées dans des configurations expérimentales différentes. Une caractérisation expérimentale de la cellule est entreprise, dans le but de compléter les recherches antérieures du même type. En particulier, une étude paramétrique plus complète est effectuée, la qualité des faisceaux Stokes est mesurée, et la faisabilité d'un mélange de deux gaz actifs est examinée. Le travail expérimental a aussi comme but d'optimiser les performances des cellules (du point-de-vue de l'énergie et de qualité de faisceau) en vue de leur intégration au sein du DIAL ozone. La meilleure configuration en terme d'énergie de pompe, de longueur focale de la lentille et de pression partielle des gaz, est déterminée pour le modèle de laser utilisé. Une simulation numérique est développée qui simule l'instrument DIAL (source laser et éléments de détection), la propagation du faisceau laser dans l'atmosphère, ainsi que l'interaction avec ses constituants. La simulation est utilisée pour étudier quelles longueurs du spectre Raman utiliser dans la cadre d'un DIAL ozone troposphérique. Les meilleurs compromis en relation avec les besoins des simulation numériques de pollution (comme entreprises au LPAS) sont déterminés.

# Contents

<b>1. Introduction</b>	<b>1.1</b>
1.1 Introduction	1.2
1.2 The stimulated Raman scattering technique	1.4
1.2.1 <i>Background on the the stimulated Raman scattering</i>	1.4
1.2.2 <i>Raman cells</i>	1.6
1.3 The lidar technique	1.8
1.3.1 <i>Overview of lidar sensing techniques</i>	1.8
1.3.2 <i>Lidar equations</i>	1.9
1.3.3 <i>solutions of the lidar scattering equation</i>	1.11
1.3.4 <i>Atmospheric pollutants absorption cross section</i>	1.12
1.3.5 <i>Lasers relevant to lidar for pollution monitoring</i>	1.15
1.3.6 <i>Pollutant concentration determined by differential absorption lidar (DIAL)</i>	1.17
1.3.7 <i>Lidar error analysis</i>	1.18
1.4 Organization of the report	1.25
1.5 Status of research	1.26
<b>2. Numerical method for the modelling of high-gain single-pass cascade stimulated Raman scattering in gases</b>	<b>2.1</b>
2.1 Introduction	2.2
2.2 Physical model for high-gain cascade single-pass Raman cells	2.3
2.3 Numerical method	2.7
2.3.1 <i>Method for the grid adjustment</i>	2.8
2.3.2 <i>Method for the nonlinear coupling</i>	2.8
2.3.3 <i>method for the diffraction</i>	2.12
2.3.4 <i>Link between the methods</i>	2.18
2.3.5 <i>Benchmarking</i>	2.23
2.3.6 <i>Step adjustment</i>	2.27
2.3.7 <i>Boundary conditions</i>	2.28
2.4 Numerical examples in a SRS configuration	2.28
2.5 Conclusion	2.34
Annex 2.A: developments leading to the main equations of §2.3.3	2.35
Annex 2.B: validity of the paraxial approximation in a HG-SP configuration	2.38
<b>3. High-gain single-pass stimulated Raman scattering and four-wave-mixing in a focused beam geometry: numerical study</b>	<b>3.1</b>
3.1 Introduction	3.2
3.2 Physical model	3.3
3.2.1 <i>General</i>	3.3
3.2.2 <i>Input data to the model</i>	3.5
3.2.3 <i>Transient gain reduction</i>	3.7
3.2.4 <i>Dimensional analysis</i>	3.12
3.3 Results and discussion	3.12
3.3.1 <i>relevance of FWM</i>	3.12
3.3.2 <i>Effect of the focusing</i>	3.13
3.3.3 <i>Effect of the pump beam quality</i>	3.16
3.3.4 <i>Deuterium and methane</i>	3.18
3.3.5 <i>Quality of the output beams (no buffer gas)</i>	3.20
3.3.6 <i>Effect of buffer gases</i>	3.22
3.3.7 <i>Anti-Stokes</i>	3.25
3.4 Comparison between the modelling and previously reported experimental results	3.29
3.4.1 <i>Qualitative features matching the modelling</i>	3.29

3.4.2 Closer qualitative comparison between the modelling and experimental results	3.30
3.5 Conclusion	3.31
Annex A: Numerical calculation of the beam quality	3.32
Annex B: Stimulated Brillouin scattering threshold	3.33
<b>4. High-power single-pass Raman shifters in the ultraviolet</b>	<b>4.1</b>
4.1 Introduction	4.2
4.2 Theoretical background	4.3
4.2.1 Raman gain and transient gain reduction	4.3
4.2.2 Four-wave-mixing	4.6
4.2.3 Buffer gas influence	4.7
4.3 Experimental setup	4.8
4.4 single Raman-active gas	4.10
4.4.1 Conversion efficiency	4.10
4.4.2 Stokes beam quality	4.26
4.5 Mixture of two Raman-active gases	4.28
4.5.1 Hydrogen and deuterium	4.28
4.5.2 Other gas fillings	4.32
4.6 Conclusion	4.33
<b>5. Experimental optimization of hydrogen and deuterium Raman cells pumped by the fourth harmonic of a Continuum Powerlite 8010 Nd:YAG laser</b>	<b>5.1</b>
5.1 Introduction	5.1
5.2 Optimization procedure	5.2
5.3 Pump beam characterization (at 266 nm)	5.3
5.4 Beam expansion before focusing	5.3
5.5 Energy conversion without beam expansion	5.4
5.6 Beam quality	5.5
5.7 Stokes energy fluctuations	5.6
5.8 Recommended Raman cell configuration	5.8
<b>6. Numerical optimization of multiwavelength differential absorption lidar (DIAL) for pollution modelling</b>	<b>6.1</b>
6.1 Introduction	6.1
6.2 Computer simulator of ozone DIAL	6.4
6.3 Theoretical background	6.8
6.3.1 Random error	6.8
6.3.2 Systematic error	6.10
6.4 Two-wavelength ozone DIAL	6.11
6.4.1 Measurement range (random error)	6.11
6.4.2 Aerosol interference (systematic error)	6.14
6.5 Dual DIAL	6.17
6.6 Raman DIAL	6.19
6.7 Simultaneous ozone and water vapor profiling	6.21
6.8 Conclusion	6.23
<b>7. Perspectives</b>	<b>7.1</b>
7.1 Conclusions	7.2
7.2 Perspectives	7.5
Acknowledgements	7.7



## **Section 1**

### **Introduction**

## 1.1 Introduction

Lasers demonstrate unique properties of high energy, narrow bandwidth and low divergence. They have been used in numerous applications since its invention more than thirty years ago, most of which are by now vital in a modern society. However, lasers have the drawback of the lack of tunability, particularly for high-power devices. Tunability is a critical feature in some applications, such a differential absorption lidar (DIAL). The present study focuses on one mean to shift the laser wavelength: a Raman cell filled with a molecular gas (as hydrogen, deuterium or methane). DIAL instruments require powerful laser beams in order to reach useful ranges in the atmosphere (i.e. of the order of kilometres). Specifically, the Raman cells considered in this study allow the shifting of high-power laser radiation.

The particular DIAL application considered here is the remote sensing of tropospheric ozone. Ozone is a long-lived secondary pollutant present in photochemical smog, with a high oxidizing effect which threatens any form of life. Photochemical smog occurs by now in every major city, particularly in summer. The DIAL sensing of ozone proceeds best in the ultraviolet, where the Hartley absorption band allows sufficient absorption for DIAL applications (even in low-level (unpolluted) ozone conditions). Therefore, Raman cells in the ultraviolet have been studied here.

High gain single-pass (HG-SP) Raman cells consist of a tube containing the Raman active gas, in which the pump laser beam is focused. In the UV spectral region, a number of frequency down-converted (Stokes) and up-converted (anti-Stokes) beams are generated with excimer or quadrupled Nd:YAG pump lasers in a single pass. The Stokes and anti-Stokes beams are sequentially produced by the combined effect of stimulated Raman scattering (SRS) and four-wave-mixing (FWM), a phenomenon denoted "Stokes cascading". Photon conversion efficiencies of several tens of percent are reported up to the third Stokes in H<sub>2</sub> or D<sub>2</sub><sup>1</sup> (the Stokes, resp. anti-Stokes, number refers to the number of times the pump beam has been frequency downconverted, resp. upconverted).

Raman cells are the preferred wavelength-shifters in a number of applications, such as DIAL<sup>1</sup> or laser ranging<sup>2</sup>. The lack of tunability of the Raman cells is compensated by the high efficiency and simplicity of the setup. The large extent of the ozone Hartley band allows the use of Raman cells in DIAL instruments. In most other DIAL applications, a (quasi-) continuously tunable laser is required. Dye lasers have the drawback of the volume, maintenance and the relatively low efficiency. Various solid-state sources are available in the UV, which are more compact and easy to maintain than dye lasers<sup>3</sup>. The titanium-doped sapphire (Ti:Al<sub>2</sub>O<sub>3</sub>) and alexandrite (Cr:Be<sub>2</sub>O<sub>4</sub>) lasers emit in the 240-315 and 240-270 nm range respectively, when tripled. The Ce:LiSAF emits in the 280-300 nm range when pumped with the Nd:YAG fourth harmonic. OPOs are also tunable source alternatives. In the UV, solid-state lasers are at this time less powerful than Raman-shifted lasers (excimer or quadrupled Nd:YAG).

The present research focuses on HG-SP Raman cells in the UV, with applications in the DIAL measurement of tropospheric ozone. Two numerical and two experimental studies were conducted on the Raman cells characterization and their configuration in the DIAL instrument. The commonalties and differences of the experimental results obtained with different Raman cell setups are still not well explained. We aim to point out the principles that allow the comparison between different experimental configurations, and possibly to make an extrapolation to other setups.

Two related researches were conducted at the Laboratory of Air and Soil Pollution (LPAS) of the Swiss Federal Institute of Technology, Lausanne (EPFL), in the same time as this one. Biemann<sup>4</sup> performed a Raman cell optimization with another laser than here, and contributed to the ozone DIAL wavelength optimization. Jeker<sup>5</sup> automated the beam quality measurement, and contributed to the practical implementation of the Raman cells in the DIAL frame.

## *Section 1: Introduction*

### **References**

1. Final report to the project EUROTRAC/TESLAS, "Tropospheric Environmental Studies by Laser Sounding", Jens Bösenberg Ed. (Max-Planck Institut für Meteorologie, Hamburg, Germany), Commission of the European Communities, in press.
2. D. W. Trainor, "Military excimer-laser technology seeks real-world uses", *Laser Focus World*, PennWell Publishing, June 1993.
3. M. J. T. Milton, "Tunable lasers for DIAL applications", *Rev. Laser Eng.*, **23**, 93-96 (1995).
4. P.-A. Biemann, "Optimisation numérique et expérimentale de la partie émission du lidar du LPAS", MSc thesis, Swiss Federal Institute of Technology Lausanne, Rural Engineering Department, Laboratory for Air and Soil Pollution (1996).
5. Dominique P. Jeker, "Optimization of the EPFL lidar for the Geneva COST-CITAIR campaign", MSc thesis, Swiss Federal Institute of Technology Lausanne, Rural Engineering Department, Laboratory for Air and Soil Pollution (1996).

## 1.2 The stimulated Raman shifting technique

### 1.2.1 Background on the stimulated Raman scattering

In the 1920s the Indian physicist C. V. Raman discovered that the light scattered by a gas, liquid, or solid ensemble of molecules can have a wavelength which is shifted from that of the incident light. In a contemporary formalism, this so-called “Raman process” is viewed as a case of four-wave-mixing process which can be either spontaneous or stimulated. The Raman process is described by a third-order susceptibility  $\chi(-\omega_s; \omega_p, -\omega_p, \omega_s)$ , in which a photon at the pump frequency  $\omega_p$  mixes with a photon at the Raman frequency  $\omega_s$  to generate an additional so-called “Stokes” photon at  $\omega_s$ . As can be demonstrated from a quantum mechanical calculation of the Raman susceptibility<sup>1</sup>, the Raman process is greatly enhanced when it is resonant i.e. when the Raman shift  $\omega_R = \omega_p - \omega_s$  corresponds to a transition of the molecule (electronic, vibrational, or rotational), as illustrated in fig. 1.

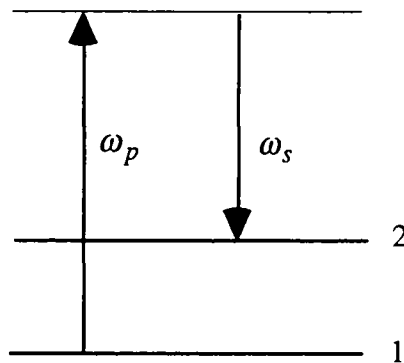


**Fig. 1.** Raman process of a pump radiation at the frequency  $\omega_p$  which leads to a Stokes radiation at  $\omega_s$ . The molecule is initially in the level “1” and is left in the excited level “2” by the scattering process. The resonance enhancement of  $\chi(-\omega_s; \omega_p, -\omega_p, \omega_s)$  occurs when  $\omega_R = \omega_p - \omega_s$ ,  $\omega_R$  being the transition frequency between the levels “1” and “2”.

In the paraxial approximation, and considering plane waves, the growth of the Stokes radiation is given by

$$\frac{dm_s}{dz} = \frac{1}{c/n} D m_L (m_s + 1) \quad (1)$$

where  $m_s$  and  $m_L$  denote respectively the (mean) number of Stokes and pump photons per mode,  $z$  is the position along the axis of propagation,  $c$  is the speed of light in vacuum,  $n$  is the index of refraction of the material medium, and  $D$  is a proportionality factor which depends on the physical properties of the material medium. The first and second terms in the parenthesis describe respectively the stimulated and spontaneous contributions. In equ. (1), a photon description is adopted for the purpose of illustration in the frame of this introduction because it is simply defined. However, a field description (wave equation) is used in the following chapters, but it requires a heavier formalism.

The initial (seed) Stokes field can be externally applied from a laser. When no initial seed Stokes radiation is present, the Stokes radiation is produced by the spontaneous Raman scattering, which is calculated as follows from equ. (1):

Section 1: Introduction

$$m_s(z) = \frac{1}{c/n} D m_L z \quad (2)$$

In the derivation of equ. (2), a constant (undepleted) pump beam has been considered. In the spontaneous process, the Stokes intensity is seen to be proportional to the length of the medium, and hence to the total number of molecules in the interaction region. The spontaneous Raman scattering, along with background noise radiation (equivalent to one photon per mode), provide the initial Stokes radiation for the stimulated process (when no Stokes seed is present). After some interaction length, the stimulated process overcomes the spontaneous process (i.e.  $m_s \gg 1$ ), and in this instance equ. (1) is solved to yield

$$m_s(z) = m_s(0) e^{Gz} \quad , \quad G = \frac{Dn m_L}{c} \quad (3)$$

where  $m_s(0)$  denotes the photon occupation number associated with the Stokes field at the input of the Raman medium, and the pump beam has been taken as undepleted.  $G$  is called the "gain coefficient" of the Raman-active medium. The Stokes intensity is seen to grow exponentially with propagation distance through the medium, and large values of the Stokes intensity are routinely observed at the output of the interaction region ( $Gz > 30$ ).

Unlike spontaneous Raman scattering, the stimulated Stokes wave propagates in the direction of the pump beam as a laser-like beam in itself. The stimulated Raman effect can therefore be used to extend the wavelength range of laser sources by varying the Raman shift  $\omega_R$ , that is, by varying the type of material medium. The growth in intensity of the Stokes radiation eventually results in the generation of additional Stokes lines, since the first Stokes wave at frequency  $\omega_{s1} = \omega_p - \omega_R$  can in turn pump a second Stokes line at the frequency

$$\omega_{s2} = (\omega_p - \omega_R) - \omega_R = \omega_p - 2\omega_R \quad (4)$$

This second Stokes radiation can further act as a pump for a third Stokes line at  $\omega_{s3} = \omega_p - 3\omega_R$ , and so forth. The second Stokes can also be generated by the mixing of the pump with the first Stokes beam via the susceptibility  $\chi(-\omega_{s2}; -\omega_p, \omega_s, \omega_s)$ . Two mixing processes contribute to generate the third Stokes, namely  $\chi(-\omega_{s3}; -\omega_p, \omega_{s1}, \omega_{s2})$  and  $\chi(-\omega_{s3}; -\omega_{s1}, \omega_{s2}, \omega_{s2})$ . Similarly, an increasing number of four-wave-mixing processes contribute to generate the higher-order Stokes. The sequential Stokes generation is usually referred as "Stokes cascade".

The stimulated Raman process can also produce radiation at an upward frequency-shifted frequency  $\omega_{as1} = \omega_p + \omega_R$ , so-called anti-Stokes (the downward-shifted Stokes frequency is given by  $\omega_{s1} = \omega_p - \omega_R$ ). In stimulated Raman processes involving vibrational molecular transitions, the anti-Stokes radiation is unlikely to be initiated by spontaneous anti-Stokes Raman scattering since the excited level is usually weakly populated (at room temperature). Rather the anti-Stokes radiation is generated by the mixing of the pump with the first Stokes, described by the susceptibility  $\chi(-\omega_{as1}; \omega_p, \omega_p, -\omega_{s1})$ . It is illustrated by the following frequency relations:

$$\omega_{as1} = 2\omega_p - \omega_{s1} = 2\omega_p - (\omega_p - \omega_R) = \omega_p + \omega_R \quad (5)$$

## Section 1: Introduction

By further mixing of Stokes and anti-Stokes lines, higher-order anti-Stokes lines at frequency  $\omega_p + i\omega_R$  ( $i$  an integer) are generated. In the same way Stokes and anti-Stokes beams mix together, as illustrated by the susceptibility  $\chi(-\omega_{s2}; -\omega_{as1}, \omega_p, \omega_{s1})$  which describes the second Stokes from the mixing of the first anti-Stokes, the pump and the first Stokes.

An important aspect of the Raman scattering is the phase-matching. The spontaneous and stimulated Raman scattering do not require phase-matching, as it is evident from the form of the susceptibility, namely  $\chi(-\omega_{s1}; \omega_p, -\omega_p, \omega_{s1})$ . In contrast, the four-wave-mixing includes a phase-matching condition. For example (fig. 2), the conservation of linear momentum for the mixing process  $\chi(-\omega_{as1}; \omega_p, \omega_p, -\omega_{s1})$  yields

$$\mathbf{k}_{as1} = 2\mathbf{k}_p - \mathbf{k}_{s1} \quad (6)$$

where  $\mathbf{k}$  denotes the wave-vector, with the same subscript notation as for the frequency  $\omega$ . In the equations describing the Stokes and anti-Stokes waves, the four-wave-mixing terms are proportional to the phase-mismatch factor  $\exp(iz\Delta k)$ . For the example chosen of the  $\chi(-\omega_{as1}; \omega_p, \omega_p, -\omega_{s1})$  process,  $\Delta k$  is given by

$$\Delta k = \left| \mathbf{k}_{as1} - (2\mathbf{k}_p - \mathbf{k}_{s1}) \right| \quad (7)$$

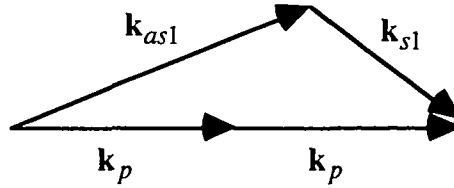


**Fig. 2.** The wave-vector diagram which expresses the conservation of momentum in the  $\chi(-\omega_{s2}; -\omega_{as1}, \omega_p, \omega_{s1})$  mixing process.

### 1.2.2 Raman cells

The Raman-shifting configuration is taken in this study as a single-pass Raman cell in a focused pump beam geometry. The pump beam spectral region considered is located in the interval 250-300 nm, i.e. in the ultraviolet. This research focuses on high power beams (i.e.  $>10$  mJ per pulse) in this spectral region, which have applications in the DIAL measurement of tropospheric ozone<sup>2</sup>, or laser ranging<sup>3</sup>. The high-power pump laser generally used in this spectral region is either a quadrupled Nd:YAG (up to 100 mJ pulse energy at 266 nm, 4-10 nsec pulse duration, round beam shape of ca. 6-10 mm diameter), or a KrF excimer laser (up to 1 J pulse energy at 248 nm, 10-20 nsec pulse duration, rectangular beam shape of ca. 2 x 0.5 cm dimension). In both cases of pump laser, the intensity is of the order of 10 mW/cm<sup>2</sup>. In the case considered, the pump beam is focused with a lens of focal length in the range 0.2 - 1 m, which typically reduces the beam surface, and hence multiplies the beam intensity, by a factor 10<sup>6</sup> at the waist.

The Raman-active medium considered is hydrogen, deuterium or methane. They all show a high Raman gain at room temperature. It has to be noted that the Raman gain of these molecules has a strong wavelength dependence (of the order of  $1/\lambda^2$  to  $1/\lambda^3$ , where  $\lambda$  is the pump wavelength). For example, the Raman gain in hydrogen is ca. 20 times bigger at the

## Section 1: Introduction

Nd:YAG fourth harmonic (266 nm) than at its fundamental (1064 nm). This spectral dependence has a very significant effect on the Raman efficiency, since the Raman amplification is typically exponential, as displayed in equ. (3).

In this configuration of high Raman gain and high pump intensity at the waist, photon conversion efficiencies of the order of several tens of percent have been routinely observed up to the third Stokes<sup>2</sup>, in a single-pass configuration.

The experimental setup of single-pass Raman cell frequently used consists of a tube with two windows mounted at each end. The pump beam is focused by a lens at the entrance window, and the shifted beams are recollimated after the output lens with a lens of comparable focal length. Usually the position along the optical axis of either of both of these lenses is adjustable so as to minimize the divergence of one selected Stokes beam. The shifted beams on exit are optionally separated by a dispersive element (prism). The material of all the pass-through elements (window, lens, prism) is generally either fused silica or sapphire, due to their high transmittance and optical damage threshold. Fig. 3 illustrates principle of such Raman cell.

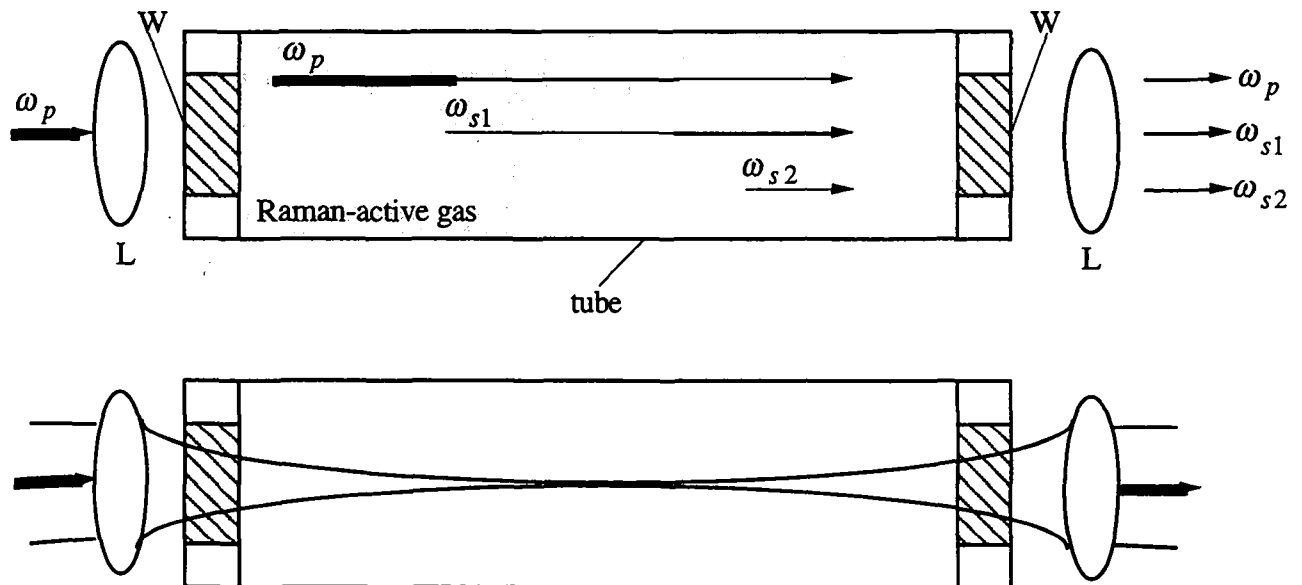


Fig. 3. Typical configuration of single-pass Raman cell. The upper panel illustrates the sequential Stokes conversion. W: window, L: lens. The lower panel shows the focusing geometry of the pump beam.

## References

1. D. C. Hanna, M. A. Yuratich, D. Cotter, *Nonlinear optics of free atoms and molecules* (Springer, Berlin, 1979).
2. Final report to the project EUROTRAC/TESLAS, "Tropospheric Environmental Studies by Laser Sounding", Jens Bösenberg Ed. (Max-Planck Institut für Meteorologie, Hamburg, Germany), Commission of the European Communities, in press.
3. D. W. Trainor, "Military excimer-laser technology seeks real-world uses", *Laser Focus World*, PennWell Publishing, June 1993.

## 1.3 The lidar technique

### 1.3.1 Overview of lidar sensing techniques

A lidar is composed of a transmitting and a receiving section (fig. 4). The laser beam is emitted in the atmosphere by the transmitter, interacts with the atmospheric constituents upon propagation, and the backscattered light is collected by a telescope and recorded by a detection unit. The interaction proceeds with the atmospheric gases and aerosols, of which the Rayleigh, Mie or (spontaneous) Raman scattering form the principle of the lidars for pollution monitoring (fig. 5). The Mie, Rayleigh and Raman backscattering cross sections are of the order of  $10^{-9}$ ,  $10^{-28}$  and  $10^{-31}$   $\text{cm}^2/\text{sr}$  respectively, for standard air and a probing laser wavelength at 500 nm. When multiplied by the molecules (gas) or aerosol number density ( $\text{m}^{-3}$ ), the backscattering cross section yields the backscattering coefficient ( $\text{m}^{-1}/\text{sr}$ ) which represents the backscatter efficiency per unit length along the laser path. In clean air, the Mie and Rayleigh backscattering coefficients are of the same order, while the Raman backscattering coefficient is ca. 1000 times smaller.

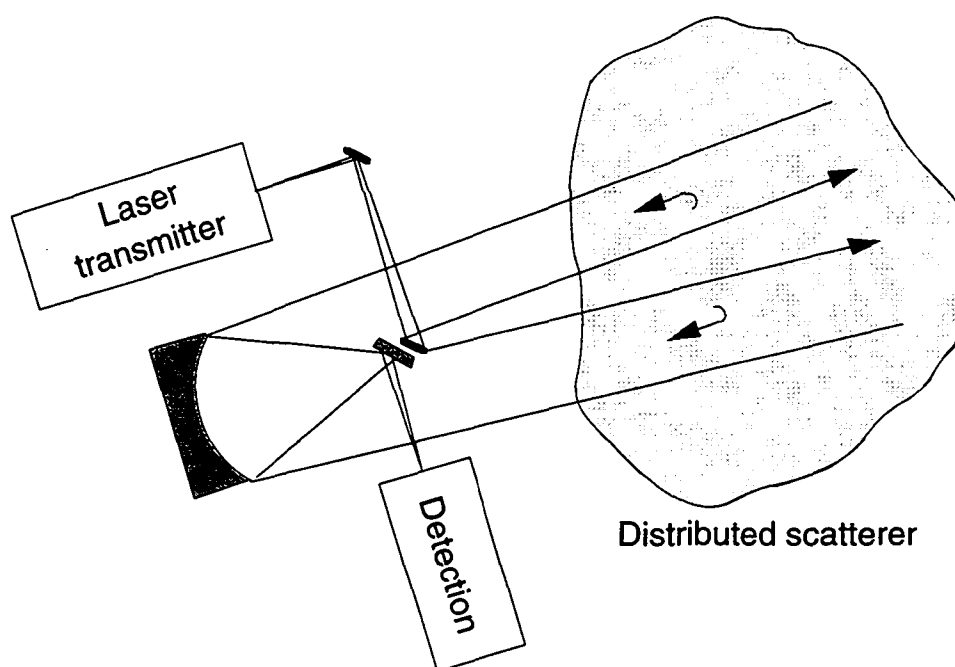
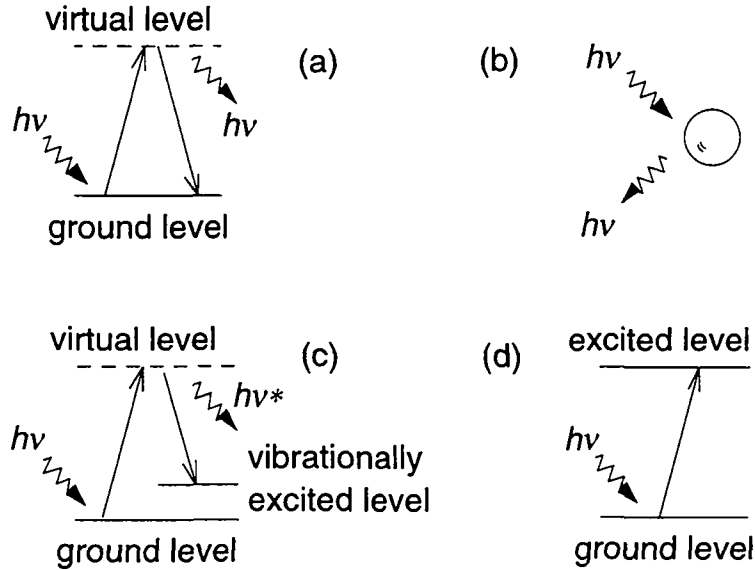


Fig. 4. Lidar principle.

Lidars for aerosol monitoring record the atmospheric Rayleigh and Mie backscattering. At one wavelength, the ratio of the aerosol to the molecular (gases) backscatter coefficient can be deduced from the return signal (§1.3.3), which is significant of the appearance of aerosol layers. When several wavelengths are used, information about the aerosol size distribution and/or composition can be retrieved.

Atmospheric gaseous species concentration can be selectively measured by using two wavelengths, one which is more absorbed by the specie than the other one. For species which show narrow absorption features (§1.3.4), typically one wavelength is tuned on an absorption line, and the other one is tuned off the line. Two such wavelengths, rather than a single one, are needed in order to cancel the effect of the Mie scattering and to rule out the instrument calibration constant (§1.3.2). The lidar which implements this principle is called differential absorption lidar (DIAL).





**Fig. 5.** Some interactions between light and atmospheric constituents of relevance to lidars. Rayleigh scattering (a), particulate (Mie) scattering (b), Raman scattering (c), absorption (d).

Due to the small backscattering cross section, the measurement of Raman returns currently requires parts-per-million (ppm) concentrations, which limits their applicability. N<sub>2</sub> or O<sub>2</sub> returns yield the aerosol extinction (vibrational Raman transition) or the temperature (rotational Raman transition). Raman lidar concentration measurements of water vapour, stratospheric ozone and species in industrial plumes have been reported.

Wind fields have been determined by measuring the Doppler shift of the atmospheric aerosols. Alternatively, the spatio-temporal correlation of the aerosol inhomogeneities can be used for that purpose. Beam scanning systems are capable of measuring the three-dimensional wind vector.

### 1.3.2 Lidar equations

#### (a) Scattering form of the lidar equation

The following relation (so-called “lidar equation”) is an approximation to the laser beam propagation in clear atmosphere (optical depth less than 0.3) which is appropriate in many lidar applications<sup>1</sup>:

$$P(\lambda, R) = C(\lambda, R) P_L(\lambda) \frac{A_r}{R^2} \Delta R \beta(\lambda, R) T^2(\lambda, R) \quad (8)$$

where

$C(\lambda, R)$  is a system function determined by the geometric considerations of the receiver optics, the quantum efficiency of the detection system at wavelength  $\lambda$ , and the overlap of the transmitted beam with the field-of-view of the receiver.

$P_L(\lambda)$  is the average power in the transmitted laser pulse at wavelength  $\lambda$ .

$A_r/R^2$  is the acceptance solid angle of the receiving optics with a collecting area  $A_r$ .

$\Delta R$  is the range resolution of the lidar signal. It cannot be smaller than  $c(\tau_L + \tau_d)/2$ , where  $\tau_L$  and  $\tau_d$  are respectively the laser pulse duration and the data acquisition resolution time, and  $c$  the speed of light.

## Section 1: Introduction

$T^2(\lambda, R)$  is the round-trip transmittance to range  $R$ , approximated by the Lambert-Beer law:

$$T^2(\lambda, R) = \exp\left(-2 \int_0^R \alpha(\lambda, r) dr\right) \quad (9)$$

$\alpha(\lambda, r)$  and  $\beta(\lambda, r)$  are respectively the volume extinction and backscattering coefficients ( $\text{m}^{-1}$  and  $\text{m}^{-1}\text{sr}^{-1}$ ), given by

$$\alpha(\lambda, R) = \sigma_m^e(\lambda) N_m(R) + \int \sigma_a^e(\lambda, x) N_a(R, x) dx + \sum_i \sigma_i^a(\lambda) N_i(R) \quad (10)$$

$$\beta(\lambda, R) = \sigma_m^b(\lambda) N_m(R) + \int \sigma_a^b(\lambda, x) N_a(R, x) dx$$

where  $\sigma$  is a scattering cross section and  $N$  a number density; the superscript “e”, “b” and “a” denote respectively the extinction, backscattering and absorption processes; the subscripts “m”, “a” and “i” denote respectively the molecular and aerosol contributions, and the one from the absorbing specie  $n^{\circ}i$ . The aerosol contribution to the extinction and backscattering coefficients is expressed as an integral over the particle size.  $\sigma^e$  and  $\sigma^b$  are resp. in units of  $\text{m}^2$  and  $\text{m}^2\text{sr}^{-1}$ ,  $N_m$  and  $N_i$  in  $\text{m}^{-3}$ , and  $N_a$  in  $\text{m}^{-3}\mu\text{m}^{-1}$ .

The scattering ratio  $R$  is defined as  $R = 1 + \beta_a/\beta_m$ , where  $\beta_a$  and  $\beta_m$  denote the aerosol and molecular contributions to the backscattering coefficient respectively.  $R$  measures the detectivity of aerosols above the molecular background. It is often used as an indicator of the aerosol loading.

Equation (1) describes single-scattering events (the laser photons are scattered once before reaching the detector). When the optical depth of the probed medium exceeds ca. 0.3, multiple scattering (i.e. there are several scattering events by molecules or particles before reaching the detector) becomes significant. Such optical depth may occur in heavily polluted environments. The analysis of multiply scattered lidar signal is much more complicated than for single scattering<sup>83</sup>. Multiple field-of-view receivers represent a means to detect selectively the multiply scattered versus single scattered portion of the return signal.

### (b) Differential absorption (DIAL) form of the lidar equation

The two wavelengths for which the target specie shows a difference in absorption cross section are denoted by  $\lambda_1$  and  $\lambda_2$ . The lidar equation (1) at each wavelength is multiplied by  $R^2$ , the natural logarithm and the derivative with respect to  $R$  are applied, the two equations are finally subtracted to yield the concentration of the target specie (noted  $N$ )<sup>1</sup>:

$$N(R) = \frac{1}{2 \Delta \sigma} \left\{ \frac{\partial}{\partial R} \ln \frac{S(R, \lambda_1)}{S(R, \lambda_2)} - \frac{\partial}{\partial R} \ln \frac{\beta(R, \lambda_1)}{\beta(R, \lambda_2)} + 2 [\alpha(R, \lambda_1) - \alpha(R, \lambda_2)] \right\} \quad (11)$$

where  $S(R, \lambda) = R^2 P(R, \lambda)$  is the range-corrected lidar signal, and  $\Delta \sigma = \sigma(\lambda_1) - \sigma(\lambda_2)$  is the differential absorption cross section of the target specie. In equ. (11) the extinction coefficient, as stated in equ. (10), does not include the absorption of the target specie. In a DIAL measurement the extinction and backscattering coefficients are in principle not known, and hence the second and third terms in the parenthesis of equ. (11) have to be neglected. This approximation is justified when the differential absorption is sufficiently strong with

## Section 1: Introduction

respect to the differential extinction and backscattering. This is the case typically when  $\lambda_1$  and  $\lambda_2$  are very close to each other and are located respectively on- and off- of an absorption line. Some species (e.g. ozone) do not exhibit any strong and narrow absorption features, and in this case some procedure is (in some conditions) to be applied in order to estimate the differential extinction and backscattering terms (§1.3.6).

Several possibilities exist to approximate numerically the derivative in equ. (4)<sup>3</sup>. The simplest approach is to use centred finite differences between adjacent layers with a range-step typically corresponding to the range resolution. In this case the operational form of the DIAL equation (11), with the differential extinction and backscatter neglected, is given by

$$N(R_{i+1/2}) = \frac{1}{2 \Delta \sigma \Delta R} \ln \frac{S(R_i, \lambda_2) S(R_{i+1}, \lambda_1)}{S(R_{i+1}, \lambda_2) S(R_i, \lambda_1)} \quad (12)$$

where  $N(R_{i+1/2})$  is the mean concentration between layers  $R_i$  and  $R_{i+1}$ .

### 1.3.3 Solutions of the lidar scattering equation

The lidar scattering equation (8) with no absorbing specie is considered in this chapter. The molecular contribution to the extinction and backscattering coefficient (respectively noted  $\alpha_m$  and  $\beta_m$ ) may be either modelled, from standard atmospheric temperature and pressure profiles<sup>8</sup>, or independently measured. Assuming the system calibration factor  $C$  known, the aerosol contribution to the extinction and the backscattering remain as unknowns (respectively noted  $\alpha_a$  and  $\beta_a$ ). This leaves two unknowns for one measurement,  $P(\lambda, R)$ , which is a mathematically unsolvable problem unless certain assumptions and/or constraints are included in the solution procedure. Numerous approaches to this problem have been developed<sup>9,10</sup>, and some of them are outlined below.

The slant-path method<sup>11</sup> assumes a horizontal homogeneity of  $\alpha$  and  $\beta$ , and can be used to retrieve the planetary boundary layer (PBL) optical depth  $\delta_{\text{PBL}}$ . Errors in the lidar signal are usually such as to prevent any useful computation of  $\alpha_a$  and  $\beta_a$  with this method.  $\delta_{\text{PBL}}$  can provide boundary value information which can be used in other inversion schemes. The iteration method<sup>10</sup> and the Fernald-Klett method<sup>12,13</sup> both make use of assumptions on the extinction-to-backscatter ratio  $s(\lambda, R) = \alpha_a(\lambda, R) / \beta_a(\lambda, R)$  and the value of  $\alpha_a$  or  $\beta_a$  at a reference range  $R_m$ , noted  $\alpha_a^{\text{ref}}$  and  $\beta_a^{\text{ref}}$  respectively. The iteration method has the drawback to require the knowledge of  $C$ , while it is less sensitive to  $\alpha_a^{\text{ref}}$  or  $\beta_a^{\text{ref}}$  than the Fernald-Klett method<sup>10</sup>. The latter has been shown efficient for extinction and backscatter profiling along a path of optical depth between 1 and 2, which is well suited to polluted environments<sup>55</sup>. In the mixing layer, lidars are seldom able to deliver more information than these optical properties, and microphysical features (e.g. number density, composition, mass) have to be retrieved by other means (e.g. contact instruments).

In the iteration method,  $R_m$  is chosen to be as close as possible to the instrument, i.e. as the first range of full overlap of the laser beam with the receiver telescope field-of-view. The optical depth  $T(\lambda, R_m) = \exp(-\alpha_a^{\text{ref}}(\lambda) R_m)$  is either directly estimated or calculated from  $\alpha_a^{\text{ref}}$ .  $\beta^{\text{ref}}$  is estimated as  $\beta^{\text{ref}}(\lambda) = S(\lambda, R_m) / C'(\lambda, R_m) T^2(\lambda, R_m)$ , with

## Section 1: Introduction

$C'(\lambda, R) = C(\lambda, R) P_L(\lambda) A_r \Delta R$  and  $S(R, \lambda) = R^2 P(R, \lambda)$ .  $\alpha$  and  $\beta$  at the subsequent range bins are sequentially calculated:

$$\begin{aligned}\alpha(R) &= \beta(R - \Delta R) s(R) \\ T^2(R) &= T^2(R - \Delta R) \exp[-2\alpha(R)\Delta R] \\ \beta(R) &= S(R)/T^2(R) C'(R)\end{aligned}\tag{13}$$

where the wavelength dependence has been omitted.

The Fernald-Klett method is summarized below in the Klett formalism<sup>13</sup>. The lidar equation (8) is written in differential form:

$$\begin{aligned}\frac{dX'}{dR} &= \frac{1}{\beta} \frac{d\beta}{dR} - 2s\beta \\ X'(R) - X'(R_m) &= X(R) - X(R_m) - \frac{16\pi}{3} \int_R^{R_m} \beta_m(r) \left[1 - \frac{3s(r)}{8\pi}\right] dr\end{aligned}\tag{14}$$

where  $X(R) = \ln[R^2 P(R)]$ , and  $\beta_m$  denotes the molecular contribution to  $\beta$ . The solution of (14) is given by:

$$\beta(R) = \frac{\exp[X'(R) - X'(R_m)]}{(\beta^{\text{ref}})^{-1} + 2 \int_R^{R_m} s(r) \exp[X'(r) - X'(R_m)] dr}\tag{15}$$

with  $\beta^{\text{ref}} = \beta_a^{\text{ref}} + \beta_m^{\text{ref}}$ .

### 1.3.4 Atmospheric pollutants absorption cross section

Absorption wavelength and cross section of a number of gaseous pollutants are listed in table 1. For some molecules larger absorption cross sections exist, but only those coinciding with lines of existing lasers are displayed. A comprehensive list of atmospheric and trace gases has been compiled by the Geophysics Laboratory, US Air Force Systems Command (Rothman<sup>39</sup>), which covers the spectral range from 0 to 23'000  $\text{cm}^{-1}$  (435 nm). A compilation of references to IR absorption spectra is found in McDowell<sup>40</sup>.

The molecular absorption features can be very different, as illustrated in the following examples for the UV spectral region. NO exhibits very narrow lines, of the order of 0.01 nm FWHM. The spectrum of SO<sub>2</sub> (fig. 4), NO<sub>2</sub>, toluene and benzene shows lines of the order of 1 nm width. The absorption features of O<sub>3</sub> (fig. 6) and Cl<sub>2</sub> are characterized by very broad structures (ca. 50 nm FWHM) with no narrow spectral lines.

The accuracy of the DIAL measurement is directly dependent on the accuracy on the differential absorption cross section. The electronic absorption lines in the visible and near-UV can be accurately measured in the laboratory, and are not much affected by the atmospheric environment (other than the temperature) in field measurements. The vibrational-rotational absorption lines in the IR are influenced by collision broadening, which can modify

*Section 1: Introduction*

the absorption profile and makes the absorption cross section more difficult to determine. Overlapping absorption profiles can be a critical point in the IR.

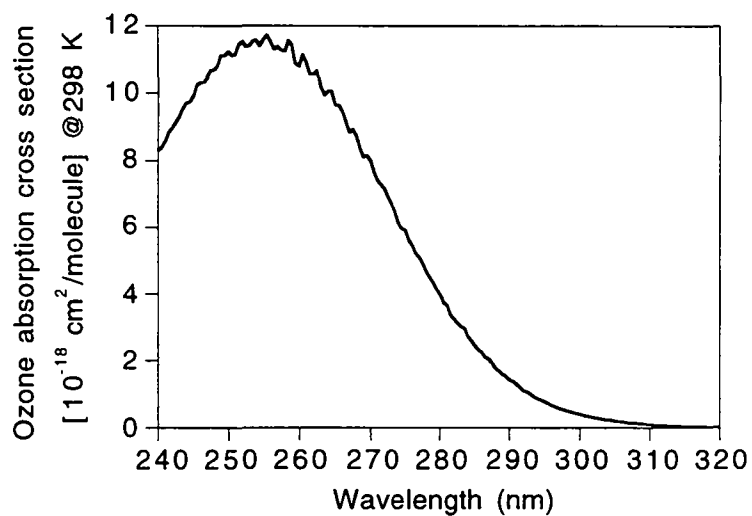


**Fig. 6.** Hartley band of the ozone absorption spectrum, at 298 K and a resolution of 0.5 nm (Molina and Molina<sup>17</sup>).

Section 1: Introduction

**Table 1.** Absorption cross section of pollutant gases at wavelengths suitable for DIAL measurement. Spectroscopic data in the 8-14  $\mu\text{m}$  wavelength region of species pointed out by the US Clean Air Act Amendments (1990) which are not shown in this table are found in Grant<sup>57</sup>. This table is adapted from ref. [Frederiksson].

Molecule	Wavelength	Laser (examples)	Absorption cross section ( $10^{-18} \text{ cm}^2$ )	Reference	Other references
Nitric oxide, NO	226.8 nm	Dye	4.6	[14]	[15,16]
Benzene, C <sub>6</sub> H <sub>6</sub>	252.9 nm	Dye	5.7	[19]	[20]
Mercury, Hg	253.65 nm	Dye	$3.3 \times 10^4$	[21]	[20]
Toluene, C <sub>7</sub> H <sub>8</sub>	266.9 nm	Dye, Ti:Sa	2.8	[19]	
Ozone, O <sub>3</sub>	266.0 nm	Dye	9.49	[17]	[18]
	289.0 nm	KrF, Nd:YAG-IV	1.59		
	299.0 nm	+ Raman cell	0.42		
		Ti:Sa			
		Ce:LiSAF			
Formaldehyde, CH <sub>2</sub> O	286.5	Dye, Ti:Sa	0.068	[27]	
Sulfur dioxide, SO <sub>2</sub>	300.0 nm	Dye, Ti:Sa	1.3	[22]	[23,24]
Chlorine, Cl <sub>2</sub>	330 nm	Dye, Ti:Sa	0.26	[25]	[26]
		XeCl + Raman cell			
Nitrous acid, HONO	354.0 nm	Dye, Ti:Sa	0.50	[28]	
Nitrogen dioxide, NO <sub>2</sub>	448.1 nm	Dye	0.69	[29]	[15,30]
Methane, CH <sub>4</sub>	3.270 $\mu\text{m}$	OPO	2.0	[31]	
	3.391 $\mu\text{m}$		0.6		
Propane, C <sub>3</sub> H <sub>8</sub>	3.391 $\mu\text{m}$	OPO	0.8	[31]	
Hydrogen chloride, HCl	3.636 $\mu\text{m}$	DF, OPO	0.20	[32]	
Methane, CH <sub>4</sub>	3.715 $\mu\text{m}$	DF, OPO	0.002	[33]	
Sulfur dioxide, SO <sub>2</sub>	3.984 $\mu\text{m}$	DF, OPO	0.42	[34]	
Carbon monoxide, CO	4.709 $\mu\text{m}$	CO <sub>2</sub>	2.8	[31]	
	4.776 $\mu\text{m}$		0.8		
Nitric oxide, NO	5.215 $\mu\text{m}$	CO	0.67	[31]	
	5.263 $\mu\text{m}$	CO <sub>2</sub>	0.6		
Propylene, C <sub>3</sub> H <sub>6</sub>	6.069 $\mu\text{m}$	CO	0.09	[31]	
1,3-Butadiene, C <sub>4</sub> H <sub>6</sub>	6.215 $\mu\text{m}$	CO	0.27	[31]	
Nitrogen dioxide, NO <sub>2</sub>	6.229 $\mu\text{m}$	CO	2.68	[31]	
Sulfur dioxide, SO <sub>2</sub>	9.024 $\mu\text{m}$	CO <sub>2</sub>	0.25	[31]	
Freon-11, CCl <sub>3</sub> F	9.261 $\mu\text{m}$	CO <sub>2</sub>	1.09	[35]	
Ozone, O <sub>3</sub>	9.505 $\mu\text{m}$	CO <sub>2</sub>	0.45	[35]	
	9.508 $\mu\text{m}$		0.9	[31]	
Fluorocarbon-113, C <sub>2</sub> Cl <sub>3</sub> F <sub>3</sub>	9.604 $\mu\text{m}$	CO <sub>2</sub>	0.77	[31]	
Benzene, C <sub>6</sub> H <sub>6</sub>	9.621 $\mu\text{m}$	CO <sub>2</sub>	0.07	[35]	
MMH, CH <sub>3</sub> N <sub>2</sub> H <sub>3</sub>	10.182 $\mu\text{m}$	CO <sub>2</sub>	0.06	[36]	
Ethyl-mercaptan, C <sub>2</sub> H <sub>5</sub> SH	10.208 $\mu\text{m}$	CO <sub>2</sub>	0.02	[35]	
Chloroprene, C <sub>4</sub> H <sub>5</sub> Cl	10.261 $\mu\text{m}$	CO <sub>2</sub>	0.34	[35]	
Monochloroethane, C <sub>2</sub> H <sub>5</sub> Cl	10.275 $\mu\text{m}$	CO <sub>2</sub>	0.12	[35]	
Ammonia, NH <sub>3</sub>	10.333 $\mu\text{m}$	CO <sub>2</sub>	1.0	[35]	
Ethylene, C <sub>2</sub> H <sub>4</sub>	10.533 $\mu\text{m}$	CO <sub>2</sub>	1.19	[35]	
Sulfur hexafluoride, SF <sub>6</sub>	10.551 $\mu\text{m}$	CO <sub>2</sub>	30.3	[37]	
Trichloroethylene, C <sub>2</sub> HCl <sub>3</sub>	10.591 $\mu\text{m}$	CO <sub>2</sub>	0.49	[35]	

Table 1. Continued.

Molecule	Wavelength	Laser (examples)	Absorption cross section ( $10^{-18} \text{ cm}^2$ )	Reference	Other references
1,2-Dichloroethane, $\text{C}_2\text{H}_4\text{Cl}_2$	10.591 $\mu\text{m}$	$\text{CO}_2$	0.02	[35]	
Hydrazine, $\text{N}_2\text{H}_4$	10.612 $\mu\text{m}$	$\text{CO}_2$	0.18	[36]	
Vinyl chloride, $\text{C}_2\text{H}_3\text{Cl}$	10.612 $\mu\text{m}$	$\text{CO}_2$	0.33	[35]	
UDMH, $(\text{CH}_3)_2\text{N}_2\text{H}_2$	10.696 $\mu\text{m}$	$\text{CO}_2$	0.08	[36]	
Fluorocarbon-12 (Freon-12), $\text{CCl}_2\text{F}_2$	10.719 $\mu\text{m}$	$\text{CO}_2$	1.33	[35]	
Perchloroethylene, $\text{C}_2\text{Cl}_4$	10.742 $\mu\text{m}$	$\text{CO}_2$	0.18	[35]	
1-Butene, $\text{C}_4\text{H}_8$	10.787 $\mu\text{m}$	$\text{CO}_2$	0.13	[31]	
Perchloroethylene, $\text{C}_2\text{Cl}_4$	10.834 $\mu\text{m}$	$\text{CO}_2$	1.14	[31]	
Fluorocarbon-11 (Freon-11), $\text{CCl}_3\text{F}$	11.806 $\mu\text{m}$		4.4	[31]	
Acetylene, $\text{C}_2\text{H}_2$	13.890 $\mu\text{m}$		9.2	[31]	

### 1.3.5 Lasers relevant to lidar for pollution monitoring

The laser source along with the detector are the most critical components of a lidar system. The ideal pulsed laser source for lidar application shows the following features: high pulse energy of short duration, high repetition rate, low divergence, small shot-to-shot energy fluctuations, good beam pointing stability, ease of use and maintenance. The bandwidth, spectral purity and tunability are critical characteristics in some DIAL applications only (when the absorption line is narrow).

The laser wavelength suited for aerosol monitoring depends on the aerosol loading and particle size. The molecular extinction and backscattering coefficients show a  $\lambda^{-4}$  dependence, while for the aerosols this dependence is variable with a coefficient ranging between -2 and 1. Therefore the scattering ratio shows a  $\lambda^m$  dependence with  $m > 2$ , and so the aerosols become more discriminated above the molecular background when the wavelength increases. For aerosol or cloud studies  $\lambda$  is generally chosen above 500 nm, while for molecular studies (which yield e.g. the atmosphere temperature or pressure) a wavelength below 500 nm is more appropriate. The size parameter  $x$  of an aerosol or cloud particle of characteristic radius  $r$  is defined as  $x = 2\pi r / \lambda$ . Particle sizing is the most effective for size parameters below  $10^{41}$ . Because the particle size in clouds (ca. 1-10  $\mu\text{m}$ ) are bigger than those in aerosols ( $< 1 \mu\text{m}$ )  $\text{CO}_2$  laser wavelengths (9-11  $\mu\text{m}$ ) are appropriate for cloud studies, whereas shorter wavelengths ( $< 1 \mu\text{m}$ ) are preferable for aerosol studies. A multiwavelength system is required when information on the particle size distribution is sought. The Nd:YAG laser (1064 nm) with its second harmonic (532 nm) is a typical example of a two-wavelength system for aerosol studies. The Ti:Sa laser (which is tunable between 720 and 950 nm) may add several additional wavelengths.

The laser spectral properties (bandwidth, spectral purity, tunability) in DIAL applications are the most stringent for species with narrow absorption lines. One extreme is represented by the broad absorption features of  $\text{O}_3$  and  $\text{Cl}_2$  in the UV which allow the use of broadband lasers with limited tunability such as Raman shifting in  $\text{H}_2$  or  $\text{D}_2$  pumped by excimer (KrF, XeCl) of quadrupled Nd:YAG lasers. In the other extreme, the very narrow absorption lines of

## Section 1: Introduction

constituents such as NO, Hg and H<sub>2</sub>O place demanding requirements on the laser spectral properties.

A review of tunable lasers suitable for DIAL applications is found in Milton<sup>43</sup>. The dye laser is a widely used source for measurements in the visible and the UV. It can be pumped directly with flashlamps or with high-power Nd:YAG laser (doubled or tripled) or excimer lasers. The tunability of a single dye is of the order of 20-50 nm. With different dyes the spectral range from the near UV to the near IR can be covered (400-800 nm). The wavelength range of a dye laser can be extended to the UV with nonlinear optical techniques (frequency doubling, sum-frequency mixing). Pulse energies of 5-10 mJ at a repetition rate up to 50 Hz have been reported<sup>3,19,44</sup>. Nonlinear optical techniques are also used to convert the frequency of dye lasers to the infrared. An example is difference-frequency mixing with parametric amplification which can generate pulse energies of 20 mJ up to 3.65  $\mu\text{m}$ <sup>45</sup>. It is difficult to achieve a spectral purity better than 99% with dye lasers. Such a spectral purity is required e.g. to perform H<sub>2</sub>O measurements with an accuracy below 5%<sup>46</sup>. The limited lifetime of the dye is another drawback of this kind of laser.

Alexandrite (Cr:Be<sub>2</sub>O<sub>4</sub>) and titanium-doped sapphire (Ti:Al<sub>2</sub>O<sub>3</sub>) lasers are solid-state devices which are tunable in the wavelength range 710-810 nm and 720-950 nm respectively. This range can be extended to the UV spectral region by frequency doubling or tripling<sup>50</sup>, or by sum-frequency mixing with a second Nd:YAG laser<sup>47,48</sup>. The linewidth of Alexandrite and Ti:Sapphire lasers can be controlled either by dispersive elements in the cavity or injection seeding. A spectral purity better than 99% can be achieved in this way. The tuning range can be extended to the infrared by using Raman shifting in H<sub>2</sub> or CH<sub>4</sub>; 10 mJ energy up to 2.2  $\mu\text{m}$  has been reported<sup>49</sup>. Several types of vibronic metal lasers emit in the mid-infrared. Particular examples are the Cr:LiSAF<sup>51</sup> (tunable between 790 and 1010 nm), the Ho:YSGG<sup>52</sup> which emits around 2.1  $\mu\text{m}$ , the Co:MgF<sub>2</sub><sup>53</sup> (tunable between 1.5 and 2.3  $\mu\text{m}$ ). Only the Co:MgF<sub>2</sub> laser has been demonstrated in DIAL applications (measurement of CH<sub>4</sub>, CO<sub>2</sub>, H<sub>2</sub>O). The Ce:LiSAF vibronic metal laser emits in the UV spectral region. When pumped with a quadrupled Nd:YAG laser, 5 mJ energy at 10Hz tunable between 284 and 299 nm has been achieved<sup>54</sup>.

Several lasers can be tuned over a certain number of emitting lines of the active medium. The line-tuning can be achieved with an intracavity grating. The use of these lasers in DIAL asks for a coincidence between the laser lines and the absorption lines of the pollutant, which can be complicated by overlapping absorption profiles. These lasers nevertheless are capable of measuring a number of species which cannot be probed in other spectral regions<sup>57</sup> (table 1). Hydrogen fluoride (HF) and deuterium fluoride (DF) lasers emit in the mid-IR spectral region, in the range 2.6-4  $\mu\text{m}$ . CO lasers emit in the 5-7  $\mu\text{m}$  range. CO<sub>2</sub> lasers emit in the range 9-11  $\mu\text{m}$ , and deliver pulse energies up to 100 mJ at a repetition rate up to 100 Hz, with pulse length longer than 50 nsec. Frequency doubling and mixing techniques for CO<sub>2</sub> lasers were at a preliminary stage at the time in 1996<sup>58,59</sup>. With the AgGeSe<sub>2</sub> doubling crystal, 2 mJ out of 35 mJ input pulse energy has been reported<sup>59</sup>. Despite the low energy, CO<sub>2</sub> doubling is one of the only methods capable to reach the 4.5-5.5  $\mu\text{m}$  spectral region.

The optical parametric oscillator (OPO) is a second-order nonlinear optical device which delivers continuous tuning out of a fixed frequency laser. The tuning range achieved is bigger than the one of the three types of lasers described above, which are based on the tunability of the lasing medium itself. The performances of the OPOs have only recently become good enough for routine DIAL measurements. When pumped by a Nd:YAG laser, the LBO (lithium triborate) and BBO (beta barium borate) crystals emit tunable radiation in the UV and visible, while KTP (potassium titanyl phosphate) and lithium niobate emit in the mid-infrared (1-4  $\mu\text{m}$ ). High pulse energies can be generated (ca. 100 mJ), with a bandwidth of the order of 1-2  $\text{cm}^{-1}$ . The linewidth can be reduced with the use of a dispersive element in the cavity (grating, etalon). With this technique, injection seeding (e.g. with a tunable diode laser) is sometimes needed in order to avoid a reduced tuning range and output energy. As an



## Section 1: Introduction

alternative OPO setup, a tunable laser can be used to pump a crystal which is not tuned for phase-matching. With a Ti:Sa laser tuned in the range 750-875 nm and pumping a KNbO<sub>3</sub> crystal, an output radiation between 1 and 4 μm is emitted with a pulse energy of ca. 5 mJ at 10 Hz.

The calibration of the laser wavelength is a critical aspect of a DIAL system when pollutants with narrow absorption bands are sensed. The calibration can be performed with a monochromator, a gas cell containing the probed gas<sup>115</sup> (or another gas with a suitable spectrum), or with discharge lamps and the optogalvanic effect<sup>61,62</sup>. A dye laser airborne DIAL system incorporating a wavelength calibration device with active feedback on the laser has been reported by Browell<sup>63</sup>.

Eye safety is an important aspect when monitoring pollution close to the ground in urban areas. The most critical wavelength region (e.g. IEC safety standards) spans from 400 nm to 1.4 μm, in which the cornea, the lens and the vitreous body of the eye transmit the radiation. To avoid the threshold light intensity, one can make use of lower pulse energies with higher repetition rates, or of a sufficient beam expansion. The most critical pollutant measured with DIAL, regarding eye-safety, is NO<sub>2</sub> (which is preferably measured at 448 nm). Eye-safe aerosol monitoring has been performed with diode lasers at high repetition frequency (kHz or MHz for pulsed or pseudo-noise continuous-wave mode, respectively) in the 700-800 nm region<sup>64</sup>, or near 1.5 μm with OPOs<sup>65</sup> or Nd:YAG lasers Raman-shifted in D<sub>2</sub> or CH<sub>4</sub><sup>66</sup>.

When several lasers are used to generate the wavelengths of a DIAL system, the energy shot-to-shot variation can induce errors in the retrieved specie concentration when the signal is averaged over successive shots (which is the usual case). In this instance, a shot-per-shot energy monitoring is required in order that a correction can be made "a posteriori"<sup>69</sup>.

### 1.3.6 Pollutant concentration determined by differential absorption lidar (DIAL)

The analysis procedure of DIAL lidar signals is summarized as follows. The signal-to-noise ratio is enhanced by averaging both spatially (over successive range bins) and temporally (over successive shots). Smooth signals are needed in the DIAL retrieval because of the derivative in the equation (11) yielding the specie concentration. The spatial averaging is usually performed either with a sliding average or a fit<sup>3</sup> (linear, polynomial, exponential). Sophisticated smoothing techniques have been proposed by some authors<sup>73-76</sup>, nevertheless bringing no very significant improvement. The smoothing procedure has been shown critical only in the cases of low SNR or high spatial specie variability<sup>3</sup>. The offset of the signal is subtracted, which has its origin in the solar background, the detector dark current and the analog-to-digital pedestal level. The range of the measurement is identified, which is determined at one end by the range of full overlap of the laser beam with the telescope field-of-view, and at the other end by the lowest allowable SNR. A first specie concentration profile is determined with equations (11) or (12). For species with broad absorption features (O<sub>3</sub>, Cl<sub>2</sub>), which implies a large separation between the two wavelengths (5-20 nm), corrections have to be applied which take into account all wavelength-dependent parameters: molecular and aerosol extinction and backscattering, and absorption by gases with overlapping lines. In the example of DIAL ozone, the wavelength pair is chosen such as to make the differential absorption of SO<sub>2</sub> to vanish (SO<sub>2</sub> is otherwise difficult to model in polluted environments), while the interference of O<sub>2</sub> is corrected with model concentration profiles. The correction of the molecular extinction and backscattering is performed either with climatological models, or with independent measurement (e.g. balloonborne). The correction of the aerosol interference is difficult to perform because no modelling can be done in polluted environments, and the lidar signal itself is not sufficient to retrieve unambiguously the aerosol microphysical parameters (§1.3.3). Strong aerosol loading and gradients are one of the characteristics of polluted air masses, and represent one major source of uncertainty in DIAL ozone measurements of the mixed layer. Several aerosol correction schemes are outlined below.

## Section 1: Introduction

The Browell algorithm<sup>77</sup> is the mostly used aerosol correction scheme. It makes use of the Fernald-Klett method (§1.3.3) at the less absorbed wavelength ( $\lambda_{off}$ ) to deduce  $\alpha$  and  $\beta$  at both wavelengths, and hence correct for differential absorption. It has the drawback to require three parameters that must be guessed "a priori": the extinction-to-backscatter ratio profile,  $\beta_a^{ref}$  at  $\lambda_{off}$ , and the extinction or backscattering wavelength dependence. These uncertainties can lead to 100% error on the ozone measurement<sup>3</sup>. The correction is enhanced when less "a priori" parameters have to be guessed, such as when more than two wavelength channels (elastic or Raman) are recorded<sup>78</sup>. Alternatively to making guesses on the aerosol microphysical properties, a "dual-DIAL" scheme has been proposed<sup>79,80</sup>, which uses at least three wavelengths in order to form two pairs, and performs a double differentiation for the retrieval of ozone. When the wavelengths are suitably located, the aerosol interference is more reduced than the ozone differential absorption cross section, hence reducing the retrieved ozone relative error with respect to the single differentiation performed with one wavelength pair (the improvement has been estimated as a factor of two in reduction in the aerosol interference).

### 1.3.7 Lidar error analysis

The accuracy analysis of lidar systems has been treated by Measures<sup>1</sup>. Several specific studies concerning DIAL systems have been reported<sup>3,26,81,82,86,88</sup>. The factors determining the accuracy in lidar measurements are summarized in table 2.

The calibration of lidar instruments can be performed by comparison with "in-situ" sensors mounted on balloons or aircraft, or by using several instruments side-by-side which probe the same atmospheric volume. Such comparative measurements are difficult due to the fact that different atmospheric volumes are usually probed by the different instruments, at different times. The instruments yield profiles with different spatial and temporal resolution. These points are critical in the mixed layer because of the high temporal and spatial variability of the pollutants. "In situ" instruments comprise<sup>3</sup> electrochemical sondes (ECC and Brewer-Mast), UV-absorption photometer, and differential optical absorption spectroscopy (DOAS). A non-exhaustive list of accuracy assessments is given in ref. [77,84,85]. A thorough intercalibration study of tropospheric DIAL ozone instruments has been reported by Bösenberg and al.<sup>3</sup>.

An alternative lidar calibration consists in using an optical path along which point monitors are installed (on buildings, towers, tethered balloons). This method is frequently used in lidar monitoring of industrial emissions<sup>87,88</sup>.

## Section 1: Introduction

**Table 2.** Factors determining the accuracy in lidar measurements. This table is reproduced from Fredriksson<sup>26</sup>.

---

Random error (detector shot-noise and atmospheric scattering fluctuations):
Atmospheric backscattered signal fluctuations
Sky background radiance
Detector dark current
Photodiode and pre-amplification thermal noise
Factors depending on atmospheric conditions:
Multiple-scattering effects
Temporal noncorrelation
Temporal and spatial averaging
Receiving system:
Photomultiplier signal-induced-noise
Linearity of the detector and the preamplifier
Timing of the transient digitizer (pseudo-random continuous-wave mode)
Factors related to the atmospheric species absorption properties (DIAL):
Uncertainties in the absorption cross sections
Overlapping absorption profiles from several species
Laser wavelength calibration
Laser spectral purity, when the probed absorption line is narrow
Laser bandwidth with respect to the absorption line bandwidth
Wavelength differential spatial-, and temporal-dependent factors:
Differential scattering (extinction and backscattering) of molecules and aerosols
Differential absorption of species other than probed
Differential overlap functions and misalignment effects
Differential atmospheric status, when the pulses are not emitted simultaneously

---

## References

1. Raymond M. Measures, "Laser remote sensing, fundamentals and applications", Wiley (New-York, 1984).
2. *Advances in Remote Sensing with Lidar*, A. Ansmann, R. Neuber, P. Rairoux, U. Wandinger Eds. (Springer, Berlin, 1996).
3. Final report to the project EUROTRAC/TESLAS, "Tropospheric Environmental Studies by Laser Sounding", Jens Bösenberg Ed. (Max-Planck Institut für Meteorologie, Hamburg, Germany), Commission of the European Communities, in press.
4. N. Takeuchi, N. Sugimoto, H. Baba, K. Sakurai, "Random modulation cw lidar", *Appl. Opt.*, **22**, 1382-1386 (1983).
5. N. Takeuchi, H. Baba, K. Sakurai, T. Ueno, "Diode-laser random-modulation cw lidar", *Appl. Opt.*, **25**, 63-67 (1986).
6. V. Mitev, R. Matthey, D. Reusser, "Development of a PRN-cw total backscatter lidar", in *European Symposium on Optics for Environmental and Public Safety*, June 20-23, 1995, Munich, Germany, Proceedings SPIE, 2505, 150-160 (1995).
7. C. Nagasawa, M. Abo, H. Yamamoto, O. Uchino, "Random modulation cw lidar using new random sequence", *Appl. Opt.*, **29**, 1466-1470 (1990).

## Section 1: Introduction

8. *Handbook of Geophysics and the Space Environment*, A. S. Jursa Ed., Air Force Geophysics Laboratory, Hanscom AFB, MA, (1985).
9. J. A. Reagan, M. P. McCormick, J. D. Spinhirne, "Lidar sensing of aerosols and clouds in the troposphere and stratosphere", *Proc. of the IEEE*, **77**, 433-448 (1989).
10. W. Krichbaumer, Ch. Werner, "Current state-of-the-art of lidar inversion methods for atmospheres of arbitrary optical density", *Appl. Phys. B*, **59**, 517-523 (1994).
11. M. C. W. Sandford, "Laser scatter measurements in the mesosphere and above", *J. Atmos. Terr. Phys.*, **29**, 1657-1662 (1967).
12. F. G. Fernald, B. M. Herman, J. A. Reagan, "Determination of aerosol height distributions by lidar", *J. Appl. Meteorol.*, **11**, 482-489 (1972).
13. J. D. Klett, "Lidar inversion with variable backscatter/extinction ratios", *Appl. Opt.*, **24**, 1638-1643 (1985).
14. H. Edner, K. A. Fredriksson, H. Hertz, S. Svanberg, "UV lidar techniques for atmospheric NO monitoring", Report n° LRAP-21, Lund Institute of Technology, Sweden.
15. H. J. Kölsch, P. Rairoux, J. P. Wolf, L. Wöste, "Simultaneous NO and NO<sub>2</sub> DIAL measurement using BBO crystals", *Appl. Opt.*, **28**, 2052-2056 (1989).
16. H. J. Kölsch, "Probing the atmosphere: air pollution studies by lidar", PhD dissertation, Free University of Berlin (1990).
17. L. T. Molina, M. J. Molina, "Absolute absorption cross sections of ozone in the 185- to 350-nm wavelength range", *J. Geophys. Res.*, **91**, 14501-14508 (1986).
18. R. J. Paur, A. M. Bass, "The ultraviolet cross sections of ozone, II, results and temperature dependence", in *Atmospheric Ozone, Proceedings of the Quadriennial Ozone Symposium, Halkidiki, Greece*, edited by C. Zerefos and A. Ghazi, pp. 611-616 (D. Reidel, Hingham, MA, 1985).
19. M. J. T. Milton, P. T. Woods, B. W. Jolliffe, N. R. W. Swann, T. J. McIlveen, "Measurements of toluene and other aromatic hydrocarbons by differential-absorption lidar in the near-ultraviolet", *Appl. Phys. B*, **55**, 41-45 (1992).
20. R. L. Byer, M. Garbuny, "Pollutant detection by absorption using Mie scattering and topographic targets as retroreflectors", *Appl. Opt.*, **12**, 1496-1505.
21. H. Edner, G. W. Faris, A. Sunesson, S. Svanberg, "Atmospheric atomic mercury monitoring using differential absorption lidar techniques", *Appl. Opt.*, **28**, 921-930 (1989).
22. D. J. Brassington, "Sulfur dioxide absorption cross section measurements from 290 to 317 nm", *Appl. Opt.*, **20**, 3774-3779 (1981).
23. S. L. Manatt, A. L. Lane, "A compilation of the absorption cross section of SO<sub>2</sub> from 106 to 403 nm", *J. Quant. Spectrosc. Radiat. Transfer*, **50**, 267-276 (1993).
24. A. C. Vandaele, P. C. Simon, J. M. Guilmot, M. Carleer, R. Colin, "SO<sub>2</sub> absorption cross section measurement in the UV using a Fourier transform spectrometer", *J. Geophys. Res.*, **99**, 25599-25605 (1994).

Section 1: Introduction

25. T. A. Jacobs, R. R. Giedt, "Absorption coefficients of Cl<sub>2</sub> at high temperatures", *J. Quant. Spectrosc. Radiat. Transfer*, **5**, 457-463 (1965).
26. K. A. Fredriksson, "Differential absorption lidar for pollution mapping", in *Laser remote chemical analysis*, R. M. Measures Ed. (Wiley, New-York, 1988).
27. J. G. Calvert, J. N. Pitts Jr., *Photochemistry* (Wiley, New-York, 1966).
28. W. R. Stockwell, J. G. Calvert, "The near ultraviolet absorption spectrum of gaseous HONO and N<sub>2</sub>O<sub>3</sub>", *J. Photochem.*, **8**, 193 (1978).
29. P. T. Woods, B. W. Joliffe, "Experimental and theoretical studies related to a dye laser differential lidar system for determination of atmospheric SO<sub>2</sub> and NO<sub>2</sub> concentrations", *Optics Laser Tech.*, **10**, 25-28 (1978).
30. J. B. Koffend, J. S. Holloway, M. A. Kwok, R. F. Heidner III, "High resolution absorption spectroscopy of NO<sub>2</sub>", *J. Quant. Spectrosc. Radiat. Transfer*, **37**, 449-453 (1987).
31. E. D. Hinkley, "Laser spectroscopic instrumentation and techniques: long path monitoring by resonance absorption", *Opt. Quant. Electr.*, **8**, 155-167 (1976).
32. G. Krüger, "Optoacoustic measurement of HCl specific absorption coefficients at DF laser wavelengths", *Appl. Opt.*, **21**, 2841-2844 (1982).
33. E. R. Murray, J. E. van der Laan, J. G. Hawley, "Remote measurement of HCl, CH<sub>4</sub>, and NO<sub>2</sub> using single-ended chemical laser system", *Appl. Opt.*, **15**, 3140-3148 (1976).
34. J. Altmann, P. Pokrowsky, "Sulfur dioxide absorption at DF laser wavelengths", *Appl. Opt.*, **19**, 3449-3452 (1980).
35. A. Mayer, J. Comera, H. Charpentier, C. Jaussaud, "Absorption coefficients of various pollutant gases at CO<sub>2</sub> laser wavelengths; application to the remote sensing of those pollutants", *Appl. Opt.*, **17**, 391-393 (1978).
36. N. Menyuk, D. K. Killinger, W. E. DeFeo, "Laser remote sensing of hydrazine, MMH, and UDMH using a differential-absorption CO<sub>2</sub> lidar", *Appl. Opt.*, **21**, 2275-2286 (1982).
37. W. Englisch, W. Wiesemann, J. Boscher, M. Rother, F. Lehman, "Laser remote sensing measurements of atmospheric species and natural target reflectivities", in *Optical and Laser Remote Sensing*, D. K. Killinger, A. Mooradian Eds., (Springer, Berlin, 1983).
38. N. Takeuchi, H. Shimizu, M. Okuda, "Detectivity estimation of the DAS lidar for NO<sub>2</sub>", *Appl. Opt.*, **17**, 2734-2738 (1978).
39. L. S. Rothman et al., "The HITRAN molecular database: editions of 1991 and 1992", *J. Quant. Spectrosc. Radiat. Transfer*, **48**, 469-507 (1992).
40. R. S. McDowell, "Vibrational spectroscopy using tunable lasers", in *Vibrational Spectra and Structure*, J. R. Durig Ed. (Elsevier, New-York, 1981).
41. H. Müller, H. Quenzel, "Information content of multispectral lidar measurements with respect to the aerosol size distribution", *Appl. Opt.*, **24**, 648-654 (1985).
42. Edward E. Uthe, "Cooling tower plume rise analyses by airborne lidar", *Atmos. Environ.*, **18**, 107-119 (1984).

*Section 1: Introduction*

43. M. J. T. Milton, "Tunable lasers for DIAL applications", *Rev. Laser Eng., Special Issue on Laser Radar*, **23**, 93-96 (1995).
44. E. V. Browell, "Differential absorption lidar sensing of ozone", *Proc. IEEE*, **77**, 419-432 (1989).
45. M. J. T. Milton, T. J. Mc Iveen, D. C. Hanna, P. T. Woods, "A high-gain optical parametric amplifier tunable between 3.27 and 3.65  $\mu\text{m}$ ", *Opt. Comm.*, **93**, 186-190 (1992).
46. G. Ehret, C. Kiemle et al., *Appl. Opt.*, **32**, 4534 (1993).
47. R. Toriumi, H. Tai, N. Takeuchi, "Tunable solid-state blue laser differential absorption lidar system for  $\text{NO}_2$  monitoring", *Opt. Eng.*, **35** (1996), in press.
48. R. Toriumi, H. Tai, H. Kuze, N. Takeuchi, "NO monitoring by a tunable solid-state UV DIAL", in *Advances in Remote Sensing with Lidar*, A. Ansmann, R. Neuber, P. Rairoux, U. Wandinger Eds. (Springer, Berlin, 1996).
49. M. Uchiumi, O. Choo Chee, K. Muraoka, M. Maeda, O. Uchino, "DIAL measurement of  $\text{CH}_4$ ,  $\text{CO}_2$ ,  $\text{CO}$  and  $\text{N}_2\text{O}$  using a tunable IR source based on the Ti:sapphire laser", *Proc. 17th International Laser Radar Conference*, 25-29 July 1994, Sendai, Japan.
50. R. Trebino, S. E. Bisson, K. W. delong, M. Mitchell, A. Jacobson, "A compact, robust, instantaneously tunable harmonic generator for lidar applications", in *Advances in Remote Sensing with Lidar*, A. Ansmann, R. Neuber, P. Rairoux, U. Wandinger Eds. (Springer, Berlin, 1996).
51. M. Stalder, B. H. Chai et al., *Appl. Phys. Lett.*, **58**, 216 (1991).
52. S. Cha, K. P. Chan et al., *Appl. Opt.*, **30**, 3938 (1991).
53. N. Menyuk, D. K. Killinger, "Atmospheric remote sensing of water vapor, HCl and  $\text{CH}_4$  using a continuously tunable Co:MgF<sub>2</sub> laser", *Appl. Opt.*, **26**, 3061-3065 (1987).
54. P. Rambaldi, M. Douard, J.-P. Wolf, "New UV tunable solid-state lasers for lidar applications", *Appl. Phys. B*, **61**, 117-120 (1995).
55. V. Mitev, I. Grigorov, V. Simeonov, "Lidar measurement of atmospheric extinction profiles: a comparison between two techniques - Klett inversion and pure rotational Raman scattering methods", *Appl. Opt.*, **31**, 6469 (1992).
56. J. B. Abshire, J. A. Rall, "AlGaAs aerosol lidar - theory and measurements", in *Optical Remote Sensing of the Atmosphere*, OSA 6th topical meeting, March 8-12 1993, Salt Lake City, Utah.
57. W. B. Grant, K. H. Kagann, W. A. McClenny, "Optical remote measurement of toxic gases", *J. Air Waste Manage. Assoc.*, **42**, 18-30 (1992).
58. R. C. Eckerdt, Y. X. Fan, R. L. Byer, R. K. Route, R. S. Feigelson, J. van der Laan, *Appl. Phys. Lett.*, **47**, 786-788 (1985).
59. A. Harasaki, S. Nishioka, M. Sugii, Y. Uchida, S. Ohkuma, J. Sakuma, "Second harmonic generation of short pulse, high peak-power, line-narrowed TEA- $\text{CO}_2$  laser using a AgGaSe<sub>2</sub> crystal", *Proc. 17th International Laser Radar Conference*, 25-29 July 1994, Sendai, Japan. Also in *Advanced Solid-State Lasers: Technical Digest*, OSA topical meeting, New-Orleans, 1-4 Feb., 1993.

## Section 1: Introduction

60. M. J. T. Milton, T. D. Gardiner, G. Chourdakis, P. T. Woods, "Injection seeding of an infrared optical parametric oscillator with tunable diode laser", *Opt. Lett.*, 281-283 (1994).
61. J. R. Nestor, "Optogalvanic spectra of neon and argon in glow discharge lamps", *Appl. Opt.*, **21**, 4154-4157 (1982).
62. A.-L. Egebäck, K. A. Fredriksson, H. M. Hertz, "DIAL techniques for the control of sulfur dioxide emission", *Appl. Opt.*, **23**, 722-729 (1984).
63. E. V. Browell, A. F. Carter et al., "NASA multipurpose airborne DIAL system and measurements of ozone and aerosol profiles", *Appl. Opt.*, **22**, 522-534 (1983).
64. V. Mitev, R. Matthey, L. Schoulepnikoff, S. Pershin, A. Bukharin, "Comparative test of PRN-cw and micro-joule pulsed total backscatter lidars", in *Advances in Remote Sensing with Lidar*, A. Ansmann, R. Neuber, P. Rairoux, U. Wandinger Eds. (Springer, Berlin, 1996).
65. J. D. Spinhirne, J. A. Rall, V. S. Scott, "Compact eye-safe lidar systems", *Rev. Laser Eng., Specie Issue on Laser Radar*, **23**, 112-118 (1995).
66. W. Carnuth, T. Trickl, "A powerful eyesafe infrared aerosol lidar: application of stimulated Raman backscattering of 1.06  $\mu\text{m}$  radiation", *Rev. Sci. Instrum.*, **65**, 3324-3331 (1994).
67. A. Harasaki, S. Nishioka, M. Sugii, Y. Uchida, S.
68. J. Reichardt, U. Wandinger, M. Serwazi, C. Weitkamp, "Combined Raman lidar for aerosol, ozone and moisture measurements", *Opt. Eng.*, **35**, 1457-1465 (1996).
69. L. Fiorani, E. Durieux, B. Calpini, M. Flamm, L. Jaquet, H. van den Bergh, "Tropospheric ozone measurements over the Great Athens area during the MEDCAPHOT-TRACE campaign with a new shot-per-shot DIAL instrument - part A: experimental system and measurements", *Atmos. Environ.*, in press.
70. M. Tanaka, S. Sakurai et al., "Possibility of photon counting in the near infrared (0.8-1.5  $\mu\text{m}$ ) region by Ge-APD", *Proc. 17th International Laser Radar Conference*, 25-29 July 1994, Sendai, Japan.
71. M. P. Bristow, D. H. Bundy, A. G. Wright, "Signal linearity, gain stability, and gating in photomultipliers: application to differential absorption lidars", *Appl. Opt.*, **34**, 4437-4452 (1995).
72. H. S. Lee, G. K. Schwemmer, C. L. Korb, M. Dombrowski, C. Prasad, "Gated photomultiplier response characterization for DIAL measurements", *Appl. Opt.*, **29**, 3603-3612 (1990).
73. R. E. Warren, "Adaptive Kalman-Bucy filter for differential absorption lidar time series data", *Appl. Opt.*, **26**, 4755-4760 (1987).
74. R. E. Warren, "Concentration estimation from differential absorption lidar using nonstationary Wiener filtering", *Appl. Opt.*, **28**, 5047-5051 (1989).
75. V. A. Kovalev, J. L. McElroy, "Differential absorption lidar measurement of vertical ozone profiles in the troposphere that contains aerosol layers with strong backscatter gradients: a simplified version", *Appl. Opt.*, **33**, 8393-8401 (1994).

## Section 1: Introduction

76. V. A. Kovalev, M. P. Bristow, J. E. McElroy, "A nonlinear approximation technique for determining vertical ozone concentration profiles with a differential absorption lidar", *Appl. Opt.*, in press.
77. E. V. Browell, S. Ismail, S. T. Shipley, "Ultraviolet DIAL measurement of O<sub>3</sub> in regions of spatially inhomogeneous aerosols", *Appl. Opt.*, **24**, 2827-2836 (1985).
78. V. Matthias, J. Bösenberg, V. Wulfmeyer, "Comparison of retrieval methods in tropospheric ozone DIAL: the impact of Raman measurements", in *Advances in Remote Sensing with Lidar*, A. Ansmann, R. Neuber, P. Rairoux, U. Wandinger Eds. (Springer, Berlin, 1996).
79. V. Kovalev, M. Bristow, "Compensational three-wavelength DIAL technique for reducing the influence of differential scattering on ozone concentrations measurements", *Appl. Opt.*, in press.
80. Z. Wang, J. Zhou, H. Hu, Z. Gong, "Evaluation of dual differential absorption lidar based on Raman-shifted Nd:YAG or KrF laser for tropospheric ozone measurements", *Appl. Phys. B*, **62**, 143-147 (1996).
81. G. Mégie, R. T. Menzies, "Complementarity of UV and IR differential absorption lidar for global measurements of atmospheric species", *Appl. Opt.*, **19**, 1173-1183.
82. N. Menyuk, D. K. Killinger, "Assessment of relative error sources in IR DIAL measurement accuracy", *Appl. Opt.*, **22**, 2690-2698 (1983).
83. C. Flesia, P. Schwendemann, "Multiple-scattering lidar experiments", *Appl. Phys.*, **B60**, 313 (1995); L. R. Bissonnette, P. Brusaglioni et al., "Lidar multiple scattering from clouds", *Appl. Phys.*, **B60**, 355-362 (1995).
84. M. Beekmann, G. Ancellet, G. Mégie, H. G. Smith, D. Kley, "Intercomparison campaign of vertical ozone profiles including electrochemical sondes of ECC and Brewer-Mast type and a ground-based UV-differential absorption lidar", *J. Atmos. Chem.*, **19**, 259-288 (1994).
85. J. A. Sunesson, A. Apituley, D. P. J. Swart, "Differential absorption lidar system for routine measurement of tropospheric ozone", *Appl. Opt.*, **33**, 7045-7058 (1994).
86. H. E. Joergensen, T. Mikkelsen, J. Streicher, H. Herrmann, Ch. Werner, "Lidar calibration experiments", *Appl. Phys. B*, in press.
87. R. A. Robinson, P. T. Woods, M. J. T. Milton, "DIAL measurements for air pollution and fugitive loss monitoring", in *Air and Pollution Monitoring*, 20-23 June 1995, Munich, FRG, pp.140-149 (SPIE n°2506).
88. M. J. T. Milton, P. T. Woods, R. H. Partridge, B. A. Goody, "Calibration of DIAL and open path systems using external gas cells", in *Air and Pollution Monitoring*, 20-23 June 1995, Munich, FRG, pp. 680-688 (SPIE n°2506).



## **1.4 Organization of the report**

As a summary of chapter 1.3.5, Raman cells are the preferred wavelength-shifters in a number of applications, such as differential absorption lidar (DIAL) or laser ranging. The lack of tunability of the Raman cells is compensated by the high efficiency and simplicity of the setup. The large extent of the ozone Hartley band (fig. 6) allows the use of Raman cells in DIAL instruments. In most other DIAL applications, a (quasi-) continuously tunable laser is required. Dye lasers have the drawback of the volume, maintenance and the relatively low efficiency. Various solid-state sources are available in the ultraviolet, which are more compact and easy to maintain than dye lasers. The titanium-doped sapphire (Ti:Al<sub>2</sub>O<sub>3</sub>) and alexandrite (Cr:Be<sub>2</sub>O<sub>4</sub>) lasers emit in the 240-315 and 240-270 nm range respectively, when tripled. The Ce:LiSAF emits in the 280-300 nm range when pumped with the Nd:YAG fourth harmonic. OPOs are also tunable source alternatives. All-in-all, KrF or quadrupled Nd:YAG lasers pumping Raman cells remain at the time being the simplest and most efficient laser source for the DIAL measurement of tropospheric ozone.

The present research focuses on high-gain single-pass (HG-SP) Raman cells in the ultraviolet, with applications in the DIAL measurement of tropospheric ozone. Two numerical and two experimental studies were conducted on the Raman cell characterization and its configuration in the DIAL instrument.

The pump beam propagation and conversion in the Raman cell is numerically modelled (sections 2 and 3). It is described here with the nonlinear Maxwell wave equation. The Stokes sequential generation results in a coupled set of partial differential equations (PDE). In a HG-SP configuration, the nonlinear coupling is very strong (the full conversion process occurs in the waist region), which leads to a complex beam interaction pattern. The high gain is a situation difficult to handle for numerical solvers of the PDE system of equations: they can give rise to numerical artefacts which can be confused with a physical phenomenon. Various numerical methods are analyzed and compared, and a suitable scheme proposed (section 2). The numerical model is used in form of a stimulated Raman scattering parametric study (section 3). General principles are deduced which help the interpretation of the stimulated Raman scattering physics in a HG-SP configuration, and to compare the results obtained with different Raman cell experimental setups.

Several previous works aimed at the experimental study of Raman cells in the UV. The characterization is however not complete. An experimental investigation is carried out here in view to complement these works (section 4). In particular, a more complete parametric study is conducted, the quality of the shifted beams is characterized, and the feasibility of a mixture of two Raman-active gases is investigated.

The experimental work also aimed at the optimization of the Raman cells in view of their implementation in the ozone DIAL (section 5). The conversion efficiency and the Stokes beam quality are the parameters optimized. The best configuration of the Raman cell in terms of pump energy, lens focal length and gas partial pressures, are determined for the particular laser used. To this end, the pump beam energy stability and drift, as well as its quality, are taken into account. A comparison is made with the performance obtained by another group, using a similar setup but a different model of pump laser.

Several possibilities exist of forming the ozone DIAL wavelength pair out of the Raman-shifted spectrum, since the Hartley absorption band extent is larger than the separation between adjacent Raman-shifted wavelengths. Joint lidar measurements and photochemical airshed modellings are undertaken by some groups (including EPFL/LPAS). The need to comply to the airshed modelling requires a complete parametric study of the DIAL wavelength optimization. A computer code has been developed, which simulates the lidar (transmitter, receiver) together with the propagation of the laser beams in the atmosphere and the interaction with its constituents. The lidar computer modelling helps to define some optimal ozone DIAL configurations in relation with the needs of the pollution airshed modelling.

## *Section 1: Introduction*

Two related researches were conducted at the LPAS in the same time as this one. Biemann<sup>7</sup> performed a Raman cell optimization with another laser than here (section 5), and contributed to the ozone DIAL wavelength optimization. Jeker<sup>8</sup> automated the beam quality measurement, and contributed to the practical implementation of the Raman cells in the DIAL frame.

### **1.5 Status of research**

The status of research, and the original contributions of the present work, concerning the topics treated in this thesis is thoroughly discussed in the introduction of sections 2,3,4 and 6. A summary is given below.

#### *(a) Numerical method for the modelling of high-gain single-pass cascade stimulated Raman scattering in gases (section 2)*

A semi-classical model is usually used in order to describe the wave propagation in a Raman-shifting configuration (Maxwell wave equations). The numerical methods generally applied to the wave equation is either finite-difference, finite-element, or spectral (e.g. Fourier decomposition). These methods have been applied successfully to numerous cases of stimulated Raman scattering, to other nonlinear optical phenomena (self-focusing, stimulated Brillouin scattering, harmonic generation, etc.), and to integrated optics applications. Some studies have shown that finite-difference and finite-element methods are preferable to spectral methods due to a higher computational efficiency. However, all these cases represent either linear optics applications, or are characterized by a low nonlinear susceptibility.

The situation considered in this study is characterized by a high gain, which arises from the high Raman gain of the medium (characteristic of the ultraviolet spectral range), the high intensity of the pump laser, and the tight focusing. This situation contrasts with the previously considered cases of low gain. Serious difficulties were encountered which are specific to this situation of high nonlinear gain: the intensity profiles of the modelled beams were seen to be corrugated (oscillations). These effects are identified to be numerical artefacts, since they are dependent on numerical parameters (such as the grid knot density, or the spacing along the propagation axis). The numerical behaviour of the three numerical schemes under consideration is analytically analyzed. The results of the analysis are tested in the frame of a benchmark (which consists of a differential equation that is close to the one to be solved, but for which an analytical solution is known). Only the spectral method is shown to be applicable to a high-gain nonlinear situation, under certain circumstances. The proper parametrization of the spectral method is determined, and tested in typical Raman cell case studies.

#### *(b) Numerical modelling of high-gain single-pass Raman cells in the ultraviolet (section 3)*

Some of the previous numerical effort had the purpose to model Raman cells in a different configuration than the one considered in this work. Either the spectral range is different (> 500 nm), or a parallel beam configuration is considered (sometimes in a multipass cell), or a molecular medium with lower Raman gain, or lower-intensity laser sources. In these configurations, the gain is low enough so that transient effects are generally negligible, a plane-wave treatment is sufficient, and the cascade Stokes with four-wave-mixing are quasi-nonexistent. A few modellings dealt with the ultraviolet spectral range, however all in a parallel beam geometry, and some in a low-gain configuration, while others deal with a steady-state description.

A realistic model of high-gain single-pass Raman cell in the ultraviolet, in a focused pump beam geometry, shall be able to treat high gain effects, which result in cascade Stokes with four-wave-mixing, diffraction in the plane transverse to the axis of propagation (especially in

## *Section 1: Introduction*

the region of the waist), and transient effects. The previous modellings obviously include these features only partially. The model considered in sections 2 and 3 incorporate all these features, with a crude approximation of the transient effects.

The transient effects are approximated with a gain reduction in a steady-state formalism, as a means to avoid time derivatives in the wave equations. The numerical solution of the set of coupled PDE in a steady-state description requires in itself powerful computing capabilities in order to describe high-gain single-pass configurations of practical importance. The addition of the time derivative would yield a computer time of the order of weeks for typical simulated situations, with the computer which was at disposal (DEC 7620, which has a speed rate of 9329 in floating point mode (SRate FP); currently one of the quickest available machines is the Cray CS64K which has a SRate FP of 72'177), while with a steady-state description it is of the order of hours which was found tractable. The choice of performing an approximation on the time derivative rather than on the spatial derivatives is motivated by the importance of the diffraction effects for the case of a high-gain single-pass Raman configuration in a tightly focused geometry.

### *c) Experimental study of high-gain single-pass Raman shifters in the ultraviolet (section 4)*

High-gain single-pass Raman cells in the ultraviolet are still not thoroughly investigated. In fact, most of the experiments so far have concentrated on the conversion efficiency optimization for a given laser model.

In this study, a number of aspects have been studied which complement former investigations. The following features have been studied and characterized: the laser-induced breakdown in these Raman shifters; the lens focal length dependence; methane and ethane as active gas media; the influence of the pump beam quality by the use of several types and models of pump laser; the Stokes beam quality. All these aspects are important in determining the conversion efficiency and beam quality of the Stokes beams, which are the features to be optimized in practical situations of DIAL ozone lidars or laser rangars. In addition, the mixture of two Raman-active gases has been investigated ( $H_2$  &  $D_2$ ,  $H_2$  &  $CH_4$ ). Such a mixture has the advantage of requiring a single pump laser in order to generate the two operating wavelengths of a DIAL ozone lidar, and also potentially to facilitate the beam alignment for their transmission in the atmosphere.

Some of the measured features are qualitatively compared with the modelling results of section 3. The understanding gained in this manner, of the physical processes occurring in high-gain single-pass Raman shifters, allows to explain some of the commonalties and discrepancies of former studies which were carried out in different configurations.

### *d) Numerical optimization of multiwavelength ozone DIAL for pollution modelling (section 6)*

Most of the current DIAL systems for tropospheric ozone studies use two operating wavelengths, which is the minimal configuration. The aerosol correction schemes are usually performed using Klett-like algorithms (§ 1.3.3) at the least absorbed wavelength, which require the guess of some aerosol optical parameters. The wavelength numerical optimizations to date have been performed for zenith or nadir probing.

In this study, an effort has been devoted towards the compatibility of the lidar measurements with airshed photochemical pollution models. To this end, the DIAL measurement has to be flexible in terms of probing angle, range binning along the probing path, sampling time, and the atmospheric conditions (ozone and aerosol loading). The numerical simulation points out that the standard two-wavelength DIAL configuration does not allow this flexibility, and to this end that more complex DIAL configurations which involve additional wavelengths and/or detection channels are necessary. Some improved DIAL configurations are proposed. An instrument with a higher complexity would also allow the simultaneous profiling of ozone

## *Section 1: Introduction*

and water vapour, and this issue is investigated with the simulation. Simultaneous ozone and water vapour profiles have potentialities for pollution studies. The water vapour information in itself is for instance useful for meteorological and GPS issues.

## **Section 2**

# **Numerical method for the modelling of high-gain single-pass cascade stimulated Raman scattering in gases**

### **Abstract**

The nonlinear Maxwell wave equation in the paraxial approximation has been solved with three standard beam propagation methods: finite-difference (FD), finite elements (FE) and spectral (Fourier). The particular case of high-gain single-pass stimulated Raman scattering in gases has been considered because of its relevance in tuning high-power ultraviolet lasers. For weak nonlinear interaction FD and FE methods are recognized to be faster than the Fourier method while of comparable stability. This situation changes when the gain reaches a certain limit: the numerical dispersion of the FD-FE methods becomes such that only the Fourier method is applicable.

## 2.1. Introduction

The case under investigation is a situation in which a high-intensity pump beam is focused in a medium with high Raman gain, resulting in substantial conversion of the pump in a single pass. This allows a simple and robust design, which has proven very useful in applications such as lidar<sup>1-4</sup> or laser ranging<sup>5-8</sup>. For the specific needs of many applications such high-gain single-pass Raman cells (denoted “HG-SP”) are well enough characterized experimentally<sup>1-4,6-8</sup>. Nevertheless a detailed investigation is lacking, sustained by the fact that the equations describing HG-SP Raman cells cannot be solved with simple analytical tools and that the numerical studies to date are incomplete.

It is usual to describe the beam propagation in nonlinear medium with the scalar Maxwell wave equations (linear polarization) in the paraxial approximation<sup>9-11</sup>. In the frame of stimulated Raman scattering (SRS) it is applied to the pump beam and all the sequentially converted beams, which results in a system of parabolic partial differential equations that are coupled by the nonlinear interaction (SRS along with coexisting nonlinear effects). In case of HG-SP Raman cells the coupling is very strong. This is illustrated by the fact that almost all the conversion occurs in the region of the beam waist, which extent is only several times the confocal parameter. Moreover the conversion can be high to the point that the most intense beam at the cell exit can be the second or the third Stokes<sup>12</sup> (the Stokes number refers to the number of times the pump beam has been down-converted). This multi-conversion process is referred as cascade SRS. Such an efficient conversion makes the numerical method very critical.

The solution of the linear or weakly nonlinear paraxial Maxwell wave equations has been treated in a number of studies (integrated optics applications, or non-cascade SRS, see e.g. ref. 11, 21, 23, 32, 33). The usual numerical methods are the spectral<sup>15,16</sup> (Fourier) and finite-difference<sup>11,17</sup> (FD) schemes. The FD method has proven faster than the Fourier method while being of comparable stability<sup>32,33</sup>. To our knowledge these methods have never been applied to a situation of strong nonlinear interaction comparable to the one considered here of high-gain single-pass SRS. The application and critical comparison of the FD and Fourier methods to the case of HG-SP SRS is the principal aim of this study. A beam propagation method using finite elements<sup>18</sup> (FE) has also been included in this framework since FEs are often used for functions with steep gradients and are hence potentially more stable in a situation of high gain.

The extrapolation of the behaviour of numerical beam propagation methods from weak to strong nonlinear interaction is not obvious due to the numerical dispersion. The FD and FE schemes have inherent numerical dispersion which can be critical in wave propagation problems<sup>18</sup>. A high amplification provokes steep beam profiles which are thus characterized by many spatial Fourier modes, which is a situation inherently delicate to handle for numerical schemes that show numerical dispersion. The dispersion characteristics of the FD, FE and Fourier methods will thus be assessed in relation with the nonlinear interaction strength, and compared on the basis on a common theoretical formalism. Another field in which strong nonlinearities bring critical issues regarding the numerical dispersion, and more generally the stability of the method, is fluid dynamics with shock waves<sup>13,14</sup>.

The present study is undertaken in a general framework that allows its applicability to the field of beam propagation in a medium with strong nonlinear amplification. This study also takes place in an effort towards a more complete understanding of the HG-SP SRS. Regarding experimental results, the essential elements of a physical model describing HG-SP SRS are: the diffraction effects<sup>9,11,21</sup>, the Stokes cascading<sup>5,20,22</sup>, and four-wave-mixing which substantially averages the energy among the Stokes beams and gives rise to conversion at anti-Stokes wavelengths<sup>5,20</sup>. The numerical modelings of SRS to date are often not specific to a HG-SP configuration in gases<sup>11,23,24</sup>, which do not need to incorporate all the aspects

## Section 2: Numerical method

just mentioned, or are incomplete<sup>5,20</sup> in that they do not consider all these aspects. The secondary purpose of the present contribution is to present a numerical method able to solve reliably the equations of a physical model incorporating all the HG-SP SRS important elements just mentioned.

Regarding the SRS modellings published to date, an important aspect is the spectral region considered. The Raman gain in gases has a strong dependence on the pump wavelength<sup>25</sup>. For instance in H<sub>2</sub> it is 20 times larger at the Nd:YAG fundamental (1064 nm) than at its fourth harmonic (266 nm)<sup>26</sup>, which is a very strong wavelength dependence regarding the exponential amplification that characterizes the SRS. Although not limited to a specific spectral region, the present work is motivated by applications of high-power SRS in the ultraviolet (UV). The spectral dependence of the gain has the consequence that the numerical difficulties encountered in the UV are usually not met in the infrared<sup>11</sup>. Only a few of the previous modelling work is dedicated to the UV spectral range, and all of them consider a collimated pump beam and hence neglect the diffraction<sup>5,20,22</sup>. Nevertheless most applications of SRS in the UV use a focused pump geometry, due to the capability of reaching a high gain and the simplicity of the set-up<sup>1-4</sup>. In that respect the present work contributes to fill the gap that exists in this spectral region.

The question of the validity of the paraxial approximation is relevant when numerically modelling high-gain nonlinear experiments. However this approximation is justified for the case of HG-SP Raman cells with high-power commercial lasers in the UV (annex 2.B). In these devices the pump beam is focused, and the formation of laser-induced plasma of the Raman-active gas precludes the level of intensity that would render the paraxial approximation invalid.

The physical model describing HG-SP SRS in gases is presented in §2.2. Chapter 2.3 first introduces the numerical method for the solution of the differential equations of the physical model (§2.3.1 to 2.3.3). In §2.3.4 the three different methods for the diffraction are compared within the same analytical framework, in relation with the strength of the nonlinear interaction. In order to demonstrate unambiguously the considerations of §2.3.4, these methods are applied in turn to a very similar differential equation, but for which an analytical solution is known (benchmark, §2.3.5). Chapter 2.3 ends dealing with the questions of step adjustment and boundary conditions, which were found to be important as well. The numerical method being introduced and discussed in §2.3, chapter 2.4 presents numerical examples of HG-SP Raman cells. The methods for the diffraction are again compared, but through these HG-SP Raman cell examples; also, the dependence on the method parameters is shown.

### 2.2. Physical model for high-gain cascade single-pass Raman cells

As mentioned in the introduction, the physical model that is adopted to describe HG-SP Raman cells includes the focusing, the effects of diffraction, Stokes cascade and four-wave-mixing. The nonlinear scalar Maxwell wave equation is used to describe the wave propagation (semi-classical approach)<sup>9,10</sup>, and is recalled below (MKS units):

$$\nabla^2 E - \epsilon_o \mu_o \partial_t^2 E = \mu_o \partial_t^2 P \quad (1)$$

where  $E$  is the electric field and  $P=P_L+P_{NL}$  is the polarization,  $P_L$  and  $P_{NL}$  being respectively its linear and nonlinear part. Within the paraxial approximation, which holds for beams with low divergence<sup>27</sup>, and in the steady-state limit, the wave equation is transformed in a first-order equation with respect to the axis of propagation:

Section 2: Numerical method

$$\partial_x^2 \mathcal{E} + \partial_y^2 \mathcal{E} + 2ik \partial_z \mathcal{E} = -\mu_0 \omega^2 P_{\text{NL}} \exp(-ikz), \quad (2)$$

where  $z$  denotes the axis of propagation,  $x$  and  $y$  are the coordinate axes perpendicular to  $z$ ,  $k$  is the wavenumber, and  $\omega$  the angular frequency.  $\mathcal{E}$  is the slow-varying envelope of the electric field:

$$E(x, y, z, t) = \mathcal{E}(x, y, z) \exp(ikz - i\omega t), \quad (3)$$

In a Raman medium the pump field  $\mathcal{E}^P$  is frequency-downconverted to a Stokes field  $\mathcal{E}_1^s$ , which is further converted to a second Stokes field  $\mathcal{E}_2^s$ , and so on. The number of Stokes to be considered in this cascade process is dependent on the gain coefficients defined by:

$$G_j = g_j \int_{z_0}^{z_N} I_p(z) dz \quad (4)$$

which is non-dimensional and must not be confused with the so-called ‘‘gain of the medium’’  $g$ <sup>9</sup>. In (4)  $g_j$  is the gain of the medium from the  $(j-1)$ -th Stokes to the  $j$ -th Stokes,  $g_1$  being the gain of the medium from the pump to the first Stokes,  $z_0$  and  $z_N$  denote respectively the position of the cell input and exit, and  $I_p = |E^P|^2$  is proportional to the pump beam intensity in vacuum. By dimensional analysis<sup>28</sup> it can be shown that the energy spectrum at the cell exit depends solely on the gain coefficients. In case of no focusing the gain coefficient has the familiar form  $G_j = g_j I_p d$ , where  $d$  is the cell length<sup>9</sup>.

In this formalism each of the beams in the cascade process is described in the paraxial approximation. When they are coupled together solely by the stimulated Raman interaction, equ. (2) becomes<sup>9,11</sup>:

$$\begin{aligned} \nabla_{\perp}^2 \mathcal{E}^P + 2ik^P \partial_z \mathcal{E}^P &= -i \frac{(k^P)^2}{k_1^s} g_1 \mathcal{E}^P |\mathcal{E}_1^s|^2 \\ \nabla_{\perp}^2 \mathcal{E}_1^s + 2ik_1^s \partial_z \mathcal{E}_1^s &= ik_1^s g_1 \mathcal{E}_1^s |\mathcal{E}^P|^2 - i \frac{(k_1^s)^2}{k_2^s} g_2 \mathcal{E}_1^s |\mathcal{E}_2^s|^2 \\ &\dots \\ \nabla_{\perp}^2 \mathcal{E}_j^s + 2ik_j^s \partial_z \mathcal{E}_j^s &= ik_j^s g_j \mathcal{E}_j^s |\mathcal{E}_{j-1}^s|^2 - i \frac{(k_j^s)^2}{k_{j+1}^s} g_{j+1} \mathcal{E}_j^s |\mathcal{E}_{j+1}^s|^2 \\ &\dots \\ \nabla_{\perp}^2 \mathcal{E}_J^s + 2ik_J^s \partial_z \mathcal{E}_J^s &= ik_J^s g_J \mathcal{E}_J^s |\mathcal{E}_{J-1}^s|^2 \end{aligned} \quad (5)$$



Section 2: Numerical method

where  $J$  Stokes have been considered and  $\nabla_{\mathbf{T}}^2 = \partial_x^2 + \partial_y^2$ . In the right-hand-side of equ. (5) the positive terms correspond to a positive gain (i.e. amplification), while the negative terms correspond to a negative gain (i.e. depletion).

When the pumping beam is focused it is necessary to introduce the new coordinates<sup>11</sup>

$$\bar{x} = x / w_x \quad , \quad \bar{y} = y / w_y \quad (6)$$

which are left invariant upon focusing, so that the number of grid points can be kept constant.  $w_x$  and  $w_y$  are the pump beam radius in vacuum (at 86% power) resp. along the  $x$ - and  $y$ -axis, given by<sup>27</sup>:

$$w_x^2(z) = w_{ox}^2 (1 + (z - z_{fx})^2 / z_{ox}^2) \quad (7)$$

$$w_y^2(z) = w_{oy}^2 (1 + (z - z_{fy})^2 / z_{oy}^2)$$

In (7),  $z_{fx}$  and  $z_{fy}$  denote the waist position,  $z_{ox}$  and  $z_{oy}$  the Rayleigh range,  $w_{ox}$  and  $w_{oy}$  the waist size, all respectively in the  $x$ - $z$  and  $y$ - $z$  plane. When the wave equations (5) are transformed in the  $(\bar{x}, \bar{y})$  coordinates, first-order derivatives with respect to  $\bar{x}$  and  $\bar{y}$  appear; it is then more convenient to avoid them with the transformation<sup>11</sup>:

$$S_j(\bar{x}, \bar{y}, z) = \mathcal{E}_j^s(\bar{x}, \bar{y}, z) \exp \left[ i \frac{k_j^s w_{ox}^2}{2 z_{ox}^2} (z_{fx} - z) \bar{x}^2 \right] \exp \left[ i \frac{k_j^s w_{oy}^2}{2 z_{oy}^2} (z_{fy} - z) \bar{y}^2 \right] \quad (8)$$

The transform  $P$  of the pump field  $\mathcal{E}^P$  is obtained by replacing  $k_j^s$  by  $k^P$  in (8). In terms of the  $(\bar{x}, \bar{y})$  coordinates and the transformed variables, the system of equations (5) becomes:

$$\begin{aligned} \partial_z P &= T(P) - \frac{g_1}{2} \frac{k^P}{k_1^s} P |S_1|^2 \\ \partial_z S_1 &= T(S_1) + \frac{g_1}{2} S_1 |P|^2 - \frac{g_2}{2} \frac{k_1^s}{k_2^s} S_1 |S_2|^2 \\ &\dots \\ \partial_z S_j &= T(S_j) + \frac{g_j}{2} S_j |S_{j-1}|^2 - \frac{g_{j+1}}{2} \frac{k_j^s}{k_{j+1}^s} S_j |S_{j+1}|^2 \\ &\dots \\ \partial_z S_J &= T(S_J) + \frac{g_J}{2} S_J |S_{J-1}|^2 \end{aligned} \quad (9)$$

where the operator  $T$  is

Section 2: Numerical method

$$T(S_j) = \frac{i}{2k_j^s w_x^2} \partial_{\bar{x}}^2 S_j + \frac{i}{2k_j^s w_y^2} \partial_{\bar{y}}^2 S_j \quad (10)$$

$$- \frac{1}{2} \left( \partial_z \ln w_x + \partial_z \ln w_y + ik_j^s \frac{w_{ox}^2 \bar{x}^2}{z_{ox}^2 + (z - z_{fx})^2} + ik_j^s \frac{w_{oy}^2 \bar{y}^2}{z_{oy}^2 + (z - z_{fy})^2} \right) S_j$$

for the Stokes field, along with the same expression for the pump field with  $k_j^s$  replaced by  $k^p$ . The wave equations (9) are initial valued parabolic partial differential equations (PDE). Therefore the PDEs are solved by specifying the fields at the cell entrance, and propagating them along the  $z$ -axis along with specified conditions at the grid boundaries. The mostly used boundary conditions are to specify that either the sought function or its derivative are zero at the boundary.

Four-wave-mixing (FWM) between the pump and Stokes beams is a process coexisting with SRS that occurs very substantially in HG-SP Raman cells<sup>12,29-31</sup>. Apart from its averaging effect among the pump and Stokes, FWM can as well sequentially produce amplification at anti-Stokes wavelengths in a process similar to the Stokes cascade. All FWM processes are considered that satisfy the resonant condition  $\omega_j - \omega_l = \omega_m - \omega_n = \omega_R$ , where  $j, l, m, n$  index either the pump, Stokes or anti-Stokes frequencies, and  $\omega_R$  is the Raman transition frequency. The example is given below of equ. (5) for the second Stokes modified when three Stokes and one anti-Stokes are coupled by SRS and FWM<sup>5,9</sup>:

$$\begin{aligned} \nabla_{\bar{T}}^2 \mathcal{E}_2^s + 2ik_2^s \partial_z \mathcal{E}_2^s = ik_2^s g_{12} \mathcal{E}_2^s |\mathcal{E}_1^s|^2 - i \frac{(k_2^s)^2}{k_3^s} g_{23} \mathcal{E}_2^s |\mathcal{E}_3^s|^2 \\ + i \frac{(k_2^s)^2}{\sqrt{k^p k_2^s}} g_{-1p12} \mathcal{E}_1^{as*} \mathcal{E}^p \mathcal{E}_1^s \exp(iz \Delta k_{p1-12}) \\ - i \frac{(k_2^s)^2}{\sqrt{k^p k_3^s}} g_{-1p23} \mathcal{E}_1^{as} \mathcal{E}^{p*} \mathcal{E}_3^s \exp(iz \Delta k_{-13p2}) \\ + i \frac{(k_2^s)^2}{\sqrt{k_1^s k_2^s}} \frac{g_{p112}}{2} (\mathcal{E}_1^s)^2 \mathcal{E}^{p*} \exp(iz \Delta k_{11p2}) \\ - i \frac{(k_2^s)^2}{\sqrt{k_1^s k_3^s}} g_{p123} \mathcal{E}^p \mathcal{E}_1^{s*} \mathcal{E}_3^s \exp(iz \Delta k_{p312}) \end{aligned} \quad (11)$$

where  $\Delta k_{jlmn} = k_j + k_l - k_m - k_n$  determines the phase-matching of the  $(jlmn)$  FWM process. The indices  $j, l, m, n$  take the value  $p$  to denote the pump,  $-1$  for the (first) anti-Stokes, and  $1$  to  $3$  for the first to third Stokes respectively. It is assumed that only the isotropic part of the transition polarisability of the SRS processes is nonzero, so that the

## Section 2: Numerical method

FWM gain is given by<sup>9</sup>  $g_{jlmn} = (g_{jl} g_{mn})^{1/2}$ . In the latter as in equ. (11), for clarity,  $g_{jl}$  is the gain of the medium for the SRS conversion  $\omega_j \rightarrow \omega_l$  (i.e.  $l=j+1$ ), which was denoted  $g_l$  for what is before equ. (11). The wave equation for the anti-Stokes has the same form as for the pump and Stokes, exemplified at equ. (11), apart from the fact that it can only be generated by FWM coupling (except from SRS down-conversion of a previously FWM-generated anti-Stokes).

The transform of the anti-Stokes field  $\mathcal{E}_j^{as}$ , denoted  $AS_j$ , has the same form as the transform of the Stokes, equ. (8), with  $k_j^s$  replaced by the anti-Stokes wavenumber. The FWM coupling terms, as exemplified in (11), have the same form in the framework of the transformed fields  $AS_j, P, S_j$ , with the term  $\exp(iz \Delta k_{jlmn})$  replaced by

$$\exp \left[ i \Delta k_{jlmn} \left( z + \frac{w_{ox}^2}{2 z_{ox}^2} (z_{fx} - z) \bar{x}^2 + \frac{w_{oy}^2}{2 z_{oy}^2} (z_{fy} - z) \bar{y}^2 \right) \right] \quad (12)$$

### 2.3. Numerical method

The two methods mostly used in nonlinear wave propagation are first the finite difference<sup>11,32,33</sup>, and second the spectral or Fourier method<sup>15,32,33</sup>. With both methods, the PDE can be either solved in bloc, or each term is solved in turn via the so-called split-step scheme (SSS)<sup>13</sup>. The split-step option has been chosen here because it gives the freedom to choose a dedicated method for each term of the PDE, and its sequential behavior helps the analysis of the numerical schemes.

The principle of the SSS is recalled briefly. The wave equation of each beam is written in the form of a sum of operators, noted  $L_i$ , each of them corresponding to one term of the PDE. Eqs (9,10) can then be written as:

$$\partial_z S = L_1 S + L_2 S + L_3 S + L_4 S \quad (13)$$

with  $L_1$  being the  $\bar{x}$  second-derivative term,  $L_2$  the  $\bar{y}$  second-derivative term,  $L_3$  being all what in (10) is in parenthesis, and  $L_4$  gathering all the nonlinear coupling terms (SRS terms with additional (e.g. FWM) nonlinear terms). Operators  $L_1$  to  $L_4$  are denoted respectively by “x-diffraction”, “y-diffraction”, “grid adjustment”, and “nonlinear coupling”.

The PDE corresponding to each of the  $L_i$  is solved sequentially:

$$\begin{aligned} \tau^1 &= L_1(s^n) \\ \tau^2 &= L_2(\tau^1) \\ \tau^3 &= L_3(\tau^2) \\ s^{n+1} &= L_4(\tau^3) \end{aligned} \quad (14)$$

where  $s^n$  denotes the approximation to  $S$  at position  $z_n$ , and the  $\tau^i$  are intermediate values that are discarded after completion of the step  $z_n \rightarrow z_{n+1}$ . The SSS is considered to be stable as long as the individual  $L_i$  are stable. In fact, physically it corresponds to the subdivision of

## Section 2: Numerical method

the continuous medium in subsequent layers, each described by an operator  $L_i$  (that is, one layer for the diffraction along the x-axis, one for the diffraction along the y-axis, one for a sole nonlinear interaction, ...), and is asymptotically equivalent to solving the original PDE in bloc.

The methods that have been applied for each of the  $L_i$  are now presented in turn.

### 2.3.1 Method for the grid adjustment

The PDE for the grid adjustment is repeated below:

$$\begin{aligned} \partial_z S = & -\frac{1}{2} \left( \partial_z \ln w_x + \partial_z \ln w_y \right. \\ & \left. + ik \frac{w_{ox}^2 \bar{x}^2}{z_{ox}^2 + (z - z_{fx})^2} + ik \frac{w_{oy}^2 \bar{y}^2}{z_{oy}^2 + (z - z_{fy})^2} \right) S \end{aligned} \quad (15)$$

where  $S$  corresponds to one of the beams modelled ( $AS_j$ ,  $P$  or  $S_j$ ). This PDE can be solved in closed form<sup>11</sup>, which yields:

$$\begin{aligned} S(z + \Delta z) = & S(z) \sqrt{\frac{w_x(z)w_y(z)}{w_x(z + \Delta z)w_y(z + \Delta z)}} \\ & \times \exp \left[ \frac{ik}{2} \left( \frac{w_{ox}^2 \bar{x}^2}{z_{ox}} \tan^{-1} \frac{z_{fx} - u}{z_{ox}} + \frac{w_{oy}^2 \bar{y}^2}{z_{oy}} \tan^{-1} \frac{z_{fy} - u}{z_{oy}} \right) \right]_{u=z}^{u=z+\Delta z} \end{aligned} \quad (16)$$

### 2.3.2 Method for the nonlinear coupling

When the pump and only one Stokes are modeled, a closed form for the Raman terms is available<sup>11</sup>. A closed form in case of more than one Stokes has not been sought because first it is not easy to find out, and second the flexibility to introduce additional terms corresponding to complementary non-linear processes wanted to be retained.

Out of equ. (9), the equations to be solved for the Raman terms are coupled ordinary differential equations (ODE):

Section 2: Numerical method

$$\begin{aligned}
 \partial_z P &= -\frac{g_1}{2} \frac{k^p}{k_1^s} P |S_1|^2 \\
 \partial_z S_1 &= \frac{g_1}{2} S_1 |P|^2 - \frac{g_2}{2} \frac{k_1^s}{k_2^s} S_1 |S_2|^2 \\
 &\dots \\
 \partial_z S_i &= \frac{g_i}{2} S_i |S_{i-1}|^2 - \frac{g_{i+1}}{2} \frac{k_i^s}{k_{i+1}^s} S_i |S_{i+1}|^2 \\
 &\dots \\
 \partial_z S_J &= \frac{g_J}{2} S_J |S_{J-1}|^2
 \end{aligned} \tag{17}$$

In (17),  $J$  Stokes have been considered, coupled solely by Raman interaction. Complementary nonlinear interactions can be considered by adding the corresponding terms on the right-hand-side.

A physical quantity which has to be conserved by the numerical scheme during propagation is the total (pump + all Stokes) photon rate (denoted by SPR, symbol  $N_p$ ). Since the photon rate of the Stokes beam  $n^\circ i$  is proportional to  $|S_i|^2 / k_i^s$  (the same for the pump and anti-Stokes beams, with the corresponding wavenumber), the SPR will have the following proportionality:

$$N_p \propto \frac{|P|^2}{k^p} + \sum_{i=1}^J \frac{|S_i|^2}{k_i^s} \tag{18}$$

The conservation of SPR during propagation is inherent to the system of ODE (17), and is illustrated below for the case of one Stokes (the generalization to an arbitrary number of Stokes is straightforward). The ODE for the pump is multiplied by  $P^*$  and is summed with the complex conjugate of the ODE multiplied by  $P$ , which yields an ODE for the pump photon rate. After the same treatment being applied to the ODE for  $S_1$ :

$$\begin{aligned}
 \frac{1}{k_1^s} \partial_z |S_1|^2 &= g_1 k^p \frac{1}{k_1^s} |S_1|^2 \frac{1}{k^p} |P|^2 \\
 \frac{1}{k^p} \partial_z |P|^2 &= -g_1 k^p \frac{1}{k_1^s} |S_1|^2 \frac{1}{k^p} |P|^2
 \end{aligned} \tag{19}$$

The sum of the two equations in (19) results in the conservation of  $N_p$  as defined in (18).

The most straightforward numerical method for a system of ODE like (17) is an explicit scheme like the Runge-Kutta<sup>13</sup>. Unfortunately, these do not conserve the SPR. It has been noticed numerically on examples that the stronger the gain (i.e. the bigger the beams intensity or the Raman gain of the medium), the higher the level of SPR non-conservation for such explicit schemes. In a HG-SP configuration the level of gain is such that the SPR is typically more than doubled between entrance and exit of the cell.

## Section 2: Numerical method

Methods that conserve “sum quantities” like the SPR for many of the ODE characterizing physical systems are the implicit central-difference (ICD) schemes<sup>13,34</sup>. The simplest of these is obtained by evaluating each variable of both left- and right-hand-side of the system (17) at the middle of the propagation step  $[z_n, z_{n+1}]$ . It is illustrated below for the case of one Stokes, and is extended to the case of arbitrary number of Stokes in a straightforward manner:

$$\frac{P^{n+1} - P^n}{\Delta z} = - \frac{g_1}{2} \frac{k^p}{k^s} |S^{n+1/2}|^2 P^{n+1/2} \quad (20)$$

$$\frac{S^{n+1} - S^n}{\Delta z} = \frac{g_1}{2} |P^{n+1/2}|^2 S^{n+1/2}$$

where  $S^n$  and  $P^n$  denote respectively the first Stokes and the pump at propagation step  $z_n$ ,  $\Delta z = z_{n+1} - z_n$ , and  $P^{n+1/2} = (P^n + P^{n+1})/2$ ,  $S^{n+1/2} = (S^n + S^{n+1})/2$ .

The SPR conservation by scheme (20) is shown as follows. The first equation of (20) is multiplied by  $(P^{n+1/2})^*$  and the second by  $(S^{n+1/2})^*$ , which yields:

$$|P^{n+1}|^2 - |P^n|^2 + 2i \Im(P^{n*} P^{n+1}) = - g_1 \Delta z \frac{k^p}{k^s} |S^{n+1/2}|^2 |P^{n+1/2}|^2 \quad (21)$$

$$|S^{n+1}|^2 - |S^n|^2 + 2i \Im(S^{n*} S^{n+1}) = g_1 \Delta z |S^{n+1/2}|^2 |P^{n+1/2}|^2$$

where  $\Im$  denotes the imaginary part. The SPR conservation between step  $z_n$  and  $z_{n+1}$  is obtained by summing the two equations in (21) and taking the real part:

$$\frac{1}{k^p} |P^{n+1}|^2 + \frac{1}{k^s} |S^{n+1}|^2 = \frac{1}{k^p} |P^n|^2 + \frac{1}{k^s} |S^n|^2 \quad (22)$$

The system of ODE for the nonlinear coupling is generally stiff, due to the fact that the Stokes waves grow at very different rates. The Runge-Kutta scheme showed exponential instabilities in most of the examples presented in §2.4. On the other hand implicit schemes like the ICD are unconditionally stable (on the expense of the computational cost).

It is readily seen from equ. (20) that the sought quantities at step  $z_{n+1}$  are expressed in an implicit way. In order to keep the flexibility to add easily other (coexisting) nonlinear terms to the Raman ones, the nonlinear system of equation of type (20) was solved numerically, with the Newton-Raphson scheme<sup>13</sup>. The latter uses derivatives with respect to  $S$  and  $P$ , and because in (20) modulus of complex numbers are involved these derivatives do not exist. We are then forced to split the system of equations of type (20) in real and imaginary parts, which is symbolized in the following way when  $J$  Stokes are considered:

$$\mathbf{f}(\mathbf{q}^{n+1}) = 0 \quad (23)$$

where  $\mathbf{f} = (f_0, \dots, f_{2J+1})$ ,  $\mathbf{q}^{n+1} = (a_0^{n+1}, b_0^{n+1}, a_1^{n+1}, b_1^{n+1}, \dots, a_J^{n+1}, b_J^{n+1})$ ,  $P = a_0 + i b_0$  and for the  $j$ -th Stokes  $S_j = a_j + i b_j$ . The explicit relations are not given because these are cumbersome and derived from straightforward calculations, but rather it is the principle of the Newton-Raphson scheme that is now recalled.  $\mathbf{f}$  is first linearized around  $\mathbf{q}^n$ :

$$\mathbf{f}(\mathbf{q}^{n+1}) \cong \mathbf{f}(\mathbf{q}^n) + \mathbf{J}(\mathbf{q}^n)\Delta \quad (24)$$

where  $\mathbf{J}(\mathbf{q}^n)$  is the Jacobian matrix of  $\mathbf{f}$  evaluated at  $\mathbf{q}^n$  and  $\Delta = \mathbf{q}^{n+1} - \mathbf{q}^n$ . Equating equ. (24) to zero and solving the linear system yields a first approximation for  $\mathbf{q}^{n+1}$ . The same procedure is repeated, with  $\mathbf{f}$  linearized around the latest obtained approximation to  $\mathbf{q}^{n+1}$ , until the desired precision is reached.

The Newton-Raphson scheme can fail to converge when the initial guess is too far from the solution. In the present case the sought functions do not change much from  $z_n$  to  $z_{n+1}$  because the step  $\Delta z$  has typically small values, and therefore the convergence is most generally reached.

ICD schemes can easily accommodate additional nonlinear processes coexisting with SRS. The corresponding nonlinear terms are discretized the same way as for the SRS terms, equ. (20), by evaluating the field at  $z_{n+1/2}$  as an average of its values at  $z_n$  and  $z_{n+1}$ . We illustrate this procedure, along with the SPR conservation, for the case of the  $(j,l,m,n)$  four-wave-mixing, with  $j \neq l \neq m \neq n$ , when three Stokes are modeled. The nonlinear ODE system to be solved, out of the equivalent of equ. (11) for three Stokes and expressed in terms of the transformed variables  $P$  and  $S_j$ , is then:

$$\begin{aligned} \partial_z P &= -\frac{k^p}{\sqrt{k_1^s k_3^s}} \frac{g_{p123}}{2} S_1 S_2 S_3^* \exp(+), \\ \partial_z S_1 &= \frac{k_1^s}{\sqrt{k_1^s k_3^s}} \frac{g_{p123}}{2} P S_2^* S_3 \exp(-), \\ \partial_z S_2 &= -\frac{k_2^s}{\sqrt{k_1^s k_3^s}} \frac{g_{p123}}{2} P S_1^* S_3 \exp(-), \\ \partial_z S_3 &= \frac{k_3^s}{\sqrt{k_1^s k_3^s}} \frac{g_{p123}}{2} P^* S_1 S_2 \exp(+), \end{aligned} \quad (25)$$

where  $\exp(+)$  is given by equ. (12), with  $jlmn$  replaced by  $12p3$ , and  $\exp(-)$  is the same as  $\exp(+)$  but which argument has opposite sign. It can be shown out of (25) that two independent photon rate quantities are conserved upon propagation<sup>9</sup>:  $N_p^1 = |P|^2 / k^p + |S_3|^2 / k_3^s$  and  $N_p^2 = |S_1|^2 / k_1^s + |S_2|^2 / k_2^s$ . The implicit central-difference scheme applied to equ. (25) yields:

## Section 2: Numerical method

$$\begin{aligned}
 \frac{P^{n+1} - P^n}{\Delta z} &= -\frac{k^p}{\sqrt{k_1^s k_3^s}} \frac{g_{p123}}{2} S_1^{n+1/2} S_2^{n+1/2} (S_3^{n+1/2})^* \exp(+), \\
 \frac{S_1^{n+1} - S_1^n}{\Delta z} &= \frac{k_1^s}{\sqrt{k_1^s k_3^s}} \frac{g_{p123}}{2} P^{n+1/2} (S_2^{n+1/2})^* S_3^{n+1/2} \exp(-), \\
 \frac{S_2^{n+1} - S_2^n}{\Delta z} &= -\frac{k_2^s}{\sqrt{k_1^s k_3^s}} \frac{g_{p123}}{2} P^{n+1/2} (S_1^{n+1/2})^* S_3^{n+1/2} \exp(-), \\
 \frac{S_3^{n+1} - S_3^n}{\Delta z} &= \frac{k_3^s}{\sqrt{k_1^s k_3^s}} \frac{g_{p123}}{2} (P^{n+1/2})^* S_1^{n+1/2} S_2^{n+1/2} \exp(+).
 \end{aligned} \tag{26}$$

where quantities of the type  $S^{n+1/2}$  are given as in equ. (20). After dividing together the first and fourth equations of (26) we get:

$$\frac{1}{k_p} |P^{n+1}|^2 - \frac{1}{k_p} |P^n|^2 + \frac{2i}{k_p} \Im(P^{n*} P^{n+1}) + \frac{1}{k_3^s} |S_3^{n+1}|^2 - \frac{1}{k_3^s} |S_3^n|^2 + \frac{2i}{k_3^s} \Im(S_3^{n*} S_3^{n+1}) = 0 \tag{27}$$

which real part yields the conservation of  $N_p^1$  between step  $z_n$  and  $z_{n+1}$ . The same way the ICD scheme is shown to conserve  $N_p^2$ .

### 2.3.3 Method for the diffraction

As will be seen in §2.3.4, the nonlinear coupling transfers energy from the lower to the higher spatial modes, which is a situation delicate to handle for numerical diffraction solvers. It is the reason why several methods were tested for the diffraction term. They are summarized below. Most usually, diffraction solvers in the frame of nonlinear wave propagation are either implicit finite-difference (Crank-Nicolson), or spectral (Fourier) methods. When the nonlinear coupling is weak enough, both approaches are more or less equivalent speaking of stability and accuracy, with the Fourier method being nevertheless several times slower<sup>32,33</sup>.

Considering diffraction alone, the wave equations are decoupled. Taken from equ. (9,10), the diffraction equation to be solved is a parabolic initial value PDE with complex diffusion coefficient:

$$\partial_z S = \frac{i}{2k w_x^2} \partial_x^2 S + \frac{i}{2k w_y^2} \partial_y^2 S \tag{28}$$

where  $S$  corresponds to one of the beams modeled, and  $k$  its wavenumber. Using the split-step scheme, the x- and y-diffraction are solved in turn, and for the rest of this chapter, we will focus only on the x-diffraction PDE, that is:

$$\partial_z S = \frac{i}{2k w_x^2} \partial_x^2 S \tag{29}$$



## Section 2: Numerical method

When the beam has circular symmetry, equ. (28) becomes, in cylindrical coordinates:

$$\partial_z S = \frac{i}{2k w^2} \left( \partial_{\bar{r}}^2 S + \frac{1}{\bar{r}} \partial_{\bar{r}} S \right) \quad (30)$$

where  $\bar{r} = \bar{x}^2 + \bar{y}^2$  and  $w = w_x = w_y$ .

For the numerical calculations, the values of the electric field are discretized on a mesh defined as

$$\begin{cases} \bar{x}_0, \bar{x}_1, \dots, \bar{x}_l, \dots, \bar{x}_L \\ \bar{y}_0, \bar{y}_1, \dots, \bar{y}_m, \dots, \bar{y}_M \\ z_0, z_1, \dots, z_n, \dots, z_N \end{cases} \quad (31)$$

for cartesian coordinates, and are denoted by  $S_{l,m}^n$ , and

$$\begin{cases} \bar{r}_0, \bar{r}_1, \dots, \bar{r}_l, \dots, \bar{r}_L \\ z_0, z_1, \dots, z_n, \dots, z_N \end{cases} \quad (32)$$

for cylindrical coordinates, and are denoted by  $S_l^n$

### a) Finite differences

The Crank-Nicolson finite-difference scheme (denoted by FD-CN) has been retained because it conserves the beam photon rate<sup>11</sup>. The latter quantity, denoted by BPR, symbol  $N_b$ , is defined below for the cartesian and cylindrical geometries, respectively:

$$N_b = \sum_{l=0}^L \sum_{m=0}^M |S_{l,m}^n|^2, \quad N_b = \sum_{l=0}^L r_l |S_l^n|^2 \quad (33)$$

In §2.3.2 the total photon rate (SPR) was introduced, which is the sum of all the beams photon rate at a particular position (x,y,z). On the other hand, the BPR is the sum of the photon rate over the entire grid (transverse to propagation), for one particular beam. In fact, the nonlinear interaction is local and couples the beams, whereas the diffraction concerns each beam separately and couples adjacent x- or y- positions via the second-order derivative.

Within the FD-CN, the PDE (29) is discretized as follows<sup>17</sup>:

$$\frac{S_{l,m}^{n+1} - S_{l,m}^n}{\Delta z} = \frac{i}{2k w_x^2} \frac{1}{2} \left( \frac{S_{l+1,m}^n - 2S_{l,m}^n + S_{l-1,m}^n}{(\Delta \bar{x})^2} + \frac{S_{l+1,m}^{n+1} - 2S_{l,m}^{n+1} + S_{l-1,m}^{n+1}}{(\Delta \bar{x})^2} \right) \quad (34)$$

The boundary conditions (BC) considered are either  $S(x_0)=S(x_L)=0$  (Dirichlet), or  $\partial_{\bar{x}} S(x_0) = \partial_{\bar{x}} S(x_L) = 0$  (Neumann), which yields in the latter case  $S(x_0)=S(x_1)$  and  $S(x_{L-1})=S(x_L)$ . Equ. (34) results in linear tridiagonal system solving, with a cost of ca.  $2L$  operations.

The so-called ‘‘fully-implicit scheme’’ (denoted by FD-CI) approximates the derivatives at  $z_{n+1}$ , instead of making the average between  $z_n$  and  $z_{n+1}$  as the FD-CN does:

Section 2: Numerical method

$$\frac{S_{l,m}^{n+1} - S_{l,m}^n}{\Delta z} = \frac{i}{2 k w_x^2} \left( \frac{S_{l+1,m}^{n+1} - 2S_{l,m}^{n+1} + S_{l-1,m}^{n+1}}{(\Delta \bar{x})^2} \right) \quad (35)$$

which results also in linear tridiagonal system solving. The FD-CI does not conserve the BPR; this is because the tridiagonal matrix of the linear system (35) is not hermitian<sup>17</sup> (whilst the one of the FD-CN scheme (34) is hermitian). Because of this, the FD-FI scheme won't be used to solve the physical problem; rather it will be indicative of the behavior of finite difference schemes.

All the standard finite-difference methods applied to the diffraction equation in cylindrical coordinates (30) fail to conserve the BPR. Finite elements or the Fourier method are preferably used for this geometry.

b) Finite elements

We concentrate first on the cartesian coordinates. The field is expanded on basis functions  $\Psi_l$ :

$$S(x, y, z) = \sum_{l=0}^L f_l(y, z) \Psi_l(x) \quad (36)$$

The simplest choice of finite element  $\Psi_l$  is triangular linear element, as shown in fig.1. With such elements, the finite element method will further on be denoted by FLE. Higher-order elements are e.g. cubic splines. It is nevertheless recommended to use the lowest-order element that can be used with the PDE<sup>35</sup>.

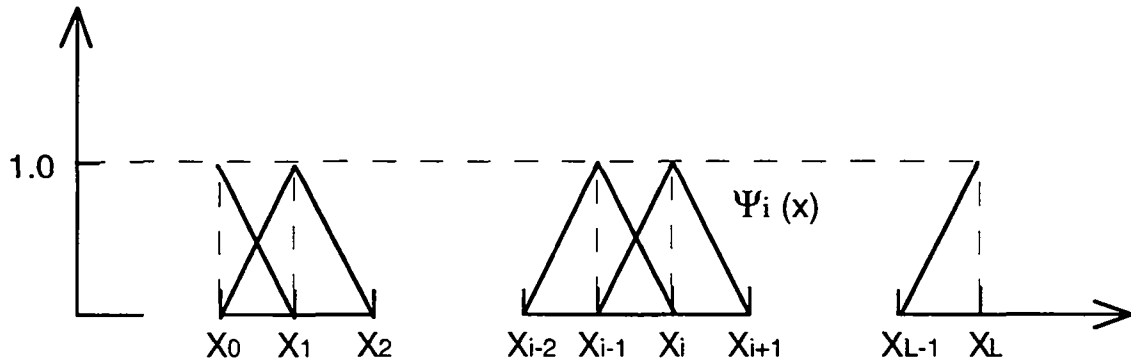


**Fig. 1.** Linear triangular element, used in the finite element method for the diffraction equation.

The application of the LFE to the diffraction equation (29), with centered integration along the z-axis in order to retain the BPR-conservation, yields the following tridiagonal system of equations<sup>18</sup>:

$$\mathbf{A}' \mathbf{f}^{n+1} = \mathbf{B}' \mathbf{f}^n \quad (37)$$

$$\mathbf{A}' = \mathbf{A} - ia \frac{\Delta z}{2} \mathbf{B} \quad , \quad \mathbf{B}' = \mathbf{A} + ia \frac{\Delta z}{2} \mathbf{B}$$

Section 2: Numerical method

where  $a(z)=[2kw_x^2(z)]^{-1}$  and  $\mathbf{f}$  is a vector defined as  $[f_0(y,z), f_1(y,z), \dots, f_L(y,z)]$ , denoted by  $\mathbf{f}^n$  when evaluated at  $z_n$ , by  $\mathbf{f}^{n+1}$  when evaluated at  $z_{n+1}$ , and  $\Delta z = z_{n+1} - z_n$ . The matrices  $\mathbf{A}$  and  $\mathbf{B}$  are given for Neumann BC by:

$$\begin{aligned} A_{11} &= 2\Delta\bar{x}/6 & A_{12} &= \Delta\bar{x}/6 \\ A_{ii-1} &= \Delta\bar{x}/6 & A_{ii} &= 4\Delta\bar{x}/6 & A_{ii+1} &= \Delta\bar{x}/6 \\ A_{LL-1} &= \Delta\bar{x}/6 & A_{LL} &= 2\Delta\bar{x}/6 \end{aligned} \quad (38.1)$$

$$\begin{aligned} B_{11} &= -1/\Delta\bar{x} & B_{12} &= 1/\Delta\bar{x} \\ B_{ii-1} &= 1/\Delta\bar{x} & B_{ii} &= -2/\Delta\bar{x} & B_{ii+1} &= 1/\Delta\bar{x} \\ B_{LL-1} &= 1/\Delta\bar{x} & B_{LL} &= -1/\Delta\bar{x} \end{aligned} \quad (38.2)$$

For Dirichlet BC, the only elements that change are:

$$\begin{aligned} A_{11} &= A_{LL} = 4\Delta\bar{x}/6 \\ B_{11} &= B_{LL} = -2/\Delta\bar{x} \end{aligned} \quad (39)$$

In case of Dirichlet BC,  $\Psi_0$  and  $\Psi_L$  must be chosen such that  $\Psi_0(x_0)=\Psi_L(x_L)=0$ , and for Neumann BC they are chosen such that  $\Psi_0(x_0)=\Psi_L(x_L)=1$ . All the matrix elements not displayed in (38)-(39) are equal to zero.  $\Delta\bar{x}$  is the mesh spacing along the  $x$ -axis, taken to be equidistant.

In case of cylindrical geometry, the matrices  $\mathbf{A}$  and  $\mathbf{B}$  of (38) are given for Neumann BC (the only choice at  $\bar{r}_0$ ) by:

$$\begin{aligned} A_{11} &= \frac{(\Delta\bar{r})^2}{12} + \frac{1}{3}\Delta\bar{r}\bar{r}_0 & A_{12} &= \frac{1}{12}\Delta\bar{r}(\bar{r}_0 + \bar{r}_1) \\ A_{i-1i} &= A_{ii-1} = \frac{1}{12}\Delta\bar{r}(\bar{r}_{i-1} + \bar{r}_i) & A_{ii} &= \frac{2}{3}\Delta\bar{r}\bar{r}_i \\ A_{LL-1} &= \frac{1}{12}\Delta\bar{r}(\bar{r}_{L-1} + \bar{r}_L) & A_{LL} &= -\frac{(\Delta\bar{r})^2}{12} + \frac{1}{3}\Delta\bar{r}\bar{r}_L \end{aligned} \quad (40.1)$$

$$\begin{aligned} B_{11} &= \frac{\bar{r}_0 + \bar{r}_1}{2\Delta\bar{r}} & B_{12} &= -\frac{\bar{r}_0 + \bar{r}_1}{2\Delta\bar{r}} \\ B_{i-1i} &= B_{ii-1} = -\frac{\bar{r}_{i-1} + \bar{r}_i}{2\Delta\bar{r}} & B_{ii} &= \frac{2\bar{r}_i}{\Delta\bar{r}} \\ B_{LL-1} &= -\frac{\bar{r}_{L-1} + \bar{r}_L}{2\Delta\bar{r}} & B_{LL} &= \frac{\bar{r}_{L-1} + \bar{r}_L}{2\Delta\bar{r}} \end{aligned} \quad (40.2)$$

The conservation of the BPR by the FLE scheme, in either cartesian or cylindrical geometry, is readily shown by seeing that  $\mathbf{A}$  and  $\mathbf{B}$  are real symmetric matrices, and hence the matrix  $\mathbf{U}$  that transforms  $\mathbf{f}^n$  to  $\mathbf{f}^{n+1}$ , which is equal to  $(\mathbf{A}')^{-1}\mathbf{B}'$ , is unitary, and as a consequence the norm of  $\mathbf{f}^n$  is equal to the norm of  $\mathbf{f}^{n+1}$ .

Section 2: Numerical method

c) Fourier (spectral) method

We begin with the cartesian geometry. The field is expanded on Fourier series truncated after  $(L+1)$  terms:

$$S(\bar{x}_l, z_n) = \sum_{j=0}^L c_j(z_n) \hat{\varphi}_j(\bar{x}_l) \quad (42)$$

where the functions  $\hat{\varphi}_j$  for Dirichlet boundary conditions are given by  $\hat{\varphi}_j = \varphi_j / \|\varphi_j\|$  and:

$$\begin{aligned} \varphi_j(\bar{x}_l) &= \sin \left[ \frac{\pi j}{\bar{x}_L - \bar{x}_0} (\bar{x}_l - \bar{x}_0) \right] \\ \|\varphi_j\|^2 &= \frac{L}{2} - \frac{(-1)^j \sin \left( \frac{j \pi L}{L+1} \right)}{2 \sin \left( \frac{j \pi}{L+1} \right)} \end{aligned} \quad (43)$$

Because the functions  $\hat{\varphi}_j$ ,  $j=0, \dots, L$ , form an orthonormal basis of all the  $(L+1)$ -dimensional vectors satisfying the Dirichlet BC, the coefficients  $c_j$  are simply given by the scalar product:

$$c_j(z_n) = \sum_{l=0}^L S(\bar{x}_l, z_n) \hat{\varphi}_j(\bar{x}_l) \quad (44)$$

which can be computed by fast Fourier transformation (FFT)<sup>13</sup>.

The diffraction PDE (29) can be solved in closed form in terms of the Fourier coefficients  $c_j$  15:

$$\begin{aligned} c_j(z_{n+1}) &= c_j(z_n) \exp(-i \lambda_j^2 A) \\ \lambda_j &= (\pi j) / (\bar{x}_L - \bar{x}_0) \end{aligned} \quad (45)$$

$$A = \frac{1}{2k} \int_{z_n}^{z_{n+1}} \frac{dz}{w_x^2(z)} = \frac{z_o}{2k w_{ox}^2} \tan^{-1} \left( \frac{u - z_{fx}}{z_{ox}} \right) \Bigg|_{u=z_n}^{u=z_{n+1}}$$

The numerical solution of the diffraction PDE with the Fourier method is updated as follows:

- The Fourier coefficients  $c_j$  of  $S$ ,  $j=0, 2, \dots, L$ , at  $z_n$ , are computed with (44) by FFT.
- The  $c_j$  are updated with (45).
- $S$  at  $z_{n+1}$  is calculated with the inverse transformation of equ. (44):

$$S(z_{n+1}, \bar{x}_l) = \sum_{j=0}^L c_j(z_{n+1}) \hat{\varphi}_j(\bar{x}_l) \quad (46)$$

Section 2: Numerical method

which can also be worked out by FFT.

For the cylindrical geometry the fields are better represented within the frame of Fourier-Bessel integrals (transforms) rather than with associated series. The Fourier-Bessel transform is defined as follows:

$$\tilde{S}(\rho) = 2\pi \int_0^{\infty} \bar{r} S(\bar{r}) J_0(2\pi\rho\bar{r}) d\bar{r} \quad (47)$$

where  $J_0$  is the zero-th order Bessel function. Practically, the integration extends from  $\bar{r}_0$  to  $\bar{r}_L$ , which must be chosen such that  $\bar{r}_0$  is sufficiently close to 0 and  $\bar{r}_L$  sufficiently big in order for the boundary conditions to hold. The inverse transform has the same form as (47).

The procedure to update the numerical solution is similar to the case of cartesian geometry<sup>15</sup>:

- The Fourier-Bessel transform  $\tilde{S}(\rho, z)$  of  $S(\bar{r}, z)$  is calculated.
- $\tilde{S}$  is updated with  $\tilde{S}(z + \Delta z, \rho) = \tilde{S}(z, \rho) \exp[-i(2\pi\rho)^2 A]$  (48)
- The inverse Fourier-Bessel transform  $S(z + \Delta z, \bar{r})$  of  $\tilde{S}(z + \Delta z, \rho)$  is calculated.

Several methods exist that allow to compute the Fourier-Bessel transform efficiently (denoted by FHT - Fast Hankel Transform), that is, in a “FFT-fashion”<sup>36,37</sup>, out of which the method of Siegman<sup>36</sup> was chosen. This method uses an exponential mesh, and has several parameters which showed to be delicate to choose. The parameter  $\alpha$  defines the mesh spacing by  $\bar{r}_l = \bar{r}_0 e^{\alpha l}$ ,  $\rho_l = \rho_0 e^{\alpha l}$ , for  $l=0,1,\dots,L$ .  $\bar{r}_0 = \bar{r}_L e^{-\alpha L}$  and  $\rho_0 = \rho_L e^{-\alpha L}$  are the minimal radius, which determines a disk centered at the origin that is not taken into account by the method. Parameters  $\{\alpha, \bar{r}_0, \rho_0\}$  are to be chosen such that  $\bar{r}_0$  and  $\rho_0$  are as small as possible, and thus the “aperturing effect” is minimized, while the biggest spacings  $\Delta\bar{r}_L = \bar{r}_L - \bar{r}_{L-1}$  and  $\Delta\rho_L = \rho_L - \rho_{L-1}$  are kept also as small as possible. Our experience on benchmarks showed that  $\rho_0$  is generally to be chosen smaller than  $\bar{r}_0$ , because for beams decaying asymptotically exponentially on the r-axis,  $\tilde{S}(\rho)$  is of smaller width (i.e. standard deviation) than  $S(\bar{r})$ . An additional parameter  $\xi$  is defined as  $\rho_0 = \bar{r}_0 / \xi$ , and another one  $K_2$  determines the sampling on the  $\rho$ -axis:  $\Delta\rho_L = (K_2 \bar{r}_L)^{-1}$ .

In practice, the parameters are determined as follows:

- Choose  $\xi$  and  $K_2$ . Generally  $\xi$  was selected to be between 1 and 3, and  $K_2 = 4$ .
- $\bar{r}_L$  and  $\Delta\bar{r}_L$  are chosen with the constraint  $\bar{r}_L \Delta\bar{r}_L = \xi / K_2$ .
- Parameters  $\alpha$ ,  $\bar{r}_0$ , and  $\rho_0$  are then calculated as:

Section 2: Numerical method

$$\alpha = \frac{\xi}{K_2 \bar{r}_L^2} \quad , \quad \bar{r}_0 = \bar{r}_L e^{-\alpha L} \quad , \quad \rho_0 = \bar{r}_0 / \xi \quad (49)$$

For the numerical results presented later, typically  $\alpha$  was of the order of  $10^{-3}$ ,  $\bar{r}_0$  and  $\rho_0$  of the order of  $10^{-4}$ ,  $\Delta \bar{r}_L \approx 10^{-2}$ .

The standard FFT or FHT schemes correspond to a discretization of the integral transform that is centered step-wise, resulting in a second-order approximation. Our experience shows that this approximation is accurate enough in most cases of UV Raman cells (cf. section 4), but because the diffraction PDE is solved iteratively with respect to  $z$ , a more precise discretization scheme is maybe needed in some applications. It is possible to use a higher-order discretization of the transform (piecewise linear or quadratic)<sup>13</sup>. In case of cylindrical geometry, Derbov<sup>38</sup> proposed a step-wise discretization of  $S(\bar{r})$ , while integrating analytically  $J_0$ , in order that for  $\rho \gg 1$  all the oscillations of  $J_0$  are correctly integrated.

### 2.3.4 Link between the methods

All three methods can be conveniently compared in the Fourier space. For convenience we will keep to cartesian geometry and Dirichlet boundary conditions; the discussion remains essentially unchanged for the case of cylindrical geometry and other boundary conditions.

As introduced in §2.3.3,  $\mathbf{C}(z) = (c_0(z), c_1(z), \dots, c_L(z))$  is denoted to be the discrete Fourier transform of the vector  $\mathbf{S}(z) = (S(\bar{r}_0, z), S(\bar{r}_1, z), \dots, S(\bar{r}_L, z))$ , equ. (44). In the Fourier space, that is, in term of  $\mathbf{C}$ , the FD and FE methods are identified the following way. The matrix

$$\mathbf{H}_d = \frac{1}{(\Delta \bar{x})^2} \begin{bmatrix} -2 & 1 & & & \\ 1 & -2 & & 0 & \\ & & \dots & & \\ & 0 & & -2 & 1 \\ & & & 1 & -2 \end{bmatrix} \quad (50)$$

corresponds to the usual discretization of the operator  $H = \partial_x^2$  of the diffraction PDE (29), with Dirichlet BC. The discretized form of (29) is then  $\partial_z \mathbf{S} = i a(z) \mathbf{H}_d \mathbf{S}$ ,  $a(z) = [2k w_x^2(z)]^{-1}$ , which solution is:

$$\mathbf{S}(z + \Delta z) = \exp[i A \mathbf{H}_d] \mathbf{S}(z) \quad (51)$$

with  $A$  given in (45).

The (R,T) Padé approximant to  $\exp(x)$ ,  $x$  real, is a rational approximation with the denominator being a polynomial of degree R and the nominator a polynomial of degree T<sup>17</sup>. For example the (1,1) Padé to  $\exp(x)$  is  $(1 + \frac{1}{2}x) / (1 - \frac{1}{2}x)$ . Analog Padé approximants can be drawn when matrices are involved, and (51) becomes with the (1,1) Padé:

$$\mathbf{S}(z + \Delta z) = \left[ 1 - \frac{1}{2} i A \mathbf{H}_d \right]^{-1} \left[ 1 + \frac{1}{2} i A \mathbf{H}_d \right] \mathbf{S}(z) \quad (52)$$

Section 2: Numerical method

When  $A = \int_z^{z+\Delta z} a(\alpha) d\alpha$  is approximated by  $a(z + \Delta z / 2) \Delta z$ , equ. (52) is shown to be exactly the FD Crank-Nicolson scheme. In a similar fashion, the FD fully implicit scheme is recovered with the (1,0) Padé:

$$\mathbf{S}(z + \Delta z) = [1 - iA H_d]^{-1} \mathbf{S}(z) \quad (53)$$

Higher-order approximations of the exponential in (51) that conserve the BPR are given by the Padé approximant with  $R=T$  and  $R \geq 2$ ; these nevertheless lead to the inversion of a matrix that is band-diagonal, with  $R$  lines each side of the diagonal.

The finite element method, whatever the underlying finite element order, leads to a discrete ODE system that has also the form of (51), but with matrix

$$H_d^{\text{FLE}} = \left[ \mathbf{1} + \frac{1}{6} H_d \right]^{-1} H_d \quad (54)$$

instead of  $H_d$ ,  $\mathbf{1}$  being the identity matrix, and corresponds to a different approximation of the operator  $H = \partial_{\bar{x}}^2$ . Similarly, the ODE integration leads to an equation of the form of (51), and the exponential is approximated by a Padé (the (1,1) Padé was used in §2.3.2).

We rewrite the equations (52-54) in the generic form:

$$\mathbf{S}(z + \Delta z) = P_{(R,T)} \mathbf{S}(z) \quad (55)$$

$P_{(R,T)}$  being the Padé approximant to matrix  $\exp(iA H_d)$ . The functions  $\varphi_j(\bar{x})$ ,  $j=1,2, \dots$ , defined in (43) are eigenfunctions of  $H$  with eigenvalue  $-(\pi j)^2 / (\bar{x}_L - \bar{x}_0)^2$ , noted  $\mu_j^{\text{FFT}}$  for reasons that will become clear later, and correspondingly the vectors  $\varphi_j = (\varphi_j(\bar{x}_0), \dots, \varphi_j(\bar{x}_L))$ ,  $j=1, 2, \dots, L+1$ , are eigenvectors of  $H_d$  with eigenvalue

$$-\frac{4}{(\Delta \bar{x})^2} \sin^2 \left[ \frac{\pi j \Delta \bar{x}}{2 (\bar{x}_L - \bar{x}_0)} \right] \quad (56)$$

noted  $\mu_j^{\text{FD}}$ . From equ. (54),  $\varphi_j$  is eigenvector of  $H_d^{\text{FLE}}$  as well, with eigenvalue  $\mu_j^{\text{FLE}} = \mu_j^{\text{FD}} / (1 + \mu_j^{\text{FD}} / 6)$ . After multiplying both sides of (55) by  $\varphi_j$ , and using the fact that  $H_d$  is a real symmetric matrix:

$$\varphi_j \mathbf{S}(z + \Delta z) = \mathbf{S}(z) P_{(R,T)} \varphi_j \quad (57)$$

Recalling from equ. (44) that the Fourier modes  $c_j$  are obtained by the scalar product between  $\mathbf{S}$  and  $\varphi_j / \|\varphi_j\|$ ,  $\|\varphi_j\|$  given in (43), the solution of the diffraction PDE in the Fourier space for either the finite-difference or the finite-element method is written as:

$$c_j(z + \Delta z) = c_j(z) P_{(R,T)}(iA \mu_j) \quad (58)$$

where  $P_{(R,T)}(iA \mu_j)$  has the same functional form as with  $P_{(R,T)}$  applied to  $(iA H_d)$ , equ. (55), but with  $(iA \mu_j)$  as argument.

## Section 2: Numerical method

We notice that equ. (58) is the same as equ. (45) of the Fourier method, with these two differences:

- (1) The eigenvalue is  $\mu_j^{\text{FD}}$  or  $\mu_j^{\text{FLE}}$  instead of  $\mu_j^{\text{FFT}}$ , equ. (56) and above. The Fourier method is a semi-analytic solution of the diffraction PDE, in that the only approximation made is to cut the Fourier series at  $L$ . Consequently  $\mu_j^{\text{FFT}}$  is the exact eigenvalue of mode  $j$ .
- (2) The exponential has been approximated by a Padé.

These two points are examined now in more detail.

### 1) Eigenvalues

Summarizing equ. (56) and above:

$$\mu_j^{\text{FFT}} = -\left(\frac{\pi j}{\bar{x}_L - \bar{x}_0}\right)^2, \quad \mu_j^{\text{FD}} = -\frac{4}{(\Delta\bar{x})^2} \sin^2\left[\frac{\pi j \Delta\bar{x}}{2(\bar{x}_L - \bar{x}_0)}\right], \quad \mu_j^{\text{FLE}} = \frac{\mu_j^{\text{FD}}}{1 + \frac{1}{6}\mu_j^{\text{FD}}} \quad (59)$$

Obviously  $\mu_j^{\text{FD}} \equiv \mu_j^{\text{FFT}}$  for small  $j$ , i.e.  $j \ll L$ . As for  $\mu_j^{\text{FLE}}$ , it must be noticed that in order for Dirichlet or Neumann boundary conditions to hold the grid has to extend several times the beam standard deviation and thus  $\bar{x}_L - \bar{x}_0 \geq 6$ , say (in reduced coordinates, that is in units of the pump beam radius as defined in (7)). In this situation, for small  $j$   $\mu_j^{\text{FLE}} \equiv \mu_j^{\text{FFT}}$  as well. The discrepancy between all three  $\mu_j$  increases as  $j$  increases, and as illustrated in fig. 2 it can reach a maximum near  $j=L$  of  $\sim 55\%$  between  $\mu_j^{\text{FFT}}$  and  $\mu_j^{\text{FD}}$  and  $\sim 20\%$  between  $\mu_j^{\text{FFT}}$  and  $\mu_j^{\text{FLE}}$ .

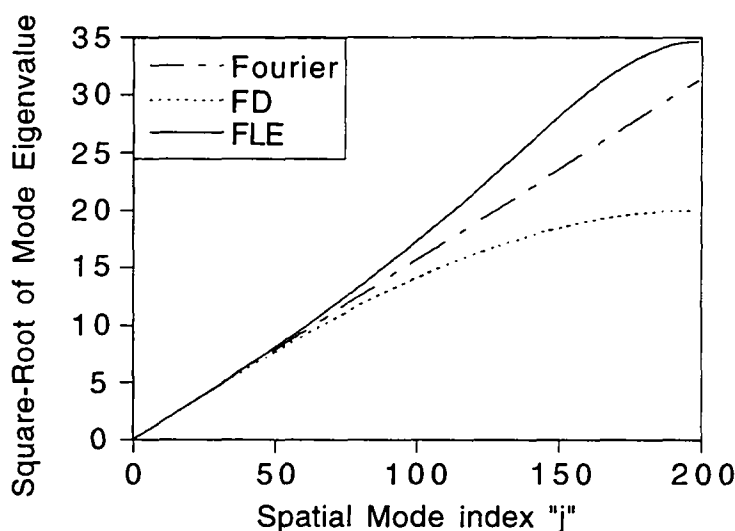


**Fig. 2.** Square-root of the absolute value of the eigenvalues in equ. (59), for the Fourier, finite-difference (FD) and linear-finite-element (FLE) methods.



2) Padé approximant

The Padé approximant is a development of the exponential around zero value of the argument. Therefore the same type of remark as for the eigenvalues holds: the higher the mode index  $j$ , the worse the approximation.

Fig. 3 illustrates the validity of the Padé approximation  $P_{(R,T)}(i\alpha)$  to  $\exp(i\alpha)$ ,  $\alpha$  real. Both (1,1) and (2,2) Padé are shown. It can be seen that for the real and the imaginary parts of the exponential a discrepancy of  $\sim 10\%$  is reached when  $\alpha \approx 1$  for the (1,1) Padé and  $\alpha \approx 2.5$  for the (2,2) Padé. Above these limits, the Padé becomes very quickly a bad approximant. In order to make the link with a real case, we can consider a diffraction-limited Nd:YAG laser quadrupled at 266nm, of diameter 8mm (at 86% power), focused to a waist of  $10 \mu\text{m}$  (obtained with a lens of 50cm focal length typically). The function  $A(z)$  in equ. (58) increases monotonically with  $z$  up to the waist  $z_w$  where it takes the maximum value  $A(z_w) = \Delta z / (2k w_0^2)$ . Taking  $\Delta z = w_0$  and  $\bar{x}_L - \bar{x}_0 = 20$  (which corresponds to 10 times the beam width  $2w$ ),  $A \approx 10^{-3}$  and hence  $\alpha = A\mu_j$  reaches the value of 1 for  $j=212$  and the value of 2.5 for  $j=335$ , with corresponding  $\Delta \bar{x} = (\bar{x}_L - \bar{x}_0) / j$  spacing of  $\sim 0.1$  and  $\sim 0.06$  respectively. As will be seen later, in case of strong non-linear coupling, substantial energy is transferred in the higher modes (one value of  $j$  corresponds to one mode), i.e. those with  $j \gg 1$ , and therefore won't be accurately approximated by a Padé. Moreover, the real part of the usual (1,1) Padé reaches asymptotically the value of -1, and as a consequence the modes with  $j \gg 1$  will oscillate and this numerical artifact will be dampened very slowly, which is typical of a so-called  $A_0$ -stable scheme<sup>17</sup>.

These discrepancies (1) and (2) of the FD and FE methods with respect to the Fourier method have the consequence that the phase velocity of each mode differs from the true one, given by the Fourier method (numerical dispersion<sup>19</sup>). The only type of error inherent to the Fourier method is associated with the Gibbs phenomenon, which is due to the fact that the Fourier series are cut at  $L$ . The reduction of this unavoidable error, which is also of course inherent to the FD and FE methods, goes only with increasing  $L$ , that is via a refinement of the mesh spacing.

Computationally, a FFT requires  $N_{\text{FFT}} = L \log_2(L)$  operations, while the inversion of a tridiagonal matrix as needed by the FD or FE methods requires  $N_{\text{FD-FE}} = 2L$  operations. The ratio between the two is  $N_{\text{FFT}} / N_{\text{FD-FE}} = (1/2) \log_2(L)$ , which equals to 4 for  $L=256$ , and 7 for  $L=16384$ . Such a computational time ratio was numerically verified for the case of optical propagation in fibers<sup>32,33</sup>. A finite difference scheme that is corrected for the higher modes and which is computationally equivalent to the FD-CN or FLE methods is for example the so-called "flux-corrected transport" scheme<sup>39</sup>.

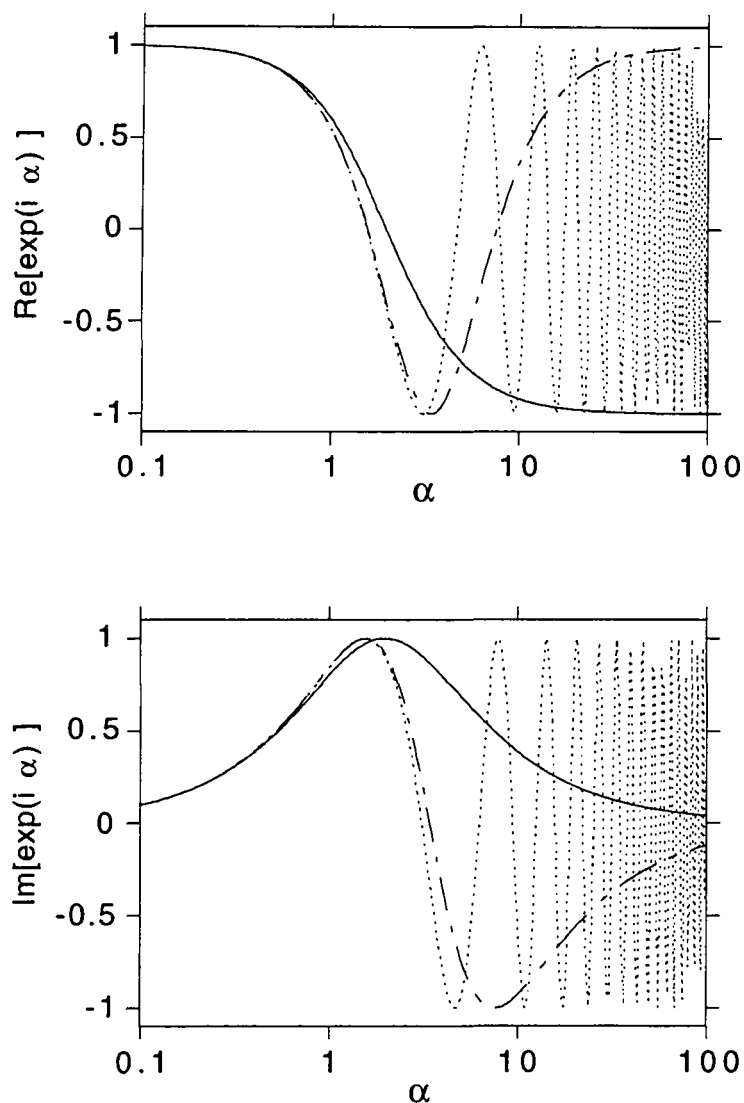


**Fig. 3.** (1,1) (continuous line) and (2,2) (broken line) Padé approximants to  $\exp(i\alpha)$ ,  $\alpha$  real (dashed line). The upper, resp. lower, panel shows the real, resp. imaginary, part.

### 2.3.5. Benchmarking

The methods presented in §2.3.3 for the solution of the diffraction PDE will be applied to a PDE very similar to the diffraction PDE, but for which an analytical solution is known (the so-called “benchmark”). The benchmark is the following PDE:

$$\partial_z f = i \alpha \partial_x^2 f \quad (60)$$

$\alpha$  being a real number independent of  $x$  and  $z$ . The PDE is defined on the interval  $[-x_L, x_L]$ , with Dirichlet boundary conditions and a square-pulse as initial condition (i.e. at  $z=0$ ), defined as taking the value 1 for  $|x| < x_c$ ,  $x_c < x_L$ , and being zero elsewhere. This benchmark has the difference with the diffraction PDE that the diffusion coefficient  $\alpha$  does not depend on  $z$ , and hence a semi-analytical solution exists in the form:

$$f(z, x) = \frac{2}{x_L} \sum_{j=0}^{\infty} \frac{(-1)^{j+1}}{\gamma_{2j+1}} \sin(\gamma_{2j+1} x_c) \exp(-\gamma_{2j+1}^2 i \alpha z) \psi_{2j+1}(x) \quad (61)$$

where  $\gamma_j = (\pi j)/(2x_L)$  and  $\psi_j(x) = \sin[\gamma_j(x - x_L)]$ .

The PDE (60) is similar to the heat equation, except that the diffusion coefficient is complex rather than real. Therefore, in its series solution (61) each mode has a propagation term that is a complex number of unit modulus, while for the heat equation it is an exponential with real negative argument. As a consequence the higher modes ( $j \gg 1$ ) of the heat equation solution are strongly dampened, whereas the ones of the benchmark have constant modulus throughout the propagation. The defects with respect to the higher modes of the FD and FE methods outlined in §2.3.4 will be apparent for the benchmark, whilst these are virtually absent for a PDE of the type of the heat equation; this will be exaggerated for an initial condition of the type considered here (square-pulse) which has modes slowly decaying with mode-index. These considerations about the benchmark hold as well for the diffraction PDE.

In order to simplify the discussion, a tag is assigned to each type of numerical error outlined in §2.3.4:

- E1: The numerical dispersion associated with wrong eigenvalue of the  $x$ -spatial mode. Inherent to the FD and FE methods.
- E2: The numerical dispersion associated with the propagation of the spatial modes along  $z$ -axis, i.e. the error of the Padé approximant. Inherent to the FD and FE methods.
- E3: The so-called Gibbs error, caused by the fact that a finite number of grid points is used. Inherent to all the numerical methods.

The diffusion parameter  $\alpha$  is taken to be  $1/\pi$ , so as to preserve simple step-like profile shapes during propagation. The other parameters kept fixed are  $x_L = 1$  and  $x_c = 0.5$ . In order to clarify the discussion only the square modulus of  $f$  defined as  $\|f\|^2 = \sum_{j=0}^J |f_j|^2$  is displayed, which is representative enough of the behaviours we will outline.

Fig. 4 shows the dependence on the number of propagation steps  $\Delta z$ . These were taken equidistant and equal to 0.1. Even after one propagation step, the FD or FE methods give truly wrong result, so that after 100 steps the FD and FE solutions have very few in common

## Section 2: Numerical method

with the true result. This exemplifies the role of the numerical dispersion for the FD and FE methods when propagating steep profiles, i.e. with modes slowly decaying with mode index.

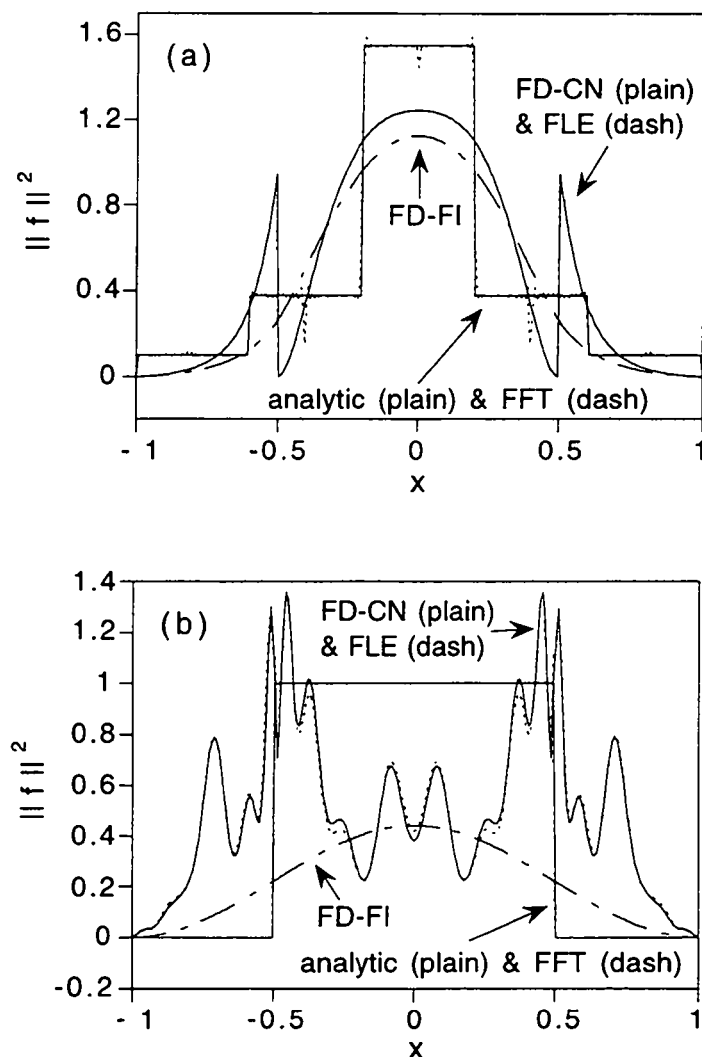


**Fig. 4.** Solution of the benchmark, equ. (60), after one (a) and 100 (b) propagation steps, obtained with the following methods: analytic, Fourier (FFT), finite-difference Crank-Nicolson (FD-CN), finite-difference fully implicit (FD-FI), and linear-finite-element (FLE). The parameters of the benchmark are  $x_c=0.5$ ,  $x_L=1$ , and  $\alpha=1/\pi$ . The propagation step is  $\Delta z=0.1$ , and a grid of 256 points has been considered. In (a) the FD-CN and FLE solutions are superimposed; in (b) the analytic and the Fourier (FFT) solutions are superimposed.

The FD-FI method dampens the higher modes, which diminishes their dispersion upon propagation. The FD-FI solution is hence closer to the reality, but its inherent smooth profile describes inadequately steep profiles, as those generated via a strong Raman coupling. Furthermore, the non-conservation of the “power” defined as  $\|f\|^2$  is clearly noticed between figs. 4a and 4b.

The FD-CN and FLE methods give very similar results, in that it is only after 100 steps that a discrepancy becomes noticeable. In fact the only difference between the two methods is E1, and thus it shows that E2 dominates.

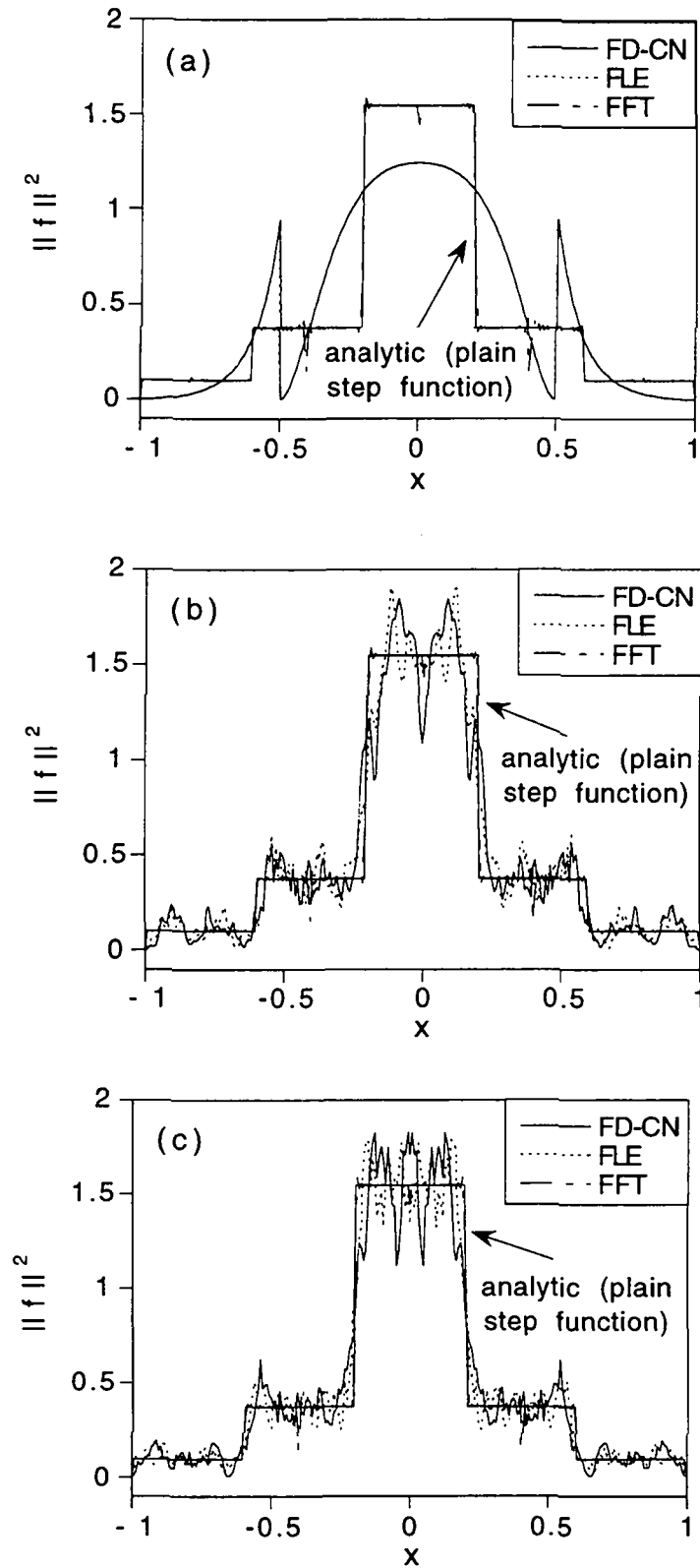
## Section 2: Numerical method

The FFT method is seen on fig.4 to be the only one that significantly reproduces the analytical solution. The ripples associated with the Gibbs error can be seen in fig. 4a, and would diminish by increasing the number of grid points.

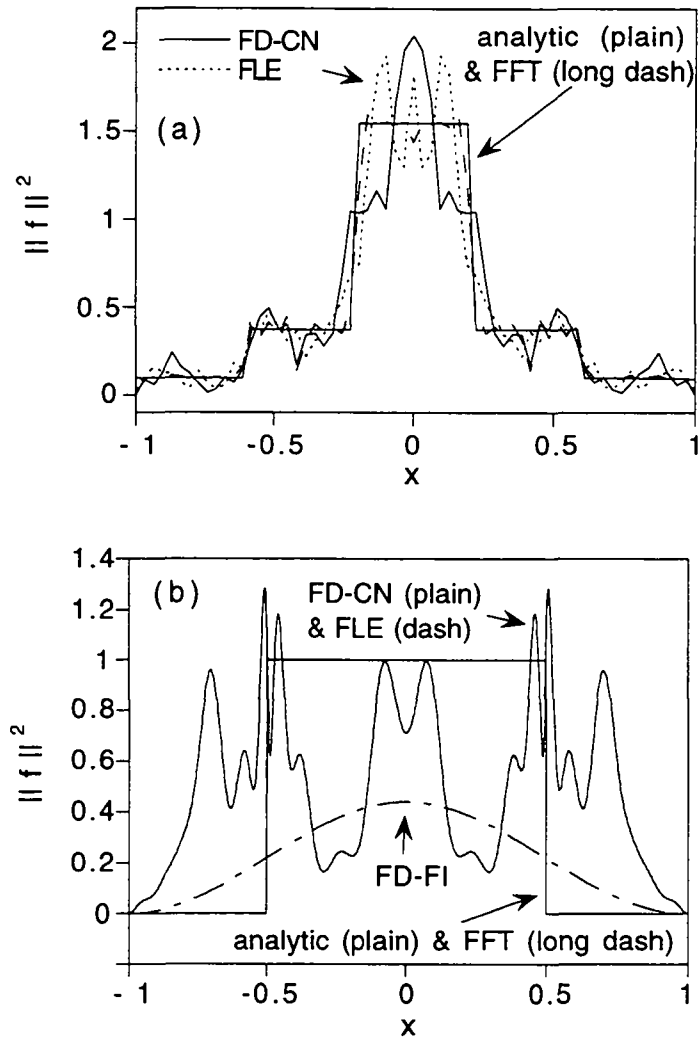
The effect of diminishing  $\Delta z$  is shown in fig. 5. The (1,1) Padé used in the FD-CN and FLE methods is of order  $O[(\Delta z)^2]$ , while the (1,0) Padé of the FD-FI method is of order  $O(\Delta z)$ . Between figs. 5a, 5b and 5c,  $\Delta z$  has been each time diminished by two orders of magnitude, while the profiles shown all correspond to the same position on the  $z$ -axis ( $z=0.1$ ). Fig.5 is another evidence that E2 dominates: dramatic improvement for the FD and FE methods occurs between  $\Delta z=10^{-1}$  and  $\Delta z=10^{-3}$ . On the other hand, there is only a slight improvement between  $\Delta z=10^{-3}$  and  $\Delta z=10^{-5}$  indicating that a kind of saturation is reached. We conclude that for the FD and FE methods an extremely low  $\Delta z/\Delta x$  ratio has to be used in order to recover such a step-like function. As for the FFT, the Gibbs error is nearly independent of  $\Delta z$ , i.e. the number of propagation steps, expressing that this type of error accumulates in a benign way.

Fig.6 shows the dependence on the number of grid points  $N$ , that is, the mesh spacing  $\Delta x$  or equivalently the number of spatial  $x$ -modes. This type of parameter variation affects only E1. Fig. 6a considers a case in which the FD and FE methods are still significant ( $\Delta z=10^{-5}$ ,  $z=0.1$ ), while fig. 6b shows the case where they become meaningless ( $\Delta z=10^{-1}$ ,  $z=10$ ). The figures with same parameters but with a different  $N$  are respectively fig. 5c ( $N=256$  instead of 64) and fig. 4b ( $N=256$  instead of 1024). In both cases reducing  $\Delta x$  has very small effect. Fig. 6b shows that the inherent difference between the FD-CN and the FLE methods, which is the error E1, diminishes when  $\Delta x$  is decreased, as expected. These figures furthermore evidence that E2 is the dominant error in the FD and FE methods. Fig. 6a shows the obvious improvement in E3 for the FFT method when increasing  $N$ .

The same benchmark applied to a gaussian function as initial condition led to no noticeable defect of any of the numerical methods, as it should be the case with most smooth functions.



**Fig. 5.** Solution of the benchmark for a propagation step  $\Delta z = 10^{-1}$  (a),  $10^{-3}$  (b) and  $10^{-5}$  (c). All other parameters are the same as for fig.3. In (a) the FD-CN and FLE solutions are superimposed. See fig. 4 caption for the abbreviations.



**Fig. 6.** Solution of the benchmark for 64 (a) and 1024 (b) grid points. The propagation step is  $\Delta z = 10^{-5}$  (a) and  $\Delta z = 0.1$  (b). These profiles are taken after  $10^4$  steps (a) and 100 steps (b). In (b) the FD-CN and FLE solutions, as well as the analytic and the Fourier (FFT) solutions, are superimposed. See fig. 4 caption for the abbreviations.

### 2.3.6 Step adjustment

#### a) Axes transverse to propagation

The Raman coupling is of third order, which means that amplification will occur in the regions of highest pump intensity. As a consequence, after a step of nonlinear conversion the Stokes beam profile is steeper than the pump one. If the nonlinear coupling is strong enough this effect of steepening the Stokes profiles is stronger than the opposite effect of smoothing of the diffraction. In this situation, energy is transferred from the lower to the higher Fourier spatial modes, and thus the grid spacing ( $\Delta \bar{r}$  in cylindrical geometry,  $\Delta \bar{x}$  and  $\Delta \bar{y}$  in cartesian geometry), shall be small enough in order that a sufficient number of modes is taken into account. This was observed numerically, in that the threshold number of points  $L_{th}$  above which the reconstructed profile becomes stable increases when the Raman gain and/or the input pump intensity increase.  $L_{th}$  was determined from case to case empirically.

## Section 2: Numerical method

### b) Axis of propagation

A variable step along the axis of propagation is essential in the situation of high-gain single-pass Raman cells since high amplification gradients are expected to occur. A divide/multiply-by-two strategy was chosen. The solution is first propagated one full (i.e. comprising all the split-steps of the SSS scheme) step  $\Delta z$  and second two steps  $\Delta z'$  that are each half of  $\Delta z$ . The relative discrepancy  $\varepsilon_r$  between the solution at  $z+\Delta z$  obtained with one single step and the one with two half steps, is calculated. When  $\varepsilon_r$  is bigger, resp. smaller, than a specified discrepancy  $\varepsilon_s$ ,  $\Delta z$  is divided, resp. multiplied, by two for the next propagation step. Although involving heavy computation, this step adjustment procedure guarantees that  $\varepsilon_s$  is achieved.

### 2.3.7 Boundary conditions

The only split-PDE that couples adjacent points on the axes perpendicular to propagation is the one for the diffraction, and is thus the only one to require boundary conditions to be considered. All the methods for the diffraction PDE presented in §2.3.3 were shown to conserve the BPR, and hence no energy can leave the boundaries. This is consistent with the Dirichlet, Neumann or periodic boundary conditions that are considered. Consequently a grid of sufficient extent has to be chosen in order that the beams intensity at the boundaries are small enough with respect to their maximum value, and thus that spurious numerical reflections on the grid boundaries are made negligible.

## 2.4. Numerical examples in a SRS configuration

It was pointed out in §2.3 that the numerical method for the diffraction PDE is critical. The analytical comparison between the methods of §2.3.4 was tested on a benchmark in §3.5. Numerical examples in a Raman cell configuration are now given. It will be seen that the behavior of the methods is consistent with what was exposed in §2.3.4.

The simulations presented in this section correspond to a diffraction-limited pump beam at 266 nm (e.g. quadrupled Nd:YAG) focused in the center of the cell. The Stokes field initial conditions (i.e. at the entrance of the cell) are taken as the sum of the spontaneous Raman scattering and the noise field. Most of the results presented are for cylindrical geometry (unless otherwise stated) because of running time CPU limitations.

The behavior of the numerical method with respect to  $G_1$ , equ. (4), is shown in fig.7. When  $G_1$  is less than  $\sim 50$  (which is roughly the threshold for  $S_2$ ), the FE and Fourier methods give similar results. Above this limit both methods disagree significantly, reflecting that enough energy is transferred in the higher modes for numerical dispersion to become apparent, as pointed out in §2.3.4 and §2.3.6.

Fig. 8 shows the effect of the energy transfer towards the higher spatial modes due to the Raman coupling. When too few grid points are considered, energy accumulates in the highest grid mode, whereas more modes would be necessary in order to recover correctly the sought function. For  $L$  increased above 4096 the FFT solution has no noticeable change. This threshold value of  $L$  increases when  $G_1$  increases. Such a convergence relative to  $L$  is also observed for the FE method, but as shown in fig. 8 (d) and (h) the major problem of numerical dispersion remains.

The decrease of numerical dispersion when  $\Delta z$  is decreased (FE method) is shown in fig.9: even for a step equal to the waist size residual dispersion is noticed. Note that the step must be further decreased when  $G_1$  is increased. Apart from the ripples the effect of the dispersion is apparent in that when  $\Delta z$  is increased the function extension decreases; this reflects the



## Section 2: Numerical method

wrong propagation of the higher modes which are those that have the higher phase velocity in the direction transverse to the propagation axis<sup>27</sup>.

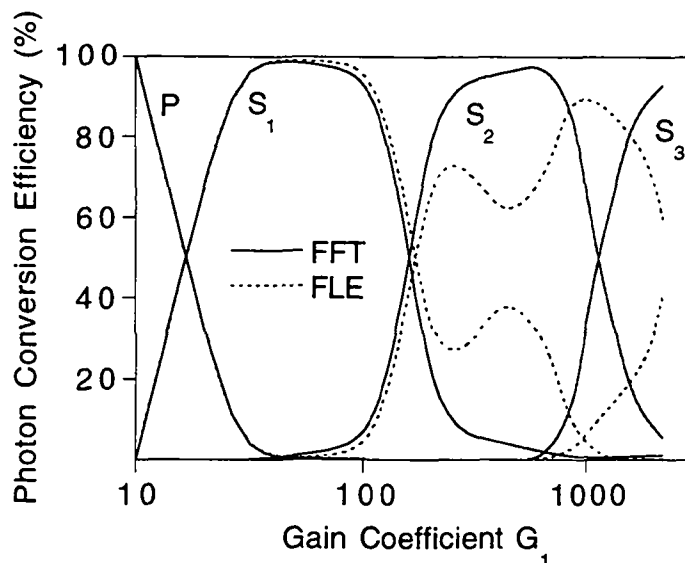


**Fig. 7.** Photon conversion efficiency  $\eta$  versus the first Stokes gain coefficient  $G_1$ , for a diffraction-limited pump beam at 266 nm, in cylindrical geometry.  $\eta$  for a particular Stokes is defined as the photon rate of that beam divided by the sum of the photon rates (pump + all the Stokes), at cell exit.  $L=16\cdot384$  grid points were considered, along with grid boundaries  $\bar{r}_L = 25$  and  $\Delta z$  equal to eight times the waist the focused pump has when no gas is present in the cell (see fig.9 caption). See fig. 4 caption for the abbreviations.

Beam profiles in cartesian geometry obtained with the FD-CN and FD-FI methods are shown in fig. 10. In fact the same input pump beam with cylindrical symmetry as for the other figures of this section has been considered. Fig. 10 is then to be compared with fig. 8 (c) (FFT) and (d) (FLE), with only different parameters being the number of grid points and grid boundaries (due to computing time limitations). The FD-CN and FLE methods are seen to yield very similar results, i.e. significant numerical dispersion, in accordance to the considerations of §2.3. The profiles obtained with the FD-FI do not show ripples because this method dampens the higher spatial modes. But as a consequence the profiles are seen to be somewhat corrugated when compared with those obtained with the FFT method (notice in particular the lateral extent of the beams). Moreover, a substantial reduction in the SPR was observed at the cell exit because of the dampening, even though it is not clear in this figure.

Fig. 11 shows the numerical reflections that occur at the grid boundaries when the grid extent is chosen too small. The ripples due to these reflections are less severe for the second Stokes. The comparison with fig. 8 (c) shows that for such kind of beams that decay exponentially in the plane transverse to propagation it is sufficient to consider a grid that has sufficient extent even though the numerical methods considered here do not allow energy to exit the grid.

In fig. 12 the four-wave-mixing has been included in the model. The FLE method is seen to yield dispersion ripples, similar to those observed for the sole SRS modeling showed in fig. 8 (d). On the other hand, the absence of such ripples in (a) suggests that even when adding other nonlinear effects the Fourier method remains stable.

Section 2: Numerical method

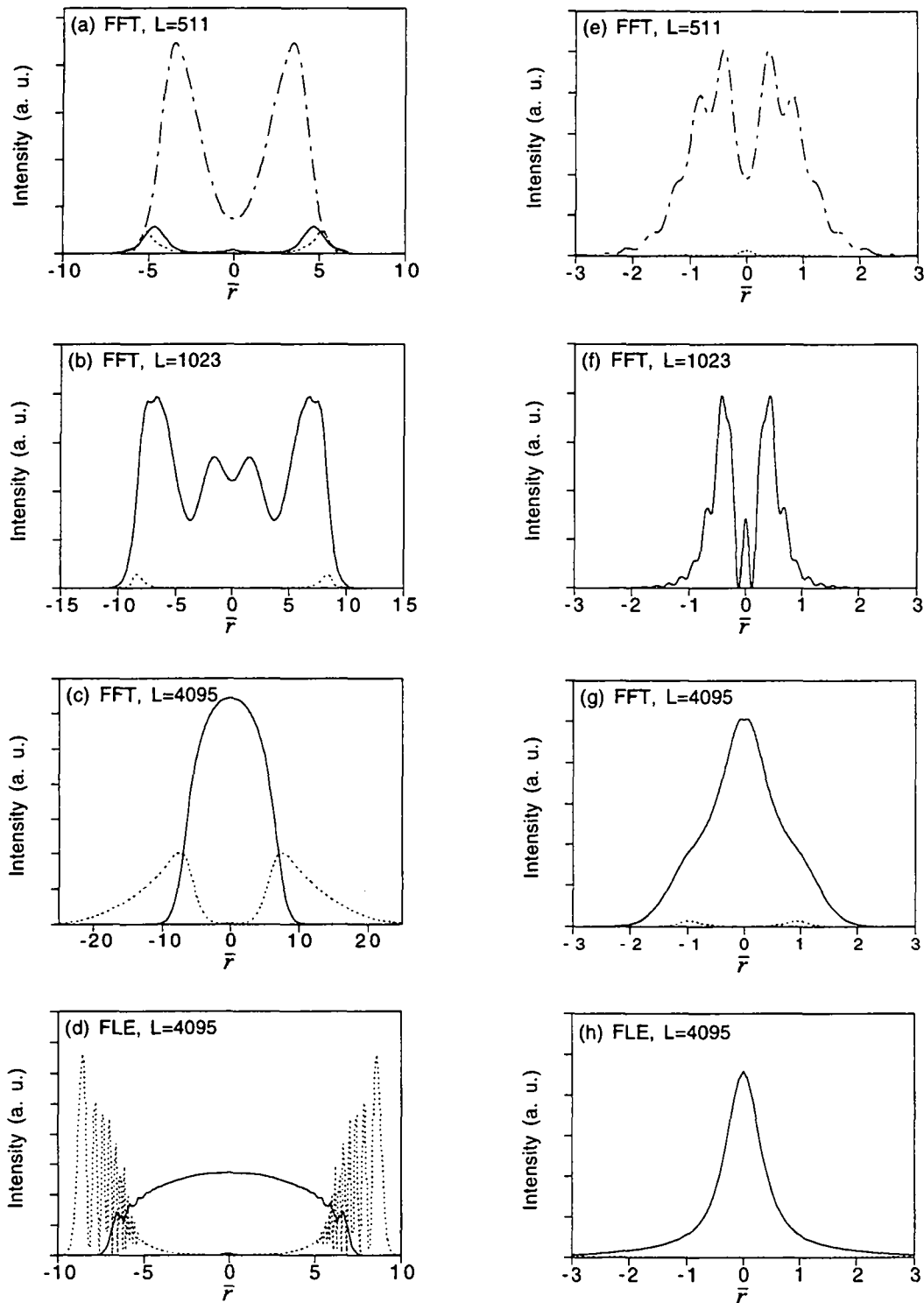


**Fig. 8.** Beam profiles as a function of the number of grid points  $L$ , for  $G_1=650$ . The curves labels are the following: dash is  $S_1$ , continuous is  $S_2$ , and short - long dashes alternating is  $S_3$ . The profiles of the left, resp. right, panel are taken at the beam waist, resp. cell exit (the beam is focused at the center of the cell). All other parameters are the same as for fig. 7. See fig. 4 caption for the abbreviations.

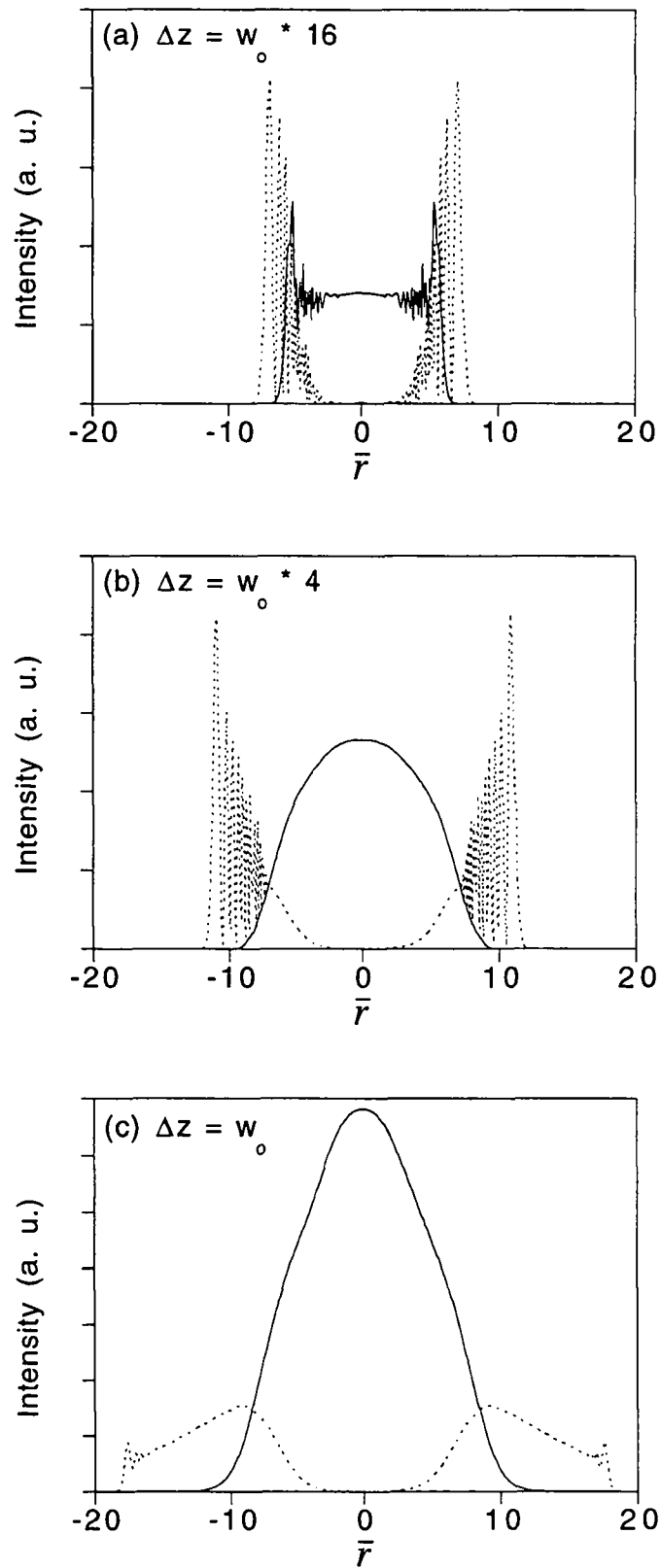


**Fig. 9.** Beam profiles obtained with the linear-finite-element method, as a function of the step  $\Delta z$  along the propagation axis.  $w_0 = 2f\lambda/\pi d = 10 \mu\text{m}$  is the waist of the focused pump beam when no gas is present in the cell, ( $\lambda = 266 \text{ nm}$  beam of  $d = 8 \text{ mm}$  diameter (at 86% power) focused at its waist with a  $f = 50 \text{ cm}$  lens). All other parameters are the same as for fig. 7 and 8.

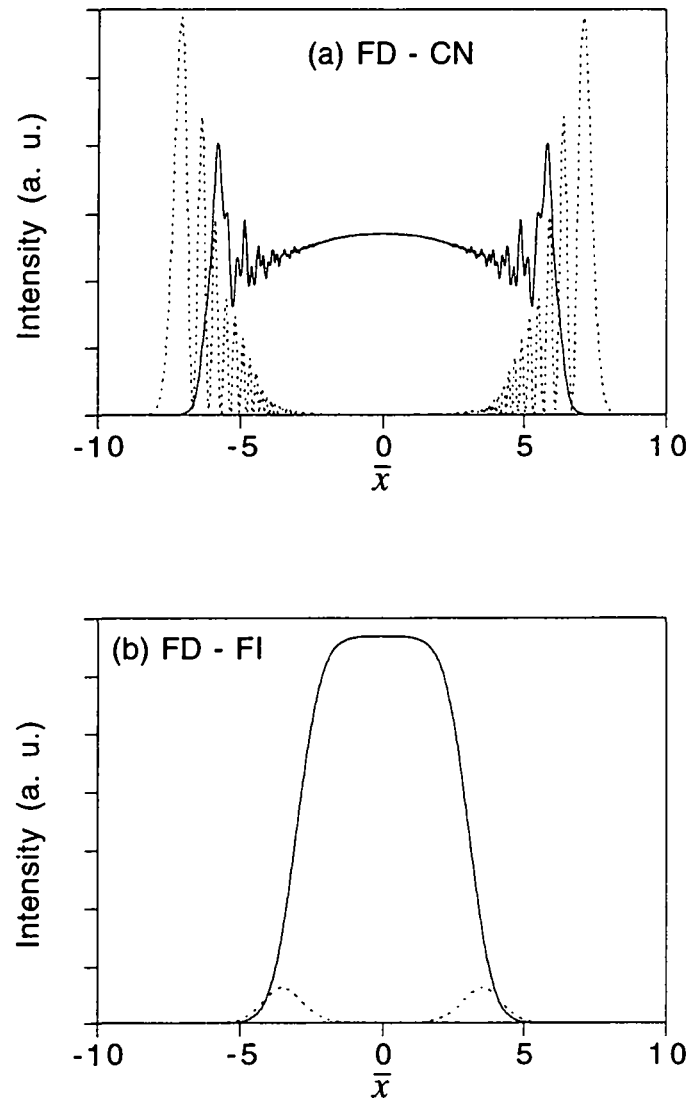


**Fig. 10.** Beam profiles at  $\bar{y} = 0$  obtained with the finite-difference Crank-Nicolson (FD-CN) and finite-difference fully-implicit (FD-FI) methods, in cartesian geometry.  $L=701$  grid points were considered, along with grid boundaries  $\bar{x}_L = \bar{y}_M = 10$ . The profiles are taken at the waist. All other parameters are the same as for figs. 7-9.

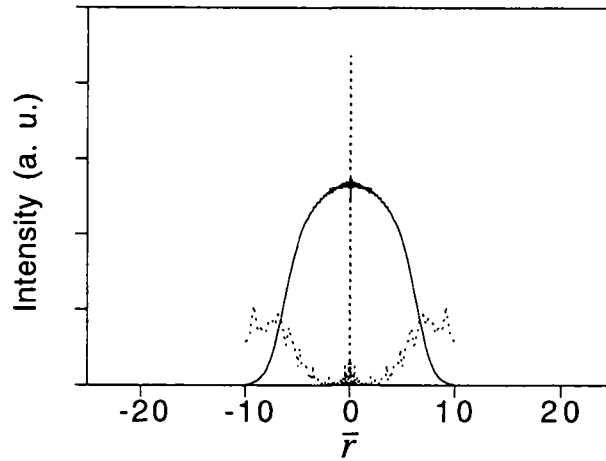


**Fig. 11.** Effect of a too small grid extent for the Fourier method. The grid boundary is  $\bar{r}_L = 10$ . This figure is to be compared with fig. 8 (c), for which the only parameter that differs is  $\bar{r}_L = 25$ .

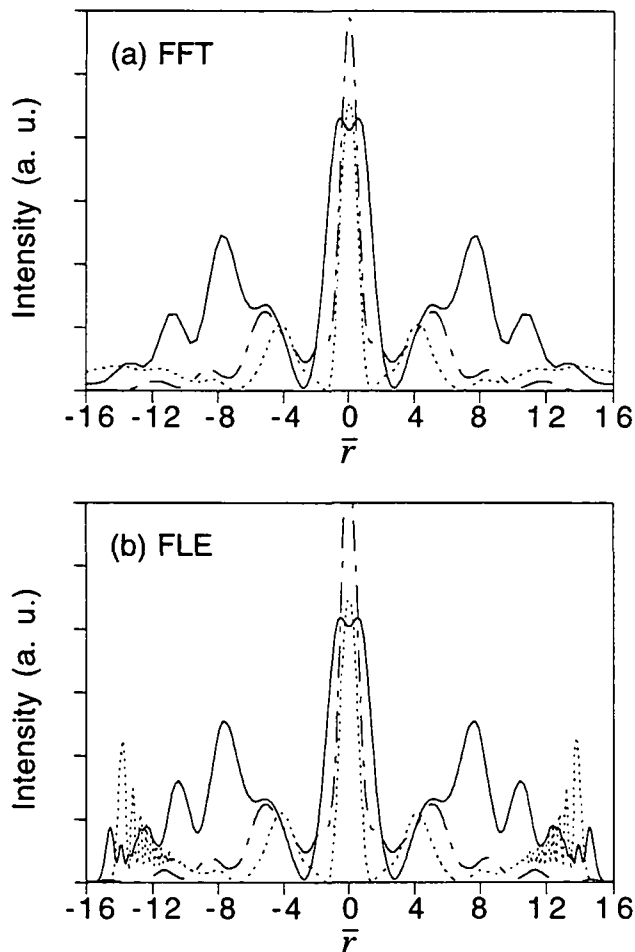


**Fig. 12.** Beam profiles taken at the waist, when four-wave-mixing is included in the model. The numerical method used was Fourier (FFT) in (a) and linear-finite-element (FLE) in (b). All other parameters are the same as for figs. 7-9.

## 2.5. Conclusion

In the formalism where the beams are expanded on plane waves (spatial modes) propagating with increasing angles with respect to the optical axis, it is seen that the nonlinear coupling transfers energy from the lower to the higher spatial modes. Consequently, first a sufficient number of spatial modes has to be considered, and second the numerical method that solves the diffraction terms of the wave equation shouldn't be dispersive. Finite difference (FD), finite element (FE) and Fourier (spectral) methods were analytically compared, tested on a prototypical PDE for which a solution is known (benchmark) and finally applied to some examples in a SRS configuration. The Fourier method is known to be the only one that is not dispersive and it was found that this point is critical when a strong nonlinear coupling is present. As a drawback, the Fourier method is  $(1/2)\log_2(L)$  times slower than the two other tested methods, where  $L$  is the number of grid points. The flux-corrected-transport method (FCT) is envisioned to be nondispersive enough for the case of interest and is computationally equivalent to the FD and FE methods, but was not tested in this study. Centered implicit differencing conserves the photon sum of the pump and all the converted beams. It is also stable for the stiff set of ordinary differential equations that describe the nonlinear coupling. On the other hand explicit schemes are inadequate regarding these two points.

The situation considered is a Stokes generation from the noise field (or the spontaneous Raman scattering) and thus the amplification proceeds essentially through the stimulated Raman scattering (SRS) coupling. The effect of four-wave-mixing (FWM) is mainly to average the energy among the SRS-amplified beams. The two aspects mentioned above regarding the numerical modeling of high-gain single-pass (HG-SP) SRS were seen to be critical because of the strong amplification. Consistent with this, problems were encountered with dispersive methods (FD, FE) when considering only the SRS coupling (no FWM) in the modeling. Consequently, most of the results that were presented consisted of a sole-SRS modeling. It was nevertheless verified that these critical points remain when adding FWM in the model.

The numerical method presented in this contribution has several areas of application<sup>1-8,12,29-31</sup>, and in particular HG-SP Raman cells. The latter are extensively used as wavelength-shifting devices of high-power lasers. The gain necessary for cascade Stokes is mainly achieved in the UV-VIS with the currently available lasers, and hence the label "HG-SP" which is the specificity of this study is relevant in this spectral range. Raman cells have found many domains of application, so that even commercial devices are available. A numerical modelling would improve the understanding of the observed complex behaviour of cascading and mixing in these devices.

## Acknowledgments

This work was funded by the Swiss National Foundation for Scientific Research, grant n° 2100-042308.94. K. Appert, M.-A. Dupertuis and M. Fivaz are gratefully acknowledged for their assistance.

**Annex 2.A:**

**Developments leading to the main equations of §2.3.3**

**A.1 Finite elements**

We concentrate first on the cartesian coordinates. The field is expanded on basis functions  $\Psi_i$  (equ. (36) repeated):

$$S(x, y, z) = \sum_{l=0}^L f_l(y, z) \Psi_l(x) \quad (\text{A.1})$$

The particularity of the basis functions  $\Psi_i$  in the finite element method is that they are local, ie. they take values only locally and are zero elsewhere. With such elements, the finite element method is further on denoted by LFE.

The application of the LFE requires the diffraction PDE (29) to be in variational form, which is done by multiplying it with a basis function  $\Psi_i$  and integrating on the x-domain:

$$\int_{\bar{x}_0}^{\bar{x}_L} \Psi_i \partial_z S d\bar{x} = i a(z) \int_{\bar{x}_0}^{\bar{x}_L} \Psi_i \partial_{\bar{x}}^2 S d\bar{x} \quad (\text{A.2})$$

where  $a(z) = [2k w_x^2(z)]^{-1}$ . After integrating by parts the right-hand-side of (A.2):

$$\int_{\bar{x}_0}^{\bar{x}_L} \Psi_i \partial_z S d\bar{x} = -i a(z) \int_{\bar{x}_0}^{\bar{x}_L} \partial_{\bar{x}} \Psi_i \partial_{\bar{x}} S d\bar{x} \quad (\text{A.3})$$

where either the Dirichlet boundary conditions (denoted BC)  $S(x_0)=S(x_L)=0$ , or the Neumann boundary conditions  $\partial_{\bar{x}} S(x_0) = \partial_{\bar{x}} S(x_L) = 0$  have been assumed. In case of Dirichlet BC,  $\Psi_0$  and  $\Psi_L$  must be chosen such that  $\Psi_0(x_0)=\Psi_L(x_L)=0$ , and for Neumann BC they are chosen such that  $\Psi_0(x_0)=\Psi_L(x_L)=1$ . Incorporating the expansion of S (A.1) into equ. (A.3) yields

$$\mathbf{A} \partial \mathbf{f} = i \alpha \mathbf{B} \mathbf{f} \quad (\text{A.4})$$

where  $\partial \mathbf{f}$  and  $\mathbf{f}$  are vectors given respectively by  $[\partial_z f_0(y, z), \partial_z f_1(y, z), \dots, \partial_z f_L(y, z)]$  and  $[f_0(y, z), f_1(y, z), \dots, f_L(y, z)]$ , and  $\mathbf{A}$  and  $\mathbf{B}$  are the matrices given in (38) and (39). The numerical integration of (A.4) (a centered scheme is chosen (like for the FD-CN), in order to ensure the conservation of the BNP) leads to equ. (37).

The FLE discretization scheme in case of cylindrical geometry is similar. The suitable variational form of the diffraction PDE (30) is the following:

Section 2: Numerical method

$$\int_{\bar{r}_0}^{\bar{r}_L} \bar{r} \Psi_i \partial_z S d\bar{r} = ia(z) \left( \int_{\bar{r}_0}^{\bar{r}_L} \bar{r} \Psi_i \partial_{\bar{r}}^2 S d\bar{r} + \int_{\bar{r}_0}^{\bar{r}_L} \Psi_i \partial_{\bar{r}} S d\bar{r} \right) \quad (\text{A.5})$$

which, after integrating the right-hand-side by parts, yields:

$$\int_{\bar{r}_0}^{\bar{r}_L} \bar{r} \Psi_i \partial_z S d\bar{r} = -ia(z) \int_{\bar{r}_0}^{\bar{r}_L} \bar{r} \partial_{\bar{r}} \Psi_i \partial_{\bar{r}} S d\bar{r} \quad (\text{A.6})$$

where the boundary conditions are: Neumann at  $\bar{r}_0$  (the only choice in case of cylindrical symmetry), and either Neumann or Dirichlet at  $\bar{r}_L$ . When the  $\Psi_i$  take the form of linear triangular elements, a linear ODE system which has the same form than (37) is found, with the matrix elements given in (40).

### A.2 Fourier (spectral) method

In the Fourier space the diffraction PDE becomes an ODE and can be integrated in closed form. Either Fourier series or Fourier integrals (ie. transforms) can be used. Even if the manipulations leading to the result are different, the two give exactly the same result, and since in both cases it is series that are truncated (the series approximating the integral for the case of the transform) they represent the same kind of approximation.

For the case of cartesian geometry, the Fourier series will be used because within this frame the comparison with the other methods (a) and (b) for solving the diffraction will be more transparent. The diffraction PDE (29) is first expressed in operator form:

$$\partial_z S = ia(z) HS \quad , \quad HS = \partial_{\bar{x}}^2 S \quad (\text{A.7})$$

The formal solution of (A.7) is:

$$S(z + \Delta z) = \exp(iAH)S(z) \quad , \quad A = \int_z^{z+\Delta z} a(\alpha) d\alpha = \frac{z_o}{2kw_o^2} \tan^{-1} \left( \frac{u - z_f}{z_o} \right) \Bigg|_{u=z}^{u=z+\Delta z} \quad (\text{A.8})$$

Within the frame of Fourier methods, most generally the boundary conditions are periodic:  $S(\bar{x}_0) = S(\bar{x}_L)$  or  $\partial_{\bar{x}} S(\bar{x}_0) = \partial_{\bar{x}} S(\bar{x}_L)$ . For what follows, Dirichlet boundary conditions are adopted. A set of functions  $\varphi_j$ ,  $j=1,2, \dots$ , is defined as follows:

$$\varphi_j(\bar{x}) = \sin \left[ \frac{\pi j}{\bar{x}_L - \bar{x}_0} (\bar{x} - \bar{x}_0) \right] \quad (\text{A.9})$$

which is the same as equ. (43). The  $\varphi_j$  are eigenfunctions of H:  $H\varphi_j = -\lambda_j^2 \varphi_j$ ,  $\lambda_j = (\pi j) / (\bar{x}_L - \bar{x}_0)$ , and can generate any function on the interval  $[\bar{x}_0, \bar{x}_L]$  that is sufficiently "well-behaved" (ie. such that the integral of its squared modulus on this interval is  $< \infty$ ), and in particular for  $S$ :



Section 2: Numerical method

$$S(\bar{x}, z) = \sum_{j=0}^{\infty} c_j(z) \varphi_j(\bar{x}) \quad (\text{A.10})$$

The expansion (A.10) is incorporated in (A.8) and the sum truncated at  $L$  :

$$S(z + \Delta z) = \sum_{j=0}^L c_j(z) \exp[-i \lambda_j^2 A] \varphi_j(x) \quad (\text{A.11})$$

The coefficients  $c_j$  are calculated the following way. Let  $\mathbf{S}$  and  $\varphi_j$  be the values of resp.  $S$  and  $\varphi_j$  on the mesh, supposed equidistant:  $\mathbf{S}(z) = (S(\bar{x}_0, z), \dots, S(\bar{x}_L, z))$ ,  $\varphi_j = (\varphi_j(\bar{x}_0), \dots, \varphi_j(\bar{x}_L))$ . The vectors  $\varphi_j$  are shown to be mutually orthogonal by noticing that they are eigenvectors of the symmetric tridiagonal matrix with element  $-2$  on the diagonal and element  $1$  on the off-diagonal bands. After normalizing them:

$$\hat{\varphi}_j = \varphi_j / \|\varphi_j\|, \quad \|\varphi_j\| = \frac{L}{2} - \frac{(-1)^j \sin\left(\frac{j\pi L}{L+1}\right)}{2 \sin\left(\frac{j\pi}{L+1}\right)} \quad (\text{A.12})$$

the coefficient  $c_j$  is given by the scalar product between  $\mathbf{S}$  and  $\hat{\varphi}_j$ , which has the form of a fast Fourier transform (FFT). Equ. (A.12) is also found in (43).

For the cylindrical geometry the calculations are much easier within the frame of Fourier-Bessel integrals (transforms) than with associated series. The Fourier-Bessel transform is defined as follows (equ. (47) repeated):

$$\bar{S}(\rho) = 2\pi \int_0^{\infty} \bar{r} S(\bar{r}) J_0(2\pi\rho\bar{r}) d\bar{r} \quad (\text{A.13})$$

where  $J_0$  is the zero-th order Bessel function. Practically, the integration extends from  $\bar{r}_0$  to  $\bar{r}_L$ , which must be chosen such that  $\bar{r}_0$  is sufficiently close to 0 and  $\bar{r}_L$  sufficiently big in order for the boundary conditions to hold. The  $[\bar{r}_0, \bar{r}_L]$  integration range is retained for what follows. The inverse transform has the same form as (A.13).

Both sides of the diffraction PDE (30) are multiplied by  $2\pi\bar{r} J_0(2\pi\rho\bar{r})$  and then integrated:

$$\frac{1}{i a(z)} \partial_z \bar{S} = 2\pi \int_{\bar{r}_0}^{\bar{r}_L} \bar{r} \partial_{\bar{r}}^2 S J_0(2\pi\rho\bar{r}) d\bar{r} + 2\pi \int_{\bar{r}_0}^{\bar{r}_L} \partial_{\bar{r}} S J_0(2\pi\rho\bar{r}) d\bar{r} \quad (\text{A.14})$$

The right-hand-side of equ. (A.14) is integrated two times by parts, which yields, considering Neumann boundary conditions:

$$\frac{1}{i a(z)} \partial_z \bar{S} = 2\pi \int_{\bar{r}_0}^{\bar{r}_L} S(\bar{r}) \left[ \bar{r} \partial_{\bar{r}}^2 J_0(2\pi\rho\bar{r}) + \partial_{\bar{r}} J_0(2\pi\rho\bar{r}) \right] d\bar{r} \quad (\text{A.15})$$

## Section 2: Numerical method

Using standard relations concerning Bessel functions<sup>40</sup>, equ. (A.15) becomes:

$$\frac{1}{i a(z)} \partial_z \tilde{S} = -(2 \pi \rho)^2 \tilde{S}(\rho, z) \quad (\text{A.16})$$

The integration of (A.16) yields equ. (48).

### Annex 2.B:

#### Validity of the paraxial approximation in a HG-SP configuration

The Maxwell wave equation for the first Stokes beam is:

$$\frac{\partial^2 \varepsilon_1^s}{\partial x^2} + \frac{\partial^2 \varepsilon_1^s}{\partial y^2} + \frac{\partial^2 \varepsilon_1^s}{\partial z^2} + 2i k_1^s \frac{\partial \varepsilon_1^s}{\partial z} = i k_1^s g_1 \varepsilon_1^s |\varepsilon^p|^2 \quad (\text{B.1})$$

where  $E(x, y, z) = \varepsilon(x, y, z) \exp(ikz)$ ,  $E$  being the electric field. A gaussian profile is assumed for either the pump or Stokes beams:

$$|\varepsilon| = \varepsilon_0 \exp\left(-\frac{x^2}{w^2(x)}\right) \quad (\text{B.2})$$

The specifications of typical commercial quadrupled Nd:YAG lasers are considered: 100 mJ at 266 nm, 5 nsec pulse duration, beam diameter (at 86% power) of 8 mm, circular symmetry. We take it as diffraction-limited since it brings the highest intensity at the waist and hence the highest gain. The waist is then of the order of 10  $\mu\text{m}$  when focusing the beam with a 50 cm lens. For the same reason we consider it as undepleted. Hydrogen is considered since it has the highest gain, which equals to 10 cm/GW at 10 atm<sup>26</sup>.

We evaluate the diffraction and gain terms which will give an estimation of  $\frac{\partial \varepsilon_1^s}{\partial z}$ , from which

$\frac{\partial^2 \varepsilon_1^s}{\partial z^2}$  will be inferred.

We have:

$$\frac{1}{\varepsilon_1^s} \frac{\partial^2 \varepsilon_1^s}{\partial x^2} = \left( \frac{2}{w^2} - \frac{4x^2}{w^4} \right) \approx \frac{2}{w^2} \quad (\text{B.3})$$

the approximation being valid in the main part of the beam around the optical axis. The diffraction term has magnitude:

$$\frac{1}{2k_1^s} \left| \frac{1}{\varepsilon_1^s} \frac{\partial^2 \varepsilon_1^s}{\partial x^2} \right| = \frac{\lambda}{\pi w^2} \approx 10^3 \text{ m}^{-1} \quad (\text{B.4})$$

The intensity of the pump beam at the waist is evaluated as:

Section 2: Numerical method

$$\frac{100 \text{ mJ}}{\pi (5 \text{ nsec}) (10 \mu\text{m})^2} \approx 5 \times 10^{16} \text{ W / m}^2 \quad (\text{B.5})$$

which yields for the gain term (normalized by  $2ik_1^s$ ):

$$\frac{g_1}{2} |\varepsilon^p|^2 \approx 10^6 \text{ m}^{-1} \quad (\text{B.6})$$

which is much stronger than the diffraction effect. The normalized first axial derivative

$\left| \frac{1}{\varepsilon_1^s} \frac{\partial \varepsilon_1^s}{\partial z} \right|$  which results from gain and diffraction thus occurs at a rate bounded by  $10^6 \text{ m}^{-1}$ .

The second derivative  $\left| \frac{1}{\varepsilon_1^s} \frac{\partial^2 \varepsilon_1^s}{\partial z^2} \right|$  will then be bounded by at most this rate squared. In the frame of the wave equation the second axial derivative term

$$\frac{1}{2k_1^s} \left| \frac{1}{\varepsilon_1^s} \frac{\partial^2 \varepsilon_1^s}{\partial z^2} \right| \approx 10^4 \text{ m}^{-1} \quad (\text{B.7})$$

is to be compared with the first axial derivative term

$$\left| \frac{1}{\varepsilon_1^s} \frac{\partial \varepsilon_1^s}{\partial z} \right| \approx 10^6 \text{ m}^{-1} \quad (\text{B.8})$$

which is seen to be roughly two orders of magnitude bigger.

In the following table,  $\left| \frac{1}{\varepsilon_1^s} \frac{\partial \varepsilon_1^s}{\partial z} \right|$  is varied several orders of magnitude around the value given in (B.8), which results from different levels of gain and pump intensity, equ. (B.6). The italic line corresponds to the case study exposed above ( $A$  taken from equ. (B.8) and  $B$  from (B.7)). The table indicates when the second derivative becomes comparable to the first derivative in the wave equation:

$A = \left  \frac{1}{\varepsilon_1^s} \frac{\partial \varepsilon_1^s}{\partial z} \right $ , [m <sup>-1</sup> ]	$B = \frac{1}{2k_1^s} \left  \frac{1}{\varepsilon_1^s} \frac{\partial^2 \varepsilon_1^s}{\partial z^2} \right $ , [m <sup>-1</sup> ]	$B / A$
1	10 <sup>-8</sup>	10 <sup>-8</sup>
10 <sup>3</sup>	10 <sup>-2</sup>	10 <sup>-5</sup>
<i>10<sup>6</sup></i>	<i>10<sup>4</sup></i>	<i>10<sup>-2</sup></i>
10 <sup>7</sup>	10 <sup>6</sup>	10 <sup>-1</sup>
10 <sup>8</sup>	10 <sup>8</sup>	1

The table shows that the rather extreme case of HG-SP Raman considered here (diffraction-limited, undepleted pump) stands at the limit of validity of the paraxial approximation ( $B / A$  differing by two orders of magnitude). Moreover in our experiment we noticed the formation of laser-induced breakdown (LIB) at the waist, using a non-diffraction-limited ( $M^2=4$ ) pump beam and otherwise the same parameters as those considered in the above example. LIB is therefore one limiting mechanism that prevents the focused beams of reaching the level of

## Section 2: Numerical method

intensity that would bring  $\left| \frac{1}{\epsilon_1^s} \frac{\partial \epsilon_1^s}{\partial z} \right| > 10^6 \text{ m}^{-1}$  which would invalidate the paraxial approximation. We therefore conclude that in most cases involving commercial high power ultraviolet pump lasers the paraxial approximation is justified.

The case of non-gaussian pump and Stokes beam can possibly bring a bigger diffraction term, equ. (4), but it is unlikely that it exceeds the gain term, equ. (B.6), (three orders of magnitude ratio). It can also bring local intensity spikes, but these would be limited by the same mechanisms as exposed above (e.g. LIB).

## References

1. D. A. Haner, I. S. McDermid, "Stimulated Raman shifting of the Nd:YAG fourth harmonic (266 nm) in H<sub>2</sub>, HD, and D<sub>2</sub>", *IEEE J. Quant. Electron.*, **26**, 1292-1298 (1990).
2. W. B. Grant, E. V. Browell, N. S. Higdon, S. Ismail, "Raman shifting of KrF laser radiation for tropospheric ozone measurements", *Appl. Opt.*, **30**, 2628-2633 (1991).
3. J. A. Sunesson, A. Apituley, D. P. J. Swart, "Differential absorption lidar system for routine monitoring of tropospheric ozone", *Appl. Opt.*, **33**, 7045-7058 (1994).
4. S. E. Bisson, "Parametric study of an excimer-pumped, nitrogen Raman shifter for lidar applications", *Appl. Opt.*, **34**, 3406-3412 (1995).
5. J. H. Newton, G. M. Schindler, "Numerical model of multiple-Raman-shifting excimer lasers to the blue-green in H<sub>2</sub>", *Opt. Lett.*, **6**, 125-127 (1981).
6. C. Higgs, J. A. Russell, D. W. Trainor, T. Roberts, E. D. Ariel, B. E. Player, B. W. Nicholson, M. J. Smith, L. C. Bradley, "Adaptive-optics compensation in a Raman amplifier configuration", *IEEE J. Quant. Electron.*, **26**, 934-941 (1990).
7. B. W. Nicholson, J. A. Russell, D. W. Trainor, T. Roberts, C. Higgs, "Phasefront preservation in high-gain Raman amplification", *IEEE J. Quant. Electron.*, **26**, 1285-1291 (1990).
8. D. W. Trainor, "Military excimer-laser technology seeks real-world uses", *Laser Focus World*, PennWell Publishing, June 1993.
9. D. C. Hanna, M. A. Yuratich, D. Cotter, *Nonlinear optics of free atoms and molecules* (Springer, Berlin, 1979).
10. Y. R. Shen, *The principles of nonlinear optics* (Wiley, New-York, 1984).
11. J. C. van den Heuvel, "Numerical modeling of stimulated Raman scattering in an astigmatic focus", *IEEE J. Quant. Electron.*, **28**, 378-385 (1992).
12. T. R. Loree, R. C. Sze, D. L. Barker, P. B. Scott, "New lines in the UV: SRS of excimer laser wavelengths", *IEEE J. Quant. Electron.*, **15**, 337-342 (1979).
13. W. H. Press, S. A. Teukolsky, W. T. Vetterling, B. P. Flannery, *Numerical recipes in FORTRAN*, 2nd edition (Cambridge, 1992).

*Section 2: Numerical method*

14. A. Rizzi, B. Engquist, "Selected topics in the theory and practice of computational fluid dynamics", *J. Comp. Phys.*, **72**, 1-69 (1987).
15. S.-C. Sheng, A. E. Siegman, "Nonlinear-optical calculations using fast-transform methods: second-harmonic generation with depletion and diffraction", *Phys. Rev. A*, **21**, 599-606 (1980).
16. L. Thylén, "The beam propagation method: an analysis of its applicability", *Opt. Quant. Electron.*, **15**, 433-439 (1983).
17. G. D. Smith, *Numerical solution of partial differential equations - finite difference methods*, 3rd edition (Clarendon press, Oxford, 1985).
18. O. C. Zienkiewicz, R. L. Taylor, *The finite element method*, 4th edition (McGraw-Hill, London, 1989).
19. A. Taflove, *Computational electrodynamics: the finite-difference time-domain method* (Artech House, Boston, 1995).
20. A. P. Hickman, J. A. Paisner, W. K. Bischel, "Theory of multiwave propagation and frequency conversion in a Raman medium", *Phys. Rev. A*, **33**, 1788-1797 (1986).
21. D. Cotter, D. C. Hanna, R. Wyatt, "Infrared stimulated Raman generation effects of gain focusing on threshold and tuning behaviour", *Appl. Phys.*, **8**, 333-340 (1975).
22. S. F. Fulghum, D. W. Trainor, C. Duzy, H. A. Hyman, "Stimulated Raman scattering of XeF\* laser radiation in H<sub>2</sub> - Part II", *IEEE J. Quant. Electron.*, **20**, 218-222 (1984).
23. O. Rahn, M. Maier, "Raman-limited beam diameters in the self-focusing of laser light", *Phys. Rev. A*, **9**, 1427-1437 (1974).
24. A. Kazzaz, S. Ruschin, I. Shoshan, G. Ravnitsky, "Stimulated Raman scattering in methane - experimental optimization and numerical model", *IEEE J. Quant. Electron.*, **30**, 3017-3024 (1994).
25. W. K. Bischel, G. Black, "Wavelength dependence of Raman scattering cross section from 200-600 nm", in *Excimer Lasers-1983*, C. K. Rhodes, H. Egger, H. Pummer, eds. (American Institute of Physics, New-York, 1983).
26. W. K. Bischel, M. J. Dyer, "Wavelength dependence of the absolute Raman gain coefficient for the Q(1) transition in H<sub>2</sub>", *J. Opt. Soc. Am. B*, **3**, 677-682 (1986).
27. A. E. Siegman, *Lasers* (Oxford University Press, 1986).
28. G. I. Barenblatt, *Dimensional analysis* (Gordon & Braech, New-York, 1987).
29. M. D. Duncan, R. Mahon, J. Reintjes, L. Tankersley, "Parametric gain suppression in D<sub>2</sub> and H<sub>2</sub>", *Opt. Lett.*, **11**, 803-805 (1986).
30. A. Luches, V. Nassisi, M. R. Perrone, "Improved conversion efficiency of XeCl radiation to the first Stokes at high pump energy", *Appl. Phys*, **B47**, 101-105 (1988).

*Section 2: Numerical method*

31. D. Diebel, M. Bristow, R. Zimmermann, "Stokes shifted laser lines in KrF-pumped hydrogen: reduction of beam divergence by addition of helium", *Appl. Opt.*, **30**, 626-628 (1991).
32. Y. Chung, N. Dagli, "An assessment of finite difference beam propagation method", *IEEE J. Quant. Electron.*, **26**, 1335-1339 (1990).
33. R. Scarmozzino, R. M. Osgood Jr., "Comparison of finite-difference and Fourier-transform solutions of the parabolic wave equation with emphasis on integrated-optics applications", *J. Opt. Soc. Am. A*, **8**, 724-731 (1991).
34. S. E. Koonin, D. C. Meredith, *Computational physics* (Addison-Wesley, Redwood City CA, 1990).
35. R. Gruber, J. Rappaz, *Finite element methods in linear ideal magnetohydrodynamics* (Springer, Berlin, 1985).
36. A. E. Siegman, "Quasi-fast Hankel transform", *Opt. Lett.*, **1**, 13-15 (1977).
37. S. M. Candel, "An algorithm for the Fourier-Bessel transform", *Comp. Phys. Comm.*, **23**, 343-353 (1981).
38. V. L. Derbov, L. A. Melnikov, A. D. Novikov, S. K. Potapov, "Transverse pattern formation and spectral characteristics of cw light beams in resonant media: an improved numerical simulation technique and mode analysis", *J. Opt. Soc. Am. B*, **7**, 1079-1086 (1990).
39. J. P. Boris, D. L. Book, "Solution of continuity equations by the method of flux-corrected transport", in *Methods of Computational Physics*, **16** (Academic Press, New-York, 1976).
40. M. Abramowitz, I. Stegun, *Handbook of mathematical function* (Dover, New-York, 1965).

## **Section 3**

### **High-gain single-pass stimulated Raman scattering and four-wave-mixing in a focused beam geometry: numerical study**

#### **Abstract**

The coupled Maxwell nonlinear equations are numerically solved to describe the cascade Stokes conversion (stimulated Raman scattering and four-wave-mixing) in a high Raman gain molecular medium. A steady-state paraxial description is assumed, with a gain reduction parameter that accounts for the transient effects. The importance of the four-wave-mixing averaging effect on the Stokes energy spectrum is shown. A parametric study is conducted in which the focusing lens focal length, the type and partial pressure of the Raman-active gas and of added rare gas, and the quality of the pump beam, are varied. The conversion efficiency and beam quality of the Stokes and anti-Stokes spectrum are computed. Four-wave-mixing is shown to degrade the beam profile, which effect is the most pronounced for the higher Stokes. Beam cleanup (i.e. the decrease of the  $M^2$  parameter of the Stokes beam compared to the pump beam) occurs at low gain (i.e. before the intensity averaging regime appears), whereas it is the reverse case at high gain. The main qualitative features of the modelling match well previously published experimental data, and help explaining the commonalities and discrepancies between the results of different experimental set-ups.

### 3.1. Introduction

A powerful laser beam which is tightly focused in a molecular gas with high Raman gain in a single pass results in the appearance of a number of frequency down-converted (Stokes) and up-converted (anti-Stokes) beams. The Stokes and anti-Stokes beams are sequentially generated by the combined effect of stimulated Raman scattering (SRS) and four-wave-mixing (FWM), a phenomenon denoted "Stokes cascading". This configuration has been studied in a number of experiments<sup>1-8</sup>, mainly in the ultraviolet and with H<sub>2</sub>, D<sub>2</sub> or CH<sub>4</sub> as Raman medium. More than 20% photon conversion efficiency is reported up to the third Stokes with high-power commercial lasers (the Stokes, resp. anti-Stokes, number refers to the number of times the pump beam has been frequency downconverted, resp. upconverted).

The beam propagation and conversion is described here with the nonlinear Maxwell wave equation. The Stokes cascade results in a coupled set of partial differential equations (PDE). In high-gain single-pass focused (denoted HG-SP) configurations the nonlinear coupling is very strong (the full conversion process occurs in the waist region), which leads to a complex beam interaction pattern. In particular, when  $n$  Stokes and anti-Stokes beams are present (total number, including the pump), as many as  $(n-1)(n-2)/2$  different FWM processes occur. It is the purpose of this contribution to solve numerically the coupled set of PDE with the aim to gain some insight in the physics of the phenomenon. A parametric study is undertaken, in which the lens focal length, Raman medium (H<sub>2</sub>, D<sub>2</sub> and CH<sub>4</sub>), buffer gases (He and Ar), and pump beam quality are varied. The energy spectrum as well as the quality of the beams are analyzed after the conversion region. The Raman gain has a very strong dependence on the pumping wavelength (in H<sub>2</sub> it is 20 times bigger at the Nd:YAG fourth harmonic than at its fundamental). We consider a pump wavelength in the ultraviolet since with commercial high-power lasers it typically leads to Stokes cascade in a HG-SP focused configuration.

Newton<sup>9</sup>, Hickman<sup>10</sup> and Goldhar<sup>11</sup> modelled a plane-wave HG-SP Raman medium. Newton showed that the ratio of the SRS gain to the FWM phase-mismatch is proportionally related to the FWM averaging effect. Hickman showed the importance of transient effects and molecular population dynamics when the pulse width is comparable to the dephasing time of the medium, but neglected the dispersion of the latter. Goldhar demonstrated the effect of finite pump correlation length in FWM processes, which agreed well with experimental results. Bjorklund<sup>12</sup> studied analytically the FWM in a focused geometry, assuming all beams gaussian and the pump beams undepleted. He showed that the FWM efficiency is proportionally related to the focusing tightness and to the FWM dephasing length  $L_D = \pi/\Delta k$  where  $\Delta k$  is the FWM phase-mismatch. Perry et al.<sup>13</sup> modelled the steady-state SRS and FWM of the coupled (pump, 1st Stokes, 1st anti-Stokes) beams at threshold and in a focused geometry, using an expansion on Gauss-Laguerre modes and assuming that all the beams have the same confocal parameter. They showed that the threshold pump power increases as the confocal parameter is reduced, and that the beam shape and the ratio of Stokes to anti-Stokes energy depend critically on the confocal parameter. The present study includes the following elements of importance in a tightly focused HG-SP Raman configuration: multiwave generation and propagation (cascade Stokes and anti-Stokes), pump depletion, arbitrary beam profiles, and transient effects. A modelling gathering all these aspects has not been reported previously, to our knowledge. The high amplification occurring in a HG-SP Raman medium makes the set of coupled PDEs (including all the elements just mentioned) difficult to handle for numerical solvers. The study of this point has been undertaken previously<sup>14</sup>. Other HG-SP SRS modellings do not include the FWM because usually a configuration with low enough gain is considered<sup>5,15-18</sup>, which takes its origin in various factors such as the pump energy and wavelength, focusing geometry, Raman media, ... .

A configuration with a linearly polarized pump has been considered in this study. Quadrupled Nd:YAG lasers (266 nm) deliver a beam which is linearly polarized. On the other hand, the output of excimer lasers is not polarized and cannot hence be adequately described by this



### Section 3: Numerical simulation

model. The advantage of a linearly polarized pump stands in the fact that no rotational Stokes is generated, which simplifies the modelling. Stimulated backward Raman scattering has not been considered neither. Backward SRS occurs in hydrogen or deuterium when the pump laser has a narrow bandwidth (typically less than  $0.1 \text{ cm}^{-1}$ ). The bandwidth of Nd:YAG lasers is typically of the order of  $1 \text{ cm}^{-1}$  (when no dedicated arrangement for line narrowing is used). The present study applies therefore to such broadband pump lasers. Stimulated Brillouin scattering (SBS) is negligible in hydrogen and deuterium, but plays a significant role in methane at high pressure ( $>15 \text{ atm}$  typically). SBS has been neglected in the present model; this point is discussed in the annex B.

The numerical solution of a HG-SP configuration requires powerful computing capabilities<sup>14</sup>. In order to save CPU time, the PDEs are solved in cylindrical geometry, in the paraxial approximation and the steady-state regime. The high amplification in a HG-SP Raman medium makes the SRS transient. We included this effect by considering in the steady-state description a Raman gain reduction that accounts for the transient features.

HG-SP Raman medium in form of high-power laser shifters in the ultraviolet have areas of application such as lidar<sup>1</sup>, laser ranging<sup>19</sup> and laser lithography. One objective of the present study is to reach the understanding required to explain qualitatively the physical behaviour of such systems. The commonalities and differences of the experimental results obtained with different set-ups are still not well explained. We aim to point out the principles that allow the comparison between different experimental configurations, and possibly to make an extrapolation to other set-ups.

The physical model (wave propagation equations, model input data, transient gain reduction, model parametrization) is detailed in §3.2. Chapter 3.3 presents the parametric study. The comparison of the modelling output with previously published experimental results is found in chapter 3.4. The conclusion summarizes the main results.

## 3.2. Physical model

### 3.2.1 General

The physical model that is adopted to describe HG-SP Raman cells includes the focusing, the diffraction, four-wave-mixing, and gain reduction due to transient scattering. The nonlinear Maxwell wave equation<sup>20</sup> is used to describe the wave propagation, in the paraxial approximation and the steady-state regime (the inclusion of transient effects in a steady-state description is discussed further in this chapter). All FWM processes are considered which satisfy the resonant condition  $\omega_j - \omega_l = \omega_m - \omega_n = \omega_R$ , where  $j, l, m, n$  index either the pump, Stokes or anti-Stokes frequencies, and  $\omega_R$  is the Raman transition frequency. The example is given below of the wave equation for the second Stokes when three Stokes and one anti-Stokes, coupled by SRS and FWM, are included in the modelling<sup>9,21</sup>:

$$\begin{aligned}
\partial_x^2 \mathcal{E}_2^s + \partial_y^2 \mathcal{E}_2^s + 2ik_2^s \partial_z \mathcal{E}_2^s = ik_2^s g_{12} \mathcal{E}_2^s |\mathcal{E}_1^s|^2 - i \frac{(k_2^s)^2}{k_3^s} g_{23} \mathcal{E}_2^s |\mathcal{E}_3^s|^2 \\
+ i \frac{(k_2^s)^2}{\sqrt{k^p k_2^s}} g_{-1p12} \mathcal{E}_1^{as*} \mathcal{E}^p \mathcal{E}_1^s \exp(iz \Delta k_{p1-12}) \\
- i \frac{(k_2^s)^2}{\sqrt{k^p k_3^s}} g_{-1p23} \mathcal{E}_1^{as} \mathcal{E}^{p*} \mathcal{E}_3^s \exp(iz \Delta k_{-13p2}) \quad (1) \\
+ i \frac{(k_2^s)^2}{\sqrt{k_1^s k_2^s}} \frac{g_{p112}}{2} (\mathcal{E}_1^s)^2 \mathcal{E}^{p*} \exp(iz \Delta k_{11p2}) \\
- i \frac{(k_2^s)^2}{\sqrt{k_1^s k_3^s}} g_{p123} \mathcal{E}^p \mathcal{E}_1^{s*} \mathcal{E}_3^s \exp(iz \Delta k_{p312})
\end{aligned}$$

$\mathcal{E}$  is the slow-varying envelope of the electric field  $E: E(x, y, z, t) = \mathcal{E}(x, y, z) \exp(ikz - i\omega t)$ ,  $z$  being the axis of propagation and  $k$  the wavenumber.  $\mathcal{E}^p$ ,  $\mathcal{E}_i^s$  and  $\mathcal{E}_i^{as}$  denote the pump, the  $i$ -th generated Stokes and the  $i$ -th generated anti-Stokes fields, respectively. The frequency of  $\mathcal{E}_i^s$  and  $\mathcal{E}_i^{as}$  is given respectively by  $\omega_i^s = \omega^p - i\omega_R$  and  $\omega_i^{as} = \omega^p + i\omega_R$ , and their wavenumber is denoted by  $k_i^s$  and  $k_i^{as}$ , while the pump wavenumber is  $k^p$ .  $g_{i(i+1)}$  is the SRS gain for the conversion  $\omega_i^s \rightarrow \omega_{i+1}^s$  ( $\omega_{i+1}^{as} \rightarrow \omega_i^{as}$  for the anti-Stokes).  $\mathcal{E}$  is normalized such that  $|\mathcal{E}|^2$  has the unit of intensity, so that  $g$  has the usual unit of m/W.  $\Delta k_{jlmn} = k_j + k_l - k_m - k_n$  determines the phase-matching of the  $(jlmn)$  FWM process. The indices  $j, l, m, n$  take the value  $p$  to denote the pump, -1 for the (first) anti-Stokes, and 1 to 3 for the first to third Stokes respectively. It is assumed that only the isotropic part of the transition polarisability of the SRS processes is nonzero, so that the FWM gain is given by<sup>21</sup>  $g_{jlmn} = (g_{jl} g_{mn})^{1/2}$ . We choose to describe the FWM by  $g_{jlmn}$ , which has the unity of gain (m/W), because of the latter approximate relation and for the homogeneity of the presentation. FWM processes are nevertheless more usually described by a susceptibility formalism<sup>21</sup>. The relation between the SRS gain and susceptibility  $\chi$  is given by  $\chi_{p1} = (\epsilon_0 c^2 g_{p1}) / (3 i \omega_1^s)$  for the pump - Stokes1 interaction.

The FWM phase-matching expresses the conservation of momentum and can be also expressed as a vector relation<sup>11</sup>  $\Delta \mathbf{k}_{jlmn} = \mathbf{k}_j + \mathbf{k}_l - \mathbf{k}_m - \mathbf{k}_n$ . The vector phase-matching shows more clearly than its scalar counterpart in the frame of equ. (1) that the FWM is optimized at definite angles of propagation.

The coupled set of equations of type (1) are solved as an initial-value problem with respect to the  $z$  coordinate. A dedicated numerical method was developed which includes the focusing and applies either in cartesian geometry or in cylindrical geometry with azimuthal symmetry<sup>14</sup>.

### Section 3: Numerical simulation

Only the latter case is considered in this study in order to save computer time (the strong nonlinear coupling which characterizes HG-SP Raman cells imposes a grid with a large extent and a high knot density).

We adopted the  $M^2$  parameter as a measure of the beam quality. The  $M^2$  of each of the beams modelled is calculated numerically from the beam profile, at every position along the optical axis<sup>5,15</sup>.

#### 3.2.2 Input data to the model

The parameters chosen for all the simulation results (§3.3) are those typical of quadrupled Nd:YAGs (266 nm) used in HG-SP Raman cell applications in the ultraviolet. The pulse energy is 80 mJ in 6 nsec duration, and has 6 mm diameter (at 86% power). Unless otherwise specified, it is assumed to be diffraction-limited, and focused by an ideal lens of 50 cm focal length (which yields a waist of 15  $\mu\text{m}$  and a Rayleigh range of 2.8 mm). There is no seed Stokes beam, and the SRS is assumed to start from spontaneous Raman scattering. Five Stokes and three anti-Stokes with all the FWM processes among them have been taken into account (36 in total). The pump is labelled by  $P$ , the  $i$ -th Stokes by  $S_i$ , and the  $i$ -th anti-Stokes by  $AS_i$ .

The steady-state gain for the P- $S_1$  SRS process is given by<sup>21</sup>

$$g_{p1} = \frac{2\lambda_{s1}^2}{hc\nu_{s1}} \frac{Nk_B}{\pi c\Delta\nu} \left( \frac{d\sigma}{d\Omega} \right) \quad (2)$$

with corresponding expressions for the other SRS processes.  $\lambda_{s1}$  is the  $S_1$  wavelength in cm and  $\nu_{s1}$  its frequency in  $\text{cm}^{-1}$ ,  $c$  the speed of light in  $\text{cm/s}$ ,  $h$  is Planck's constant ( $6.626 \times 10^{-34}$  Js),  $N$  the molecules number density in  $\text{cm}^{-3}$ ,  $k_B$  the Boltzman population factor,  $\Delta\nu$  the Raman linewidth (FWHM) in  $\text{cm}^{-1}$ , and  $d\sigma/d\Omega$  the P- $S_1$  the differential Raman cross section in  $\text{cm}^2/\text{sr}$ . The data used for the Raman gain calculation at 295 K for  $\text{H}_2$ ,  $\text{D}_2$  and  $\text{CH}_4$ , is found at table 1.

**Table 1.** Parameters used in the calculation of the Raman gain at 295 K, equ. (9). The Raman scattering cross section is given as a single resonance fit:  $d\sigma/d\Omega = A\nu_s^4 / (\nu_i^2 - \nu_p^2)^2$ , where  $\nu_p$  and  $\nu_s$  is the pump and Stokes frequency respectively.  $p$  is the Raman-active gas pressure.

Gas	Raman shift ( $\text{cm}^{-1}$ )	$k_B$	$\Delta\nu$ ( $10^{-3} \text{ cm}^{-1}$ ) as a function of $p$ (atm)	$A$ ( $10^{-28} \text{ cm}^2/\text{sr}$ ) [38]	$\nu_i$ ( $10^4 \text{ cm}^{-1}$ ) [38]
$\text{H}_2$ Q(1)	4155	0.66	$\frac{11.2}{p} + 1.58p$ [35]	8.74	8.48
$\text{D}_2$ Q(2)	2987	0.38	$\frac{3.67}{p} + 3.58p$ [36]	3.90	7.81
$\text{CH}_4$ Q	2917	1	$320 + 12p$ [37]	10.4	7.23

### Section 3: Numerical simulation

In practice, rare-gas (further on called “buffer gas”) is often mixed with the Raman-active molecules in order to control the energy sharing between the Stokes beams as well as their divergence<sup>3,4</sup>, by reducing the gain and increasing the FWM phase-mismatch. The Raman linewidth in case of gas mixing can be approximated by<sup>42</sup>

$$\Delta\nu = \Delta\nu_0 + \gamma p_b \quad (3)$$

$\Delta\nu_0$  being the self-broadened linewidth,  $\gamma$  the broadening coefficient and  $p_b$  the buffer gas partial pressure. The underlying assumptions to (3) are that first the self-broadening occurs independently from the buffer gas broadening, and second that there is no shift of the molecule vibrational frequency. The broadening coefficients used in the simulation are found at table 2.

The dispersion formula of H<sub>2</sub> and D<sub>2</sub> was derived from a double-resonance fit to the data of table 4a of [22]. Note that the resonance-fit parameters of [22] table 4b for H<sub>2</sub> and D<sub>2</sub> show an average discrepancy of 5% and 30% with the data of table 4a of the same reference, respectively. We take [22] table 4a as input data for the resonance fit because it agrees for the case of H<sub>2</sub> within 0.1% with two independent measurements ([22] table 5 and ref. [23] table 4). On the other hand the resonance-fit parameters of [22] table 4b for CH<sub>4</sub>, He and Ar agree within 0.1% with the data of [22] table 4a, and were used in this study. The data of ref. [22] table 4a for He and Ar was checked to agree within 0.1% with the data of the more recent measurements of ref. [24] table II. The resonance-fit parameters of the dispersion formulae used in the phase-mismatch calculations are found at table 3; the perfect gas law was used for the calculation of the refractive index at other pressures and temperatures.

**Table 2.** Broadening coefficients  $\gamma$  used in the calculation of the Raman linewidth, equ. (10).

Raman-active gas	Buffer gas	Broadening coefficient (10 <sup>-3</sup> cm <sup>-1</sup> /Amagat)	Reference
H <sub>2</sub> Q(1)	Ar	5.3	[39]
	Ne	2.7	[39]
	He	1.58	[40]
D <sub>2</sub> Q(2)	Ar	3.37	[41]
	He	2.35	[41]

**Table 3.** Resonance-fit parameters at 272 K and 1 atm to the dispersion relation

$$\frac{3n^2 - 1}{2n^2 + 2} = \frac{C_1}{\lambda_1^{-2} - \lambda^{-2}} + \frac{C_2}{\lambda_2^{-2} - \lambda^{-2}} + \frac{C_3}{\lambda_3^{-2} - \lambda^{-2}}$$

where  $n$  is the index of refraction and  $\lambda$  the wavelength in cm<sup>22</sup>.

	$C_1$ 10 <sup>4</sup> cm <sup>-2</sup>	$C_2$ 10 <sup>4</sup> cm <sup>-2</sup>	$C_3$ 10 <sup>4</sup> cm <sup>-2</sup>	$\lambda_1^{-2}$ 10 <sup>8</sup> cm <sup>-2</sup>	$\lambda_2^{-2}$ 10 <sup>8</sup> cm <sup>-2</sup>	$\lambda_3^{-2}$ 10 <sup>8</sup> cm <sup>-2</sup>
H <sub>2</sub>	123.20	162.04		111.37	636.19	
D <sub>2</sub>	125.50	140.54		114.08	580.94	
CH <sub>4</sub>	55.813	626.0279		64.2208	181.2638	
He	147.574			425.91		
Ne	288.14			432.40		
Ar	25.2582	25.2582	595.379	87.882	91.001	269.636

### 3.2.3 Transient gain reduction

For plane wave, the SRS can be considered as steady-state if  $t_p \gg GT_2$ <sup>21</sup> where  $t_p$  represents the characteristic time scale of changes of the pump intensity, and  $T_2$  is the dephasing time ( $T_2 = 1/(\pi\Delta\nu)$ ).  $G = gI_p z$  is the amplification factor, with  $I_p$  the intensity of the pump wave and  $z$  the length of the medium. As taken from table 1, the linewidth of H<sub>2</sub> and D<sub>2</sub> increases monotonically with respect to the pressure above 2.7 and 1.0 atm respectively, whereas the linewidth of CH<sub>4</sub> increases at any pressure. Considering the value  $G=30$  for the threshold (which is usual<sup>21</sup>) and a pulse duration  $t_p=5$  nsec, we have  $t_p > GT_2$  for pressures above 40.0 and 17.7 atm for H<sub>2</sub> and D<sub>2</sub> respectively. Most HG-SP Raman cell applications seek a maximum of energy conversion to a given Stokes, and hence operate well above the threshold (typically more than ten times the  $G$  value of the threshold). Considering  $G=300$  and  $t_p=5$  nsec, we have  $t_p < GT_2$  for both H<sub>2</sub> and D<sub>2</sub> for pressures below 100 atm, whereas for CH<sub>4</sub> it is the case for pressures below 26 atm. For typical lasers pumping HG-SP Raman cells, the pulse duration is 4-8 nsec for the Nd:YAG and 10-30 nsec for excimers. We conclude that for most practical cases of HG-SP Raman cells the SRS is transient.

For plane-wave, non-depleted pump and rectangular temporal pump pulse, Wang<sup>25</sup> showed that in case  $G > \Delta\nu t_p$  and  $G t_p \Delta\nu \gg 1$  (i.e. high gain) the growth of the Stokes wave is approximated by

$$\mathcal{E}^s = \mathcal{E}_o^s \frac{\exp\left(2\sqrt{G} \tau_o - \tau_o^2\right)}{\left(8\pi\sqrt{G} \tau_o\right)^{1/2}} \quad (4)$$

with  $\tau_o^2 = t_p \Delta\nu$ . Equ. (4) can be interpreted as a steady-state description, provided that the steady-state gain is reduced by a so-called ‘‘gain reduction factor’’<sup>26</sup>. To this end, the equation is differentiated with respect to  $z$ , which yields

Section 3: Numerical simulation

$$\frac{\partial \mathcal{E}^s}{\partial z} = \mathcal{E}^s I_p \frac{g}{2} \frac{1}{\sqrt{G}} \left( \sqrt{t_p \Delta \nu} - \frac{1}{4\sqrt{G}} \right) \quad (5)$$

with  $I_p$  having been defined as  $|\mathcal{E}|^2$  (that is,  $\mathcal{E}$  suitably normalized). When comparing equ. (5) with the steady-state Raman term as found in equ. (1), the gain reduction factor  $R$  is identified as

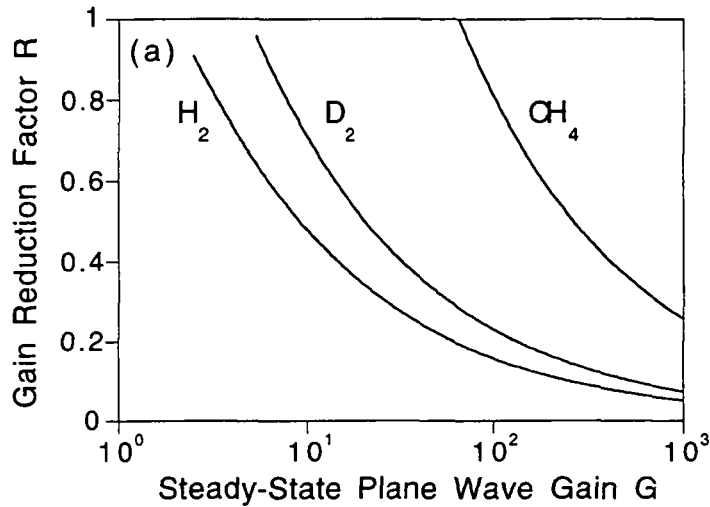
$$R = \frac{1}{\sqrt{G}} \left( \sqrt{t_p \Delta \nu} - \frac{1}{4\sqrt{G}} \right) \quad (6)$$

Note that the gain reduction factor (6) differs slightly from the one defined in [26]. In the latter the transient and steady-state descriptions are not compared at the level of the differential equation (as here), but from the propagation equation of type (4). The definition adopted here is more suited to the present physical model, which stands in differential form.

When the conditions of validity of (6) are met, then  $R < 1$  (gain reduction). Since it is required that  $G t_p \Delta \nu \gg 1$ , in most cases the second term in the parenthesis is much smaller than the first term, so that

$$R \cong \sqrt{t_p \Delta \nu / G} \quad (7)$$

The gain reduction for  $H_2$ ,  $D_2$  and  $CH_4$  at a pressure of 10 atm and for  $t_p = 5$  nsec is presented at fig. 1a. The SRS and FWM processes are local, and the gain reduction applies independently at any position of the beam profile. For gaussian-shaped beams,  $R$  is at its minimum on the optical axis and increases with respect to the distance to the axis. Fig. 1b illustrates this effect of smoothing the gain profile of the pump beam. The amplification rate  $A$  is defined as  $g_{p1}$  times the pump beam intensity (unit of  $m^{-1}$ ).  $A$  is seen to decay in proportion slower in the transient than in the steady-state case, yielding for example a factor  $\sim 2.5$  at a distance of two gaussian radii to the optical axis. It is a very consequent discrepancy considering the exponential amplification that characterizes the SRS. From a distance of 3 gaussian radii on, the discrepancy reaches the order-of-magnitude level.



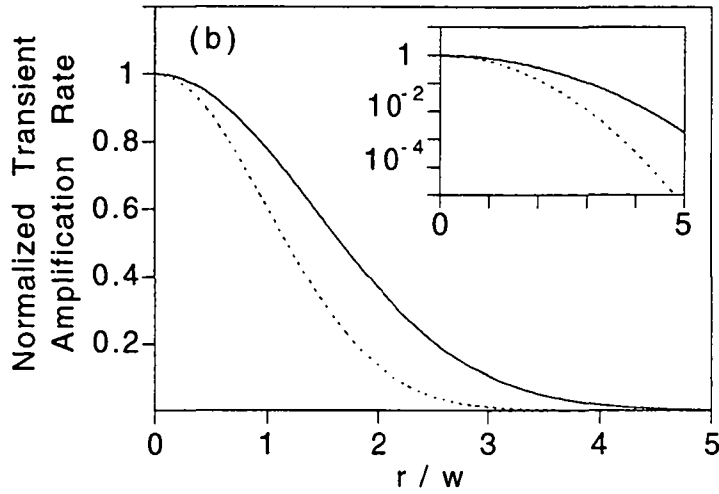


**Fig. 1.** In (a), transient plane wave gain reduction, equ. (3), for hydrogen, deuterium and methane, at 10 atm and for  $t_p=5$  nsec. Only those values are displayed which comply to the conditions of validity of equ. (3). In (b), normalized transient amplification rate at the waist, defined as  $g_{p1}$  times the pump beam intensity (unit of  $m^{-1}$ ), as a function of the transverse axis coordinate in units of gaussian beam radius. A gaussian beam profile is assumed, of radius 3mm (at 86% power),  $t_p=5$  nsec, 80 mJ pulse energy, which is focused in  $H_2$  to a waist of 15  $\mu m$  by a 50 cm lens. The dashed line corresponds to the normalized steady-state amplification rate. The small inside frame contains the same plot but with a log scale ordinate.

In fig. 2 it is seen that the pressure-dependence of  $H_2$ ,  $D_2$  and  $CH_4$  is different for the steady-state and transient gain  $g_t$ , defined as  $g_t = g R$ , since  $g_t$  is proportional to the square-root of the Raman linewidth. At high gain  $g_t$  is proportional to the square-root of the pressure, as seen from equ. (2) and (6), whilst the steady-state gain tends towards a constant value for high pressures.

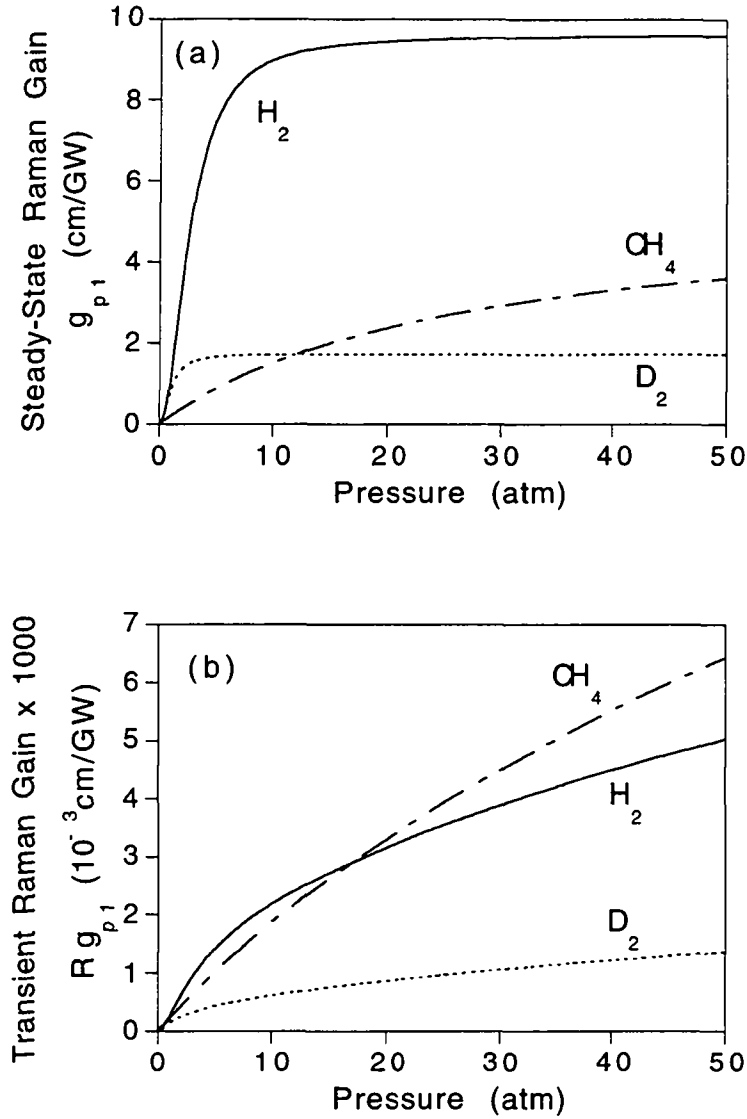


**Fig. 2.** In (a), steady-state gain for hydrogen, deuterium and methane, based on table 1. In (b), transient gain of a gaussian-shaped beam, taken on the optical axis and at the waist. The beam parameters are the same as for fig. 1b.

The gain reduction formula (6) has been verified experimentally for a configuration at threshold<sup>26</sup>. For the cases envisaged in this study of high gain (i.e. depleted pump) and focused geometry the non-depleted pump theory of Wang is no more directly applicable. We can nevertheless use this theory in the frame of the split-step scheme (SSS) that is adopted to solve the partial differential equation (PDE) of type (1) describing the beam propagation<sup>14</sup>. The PDE, after a change of variables that relates to the focusing, is written in the form of a sum of operators, noted  $L_i$ , each of them corresponding to a group of terms. Equ. (1) is in this way expressed as:

$$\partial_z S = L_1 S + L_2 S + L_3 S + L_4 S \quad (8)$$

where  $S$  is a variable directly related to the field.  $L_1$  and  $L_2$  are the  $x$  and  $y$  second-derivative terms respectively,  $L_3$  relates to the focusing, and  $L_4$  gathers all the nonlinear coupling terms. A PDE is associated to each of the  $L_i$  that is solved sequentially:



$$\begin{aligned}
 \tau^1 &= L_1(s^n) \\
 \tau^2 &= L_2(\tau^1) \\
 \tau^3 &= L_3(\tau^2) \\
 s^{n+1} &= L_4(\tau^3)
 \end{aligned} \tag{9}$$

where  $s^n$  denotes the approximation to  $S$  at position  $z_n$ , and the  $\tau^i$  are intermediate values that are discarded after completion of the step  $z_n \rightarrow z_{n+1}$ . Physically the SSS corresponds to the subdivision of the continuous medium in subsequent layers, each described by an operator  $L_i$ : one layer for the diffraction along the x- and y-axis, one for the intensity and phase adjustment due to the focusing, and one for the nonlinear coupling. The latter can be further divided in sublayers (each of the SRS term of equ. (1)), each describing the growth of a Stokes plane wave with undepleted pump. The FWM terms are interpreted the same way, since they can be viewed as the combination of two SRS processes. This way, the undepleted pump plane wave theory of Wang applies to our situation of focused pump with depletion, provided that the medium is subdivided in sufficiently small layers.

The numerical solution of the set of coupled PDE in a steady-state description requires in itself powerful computing capabilities in order to describe high-gain single-pass (HG-SP) configurations of practical importance<sup>14</sup>. The addition of the time derivative would yield a computer time of the order of weeks for typical simulated situations, with the computer we had at disposal (DEC 7620, which has a speed rate of 9329 in floating point mode<sup>43</sup> (SRate FP); currently one of the quickest available machines is the Cray CS64K which has a SRate FP of 72177<sup>44</sup>), while with a steady-state description it is of the order of hours which was found tractable. The choice of performing an approximation on the time derivative rather than on the spatial derivatives is motivated by the crucial importance of the diffraction effects in HG-SP tightly focused Raman configurations. The computing time is further reduced by assuming a cylindrical geometry (which is relevant for several types of lasers, such as the Nd:YAG), and the paraxial approximation.

Transient effects are essential in explaining several phenomena in some stimulated Raman scattering (SRS) experiments. Namely, solitons<sup>46-49</sup>, pump-Stokes oscillations<sup>50,51</sup>, Stokes pulse compression<sup>52-54</sup>, gain enhancement by delayed seeding<sup>45,54,55</sup>. The situation considered in this study differs from the other transient SRS studies. For example, solitons appear in unfocused multi-pass cells (interaction length of several tens of meters instead of several mm as in our case) when a seed Stokes beam shows random phase fluctuations. Therefore we cannot infer from previous work whether the time derivatives are essential or not in our case. The complexity of the problem forced us to make an assumption, which we adopted to affect the time derivative. Since the present modelling of HG-SP SRS is new, one aim of the study is to determine to which extent the time derivatives are important. The modelling features to be improved stand clearly in the solution of the time derivatives, but also in a better characterization of the input pump field, the treatment of the molecular ground-state depletion and dynamics, and of multi-photon ionization at the waist.

To summarize, it is acknowledged that the steady-state gain reduction formalism represents a crude approximation of the transient features in the cases studied, although very practical. We argue that our methodology of making simplifying assumptions on the transient rather than on the spatial description, due to computer constraints, is unavoidable because the diffraction effects are essential to understand the principal features of HG-SP configurations such as the beam quality. The methodology of this contribution, which is motivated by the lack of previous similar numerical work, determined to which extent the time derivatives are needed in the description, and this process is based on the agreement between the model predictions and

### Section 3: Numerical simulation

experimental results. The use of a plane-wave gain reduction theory has been experimentally confirmed in a previous study, and has its justification in the frame of the present arbitrary-wave description in the numerical method adopted. In conclusion, we think that the trade-off we were conducted to adopt is adequate to the cases studied in view of the present status of the research.

#### 3.2.4 Dimensional analysis

Several possibilities exist to combine the parameters of the problem in order to obtain non-dimensional quantities that help interpreting the physics of HG-SP Raman cells. For reasons that will become clear in the course of the discussion (§3.3) we choose to work with the three following non-dimensional parameters:

1)  $G_f = R_f G_{ss}$ , with  $G_{ss} = g_{p1} I_{pf} (2z_o)$ , where  $I_{pf}$  is the average (e.g. top-hat) pump intensity in vacuum at the waist,  $z_o$  the Rayleigh range of the pump in vacuum,  $R_f$  is defined below, and the steady-state gain is arbitrarily chosen to be  $g_{12}$  (instead of the gain of other SRS processes). As suggested by plane-wave analysis at the waist, the parameter  $G_f$ , named “gain parameter”, is proportionally related to the strength of the SRS and FWM processes.

2)  $R_f = \sqrt{t_p \Delta\nu / G_{ss}}$ , the transient gain reduction at the waist, equ. (7).

3)  $\xi = G_f / (\Delta k_{12p3} 2z_o)$ , where the phase-mismatch is arbitrarily chosen to be  $\Delta k_{12p3}$  (corresponding to the (P,S<sub>1</sub>,S<sub>2</sub>,S<sub>3</sub>) mixing), is proportionally related to the FWM strength since the FWM terms in equ. (1) are proportional to the gain, and the complex exponential tends to equalize to zero when the phase-mismatch increases. This proportionality dependence has been showed numerically by Newton<sup>9</sup> in case of plane-wave.

$G_f$ ,  $R_f$  and  $\xi$  are expressed as a function of the three independent non-dimensional parameters  $G_{ss}$ ,  $t_p \Delta\nu$  and  $\Delta k_{12p3} z_o$ . Nevertheless the former set of parameters proved to be more significant in the analysis of the HG-SP Raman cell physics (§3.3).

### 3.3. Results and discussion

The study is conducted in form of a parametric variation: with/without FWM (§3.3.1), lens focal length (§3.3.2), pump beam quality (§3.3.3), type of Raman-active gas (§3.3.4), type and pressure of an added buffer gas (§3.3.6). The quantities analyzed are the energy spectrum after the conversion region and the beam quality (via the  $M^2$  parameter). The results are displayed in form of plots with the active or buffer gas pressure on the abscissa.

#### 3.3.1 Relevance of FWM

Calculations were carried out with or without including the FWM terms in the wave equations of type (2), shown in fig. 3. The averaging effect of FWM is clearly noticeable. The threshold pressure  $P_t$  is defined as the one corresponding to 1% photon conversion efficiency. The higher the Stokes the more FWM processes lead to that Stokes. This has the effect for the higher Stokes (S<sub>3</sub>, S<sub>4</sub>) first to decrease the threshold pressure, and second to be more intensity averaged. The  $P_t$  decrease due to FWM is especially pronounced for S<sub>3</sub>-S<sub>5</sub>, whereas it is slightly reduced (10%) for S<sub>2</sub>, and for S<sub>1</sub> the effect is reversed. The FWM effect of intensity averaging is evidenced by the conversion efficiency maximum (noted  $\hat{\eta}$ ) of each of the Stokes, which is smaller than without FWM. Also, the averaging is stronger in the 3-10 atm range (S<sub>3</sub> & S<sub>4</sub> dominant) than in the 1-3 atm range (S<sub>1</sub> & S<sub>2</sub> dominant).

### Section 3: Numerical simulation

Above 10 atm, the H<sub>2</sub> steady-state gain is almost constant (fig. 2). Because of the gain reduction dependence on the active gas pressure (through the linewidth), the transient gain continues to grow with increasing pressure, which is evidenced by the further Stokes cascading between 10 and 20 bar in fig. 3a and 3b.

#### 3.3.2 Effect of the focusing

As shown in fig. 3b and 4, for any Stokes the higher the lens focal length (noted  $f$ ), the lower the threshold pressure, and in particular the lower the pressure at which the maximum of the Stokes arises (noted  $P_m$ ). Perry et al.<sup>13</sup> obtained the same dependence. The parameter  $G_f$  is seen to be independent of the lens focal length since the pump area at the waist and the Rayleigh range are proportional to  $f^2$  and hence  $G_{ss}$  is independent of  $f$ . In order to better take into account the geometry of focusing,  $G_f$  can be evaluated as  $G'_f = g_{12} \int_{z_f - z_o}^{z_f + z_o} I_p(z) R(z) dz$ . This expression cannot be evaluated analytically. For the parameters corresponding to fig. 3b and fig. 4,  $G'_f$  is ~30% smaller for the  $f=50$  cm case than for  $f=100$  cm, and also 30% smaller for the  $f=25$  cm case than for  $f=50$  cm. One reason for the observed  $f$ -dependence is therefore the transient gain reduction (note that when  $R$  is omitted in the integrand, then  $G'_f$  is independent of  $f$ ). Alternatively we notice that the  $\xi$  parameter is inversely proportional to  $f^2$ , and therefore the FWM strength increases as  $f$  is reduced. Moreover there are more possibilities for wave-vector matching when  $f$  (and hence the numerical aperture) decreases. As noticed in §3.3.1 a stronger FWM increases  $P_t$  of  $S_1$  (which explains the result of Perry et al., obtained with a steady-state description) while it reduces  $P_t$  of  $S_i$ ,  $i \geq 3$ . Concerning the  $P_t$  dependence on  $f$  the transient gain reduction seems therefore stronger than the FWM effect for the higher Stokes.

The FWM averaging effect dependence on  $f$  is noticeable on the figures: the maximum conversion efficiency  $\hat{\eta}$  for the higher Stokes decreases with  $f$  (which is clearly noticeable for  $S_3$  and  $S_4$ ). As a result the conversion efficiencies of the remaining pump and the lower Stokes ( $S_1$  and  $S_2$  on these figures) increase. The maximum conversion efficiency of P,  $S_1$  and  $S_2$  is difficult to predict. For example the  $S_1$  optimum is reached for the medium focusing, while the focusing is less critical for  $S_2$ .

It has to be stressed that the conversion efficiency represented in all graphs of this section is the photon conversion efficiency. Experimental conversion efficiency curves are usually represented as the energy conversion efficiency. The ratio of the photon to energy conversion efficiency is proportional to the ratio of the Stokes to the pump wavelength. Therefore this ratio increases with the Stokes order (it equals for instance 1.8 for the fourth Stokes, in hydrogen). This fact explains why high photon conversion efficiencies are found for the higher Stokes, as in fig. 3b.

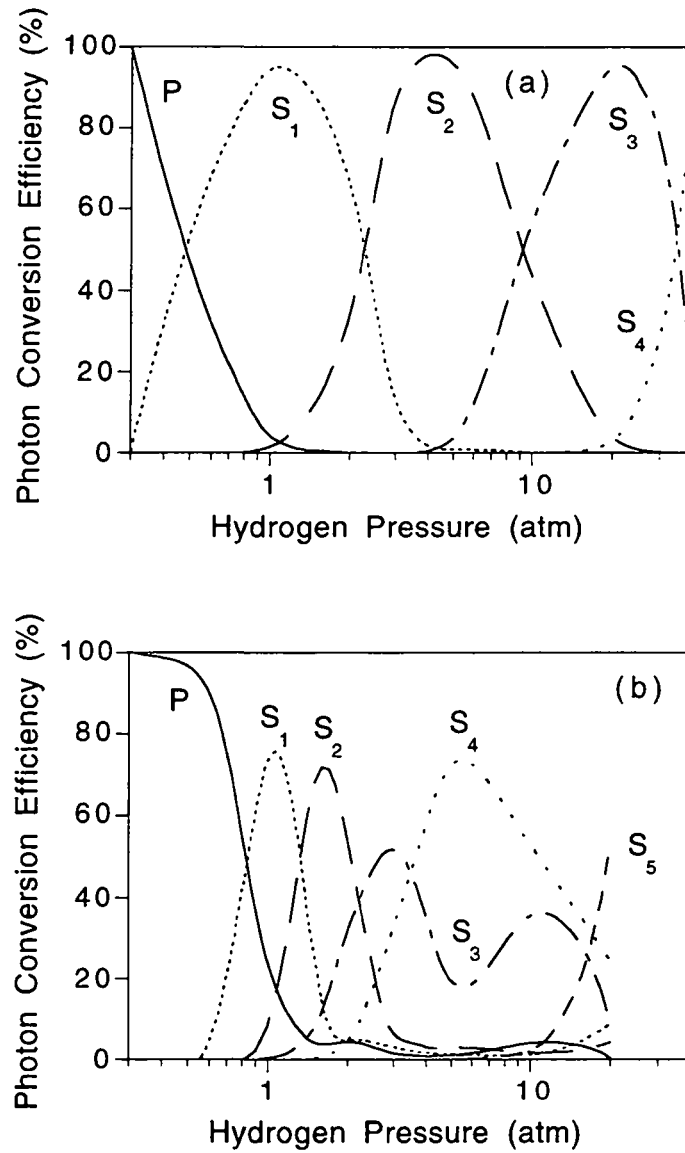


**Fig. 3.** Stokes energy spectrum after the conversion region. The pump is a diffraction-limited quadrupled Nd:YAG (266 nm) of 80 mJ pulse energy, 6 nsec duration, 6 mm diameter (86% power), focused by a 50 cm lens in the center of a cell filled with hydrogen. In (a) only the SRS coupling is included, while in (b) all possible FWM processes among the Stokes beams have been added (5 Stokes and 3 anti-Stokes modelled).

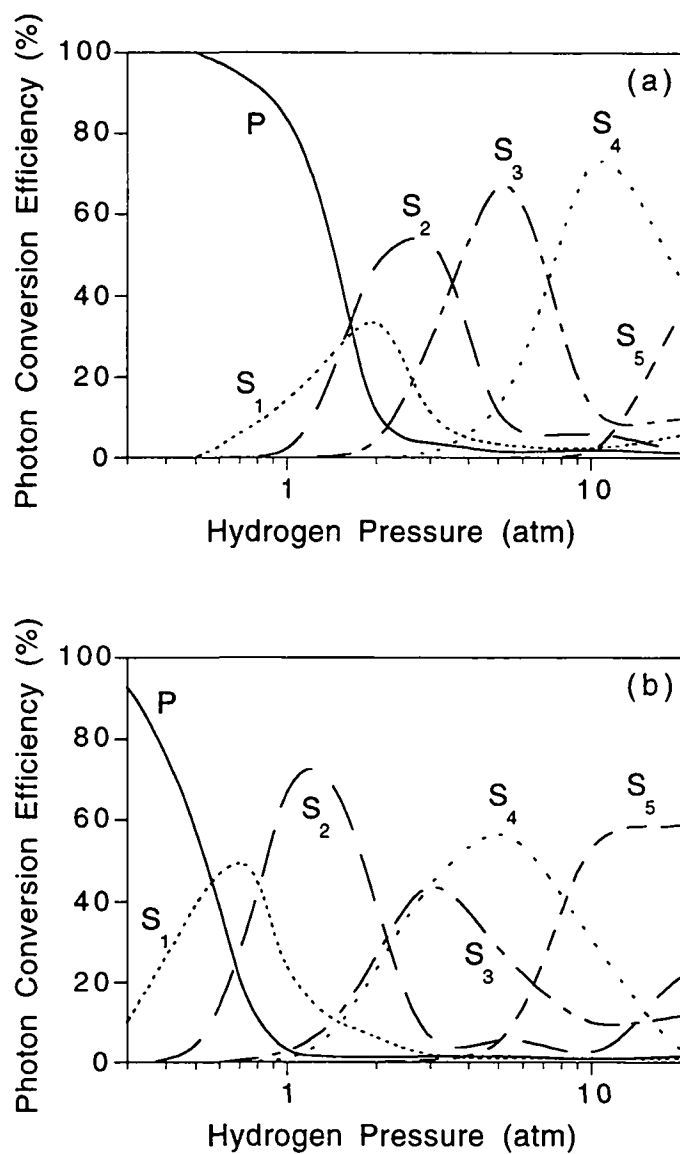


Fig. 4. Same as fig. 3b, except that the lens focal length is 25 cm in (a) and 100 cm in (b).

### 3.3.3 Effect of the pump beam quality

The Gauss-Laguerre (GL) modes were chosen as the most convenient way of numerically modelling non-diffraction-limited pump beams with azimuthal symmetry. The GL TEM<sub>pl</sub> modes are of the form<sup>27</sup>

$$\mathcal{E}_{pl}(r, \phi, z) = \frac{\mathcal{E}_0}{w(z)} \left( \frac{r\sqrt{2}}{w(z)} \right)^l L_p^l \left( \frac{2r^2}{w^2(z)} \right) \cos l\phi \exp \left( \frac{-r^2}{w^2(z)} \right) \quad (10)$$

where  $L_p^l(x)$  is the Laguerre polynomial.  $M^2 = 1 + 2p + l$  for  $l \neq 1$ , and for  $l=1$   $M_x^2 = 3(1+p)$  and  $M_y^2 = 1+p$ .  $r^2 = x^2 + y^2$ ,  $\phi$  is the azimuthal angle, and  $w$  is the beam radius of the corresponding gaussian beam.

In fig. 5 (a) - (c),  $l=0$  and  $p$  varies, so that the  $M^2$  parameter equals to 3 (a), 5 (b) and 7 (c). Note that the diffraction-limited (DL) pump case, i.e.  $L_0^0$  and  $M^2=1$ , was considered at fig. 3b. Since the input pump beam size is kept fixed, the waist size and the Rayleigh range are  $M^2$  times bigger than for the DL case. Concerning the geometry of focusing, it is therefore expected that increasing the  $M^2$  has similar effects as increasing the lens focal length. For instance  $\xi$  is proportional to  $1/f^2$  and to  $1/M^2$ . Such a dependence is verified for the FWM (explained by  $\xi$ ). The averaging effect is seen to lessen for increasing  $M^2$ :  $S_3$  and  $S_4$  reach their maximum in the same pressure range for  $M^2=1$ , whereas it is  $S_2$  and  $S_3$  for  $M^2=5$ , while for  $M^2=7$  no beams are seen to overlap. Also, the  $S_3$ - $S_4$  pressure dependence of the DL case is quite alike the  $S_2$ - $S_3$  pressure dependence of the  $L_2^0$  case. A similar reduction in the FWM averaging effect was noticed when increasing  $f$ . On the other hand the  $P_t$  and  $P_m$  dependence on  $M^2$  is not alike that on  $f$ : they are seen to increase with  $M^2$  while the reverse is true for  $f$  (especially for  $S_i$ ,  $i \geq 2$ , and between  $L_0^0$  and  $L_1^2$  or  $L_0^4$ ). Notice for instance the  $S_4$  threshold pressure increase between  $M^2=1$  and  $M^2=5$ . This  $M^2$  dependence is explained by the reduced pump intensity for increasing  $M^2$ , due to a higher number of side lobes ( $L_p^0$ ) or a ringing structure with enlarging diameter ( $L_p^l$ ,  $p \neq 0$ ).

The pump beam shape influences the FWM through the phase-matching angle of the latter, as shown in fig. 5 (b), (d) and (e) where three cases of GL pump with  $M^2=5$  are given. The beam shape of the higher Stokes ( $S_3$ ,  $S_4$ , to a lesser extent  $S_2$ ) is seen to change dramatically depending of the pump shape. The difference in the input pump profile between the  $L_2^0$  and  $L_1^2$  pumps is the most pronounced at lower radii than between  $L_1^2$  and  $L_0^4$ , with the consequence that between the two former  $S_2$  is the most different while between the two latter it is  $S_3$  and  $S_4$  that are the most different (the higher the  $S_i$ , the bigger the angle of phase-matching).

Section 3: Numerical simulation

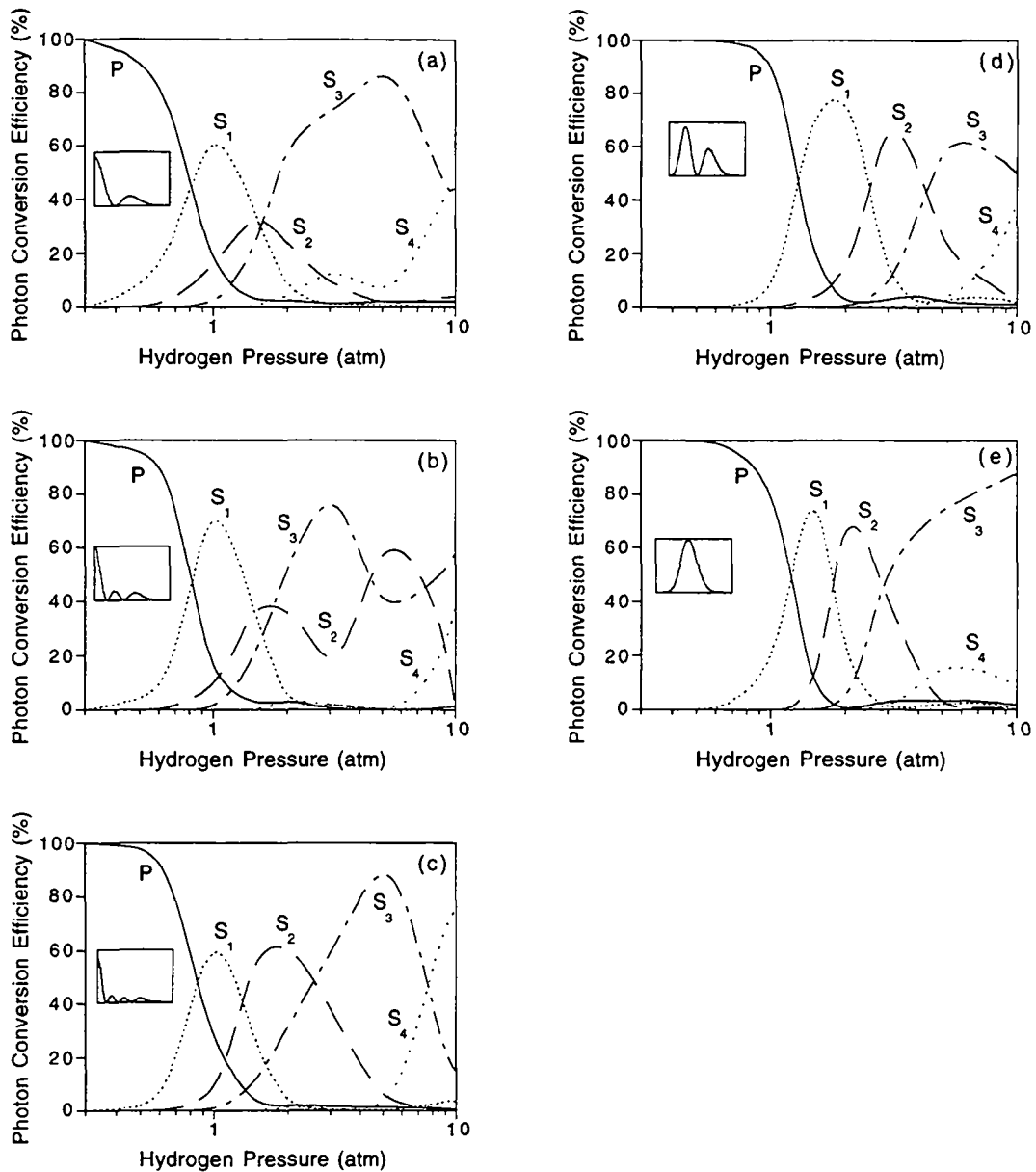


**Fig. 5.** Same as fig. 3b, except that the pump beam is one of the following Gauss-Laguerre modes:  $L_1^0$  (a),  $L_2^0$  (b),  $L_3^0$  (c),  $L_1^2$  (d),  $L_0^4$  (e), with respective  $M^2$  parameter of 3, 5, 7, 5, and 5. The input beam profile (positive part of the x-axis) is displayed in the small rectangle in each figure.

### Section 3: Numerical simulation

#### 3.3.4 Deuterium and methane

In order to facilitate the comparison between the hydrogen, deuterium and methane cases, all the relevant configuration parameters are gathered in table 4. The lower gain of deuterium with respect to hydrogen reflects on the Stokes threshold, as shown in fig. 3b and fig. 6. The much higher linewidth of CH<sub>4</sub> relative to H<sub>2</sub> and D<sub>2</sub> has the consequence that the transient gain reduction is less: figs. 3b, 6 and 7 show that the Stokes threshold is significantly smaller for CH<sub>4</sub> than for the two other gases, although at pressures below 10 atm the steady-state CH<sub>4</sub> gain is smaller than the H<sub>2</sub> gain.

**Table 4.** Raman cell parameters for a diffraction-limited pump at 266 nm of 80 mJ pulse energy in 6 nsec duration and 6 mm diameter (at 86% power). The beam is focused by an ideal lens of 50 cm focal length (which yields a waist of 15  $\mu$ m and a Rayleigh range  $z_0=2.8$  mm). All quantities displayed correspond to the S<sub>2</sub> photon conversion efficiency maximum (which occurs at a pressure noted  $P_m$ ), see fig. 3b (H<sub>2</sub>), 6 (D<sub>2</sub>) and 7 (CH<sub>4</sub>).

	H <sub>2</sub>	D <sub>2</sub>	CH <sub>4</sub>
$P_m$ (atm)	2	4	0.5
$g_{12}$ (cm/GW)	3.56	1.62	0.101
$\Delta k_{12p3}$ (m <sup>-1</sup> )	104.5	116.5	48.1
$\Delta\nu$ , FWHM (10 <sup>-3</sup> cm <sup>-1</sup> )	8.76	15.2	326
$G_{ss} = g_{p1} I_{pf} (2z_0)$	3568	1624	101.2
$R_f = \sqrt{t_p \Delta\nu / G_{ss}}$	0.0210	0.0411	0.761
$G_f = R_f G_{ss}$	74.9	66.7	77.1
$\xi = \frac{G_f}{\Delta k_{p123} 2z_0}$	256	204.5	572

The parameter  $\xi$  for the pressure corresponding to the S<sub>2</sub> maximum is two times bigger for CH<sub>4</sub> than for H<sub>2</sub>, and is ~20% bigger for H<sub>2</sub> than for D<sub>2</sub> (table 4). Consequently the intensity averaging by FWM is the strongest for CH<sub>4</sub>. In particular  $\hat{\eta}$  of S<sub>1</sub> and S<sub>2</sub> are smaller for CH<sub>4</sub> than for H<sub>2</sub> and D<sub>2</sub> (factor of two), because of the higher energy sharing among the Stokes. On the other hand the FWM is seen to be more efficient for D<sub>2</sub> than for H<sub>2</sub> (e.g.  $\hat{\eta}$  is ca. 25% lower and is more equalized between one Stokes and another), which is not explained by the  $\xi$  parameter. The gain of H<sub>2</sub> and D<sub>2</sub> has a similar wavelength dependance (table 1), and because the Raman shift of D<sub>2</sub> is smaller than that of H<sub>2</sub> (25%, table 1), the gain of D<sub>2</sub> decreases at a lower rate with respect to the Stokes index, which explains a bigger cascading, and hence averaging effect, in D<sub>2</sub>. than in H<sub>2</sub>.



Section 3: Numerical simulation

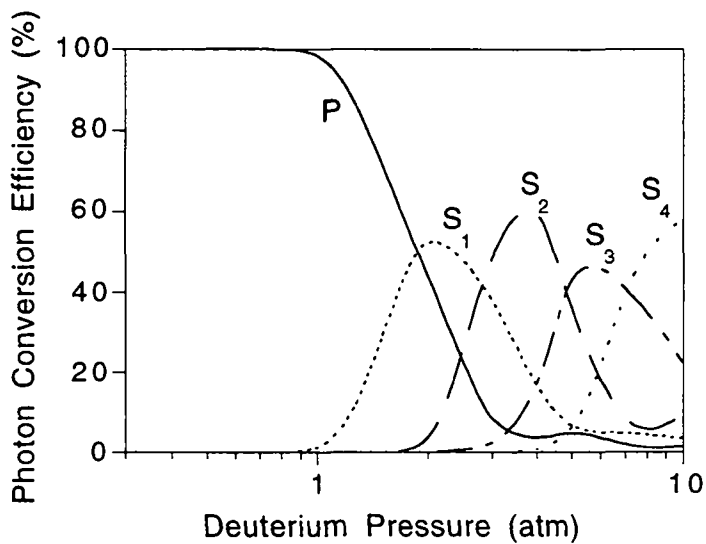


Fig. 6. Same as fig. 3b, but for deuterium.

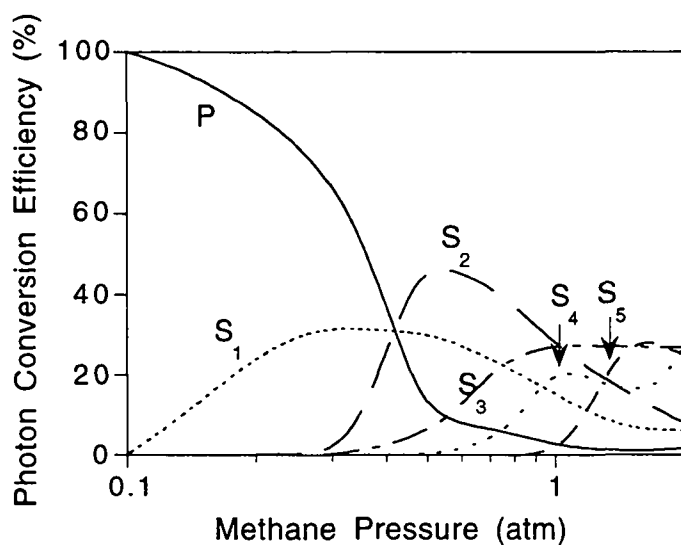


Fig. 7. Same as fig. 3b, but for methane.

### 3.3.5 Quality of the output beams (no buffer gas)

As shown in fig. 8, the  $M^2$  parameter is proportional to the gain ( $H_2$  pressure for the case of the figure). Fig. 9 shows that the higher the gain, the more corrugated is the beam profile: in the saturation regime the SRS acts on the central part of the beam (amplification or depletion), whereas the FWM acts most efficiently off-axis (due to the angle of phase-matching). The  $M^2$  parameter equals to 1.2, 1.5, 3.5, 4.9 at the maximum conversion efficiency of  $S_1$ ,  $S_2$ ,  $S_3$  and  $S_4$  respectively. The higher Stokes are substantially produced by FWM, and consequently lobes appear on the beam profile, which degrade the beam quality as shown in fig. 10. The beam quality degradation is the most severe for pressures above the one yielding the maximum conversion.

The expressions of “beam cleanup” and “beam degradation” are used when the  $M^2$  parameter of the output Stokes is respectively lower and higher than the  $M^2$  of the input pump. Fig. 11 shows the output beam quality for a  $L_2^0$  input pump ( $M^2=5$ ). The  $G_f$  gain parameter at which the Stokes reaches its photon conversion maximum is denoted by  $\hat{G}_f$  (see fig. 5b for the  $\hat{G}_f$  corresponding to a given Stokes). Clearly at low gain ( $G_f < \hat{G}_f$ ) there is beam cleanup ( $M^2 < 5$ ), whereas at high gain ( $G_f > \hat{G}_f$ ) there is beam degradation ( $M^2 > 5$ ). The beam profiles shown in fig. 12 illustrate the beam cleanup case (low gain): the Stokes profile is smoothed compared to the pump profile.

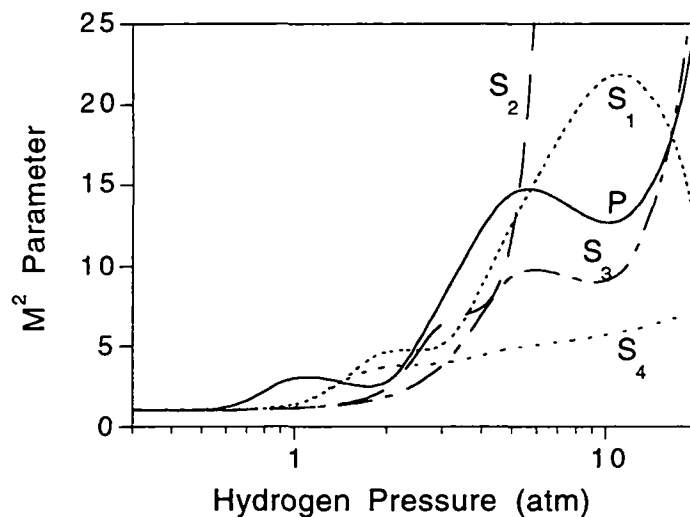
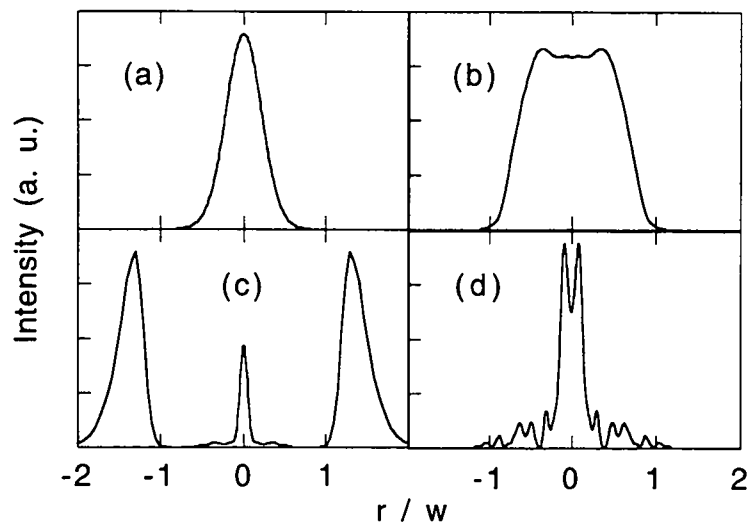
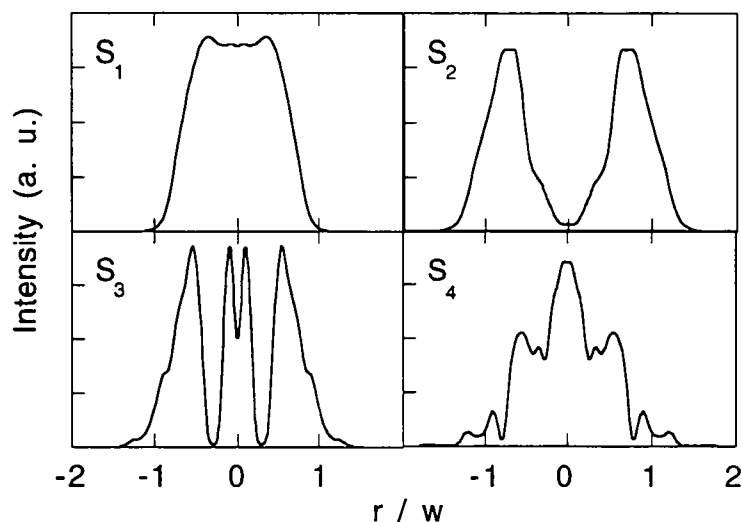


Fig. 8. Same as fig. 3b, but for the beam quality.

Section 3: Numerical simulation



**Fig. 9.** Output  $S_1$  beam profiles for 0.6 atm (a), 1 atm (b), 2 atm (c) and 5 atm (d). The other parameters are the same as for fig. 3b. The abscissa scale is in units of  $w$ , the radius of the pump beam when no Raman medium is present.



**Fig. 10.** Output beam profiles for pressures corresponding to the maximum conversion efficiency of the plotted Stokes in fig. 3b: 1 atm ( $S_1$ ), 2 atm ( $S_2$ ), 3 atm ( $S_3$ ), 5 atm ( $S_4$ ). The abscissa scale is in units of  $w$ , the radius of the pump beam when no Raman medium is present.

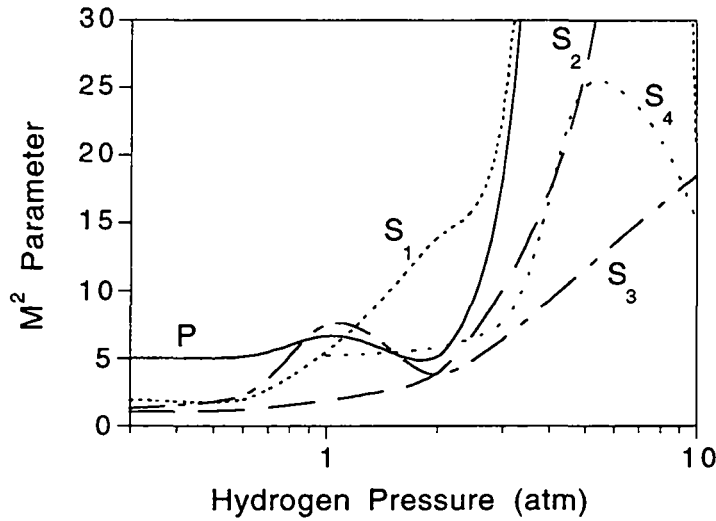


Fig. 11. Same as fig. 5b, but for the beam quality.

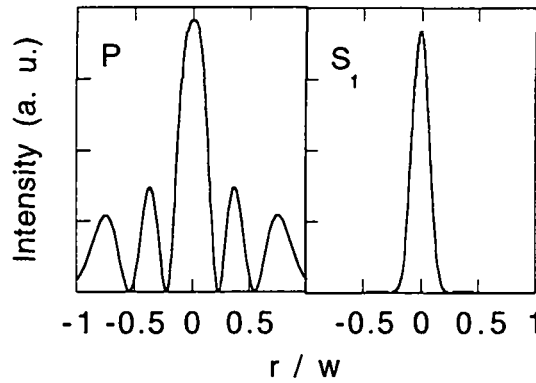


Fig. 12. Input  $L_2^0$  pump beam profile (left panel), and output  $S_1$  profile at 0.6 atm  $H_2$  pressure. The other parameters are the same as for fig. 5b.

### 3.3.6 Effect of buffer gases

The addition of buffer gas has the double effect of reducing the gain (by increasing the Raman linewidth, equ. (3)) and increasing the FWM wave-vector mismatch. Both effects tend to reduce the FWM (decrease of the  $\xi$  parameter). Fig. 13 shows that the addition of buffer gas sequentially reduces the FWM: each of the Stokes is characterized by a maximum which occurs at increasing pressures for decreasing order of the Stokes (2, 5 and 30 atm for  $S_4$ ,  $S_3$  and  $S_2$  respectively).

We denote by  $\hat{\eta}_b$  and  $P_{mb}$  respectively the Stokes peak conversion efficiency and the pressure at which it occurs, in a graph versus buffer gas pressure (e.g. fig. 13). The addition of buffer gas has a very significant effect on the Stokes beam quality, as shown in fig. 14. For instance  $S_2$  and  $S_3$  get almost diffraction-limited ( $M^2 < 1.2$ ) at argon pressures around  $P_{mb}$ . This effect is apparent on the output beam profiles, when comparing fig. 9cd with fig. 15 ( $S_1$ ), and fig. 10 with fig. 15 ( $S_2$ ,  $S_3$ ,  $S_4$ ): the profiles become less lobed with the addition of argon, which is attributed to the reduction in FWM. It is also noticed that the  $M^2$  parameter tends to decrease with Ar pressure when the slope of the conversion efficiency curve vs. Ar pressure is positive, and increase otherwise. The Stokes profile at  $P_{mb}$  show a bell-shape without off-axis

Section 3: Numerical simulation

components ( $S_2, S_3$  in fig. 15), whereas the latter are seen at other pressures (not displayed in the figure). Not shown are calculations performed with the sole SRS: the Stokes profile replicates the pump profile until the gain reaches the level for  $\hat{\eta}$ , above which the profile gets ringed (with sometimes an Arago spot) due to center-depletion by SRS. We therefore infer that  $\hat{\eta}_b$  occurs when the SRS is optimized versus FWM, that is, when the Stokes beam shape replicates the pump beam shape (taken as diffraction-limited in fig. 13-15).

The addition of helium buffer has a smaller effect than argon in terms of conversion efficiency, as shown when comparing fig. 13 with fig. 16. This is explained by the lower dispersion of helium with respect to argon (table 3). The beam cleanup is accordingly less pronounced than for argon, but leads nevertheless to factor of two reduction in the  $M^2$  parameter for P,  $S_2$  and  $S_3$  between 0 and 40 atm of helium. We note in particular that the  $S_3$  conversion efficiency is almost unchanged adding helium, whereas the  $M^2$  improves by ca. a factor two between 0 and 40 atm.

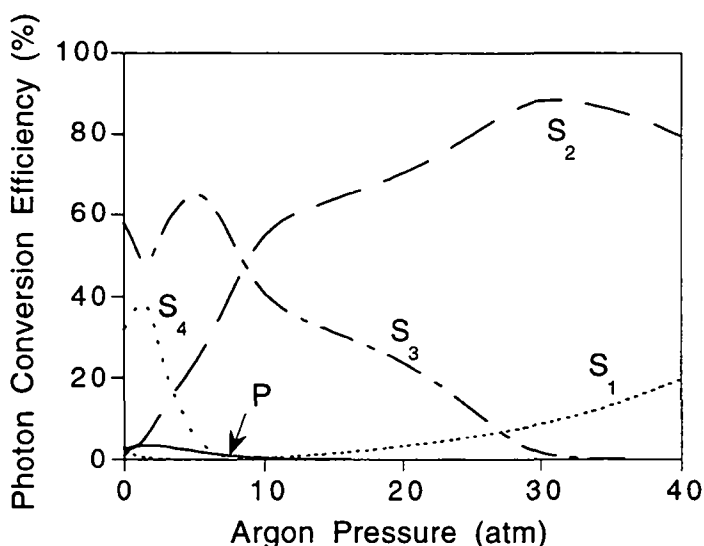


Fig. 13. Effect on the photon conversion efficiency of adding argon to 3 atm  $H_2$ . The other parameters are the same as for fig. 3b.

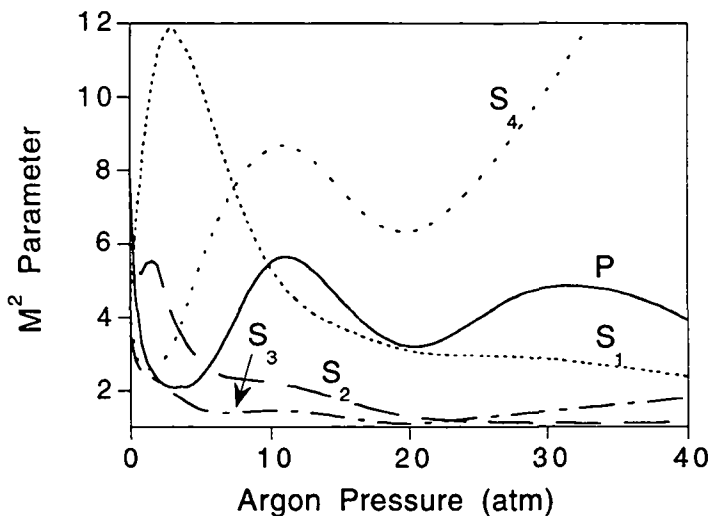
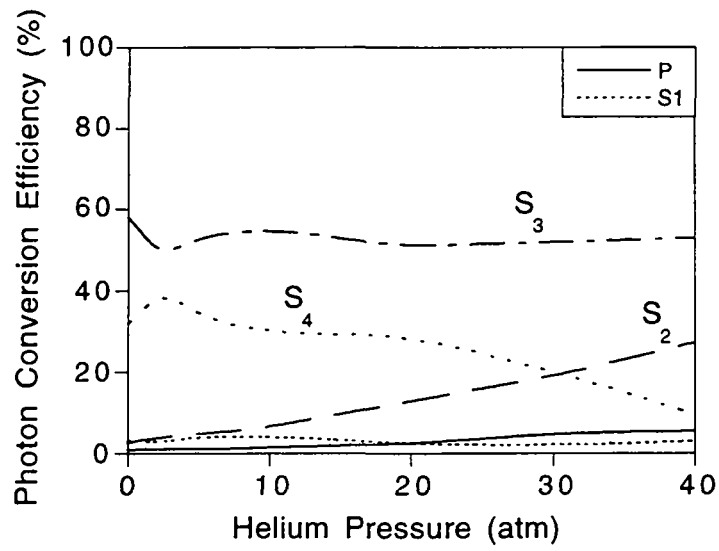
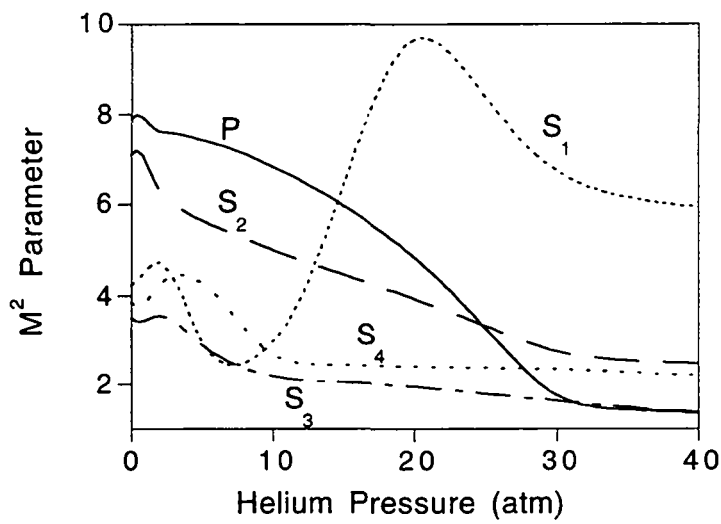


Fig. 14. Same as fig. 13, but for the  $M^2$  parameter.

Section 3: Numerical simulation



**Fig. 16.** Effect on the photon conversion efficiency of adding helium to 3 atm H<sub>2</sub>. The other parameters are the same as for fig. 3b.



**Fig. 17.** Same as fig. 16, but for the M<sup>2</sup> parameter.

### 3.3.7 Anti-Stokes

Conversion to anti-Stokes wavelengths from the pump and the Stokes can only proceed by FWM. Nevertheless, once the anti-Stokes beam is created there is SRS downconversion to lower anti-Stokes (i.e.  $AS_{i+1} \rightarrow AS_i$ ). The anti-Stokes conversion efficiency for hydrogen, deuterium and methane is shown at fig. 18. The AS1 maximum conversion is seen in fig. 18 (a) to occur at the same pressure than for  $S_1$  (fig. 3b), which outlines that  $AS_1$  is first produced by the  $\omega_{AS_1} = 2\omega_P + \omega_{S_1}$  process. When the pressure increases such that  $S_2$  reaches the threshold, it is the  $\omega_{AS_1} = \omega_P + \omega_{S_1} - \omega_{S_2}$  process that begins to be efficient in the conversion to  $AS_1$ .  $AS_2$  can only be generated by FWM through  $AS_1$ , by e.g. the following processes:  $\omega_{AS_2} = 2\omega_{AS_1} - \omega_P$ ,  $\omega_{AS_2} = \omega_{AS_1} + \omega_P - \omega_{S_1}$ ,  $\omega_{AS_2} = \omega_{AS_1} + \omega_{S_1} - \omega_{S_2}$ , ... . Therefore the higher anti-Stokes (i.e.  $AS_i$ ,  $i \geq 2$ ) are sequentially generated by FWM in much the same manner that the Stokes ( $P_m$  of  $AS_2$  is higher than  $P_m$  of  $AS_1$ , with  $AS_1$  depletion). At the difference of the Stokes cascading, the anti-Stokes cascading is much more sensitive to the pressure since it is only driven by FWM: all the anti-Stokes efficiencies are seen ultimately to decrease with pressure.

The situation for deuterium, fig. 18 (b), is very much the same as for hydrogen, fig. 18 (a), except that the lower gain of deuterium induces a higher anti-Stokes pressure threshold than for hydrogen. As for the Stokes, the situation is somewhat different for methane than for hydrogen and deuterium due to the lower gain reduction, fig. 18 (c). The lower threshold makes the effect of pressure on FWM lower.

Alike the Stokes the geometry of pump focusing has a definite effect on the anti-Stokes generation (fig. 19): the  $AS_2$  conversion is reduced with increasing  $f$ . The dramatic decrease in conversion efficiency between  $f=50$  cm and  $f=100$  cm (ca. factor of 10) is due to the FWM phase-matching angle exceeding the numerical aperture.

As for the higher Stokes ( $S_i$ ,  $i \geq 3$ ) the pump beam shape has a significant effect on the anti-Stokes conversion efficiency. For example  $\hat{\eta}$  of  $AS_1$  was noticed to be as high as 6% for LG(1,0) and as low as 0.8% for LG(3,0). As another example, for LG(1,2)  $\hat{\eta}$  of  $AS_2$  is 50% higher than the one of  $AS_3$  which is 20% higher than the one of  $AS_1$ , whereas for LG(0,4) the peak  $AS_1$  conversion is ten times the one of  $AS_2$  and  $AS_3$ .

The reduction in cascading by the addition of buffer gas is more pronounced for the anti-Stokes than for the Stokes, as shown in fig. 20 for the case of H<sub>2</sub>:Ar. The  $AS_2$  and  $AS_3$  conversion is virtually absent for argon pressure above 25 atm, whereas it is reduced by a factor of two for  $AS_1$  between 20 and 40 atm.

The beam quality dependence with respect to the gain coefficient  $G_f$  was found to be similar to that of the Stokes, fig. 8. The addition of buffer gas has a very pronounced effect on the anti-Stokes beam quality, as shown in fig. 21 for the case of H<sub>2</sub>:Ar. The effect is more pronounced than for the Stokes (fig. 13), which once more evidences the effect of FWM in degrading the beam quality. The beam profiles of fig. 22 illustrate this behaviour.

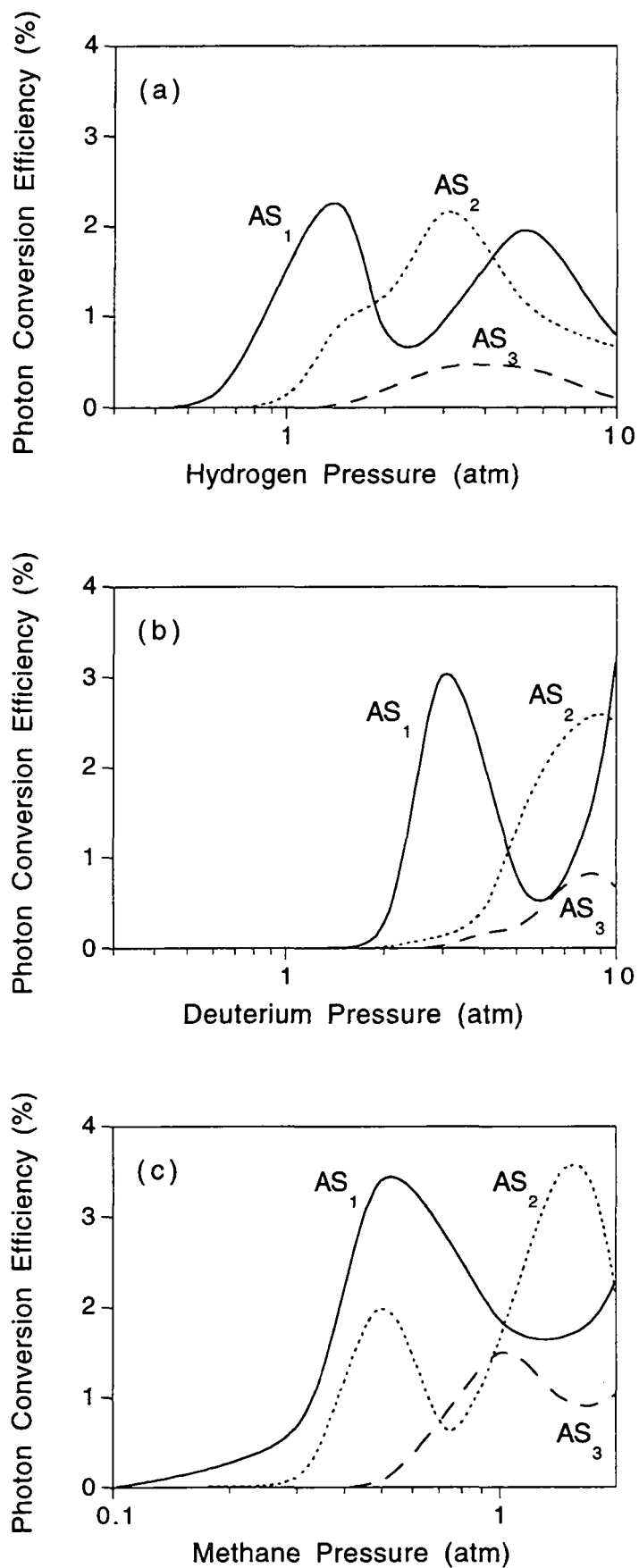


**Fig. 18.** Anti-Stokes conversion efficiency after the conversion region, for hydrogen (a), deuterium (b) and methane (c). The other parameters are the same as for fig. 3b.



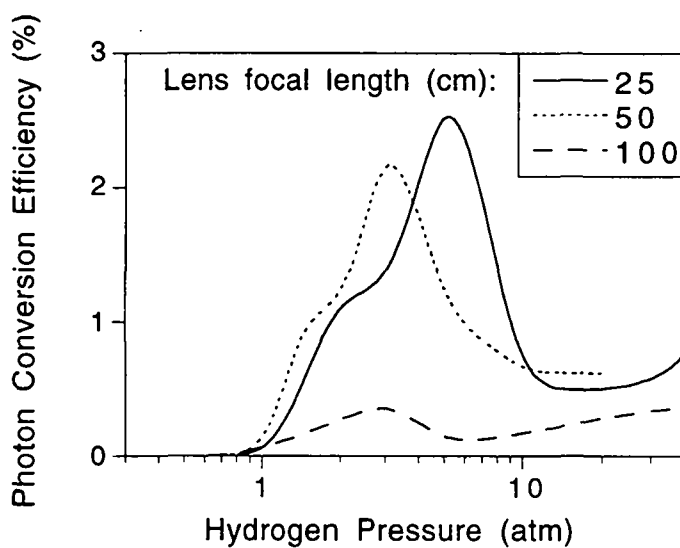


**Fig. 19.** Second anti-Stokes conversion efficiency, for three focal lengths of the lens. The other parameters are the same as for fig. 3b.

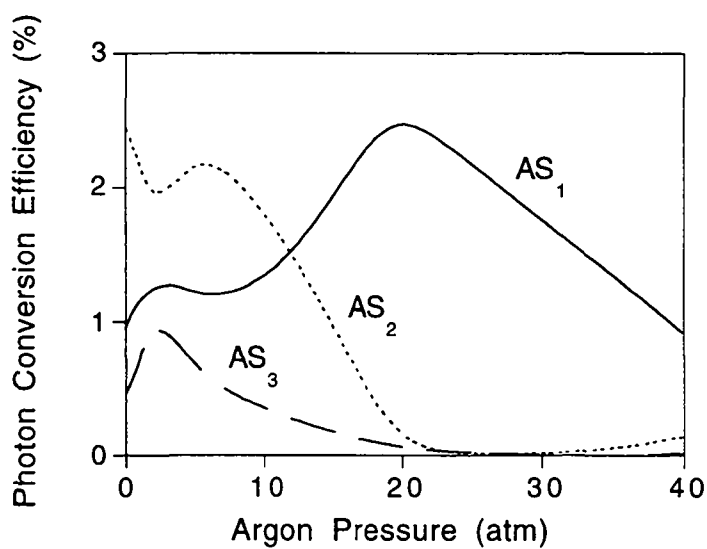


**Fig. 20.** Effect on the anti-Stokes photon conversion efficiency of adding argon to 3 atm H<sub>2</sub>. The other parameters are the same as for fig. 3b.

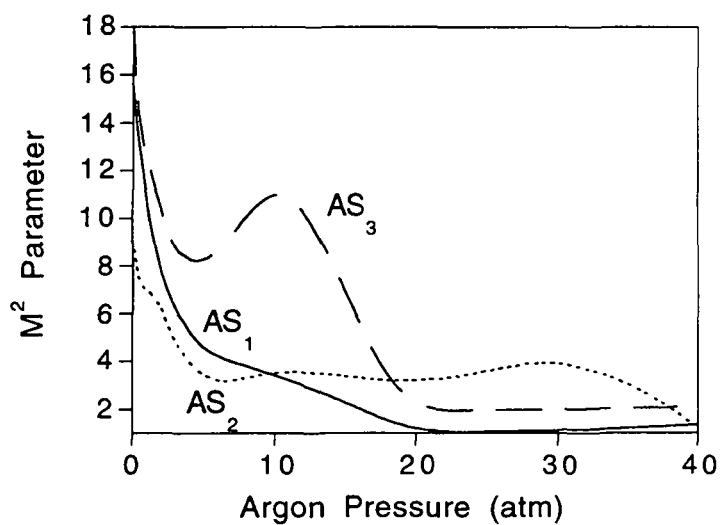


Fig. 21. Same as fig. 20, but for the  $M^2$  parameter.

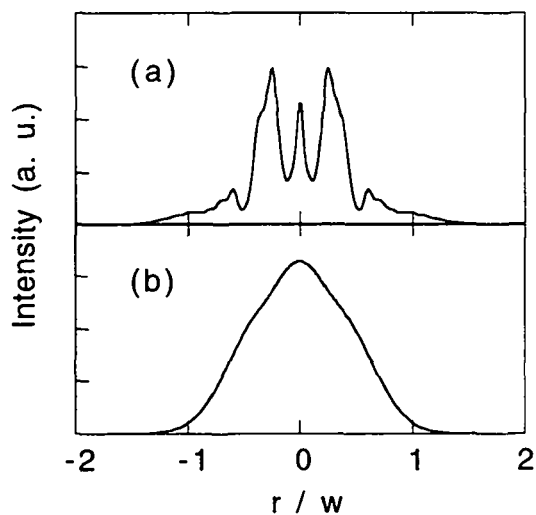


Fig. 22. First anti-Stokes output beam profile, for 3 atm hydrogen with no buffer gas (a) and 20 atm argon (b). The abscissa scale is in units of  $w$ , the radius of the pump beam when no Raman medium is present. The other parameters are the same as for fig. 3b.

### 3.4. Comparison between the modelling and previously reported experimental results

A quantitative comparison of the model with experimental results is made difficult due to the fact that the high amplification leads to other effects coexisting with the SRS and FWM. Namely, laser-induced gas breakdown and population dynamics between the energy levels of the molecules. Moreover a good characterization of the input pump beam is needed (intensity profile and spatial coherence), because of the nondiffraction-limited properties of the typical high-power lasers in the ultraviolet. In this study we perform the parametric study with a diffraction-limited (i.e. gaussian) input pump beam (but beams with arbitrary profiles upon conversion and propagation), and analyze the influence of the input pump beam quality considering Gauss-Laguerre profiles. These simple pump beam profiles along with the model presented in §3.2 allow nevertheless a qualitative comparison of several features with experimental results.

We retain for the comparison the previously published data of experiments in a focused geometry, single-pass configuration, and with cascade Stokes output. Several authors report on conversion efficiencies: Chu et al.<sup>6</sup> (Nd:YAG second harmonic (532 nm) in H<sub>2</sub>, D<sub>2</sub> and CH<sub>4</sub>, lens focal length  $f=0.5, 0.75, 1$  m), Sentrayan et al.<sup>7</sup> (Nd:YAG third harmonic (355 nm) in H<sub>2</sub>,  $f=0.1$  m), Haner and McDermid<sup>1</sup> (Nd:YAG fourth harmonic (266 nm) in D<sub>2</sub> and HD,  $f=2$  m), Trainor et al.<sup>2</sup> (XeF (353 nm) in H<sub>2</sub>,  $f=1.35, 3.6, 5.1$  m), Luches et al.<sup>3</sup> (XeCl (308 nm) in H<sub>2</sub> with He, Ne, Ar or N<sub>2</sub> buffer,  $f=1$  m), Bösenberg et al.<sup>8</sup> (KrF (248 nm) and Nd:YAG fourth harmonic in H<sub>2</sub> and D<sub>2</sub>, with He or Ar buffer,  $f=1, 1.1$  m), the latter including the work of Sunesson and Apituley<sup>28</sup> and of Kempfer et al<sup>29</sup>. Other studies deal with the beam quality of the Stokes or the influence of the beam quality of the pump: van den Heuvel et al.<sup>5</sup> (Nd:YAG fundamental (1064 nm) in CH<sub>4</sub>,  $f=0.1$  m), Diebel et al.<sup>4</sup> (KrF in H<sub>2</sub> and D<sub>2</sub> with He buffer,  $f=0.675, 0.9$  m), Cheng and Kobayashi (1988)<sup>30</sup> (XeCl in H<sub>2</sub>,  $f=0.25, 1$  m), Cheng et al. (1987)<sup>31</sup> (XeCl in H<sub>2</sub>,  $f=1$  m). Most of the beam quality studies in stimulated Raman scattering are performed in unfocused geometry<sup>32</sup> (oscillator-amplifier configuration typically). We do not take into account these works since the Stokes beam quality depends on the focusing geometry<sup>30</sup>.

#### 3.4.1 Qualitative features matching the modelling

About the conversion efficiency dependence on  $f$  (§3.3.2): the Stokes threshold pressure is inversely proportional to  $f^{2,6}$ , and when  $f$  increases the peak conversion efficiency  $\hat{\eta}$  decreases for the higher Stokes ( $S_2$  in [6],  $S_3$  in [2]) and increases for the lower Stokes ( $S_1$  in [6],  $S_1, S_2$  in [2]). Luches et al.<sup>3</sup> found that when the  $M^2$  of the pump beam decreases the Stokes threshold pressure increases and the conversion efficiency of the lower Stokes ( $S_1$ ) increases, whereas that of the higher Stokes ( $S_2, S_3$ ) decreases (§3.3.3). The measurements show a higher threshold and averaging effect for D<sub>2</sub> than for H<sub>2</sub><sup>6,8</sup> (§3.3.4).

Cheng (1987)<sup>31</sup> measures the beam profile in the near field and at the waist of a 1m lens (i.e. far-field), from which the divergence is calculated. The divergence is proportional to the  $M^2$  parameter provided that the beam size at the focusing lens is fixed. He finds a similar divergence of  $S_1$  with that of the input pump in case of XeCl laser with unstable resonator, and a  $S_1$  divergence ca. 5 times lower than that of the input pump in case of Fabry-Perot (F-P) resonator. Beams out of F-P resonators are known to yield lower conversion efficiencies than the beams out of unstable resonator, due to the much worse beam quality ( $M^2$  ca. 10 times bigger in the experiment of Cheng (1987)<sup>31</sup>). These results are consistent with the modelling (§3.3.5): beam cleanup occurs only at low gain (situation similar to the F-P arrangement), whereas the beam quality is unchanged or degraded at high gain (situation similar to the unstable cavity set-up). Cheng (1988)<sup>30</sup> shows the effect of FWM which adds side-lobes to the higher Stokes ( $S_2, S_3$ ) beam profile: the lobes disappear when  $f$  is increased, which is

### Section 3: Numerical simulation

indicative of a FWM effect. The modelling also showed the link between the off-axis lobes and the beam quality (§3.3.5). Diebel<sup>4</sup> uses the same technique as Cheng (1987)<sup>31</sup> to measure the beam divergence. She finds that the higher the H<sub>2</sub> pressure the higher the divergence, which effect is more pronounced for S<sub>3</sub> than for S<sub>2</sub> (§3.3.5).

The reduction of the higher Stokes conversion efficiency by addition of buffer gas (§3.3.6) has been noticed by Luches et al.<sup>3</sup> and Bösenberg et al.<sup>8</sup>. Diebel<sup>4</sup> found that adding helium the divergence of the higher Stokes (S<sub>2</sub>, S<sub>3</sub>) improves considerably (by factors up to 4) (§3.3.6). The anti-Stokes conversion efficiency is reduced with decreasing numerical aperture<sup>2</sup> (§3.3.7), and by the addition of buffer gas<sup>8</sup> (§3.3.7).

#### 3.4.2 Closer qualitative comparison between the modelling and experimental results

The pressure dependence of the conversion efficiency in H<sub>2</sub> and D<sub>2</sub> shows qualitative features that are common to all experimental set-ups cited at the beginning of §3.4, irrespective of the type of laser and pump wavelength (see in particular [6] and [8]). These experimental results (noted “ER”) mainly differ regarding the threshold and peak conversion efficiency, especially for the higher Stokes (S<sub>3</sub>, S<sub>4</sub>, to a lesser extent S<sub>2</sub>). These variations are noticed with the modelling results (noted “MR”) when varying the M<sup>2</sup> parameter and/or the pump beam shape. It suggests that these pump beam characteristics largely determine the discrepancy in the experimental results relative to different set-ups.

$P_m$  and  $\hat{\eta}$  of S<sub>1</sub> in H<sub>2</sub> or D<sub>2</sub> (MR, fig. 3-7) agree well with the ER<sup>1,8</sup>, showing a narrow peak (1-2 and 2-4 atm FWHM in H<sub>2</sub> and D<sub>2</sub> resp.) occurring in the 0.5-2 and 2-5 atm range in H<sub>2</sub> and D<sub>2</sub> resp. However the MR show the following qualitative disagreements with the ER: the remaining pump and S<sub>1</sub> are more depleted above 5 atm of pressure gas in the MR, whereas the higher Stokes (S<sub>2</sub>, S<sub>3</sub>, S<sub>4</sub>) pressure dependence is more peaked in the MR.

Fig. 5 shows that these points of disagreement remain when the shape of the pump beam is modified taking Gauss-Laguerre modes. The gaussian-shell-model (GSM) beam<sup>15</sup> represents another way of specifying the pump beam with a given M<sup>2</sup> parameter. The GSM beam has a gaussian intensity when averaged over pulses, but its spatial coherence is degraded with respect to the TEM<sub>00</sub> mode such as to yield the given M<sup>2</sup> in average. Calculations with GSM beams did not change the disagreement pattern with the ER.

The disagreement is mainly attributed to a too strong Raman gain increase with pressure. The transient gain reduction (TGR) formalism exposed in chapter 3.2 has a physical basis, provided that the stepping along the optical axis is small enough. Nevertheless we tested a more arbitrary way of accounting for the TGR which does not have a pressure dependence: a constant value of  $G$  in equ. (6) is arbitrarily chosen such that  $P_m$  of S<sub>1</sub> matches typical experimental values ( $P_m=1$  atm in H<sub>2</sub>). Fig. 23 shows the case of a diffraction-limited pump beam in H<sub>2</sub>: the qualitative match with the ER is better (the remaining pump and S<sub>1</sub> decrease less above 5 atm, the higher Stokes show a broader peak). However in this example the transient gain for pressures above  $P_m$  of S<sub>1</sub> is still too high, inducing a too strong Stokes cascade (S<sub>2</sub>, S<sub>3</sub> and S<sub>4</sub> do qualitatively resemble well S<sub>1</sub>, S<sub>2</sub> and S<sub>3</sub> of the ER). Calculations with Gauss-Laguerre beam shapes led to the same pressure dependence behaviour.

One mechanism which tends to reduce the transient gain dependence with pressure is the ground-state depletion of the Raman-active molecules. It would be taken into account in the model with the addition of the time derivative<sup>10</sup>. Another such mechanism is laser-induced breakdown (LIB) of the Raman-active or buffer molecules. This process has been observed in HG-SP SRS experiments<sup>33,34</sup>. LIB leads to a loss of pump photons and a degradation of the pump and Stokes beam coherence. The former reduces the conversion efficiency, while the latter increases the averaging effect of FWM by reducing the coherence length of the pump beam<sup>11</sup>.

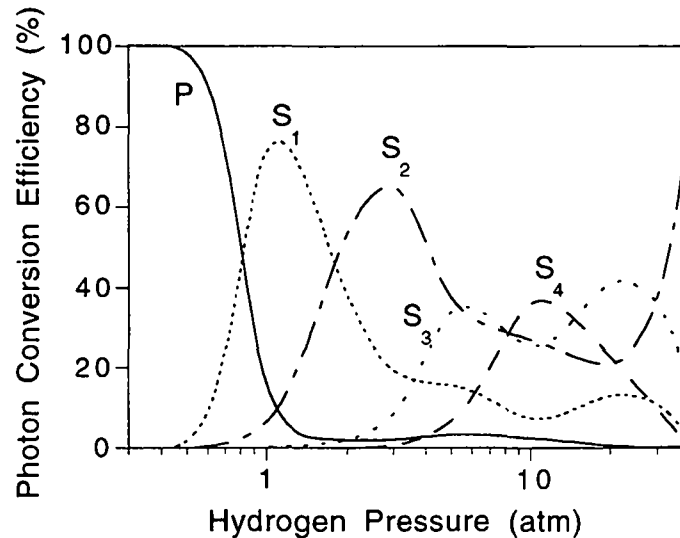


**Fig. 23.** Same as fig. 3b, but with the parameter  $G$  of equ. (3) taken as 10'000, which is arbitrarily chosen so that  $P_m$  of  $S_1$  equals 1 atm (which is consistent with previously published experimental results). In all other figures  $G = g I_p z$ .

### 3.5. Conclusion

This work exposes a parametric study of high-gain single-pass (HG-SP) stimulated Raman scattering (SRS) and four-wave-mixing (FWM) in a focused geometry. The transient nature of the SRS due to the high conversion rate is confirmed by a steady-state description with a transient reduced Raman gain: the predicted first Stokes threshold and peak conversion efficiency matches data observed previously. The high gain leads to Stokes cascade with coexisting FWM processes, which were shown to modify the output energy spectrum by reducing the threshold and averaging the energy among the Stokes. FWM is reduced by a softer focusing and an increase of the pressure (Raman active and buffer gases). Hydrogen, deuterium and methane are characterized by a very different dependence of the gain on the pressure, and consequently FWM is stronger in  $\text{CH}_4$  than in  $\text{D}_2$ , which is stronger than in  $\text{H}_2$ . The FWM averaging effect depends on the pump beam quality ( $M^2$  parameter) in a way similar to the lens focal length. The higher Stokes ( $S_3$ ,  $S_4$ , to a lesser extent  $S_2$ ) are partly generated by FWM, which effect depends strongly on the pump beam shape due to the FWM wave-vector mismatch condition.

FWM degrades the Stokes beam quality by adding off-axis lobes to the profile. The higher the Stokes the stronger this effect, due to the increasing number of FWM processes leading to that Stokes. Beam cleanup (reduction of the  $M^2$  between the pump and Stokes beams) occurs only at low gain, i.e. before the Stokes cascade occurs, above which beam degradation takes place (respective increase of the  $M^2$ ). The addition of buffer gas (He, Ar) improves the Stokes beam quality by increasing the FWM wave-vector mismatch. Beam profiles with off-axis lobes become in this way near diffraction-limited.

Previously published experimental results on HG-SP SRS in a focused geometry (with excimer and Nd:YAG pump lasers, wavelength ranging from 248 to 532 nm) show among them a similar qualitative behaviour but differ in threshold (pressure or energy) and peak conversion efficiencies. Several of the similarities were confirmed by this modelling: dependence on the lens focal length, on the pump beam quality, qualitative difference between the Raman active gases ( $\text{H}_2$ ,  $\text{D}_2$ ,  $\text{CH}_4$ ), beam quality of the Raman-shifted beams, effect of buffer gases. This modelling points out that the following parameters are important when analyzing the discrepancies between the results of different set-ups: converging lens focal length, beam

### Section 3: Numerical simulation

quality of the pump ( $M^2$  parameter), and beam shape of the pump (which is especially relevant for the higher Stokes, i.e.  $S_3, S_4$ , to a lesser extent  $S_2$ ). The pump pulse energy and temporal profile are also important but were not investigated in this study.

The computer limitations as well as the agreement of some of the model predictions with experimental results do not represent a justification of the reduced gain approximation from a theoretical point-of-view. This study demonstrated that the present model is able to predict a number of features of previous experimental work which were largely unexplained to date (see above), however the model is not able to reach a precise agreement with experimental results. The modelling features to be improved stand clearly in the solution of the time derivatives, but also in a better characterization of the input pump field, the treatment of the molecular ground-state depletion and dynamics, and of multi-photon ionization at the waist.

### Acknowledgments

This work was funded by the Swiss National Foundation for Scientific Research, grant n° 2100-042308.94.

### Annex A: Numerical calculation of the beam quality

Most generally the two first moments of the beam intensity profile satisfy the following propagation formula<sup>15</sup>:

$$\begin{aligned}\bar{x} &= \frac{1}{N} \iint x |\mathcal{E}(x, y, z)|^2 dx dy \\ &= \frac{z}{kN} \text{Im} \iint \frac{\partial \mathcal{E}_o}{\partial x} \mathcal{E}_o^* dA + \frac{1}{N} \iint x |\mathcal{E}_o|^2 dA = Dz + E\end{aligned}\tag{A.1}$$

$$\begin{aligned}\overline{x^2} &= \frac{1}{N} \iint x^2 |\mathcal{E}(x, y, z)|^2 dx dy \\ &= \frac{z^2}{k^2 N} \iint \left| \frac{\partial \mathcal{E}_o}{\partial x} \right|^2 dA + \frac{2z}{kN} \text{Im} \iint x \frac{\partial \mathcal{E}_o}{\partial x} \mathcal{E}_o^* dA + \frac{1}{N} \iint x^2 |\mathcal{E}_o|^2 dA = Az^2 + Bz + C\end{aligned}\tag{A.2}$$

with  $N = \iint |\mathcal{E}_o|^2 dA$  and  $\mathcal{E}_o = \mathcal{E}(x, y, z=0)$ . The  $M^2$  parameter is then given by

$$\begin{aligned}M_x^2 &= k \sqrt{4ac - b^2}, \\ a &= A - D^2 \quad , \quad b = B - 2DE \quad , \quad c = C - E^2\end{aligned}\tag{A.3}$$

which depends on  $z$  due to the Raman gain. In case of cylindrical geometry  $\bar{x} = 0$  and  $M_x^2 = k \sqrt{4AC - B^2}$ . The  $M_y^2$  is obtained from the expressions similar to (A.1) - (A.3) for  $\bar{y}$  and  $\overline{y^2}$ . When  $M_x^2 = M_y^2$  the parameter is simply noted  $M^2$ .

### Annex B: Stimulated Brillouin scattering threshold

Murray et al.<sup>56</sup> showed that in gases the ratio of the stimulated Brillouin scattering (SBS) gain  $g_{\text{SBS}}$  to the SRS gain  $g_{\text{SRS}}$  is given by

$$\frac{g_{\text{SBS}}}{g_{\text{SRS}}} = C \frac{p}{v_s} \quad (\text{B.1})$$

where  $p$  is the gas pressure,  $v_s$  the first Stokes frequency, and  $C$  is a constant which is dependent on the type of Raman-active gas but independent of the pressure and Stokes frequency. For methane, equ. (B.1) yields  $g_{\text{SBS}}/g_{\text{SRS}} = p/40$ , where  $p$  is in atmospheres and the 266 nm pumping wavelength has been considered. Therefore, SBS will have an effect comparable to SRS for methane pressures above 10 atm, say. It has to be noted that the backward SBS gain exceeds the forward SBS gain<sup>56</sup>.

### References

1. D. A. Haner, I. S. McDerimid, "Stimulated Raman shifting of the Nd:YAG fourth harmonic (266 nm) in H<sub>2</sub>, HD, and D<sub>2</sub>", IEEE J. Quant. Electron., **26**, 1292-1298 (1990).
2. D. W. Trainor, H. A. Hyman, R. M. Heinrichs, "Stimulated Raman scattering of XeF\* laser radiation in H<sub>2</sub>", IEEE J. Quant. Electron., **18**, 1929-1934 (1982).
3. A. Luches, V. Nassisi, M. R. Perrone, "Improved conversion efficiency of XeCl radiation to the first Stokes at high pump energy", Appl. Phys, **B47**, 101-105 (1988).
4. D. Diebel, M. Bristow, R. Zimmermann, "Stokes shifted laser lines in KrF-pumped hydrogen: reduction of beam divergence by addition of helium", Appl. Opt., **30**, 626-628 (1991).
5. J. C. van den Heuvel, F. J. M. van Putten, R. J. L. Lerou, "Quality of the Stokes beam in stimulated Raman scattering", IEEE J. Quant. Electron., **30**, 2211-2219 (1994).
6. Z. Chu, U. N. Singh, T. D. Wilkerson, "Multiple Stokes wavelength generation in H<sub>2</sub>, D<sub>2</sub> and CH<sub>4</sub> for lidar aerosol measurements", Appl. Opt., **30**, 4350-4357 (1991).
7. K. Sentrayan, A. Michael, V. Kushawaha, "Design of a compact blue-green stimulated hydrogen Raman shifter", Appl. Phys. B, **62**, 479-483 (1996).
8. Final report to the CEC project EUROTRAC/TESLAS, Jens Bösenberg Ed. (Max-Planck Institut für Meteorologie, Hamburg, Germany), in press.
9. J. H. Newton, G. M. Schindler, "Numerical model of multiple-Raman-shifting excimer lasers to the blue-green in H<sub>2</sub>", Opt. Lett., **6**, 125-127 (1981).
10. A. P. Hickman, J. A. Paisner, W. K. Bischel, "Theory of multiwave propagation and frequency conversion in a Raman medium", Phys. Rev. A, **33**, 1788-1797 (1986).
11. J. Goldhar, J. R. Murray, "Intensity averaging and four-wave-mixing in Raman amplifiers", IEEE J. Quant. Electron., **18**, 399-409 (1982).

### Section 3: Numerical simulation

12. Gary C. Bjorklund, "Effects of focusing on third-order nonlinear processes in isotropic media", *IEEE J. Quant. Electron.*, **11**, 287-296 (1975).
13. B. N. Perry, P. Rabinowitz, D. S. Bomse, "Stimulated Raman scattering with a tightly focused pump beam", *Opt. Lett.*, **10**, 146-148 (1985).
14. L. Schoulepnikoff, V. Mitev, "Numerical method for the modelling of high-gain single-pass cascade stimulated Raman scattering in gases", submitted to the *J. Opt. Soc. Am. B*.
15. J. C. van den Heuvel, "Numerical study of beam cleanup by stimulated Raman scattering", *J. Opt. Soc. Am. B*, **12**, 650-657 (1995).
16. J. C. van den Heuvel, F. J. M. van Putten, R. J. L. Lerou, "Experimental and numerical study of stimulated Raman scattering in an astigmatic focus", *IEEE J. Quant. Electron.*, **29**, 2267-2272 (1993).
17. J. C. van den Heuvel, F. J. M. van Putten, R. J. L. Lerou, "The stimulated Raman scattering threshold for a nondiffraction-limited pump beam", *IEEE J. Quant. Electron.*, **28**, 1930-1936 (1992).
18. A. Kazzaz, S. Ruschin, I. Shoshan, G. Ravnitsky, "Stimulated Raman scattering in methane - experimental optimization and numerical model", *IEEE J. Quant. Electron.*, **30**, 3017-3024 (1994).
19. D. W. Trainor, "Military excimer-laser technology seeks real-world uses", *Laser Focus World*, PennWell Publishing, June 1993.
20. M. G. Raymer, I. A. Walmsley, "The quantum coherence properties of stimulated Raman scattering", in *Progress in Optics* vol. XXVIII, E. Wolf Ed. (Elsevier, Amsterdam, 1990).
21. D. C. Hanna, M. A. Yuratich, D. Cotter, *Nonlinear optics of free atoms and molecules* (Springer, Berlin, 1979).
22. J. Bartels, H. Borchers, H. Hausen, K.-H. Hellwege, K. L. Schafer, E. Schmidt, *Landolt-Börnstein Zahlenwerte und funktionen* (Springer-Verlag, Berlin, 1962), pp. 6.871-6.885.
23. *International critical tables of numerical data, physics, chemistry and technology*, vol. VII, E. W. Washburn Ed. (McGraw-Hill, New-York, 1930), pp.1-11.
24. P. J. Leonard, "Refractive indices, Verdet constants, and polarizabilities of the inert gases", *Atomic Data and Nuclear Data Tables*, **14**, 21-37 (1974).
25. C.-S. Wang, "Theory of stimulated Raman scattering", *Phys. Rev.*, **182**, 482-494 (1969).
26. R. J. Heeman, H. P. Godfried, "Gain reduction measurements in transient stimulated Raman scattering", *IEEE J. Quant. Electron.*, **31**, 358-364 (1995).
27. H. Kogelnick, T. Li, "Laser beams and resonators", *Appl. Opt.*, **5**, 1550-1567 (1966).
28. J. A. Sunesson, A. Apituley, "RIVM tropospheric ozone lidar, report II: system description and first results", report n° 222201006, RIVM, Dutch National Institute of Public Health and Environmental Protection (1991).



Section 3: Numerical simulation

29. U. Kempfer, W. Carnuth, R. Lotz, T. Trickl, "A wide-range UV lidar system for tropospheric ozone measurements: development and application", *Rev. Sci. Instrum.*, **65**, 3145-3164 (1994).
30. Xusan Cheng, Takayoshi Kobayashi, "Raman wave front of higher-order Stokes and four-wave-mixing processes", *J. Opt. Soc. Am. B*, **5**, 2363-2367 (1988).
31. Xusan Cheng, Runwen Wang, Qihong Lou, Zhijiang Wang, "Investigation of the Raman wavefront of higher-order gaussian-hermite modes", *Opt. Comm.*, **64**, 67-71 (1987).
32. See e.g. J. Reintjes, R. H. Lehmborg, R. S. F. Chang, M. T. Duignan, G. Calame, "Beam cleanup with stimulated Raman scattering in the intensity-averaging regime", *J. Opt. Soc. Am. B*, **3**, 1408-1427 (1986).
33. Dorothee Diebel, Michael Bristow, Rainer Zimmermann, "UV DIAL for simultaneous measurement of tropospheric O<sub>3</sub> and SO<sub>2</sub>: optimization of the transmitter section", *Proc. 15th International Laser Radar Conference (Tomsk, USSR, 1990)*.
34. D. J. Brink, H. P. Burger, T. N. de Kock, J. A. Strauss, D. R. Preussler, "Importance of focusing geometry with stimulated Raman scattering of Nd:YAG laser light in methane", *J. Phys. D*, **19**, 1421-1427 (1986).
35. W. K. Bischel, M. J. Dyer, "Wavelength dependence of the absolute Raman gain coefficient for the Q(1) transition in H<sub>2</sub>", *J. Opt. Soc. Am. B*, **3**, 677-682 (1986).
36. D. A. Russel, W. B. Roh, "High-resolution CARS measurement of Raman linewidths of deuterium", *J. Mol. Spectrosc.*, **124**, 240-242 (1987).
37. Y. Taira, K. Ide, H. Takuma, "Accurate measurement of the pressure broadening of the  $\nu_1$  Raman line of CH<sub>4</sub> in the 1-50 atm region by inverse Raman spectroscopy", *Chem Phys. Lett.*, **91**, 299-302 (1982).
38. W. K. Bischel, G. Black, "Wavelength dependence of the Raman scattering cross section from 200-600 nm", in *Excimer Lasers - 1983*, C. K. Rhodes, H. Egger, H. Pummer, Eds. (American Institute of Physics, New-York, 1983).
39. D. Robert, J. Bonamy, F. Marsault-Herail, G. Levi, J.-P. Marsault, "Evidence for vibrational broadening of Raman lines in H<sub>2</sub>-rare gas mixtures", *Chem. Phys. Lett.*, **74**, 467-471 (1980).
40. G. E. Hahne, C. Chackerian, Jr., "Vibration-rotation line shifts for  $^1\Sigma_g^+ \text{H}_2(\nu, J) - ^1S_0 \text{He}$  computed via cloe coupling: temperature dependence", *J. Chem. Phys.*, **73**, 3223-3231 (1980).
41. K. C. Smyth, G. J. Rosasco, W. S. Hurst, "Measurement and rate law analysis of D<sub>2</sub> Q-branch line broadening coefficients for collision with D<sub>2</sub>, He, Ar, H<sub>2</sub> and CH<sub>4</sub>", *J. Chem. Phys.*, **87**, 1001-1011 (1987).
42. G. Herzberg, *Molecular spectra and molecular structure*, second edition (Krieger, Malabar, Florida, 1989), volume 1, chapter VII.
43. DECinfo, April 1994.
44. SPEC newsletters, April 1994.

*Section 3: Numerical simulation*

45. R. J. Heeman, H. P. Godfried, "Gain reduction measurements in transient stimulated Raman scattering", *IEEE J. Quant. Electron.*, **31**, 358-364 (1995).
46. K. Drühl, R. G. Wenzel, J. L. Carlsten, "Observations of solitons in stimulated Raman scattering", *Phys. Rev. Lett.*, **51**, 1171-1174 (1983).
47. K. Drühl, J. L. Carlsten, R. G. Wenzel, "Aspects of soliton propagation in stimulated Raman scattering", *J. Statist. Phys.*, **39**, 615-620 (1985).
48. D. C. MacPherson, R. C. Swanson, J. L. Carlsten, "Spontaneous solitons in stimulated Raman scattering", *Phys. Rev. A*, **40**, 6745-6747 (1989).
49. J. R. Ackerhalt, P. W. Milonni, "Solitons and four-wave-mixing", *Phys. Rev. A*, **33**, 3185-3198 (1986).
50. J. N. Elgin, T. B. O'Hare, *J. Phys. B*, **12**, 159 (1979).
51. M. J. Colles, *Appl. Phys. Lett.*, **19**, 23 (1972).
52. M. E. Mack, R. L. Carman, J. Reintjes, N. Bloembergen, *Appl. Phys. Lett.*, **16**, 209 (1970).
53. M. D. Duncan, R. Mahon, L. L. Tankersley, J. Reintjes, "Transient stimulated Raman amplification in hydrogen", *J. Opt. Soc. Am. B*, **5**, 37-52 (1988).
54. R. J. Heeman, H. P. Godfried, "Control of Stokes pulse duration in stimulated Raman scattering". *IEEE J. Quant. Electron.*, **31**, 715-722 (1995).
55. L. Marshall, J. Piper, "Novel delayed pulse techniques for stimulated Raman scattering", *IEEE J. Quant. Electron.*, **29**, 515-524 (1993).
56. J. R. Murray, J. Golshar, D. Eimerl, A. Szöke, "Raman pulse compression of excimer lasers for application to laser fusion", *IEEE J. Quant. Electron.*, **QE-15**, 342-368.

## **Section 4**

### **High-power single-pass Raman shifters in the ultraviolet: experimental study**

#### **Abstract**

Single-pass Raman cells pumped by either a quadrupled Nd:YAG (266 nm) or a KrF excimer laser are studied. The Raman-active gas comprise hydrogen, deuterium and methane, as well as a mixture of them, with the addition of helium, neon or argon. A parametric study has been undertaken, with the Stokes conversion efficiency and beam quality ( $M^2$ ) measured. The first Stokes efficiency increases, and the threshold of all the Stokes decreases, with increasing lens focal length or  $M^2$  parameter of the pump beam. The quality of the Stokes beams gets worse with increasing active gas pressure, but is improved by the addition of inert gas. Laser-induced breakdown is shown to be a factor limiting the conversion efficiency and the quality of the Stokes beams. With a mixture of  $D_2$ ,  $H_2$ , and Ar, between 10 and 15 mJ pulse energy is obtained (depending on the pump  $M^2$  parameter) in the first Stokes of  $D_2$  (289 nm) and  $H_2$  (299 nm), with a full-angle divergence of 0.5 mrad (at 86% power).

#### 4.1. Introduction

Raman cells in the UV, pumped by quadrupled Nd:YAG or KrF excimer, are used in applications such as differential absorption lidar (DIAL) <sup>1-5</sup> or laser ranging<sup>6-8</sup>. Even though solid-state powerful tunable sources in the UV are being developed, Raman cells remain the preferable wavelength-shifters for DIAL measurements of tropospheric ozone<sup>9</sup>, due to the high efficiency and simplicity of the setup. In the configuration considered here the pump beam is focused in a cell containing the Raman-active gas, and recollimated at the exit after a single pass. Photon conversion efficiencies of several tens of percent are reported up to the third Stokes with commercial high-power lasers (the Stokes, resp. anti-Stokes, number refers to the number of times the pump beam has been frequency downconverted, resp. upconverted).

The optimization process in view of obtaining the highest conversion efficiency and beam quality depends mainly on the pressure of the Raman-active gas, the type and pressure of added inert gas (further on called "buffer gas"), the cell lens focal length, the quality and power of the pump beam. The optimization of the conversion efficiency for a pump laser in the visible or the UV has been reported by: Chu et al.<sup>5</sup> (Nd:YAG second harmonic (532 nm) in H<sub>2</sub>, D<sub>2</sub> and CH<sub>4</sub>, lens focal length  $f=0.5, 0.75, 1$  m), Sentrayan et al.<sup>10</sup> (Nd:YAG third harmonic (355 nm) in H<sub>2</sub>,  $f=0.1$  m), Haner and McDermid<sup>1</sup> (Nd:YAG fourth harmonic (266 nm) in D<sub>2</sub> and HD,  $f=2$  m), Trainor et al.<sup>11</sup> (XeF (353 nm) in H<sub>2</sub>,  $f=1.35, 3.6, 5.1$  m), Luches et al.<sup>12</sup> (XeCl (308 nm) in H<sub>2</sub> with He, Ne, Ar or N<sub>2</sub> buffer,  $f=1$  m), Bösenberg et al.<sup>9</sup> (KrF (248 nm) and Nd:YAG fourth harmonic in H<sub>2</sub> and D<sub>2</sub>, with He or Ar buffer,  $f=1, 1.1$  m), the latter including the work of Sunesson and Apituley<sup>13</sup> and of Kempfer et al.<sup>14</sup>. Other studies deal with the beam quality of the Stokes or the influence of the beam quality of the pump: van den Heuvel et al.<sup>15</sup> (Nd:YAG fundamental (1064 nm) in CH<sub>4</sub>,  $f=0.1$  m), Diebel et al.<sup>16</sup> (KrF in H<sub>2</sub> and D<sub>2</sub> with He buffer,  $f=0.675, 0.9$  m), Cheng and Kobayashi (1988)<sup>17</sup> (XeCl in H<sub>2</sub>,  $f=0.25, 1$  m), Cheng et al. (1987)<sup>18</sup> (XeCl in H<sub>2</sub>,  $f=1$  m). Most of the beam quality studies in stimulated Raman scattering are performed in parallel geometry<sup>19</sup> (oscillator-amplifier configuration typically). These works have a limited applicability to the configuration considered here, due to the fact that the beam quality depends on the cell lens focal length<sup>17</sup>.

The present study complements a number of aspects regarding former investigations of single-pass Raman cells. A parametric study has been carried out by varying the cell parameters and measuring the Stokes conversion efficiency and beam quality ( $M^2$  parameter). The parameters varied are the following: pulse energy at cell input, focal length of the cell lens, type and pressure of the Raman-active gas (H<sub>2</sub>, D<sub>2</sub>, CH<sub>4</sub>), type and pressure of the buffer gas (He, Ne, Ar). The measurements are interpreted with a model of the stimulated Raman scattering, four-wave-mixing, buffer gas Raman linewidth broadening, and transient effects<sup>20,21</sup>.

The influence of the pump beam quality is studied by using two models of quadrupled Nd:YAG lasers with different  $M^2$  parameter, as well as a KrF excimer laser with stable resonator characterized by an  $M^2$  10 to 100 times higher (resp. for the direction of smallest and biggest dimension of the beam). The study of this excimer configuration cannot be fully generalized to excimer lasers with unstable resonator (which are the usual choice for high-power excimer-pumped Raman cells due to the higher beam quality). The effect of adding helium, neon or argon is compared (reported previously in the case of H<sub>2</sub> with XeCl pumping<sup>12</sup>). The influence of the lens focal length is studied (formerly outlined in the case of Nd:YAG second harmonic<sup>5</sup> and XeF<sup>11</sup> pumping). Methane is investigated as an alternative to deuterium since both molecules have similar Raman shifts (resp. 2917 and 2987 cm<sup>-1</sup>), but methane is cheaper and possibly brings a higher first Stokes conversion efficiency. The mixture of hydrogen and deuterium is investigated as a means to obtain similar energy in the first Stokes of deuterium and hydrogen from a single cell (to our knowledge not reported yet), which is for example useful in the differential absorption lidar measurement of tropospheric ozone<sup>9</sup>.

## Section 4: Experimental investigation

Diebel et al.<sup>16</sup> and Bösenberg et al.<sup>9</sup> reported the measurement of the Stokes beam divergence in case of KrF pumping. In Cheng et al.<sup>18</sup> two models of XeCl pump laser are used (one with stable resonator and the other one with unstable resonator) and the Stokes beam divergence is measured. In this work a characterization of the Stokes and the residual pump is performed by the measurement of the  $M^2$  parameter. In our experimental setup, laser-induced breakdown of the Raman-active and buffer gas is identified as a factor limiting the conversion efficiency and Stokes beam quality. It has been previously noticed by Yagi and Huo<sup>22</sup>, and by Diebel et al.<sup>22</sup>, for KrF pumping.

Section 2 contains the theoretical background: Raman gain, transient effects, four-wave-mixing and how these are affected by the addition of buffer gas. The experimental setup is described in section 3. Section 4 presents results with a single Raman-active gas. Chapter 4.1 contains the aspects relevant to the conversion efficiencies (input beam quality, lens focal length, buffer gas, ...), whereas the Stokes beam quality is discussed in chapter 4.2. Section 5 reports on the mixture of hydrogen and deuterium, and alternatively a mixture of hydrogen and methane, and ethane. The main results are summarized in the conclusion.

## 4.2. Theoretical background

### 4.2.1 Raman gain and transient gain reduction

The  $i$ -th Stokes, the  $i$ -th anti-Stokes, and the output pump are respectively denoted by  $S_i$ ,  $AS_i$ ,  $P$ , its frequency by  $\nu_i^s$ ,  $\nu_i^{as}$ ,  $\nu_p$ , its wavelength by  $\lambda_i^s$ ,  $\lambda_i^{as}$ ,  $\lambda_p$ , and its wavenumber by  $k_i^s$ ,  $k_i^{as}$ ,  $k_p$ . The  $S_i$  and  $AS_i$  frequency is given by  $\nu_i^s = \nu^p - i \nu_R$  and  $\nu_i^{as} = \nu^p + i \nu_R$  respectively,  $\nu_R$  being the Raman transition frequency. The steady-state gain (in units of m/W) for the P- $S_1$  stimulated Raman scattering (SRS) process is given by<sup>23</sup>

$$g_{p1} = \frac{2 \left( \lambda_1^s \right)^2}{hc \nu_1^s} \frac{N k_B}{\pi c \Delta \nu} \left( \frac{d\sigma}{d\Omega} \right) \quad (1)$$

$c$  is the speed of light,  $h$  the Planck constant,  $N$  the Raman-active molecules number density,  $k_B$  the Boltzman population factor,  $\Delta \nu$  the Raman linewidth (FWHM), and  $d\sigma/d\Omega$  the P- $S_1$  differential Raman cross section.  $g_{p1}$  as a function of pressure (at 295 K) for  $H_2$ ,  $D_2$ , and  $CH_4$ , is shown in fig. 1, and the corresponding cross section and linewidth data in table 1.

The condition for the validity of the steady-state description is  $t_p \gg G T_2$ <sup>23</sup>, where  $t_p$  is the pump duration,  $T_2$  is the dephasing time ( $T_2 = 1/(\pi \Delta \nu)$ ),  $G = \frac{I_p}{I_s} \frac{\partial I_s}{\partial I_p}$  is the steady-state amplification factor with  $I_p$  and  $I_s$  the pump and Stokes intensity respectively. In a focused geometry  $G$  can be roughly estimated as  $G = (2z_0) g_{p1} I_p(z_f)$ , noted  $G_f$ , where  $I_p(z_f)$  is the pump intensity at the waist in vacuum, and  $z_0$  the Rayleigh range.  $G_f$  is estimated as  $G_f \cong 1300$  for 10 atm  $H_2$  ( $g_{p1}=9.0$  cm/GW) with the pump beam parameters taken as: 80 mJ pulse energy at 266 nm, 5 nsec pulse duration, 3 mm radius (at 86% power),  $M^2=1$ , focused by a 50 cm focal length lens to a waist radius of 15  $\mu$ m and a Rayleigh range of 2.8 mm, the pump intensity is estimated assuming a top-hat temporal and spatial profile. In this case  $G_f \gg t_p \Delta \nu$  (and hence  $t_p \gg G_f T_2$ ) since  $t_p \Delta \nu = 8.2$  ( $\Delta \nu = 17.4 \cdot 10^{-3}$  cm<sup>-1</sup> at 10 atm  $H_2$ , table 1), showing that the SRS is transient even though  $t_p \gg T_2$  ( $T_2=0.6$  nsec). When the pulse

Section 4: Experimental investigation

energy is taken ten times less (10 mJ) and the  $M^2$  parameter of the pump ten times bigger ( $M^2=10$ ) ( $w_0$  and  $z_0$  are proportional to  $M^2$ ), then  $G_f=16$  which is still bigger than  $t_p \Delta v$ .

**Table 1.** Parameters used in the calculation of the Raman gain at 295 K, equ. (1). The Raman scattering cross section is given as a single resonance fit:  $d\sigma/d\Omega = A (v_i^s)^4 / (v_i^2 - v_p^2)^2 \cdot p_a$  is the Raman-active gas pressure (atm).

Gas	Raman shift (cm <sup>-1</sup> )	$\lambda_1^{as}, \lambda_1^s, \lambda_2^s, \lambda_3^s, \lambda_4^s$ (nm)				$k_B$	$\Delta v$ (10 <sup>-3</sup> cm <sup>-1</sup> )	A (10 <sup>-28</sup> cm <sup>2</sup> /sr) [27]	$v_i$ (10 <sup>4</sup> cm <sup>-1</sup> ) [27]
		248.4 nm pump		266.0 nm pump					
H <sub>2</sub> Q(1)	4155	225.2	239.5	0.66	$\frac{11.2}{p_a} + 1.58p_a$ [24]	8.74	8.48		
		277.0	299.0						
		313.0	341.5						
		359.8	397.9						
		423.1	476.8						
D <sub>2</sub> Q(2)	2987	231.2	246.4	0.38	$\frac{3.67}{p_a} + 3.58p_a$ [25]	3.90	7.81		
		268.3	289.0						
		291.7	316.2						
		319.5	349.2						
		353.2	389.9						
CH <sub>4</sub> Q	2917	231.6	246.8	1	$320 + 12p_a$ [26]	10.4	7.23		
		267.8	288.4						
		290.5	314.9						
		317.4	346.7						
		349.8	385.7						

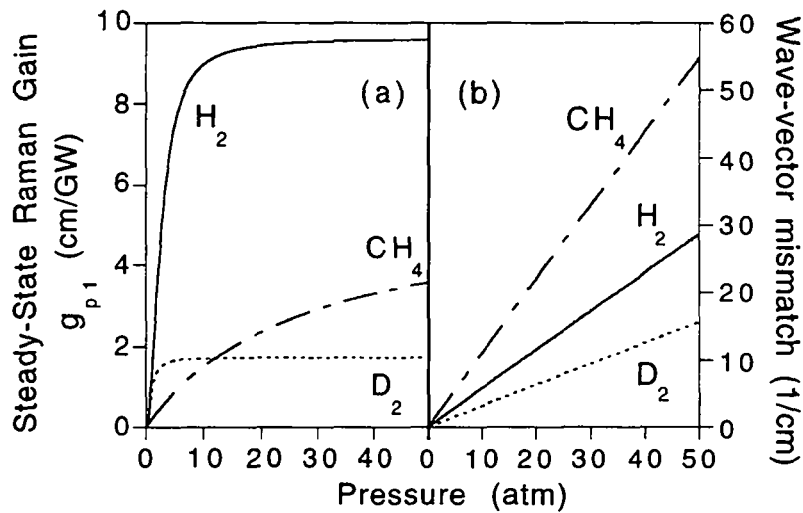


**Fig. 1.** Steady-state Raman gain for H<sub>2</sub>, D<sub>2</sub> and CH<sub>4</sub> (left panel), calculated from the data in table 1. Wave-vector mismatch of the four-wave-mixing process (P, S<sub>1</sub>, S<sub>2</sub>, S<sub>3</sub>) for H<sub>2</sub>, D<sub>2</sub> and CH<sub>4</sub> (right panel), calculated from the data in table 3.

#### Section 4: Experimental investigation

In a previous numerical study<sup>21</sup> the transient effects were taken into account by a gain reduction formalism in the steady-state description. When  $G > \Delta\nu t_p$  and  $G t_p \Delta\nu \gg 1$  (i.e. high gain), equ. (2) gives the factor  $R$  by which the steady-state gain is multiplied (yielding the transient gain):

$$R = \frac{1}{\sqrt{G}} \left( \sqrt{t_p \Delta\nu} - \frac{1}{4\sqrt{G}} \right) \quad (2)$$

following the plane-wave, undepleted pump theory of Wang<sup>28</sup>, which has been verified experimentally in a focused geometry at threshold by Heeman and Godfried<sup>29</sup>. Since  $G t_p \Delta\nu \gg 1$ ,  $R$  is approximated by  $R \approx \sqrt{t_p \Delta\nu} / G$ . At the wavelength of 266 nm and at 300 K the steady-state Raman gain of H<sub>2</sub> (resp. D<sub>2</sub>) has reached 95% of its saturation value at 11.7 (4.5) atm (fig. 1a). In the pressure-broadening regime (i.e. > 2.7, 1.0 atm for H<sub>2</sub> and D<sub>2</sub> respectively, table 1) the Raman linewidth increases with pressure, and thus the transient gain continues to grow with pressure (due to the dependance of  $R$  with the linewidth) even though the steady-state gain has already reached saturation, equ. (1). The gain reduction  $R$  as a function of pressure for two values of  $t_p$ , and the transient Raman gain  $g_t$  defined as the steady-state Raman gain multiplied by  $R$ , are shown in fig.2.

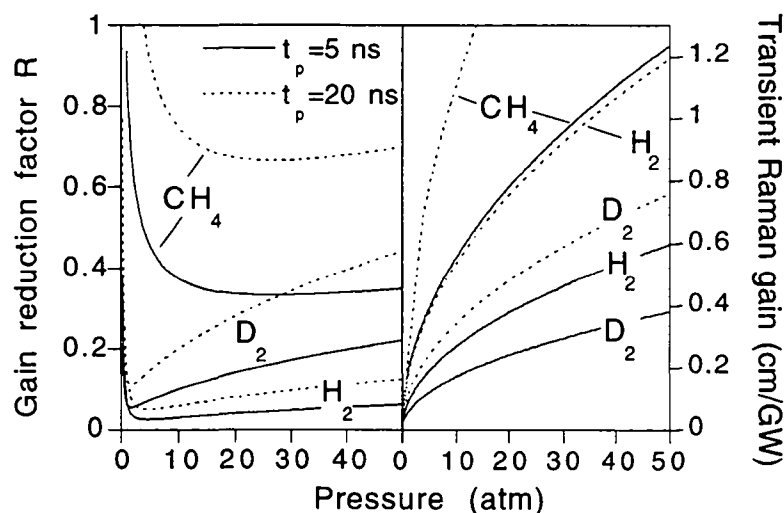


**Fig. 2.** On the left panel, transient plane wave gain reduction for H<sub>2</sub>, D<sub>2</sub> and CH<sub>4</sub>, calculated from equ. (2) with  $G$  taken as  $G_f$ . On the right panel, transient Raman gain for H<sub>2</sub>, D<sub>2</sub> and CH<sub>4</sub>, defined as the steady-state Raman gain times the transient gain reduction. The pump beam parameters are: pulse duration of 5 nsec (plain line) or 20 nsec (dashed line), 80 mJ pulse energy, 3 mm radius (at 86% power),  $M^2=1$ . It is focused by a 50 cm lens, which yields a waist of 15  $\mu$ m and a Rayleigh range of 2.8 mm.

When the SRS is considered as steady-state, with the pump beam parameters previously stated, an analytical model valid at threshold<sup>30</sup> predicts 0.17 mJ for the S<sub>1</sub> threshold energy at 10 atm H<sub>2</sub> (defined as the pulse energy corresponding to  $G_f=25$ ). This value agrees with a numerical modelling<sup>21</sup> which yields 0.12 mJ. The modelling predicts that the peak conversion efficiency of S<sub>1</sub> occurs at 0.29 mJ. Experimental S<sub>1</sub> threshold values for quadrupled Nd:YAG setups are in the range 1-10 mJ (5 mJ typically) at 10 atm H<sub>2</sub> and the peak conversion efficiency occurs above 20 mJ<sup>1,9</sup>, both of which are one order of magnitude higher than calculated by the steady-state description. With the gain reduction included ( $R=0.030$ , equ. (2)), the analytical model and the numerical modelling yield a threshold energy of 3.3 and 3.9 mJ respectively, and

#### Section 4: Experimental investigation

the latter predicts the  $S_1$  maximum conversion at 26 mJ, which lie in the range of values observed experimentally.

#### 4.2.2 Four-wave-mixing

Four-wave-mixing (FWM) is a third-order nonlinear process coexisting with the SRS<sup>21,23,31</sup>. At low pressure or pump energy, the conversion to the  $S_1$  proceeds by SRS. When  $S_1$  reaches the threshold for the  $S_2$  generation, the latter is produced by SRS and the FWM process which modifies the  $S_2$  electric field in accordance to

$$2ik_2^s \partial_z \mathcal{E}_2^s = i \frac{(k_2^s)^2}{\sqrt{k_1^s k_2^s}} \frac{g_{p112}}{2} (\mathcal{E}_1^s)^2 \mathcal{E}^{p*} \exp(iz \Delta k_{11p2}) \quad (3)$$

where the indices of the electric field  $\mathcal{E}$  follow the same rule as for  $k$ .  $g_{p112} = (g_{p1} g_{12})^{1/2}$  is the FWM gain and  $\Delta k_{11p2} = 2k_1^s - k_p - k_2^s$  determines its wave-vector mismatch. The third Stokes is produced from P,  $S_1$  and  $S_2$  through the FWM processes  $(\mathcal{E}_2^s)^2 \mathcal{E}_1^{s*} \exp(iz \Delta k_{2213})$  and  $\mathcal{E}^{p*} \mathcal{E}_1^s \mathcal{E}_2^s \exp(iz \Delta k_{12p3})$ . The higher the Stokes order, the more FWM processes lead to it, and hence the FWM to SRS ratio increases. When  $n$  Stokes and anti-Stokes beams are present (total number, including the pump), there is a total of  $(n-1)(n-2)/2$  distinct FWM processes among them. Without the averaging effect of FWM all the energy would be shared in at most two beams (P- $S_1$ ,  $S_1$ - $S_2$ , ...) <sup>21</sup>. The FWM is reduced by increasing the pressure (and hence the wave-vector mismatch). Fig. 1b shows that the wave-vector mismatch in  $\text{CH}_4$  is roughly twice that in  $\text{H}_2$ , which is twice that in  $\text{D}_2$ . The dispersion relation of the gases used in this study is found in table 2.

**Table 2.** Resonance-fit parameters at 272 K and 1 atm to the dispersion relation

$$\frac{3n^2 - 1}{2n^2 + 2} = \frac{C_1}{\lambda_1^{-2} - \lambda^{-2}} + \frac{C_2}{\lambda_2^{-2} - \lambda^{-2}} + \frac{C_3}{\lambda_3^{-2} - \lambda^{-2}}$$

where  $n$  is the index of refraction and  $\lambda$  the wavelength in cm.

	$C_1$ ( $10^4 \text{ cm}^{-2}$ )	$C_2$ ( $10^4 \text{ cm}^{-2}$ )	$C_3$ ( $10^4 \text{ cm}^{-2}$ )	$\lambda_1^{-2}$ ( $10^8 \text{ cm}^{-2}$ )	$\lambda_2^{-2}$ ( $10^8 \text{ cm}^{-2}$ )	$\lambda_3^{-2}$ ( $10^8 \text{ cm}^{-2}$ )	Reference
$\text{H}_2$	123.20	162.04		111.37	636.19		[21, 32]
$\text{D}_2$	125.50	140.54		114.08	580.94		[21, 32]
$\text{CH}_4$	55.813	626.0279		64.2208	181.2638		[32]
He	147.574			425.91			[32]
Ne	288.14			432.40			[33]
Ar	25.2582	25.2582	595.379	87.882	91.001	269.636	[32]



#### Section 4: Experimental investigation

The FWM phase-matching expresses the conservation of momentum and is also written as a vector relation  $\Delta k_{jlmn} = k_j + k_l - k_m - k_n$ . The vector phase-matching shows more clearly than its scalar counterpart in equ. (3) that the FWM is optimized at definite angles of propagation. As a consequence the FWM strength decreases when the lens focal length increases because of the reduced potential of vector phase-matching due to the reduced numerical aperture.

#### 4.2.3 Buffer gas influence

The addition of buffer gas simultaneously reduces the FWM (by increasing the wave-vector mismatch, equ. (3)) and the gain (by increasing the Raman linewidth, by a factor which increases with the molecular mass of the gas). The Raman linewidth of a gas mixture can be approximated by<sup>34</sup>

$$\Delta\nu = \Delta\nu_0 + \gamma p_b \quad (4)$$

$\Delta\nu_0$  being the self-broadened linewidth,  $\gamma$  the broadening coefficient and  $p_b$  the buffer gas partial pressure. The underlying assumptions to (6) are that first the self-broadening occurs independently from the buffer gas broadening, and second that there is no shift of the molecule vibrational frequency. The broadening coefficients of the buffer gases used in this study are found in table 3.

Fig. 3 shows the Raman gain and wave-vector mismatch when adding buffer gas to 5 atm hydrogen. The gain decays sharply at low buffer gas pressure, and eventually tends asymptotically to a constant value. The gain reduction is seen to be approximately proportional to the buffer gas molecular mass. The proportion between the wave-vector mismatch of He, Ne and Ar is respectively 1.0:1.1:3.8 at 10 atm buffer gas pressure, and 1.0:1.3:7.8 at 30 atm.

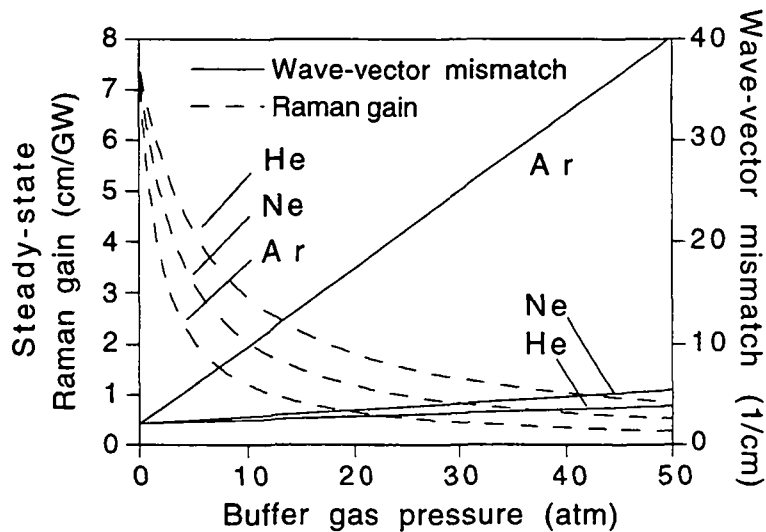


**Fig. 3.** Steady-state Raman gain (dashed line), and wave-vector mismatch

$\Delta k_{12p3} = k_1^s + k_2^s - k_p - k_3^s$  of the FWM process involving P, S<sub>1</sub>, S<sub>2</sub>, S<sub>3</sub> (continuous line), for 5 atm H<sub>2</sub>.

**Table 3.** Broadening coefficients  $\gamma$  used in the calculation of the Raman linewidth, equ. (4).

Raman-active gas	Buffer gas	Broadening coefficient ( $10^{-3} \text{ cm}^{-1}/\text{Amagat}$ )	Reference
H <sub>2</sub> Q(1)	He	1.58	[36]
	Ne	2.7	[35]
	Ar	5.3	[35]
D <sub>2</sub> Q(2)	He	2.35	[37]
	Ar	3.37	[37]

### 4.3. Experimental setup

The fourth harmonic of a 10 Hz Q-switched Nd:YAG (266 nm) from Continuum, either model Powerlite 8010 (oscillator-amplifier) (further on denoted “Po”) or Surelite III (single oscillator) (denoted “Su”), was used as pump source. In both cases the harmonics are separated by dichroic mirrors. Alternatively we used a Lumonics Excimer 500 (operated at 10 Hz) with stable resonator (denoted “Ex”). This type of excimer laser is a much less common choice for high-power Raman cells because of its bad beam quality, with the consequence of a loose focusing capability which results in low conversion efficiencies. The excimer configuration is studied in order to investigate the dependence on the pump beam quality.

The Raman cell experimental setup is standard (fig. 4). The pump beam passes through a Pellin-Broca prism (in order to avoid backward shifted radiation), it is focused by a lens in the center of the cell, the pump and Stokes beams are recollimated on exit with a lens of the same type and dispersed by a prism. The pulse energies are measured after the prism with a calibrated pyroelectric detector (Gentec ED500 & EM-1), and averaged over 100 shots. All the beams above the detector energy threshold (0.2 mJ) are measured. Since the number of photons is conserved by the Raman process, the photon conversion efficiency  $\eta_i^s$  of the Stokes  $n^{\circ}i$  is approximated as

$$\eta_i^s = \frac{P_i^s / \nu_i^s}{\sum_{j=1}^J P_j / \nu_j} \quad (5)$$

where  $P$  denotes the pulse energy,  $\nu$  the frequency, and  $J$  the number of beams above the detector threshold (pump, Stokes and anti-Stokes).

The energy stability (standard deviation) is of the order of 5% for the Nd:YAGs (at 266 nm), and 2% for the excimer. In pure active gas the energy stability of the Stokes beam was noticed to reproduce that of the pump at the pressure corresponding to the conversion efficiency maximum. At lower pressures the stability can reach more than three times that of the pump (because the slope of the conversion curve vs. pressure is steep), and at higher pressures it is roughly two times that of the pump. When adding buffer gas the Stokes energy stability improves when the conversion rises and degrades otherwise. As for pure active gas, the Stokes stability reproduces the one of the pump at the buffer gas pressure which yields the maximum conversion efficiency.

Section 4: Experimental investigation

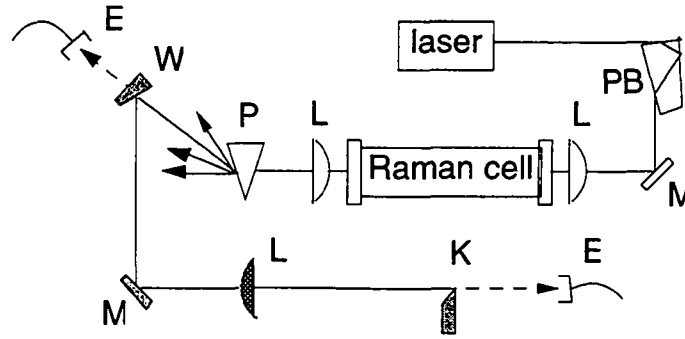


**Fig. 4.** Experimental setup for the conversion efficiency and beam quality (shaded elements) measurement. PB: Pellin-Broca prism, M: mirror, L: lens, P: prism, W: wedge plate, E: energy meter, K: knife-edge. For the pump beam quality measurement, the set-up comprising the shaded elements is put at the exit of the laser.

The  $M^2$  parameter of the input pump and the output Stokes beams is determined by focusing with either a 50 or 75 cm focal length lens and measuring the beam width at various positions before and after the waist. The knife-edge technique with either the (16, 84%) or the (10, 90%) clip levels is used to measure the beam size<sup>38</sup>. The sampled beam sizes are fitted to the curve

$$w^2(z) = w_0^2 \left[ 1 + \frac{(z - z_f)^2}{z_0^2} \right], \quad z_0 = \frac{\pi w_0^2}{M^2 \lambda} \quad (6)$$

where  $w(z)$  is the beam size at the position  $z$  along the optical axis and  $z_f$  the waist position. The uncertainty was estimated to be lower than 10%, from the dispersion of the measurement points around the model curve (6) and the difference between the two sets of clip levels. Fig. 5 shows a typical example of beam size sampling along the optical axis. The curve fitting yields an uncertainty in  $M^2$  of ~5% from the dispersion of the measurement points and ~5% difference between the (16,84%) and (10,90%) clip level sets, from which the total uncertainty in  $M^2$  is estimated as 10%. The  $M^2$  parameter at laser output was measured to be 6.2 (Su), 3.9 (Po), and 260x25.4 (Ex), the values for the excimer corresponding to the axis of resp. larger and smaller dimension.

The pump pulse energy (at 266 nm for the Nd:YAG) at the cell input is 80 mJ (unless otherwise stated), with diameter (at 86% power) of 8 (Su), 7 (Po) and 30x10 mm (Ex) (measured with the knife-edge technique), and pulse duration of 4 (Su), 6 (Po) and 12 nsec (Ex) (measured by the constructor). The cell focusing lenses are of 25, 50 or 75 cm focal length, along with a cell length of twice the lens focal length at 266 nm. All mentioned focal lengths are defined at the wavelength of 587 nm. The lenses and the cell windows are anti-reflection coated (reflection coefficient less than 0.5% for 245-390 nm, 0° angle of incidence).

For simple estimations that will be carried out below, standard approximate formulas are used (rather than the beam sampling and the fit, equ. (6)) to calculate  $w_0$  and  $z_0$  from the measured beam size at the lens ( $w_L$ ):

$$w_0 = \frac{\lambda f M^2}{\pi w_L}, \quad z_0 = \frac{\lambda f^2 M^2}{\pi w_L^2} \quad (7)$$

$w_0$  and  $z_0$  calculated with (7) were checked to be within 25% of the values retrieved from the fit, equ. (6).

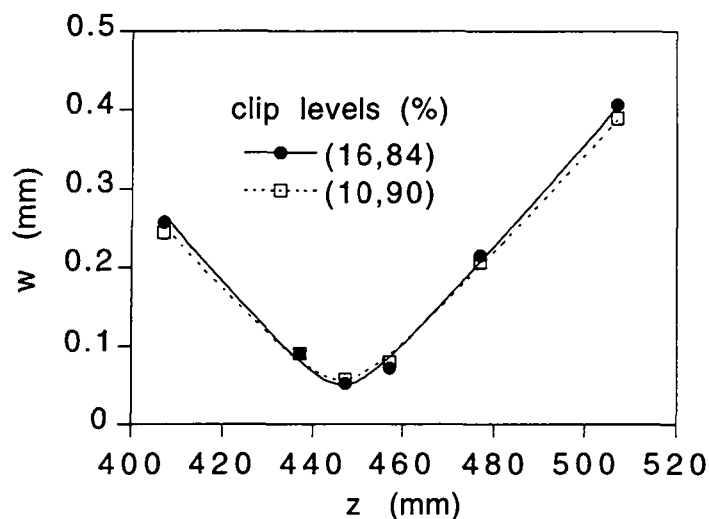


**Fig. 5.**  $M^2$  measurement at the output of the Po laser, with a 50 cm focal length lens (defined at 587 nm). Displayed is the beam width  $w$  as a function of the distance  $z$  along the optical axis from the focusing lens. The curve equ. (6) is fitted to the measured  $w(z)$  which yields  $w_0=0.051 \pm 0.005$  mm,  $z_f=446.5 \pm 1.0$  mm,  $M^2=3.8 \pm 0.2$  for the (16,84%) clip levels, and  $w_0=0.058 \pm 0.004$  mm,  $z_f=446.1 \pm 0.8$  mm,  $M^2=4.0 \pm 0.2$  for the (10,90%) clip levels. The uncertainties are determined from the dispersion of the measurement points around the model curve.

#### 4.4. Single Raman-active gas

##### 4.4.1 Conversion efficiency

The threshold pressure (at a given pump pulse energy) is defined here as the one corresponding to 1% photon conversion efficiency ( $\eta_t$ ), and is denoted by  $p_t(S_i)$  for the Stokes  $n^{\circ}i$ . In Hanna et al.<sup>23</sup> and Cotter and al.<sup>30</sup> the threshold conversion efficiency is used to define the threshold pump intensity  $I_t$ , by assuming that for  $I_t$  the product  $I_t g_{p1} z$  (which is the argument of the exponential amplification in a plane-wave description) lies between 20 and 30. In a similar fashion, in a focused geometry we assume (§2.1) that  $I_t$  is defined by  $G_f=25$ . The present study reports investigations carried out at constant pump pulse energy, which level (80 mJ) is close to the maximum available with high-power commercial quadrupled Nd:YAG lasers (~100 mJ). In this framework the definition of threshold as pressure rather than energy is more natural. The photon conversion efficiency of the Stokes  $n^{\circ}i$  is denoted by  $\eta(S_i)$ , the peak  $\hat{p}_a(S_3)$  that could be achieved by  $\hat{\eta}(S_i)$ , and the active gas pressure at which the latter occurs by  $\hat{p}_a(S_i)$ .

The excimer configuration at low energy (input pump pulse of 20 mJ, fig. 6) shows best the effect of the transient gain which increases with pressure even though the steady-state gain is in the saturation regime. Between 15 and 25 atm pressure the steady-state gain  $g_{p1}$  increases from 9.5 to 9.7 cm/GW respectively, which cannot solely explain the  $S_1$  and  $S_2$  photon conversion efficiency increase from 15 to 26% ( $S_1$ ) and from 4 to 5% ( $S_2$ ). At such pump energy the anti-Stokes and the higher Stokes ( $> S_2$ ) are under the detector threshold, so that the increase in the  $S_1$  and  $S_2$  photon conversion efficiency with pressure cannot be attributed to a backconversion due to FWM decrease. This effect is therefore interpreted as the dependence of the transient gain reduction with pressure. At higher pump energy the dependence of the FWM with pressure dominates.

Section 4: Experimental investigation

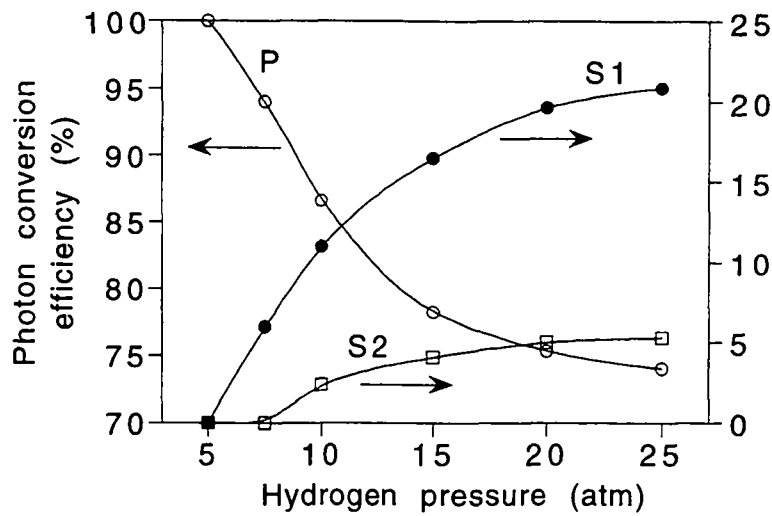


Fig. 6. Photon conversion efficiency in hydrogen for the excimer laser, with pump pulse energy of 20 mJ and lens focal length of 75 cm.

Fig. 7 shows the photon conversion efficiency in pure H<sub>2</sub>, D<sub>2</sub> and CH<sub>4</sub> for the Po laser (similar curves are obtained with the Su laser). The higher gain of H<sub>2</sub> with respect to D<sub>2</sub> makes, for H<sub>2</sub>,  $\hat{\eta}(S_1)$  higher and  $p_t$  lower for  $S_i$  ( $1 \leq i \leq 4$ ). The transient gain of CH<sub>4</sub> is the highest (fig. 2), and consequently  $p_t(S_i)$ ,  $1 \leq i \leq 4$ , is noticed to be lower than for D<sub>2</sub> and quite similar with H<sub>2</sub>.  $\hat{\eta}(S_1)$  in CH<sub>4</sub> is noticed to be lower than H<sub>2</sub> and D<sub>2</sub>, despite of the highest transient gain, which is attributed to a more pronounced laser-induced breakdown in CH<sub>4</sub> (see below, § 4.1.1). In accordance with the  $\hat{\eta}(S_1)$  dependence, the residual pump is seen to be the most depleted in H<sub>2</sub>, followed by D<sub>2</sub> and CH<sub>4</sub> (at 3 atm,  $\eta(P)=10, 15, 28\%$  for H<sub>2</sub>, D<sub>2</sub> and CH<sub>4</sub> respectively). The decrease of the FWM with pressure is the most pronounced for CH<sub>4</sub>, followed by H<sub>2</sub> and D<sub>2</sub>, following the wave-vector mismatch proportionality between H<sub>2</sub>, D<sub>2</sub> and CH<sub>4</sub> (fig. 1b). It is evidenced e.g. by the positive slope of  $\eta(S_1)$  versus  $p_a$  and the negative slope of  $\eta(S_3)$  at high pressure ( $> 10$  atm), which are inversely proportional to the averaging effect due to FWM.

For  $f=75$  cm, above 15 atm of CH<sub>4</sub> the fused silica of the entrance window inner face was etched at the exact location of the laser spot after a few minutes to a few hours of operation. This effect is attributed to the laser-induced dissociation of CH<sub>4</sub>, leading to reactive radicals. No such effect was noticed at a pressure below 15 atm, even after hours of operation. The threshold pressure of etching was noticed to be inversely proportional to  $f$ , so that it was found to be around 5 atm for  $f=25$  cm.

Section 4: Experimental investigation

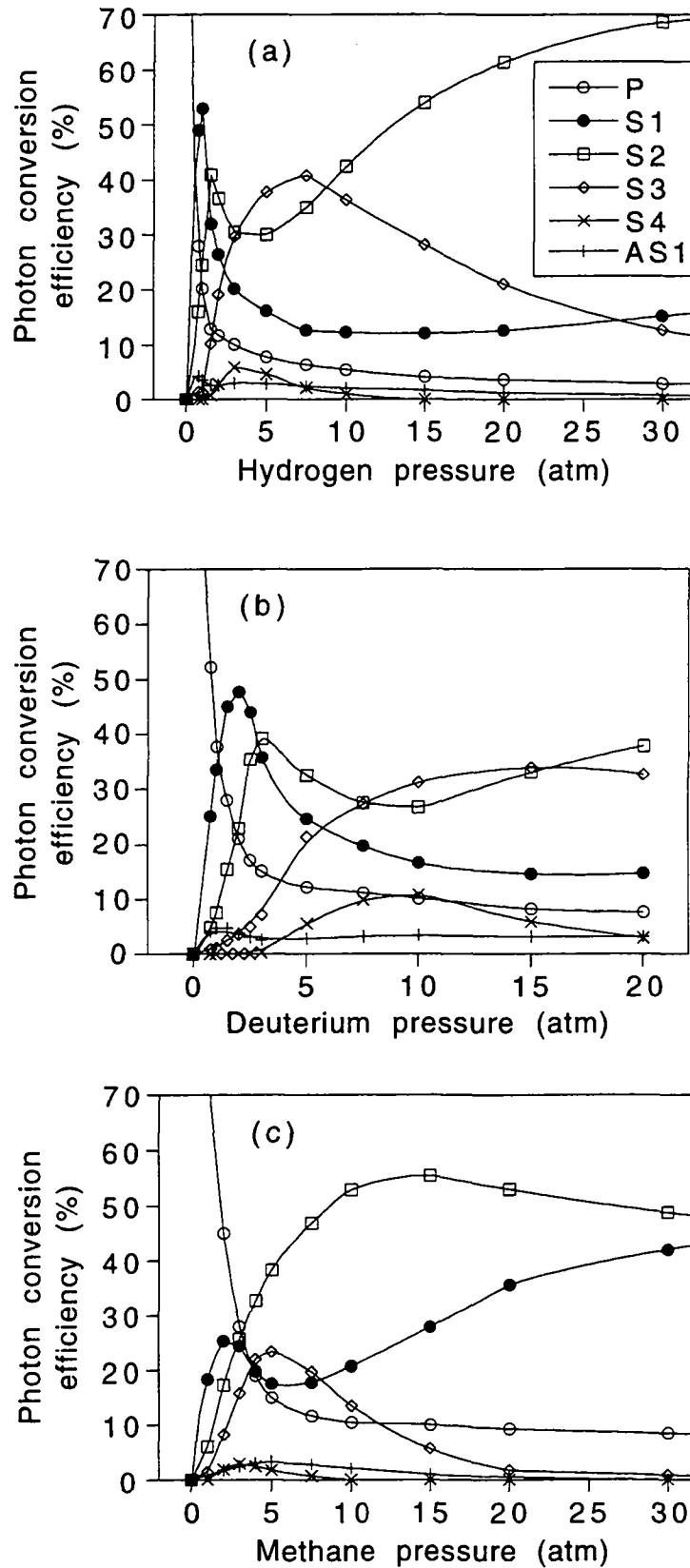


Fig. 7. Photon conversion efficiency as a function of pressure for H<sub>2</sub>, D<sub>2</sub> and CH<sub>4</sub>. Po laser, 75 cm focal length lens.

Section 4: Experimental investigation

4.4.1.1 Laser-induced breakdown

Multiphoton ionization is a nonlinear process coexisting with the SRS and FWM, which leads to the gas breakdown<sup>39</sup>. Alternatively seed electrons from impurities with subsequent laser-induced avalanche ionization contribute to the formation of plasma. In a simple model which takes into account only the energy balance of the multiphoton ionization [ref. 39, §9.8], the laser-induced breakdown (LIB) threshold  $I_{th}^{LIB}$  shows the following proportionality:

$$I_{th}^{LIB} \propto \frac{v^2 U_i}{t_p p} \quad (8)$$

with  $U_i$  the atom ionization potential and  $p$  the gas pressure.

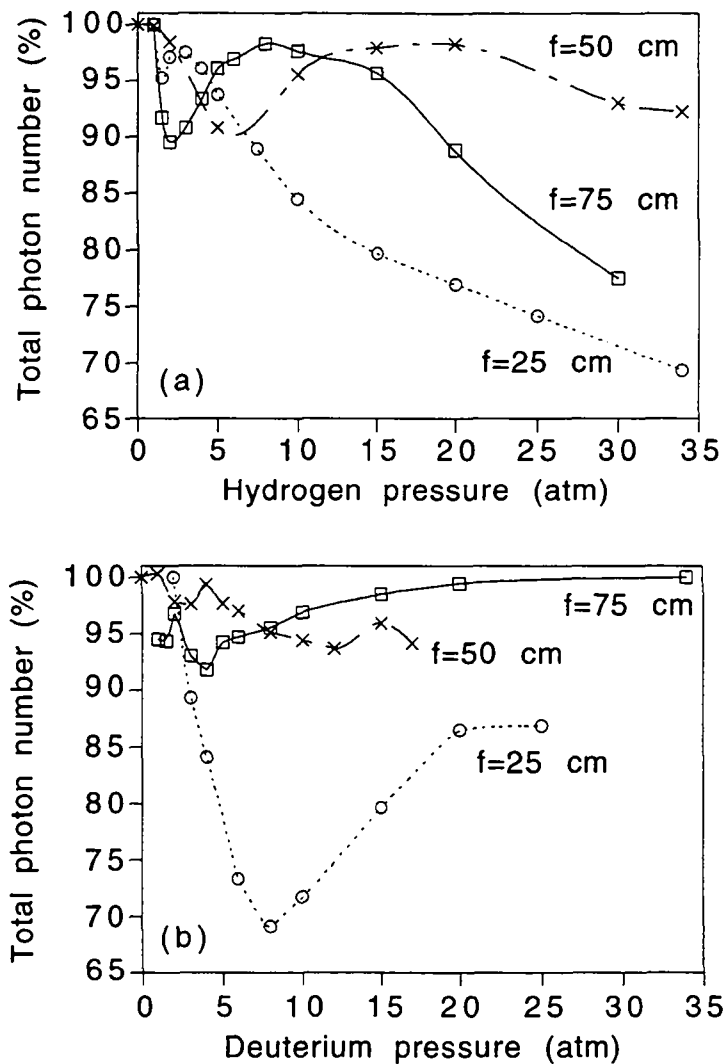
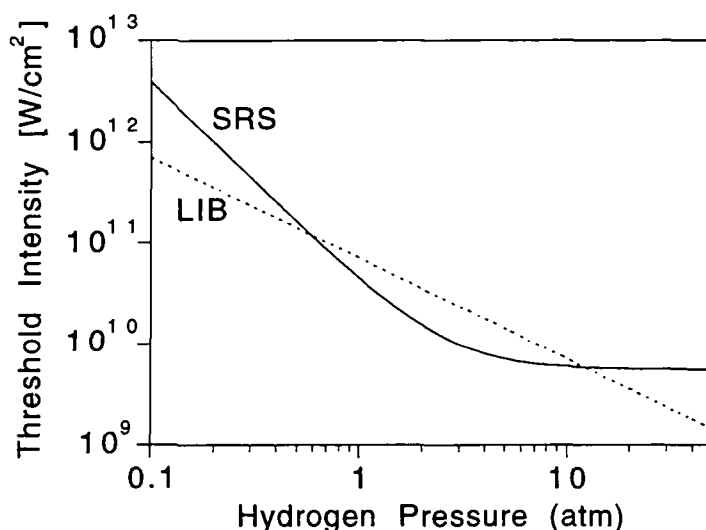


Fig. 8. Total number of photons in one pulse at cell exit (Su laser), normalized to its maximum value (i.e. when the cell is filled with 1 atm of air), as a function of the lens focal length and the hydrogen (a) or deuterium (b) pressure.

#### Section 4: Experimental investigation

LIB has been observed in KrF-pumped Raman cells<sup>22</sup>. In the Nd:YAG setup we detected LIB by looking in the cell from behind the folding mirror that injects the pump beam in the cell: white sparks were visible. Alternatively, the total number of photons (denoted TNP, given by the denominator of the right-hand-side of equ. (5)) at cell output was calculated from the measured Stokes energy spectrum. The TNP variation with hydrogen pressure is shown in fig. 8 for several lens focal lengths. With increasing pressure the TNP shows a dip, a maximum and a decrease. Fig. 9 helps explaining this behaviour: it shows the steady-state SRS and LIB threshold intensity  $I_{th}$ . The SRS  $I_{th}$  is calculated as  $G / (g2z_0)$ , with  $G=25$  and  $z_0=2.8$  mm (diffraction-limited beam of 6 mm diameter focused by an ideal 50 cm focal length lens). A  $1/p$  dependence has been taken for the LIB  $I_{th}$ , normalized to  $7 \times 10^{11}$  W/cm<sup>2</sup> at zero pressure, which is extrapolated from a doubled ruby laser (347 nm, 10 nsec pulse duration) experimental data<sup>40</sup>. These crude threshold estimates serve to illustrate the connection between the pump photon loss by LIB and SRS: at low pressure the SRS  $I_{th}$  is high so that the LIB pressure-dependence dominates (decrease of the TNP pressure curve), but the SRS  $I_{th}$  decreases at a higher rate than the LIB  $I_{th}$  so that the Raman conversion becomes gradually the dominant process (increase of the TNP curve), but when the SRS  $I_{th}$  saturates with pressure it decreases at a lower rate than the LIB  $I_{th}$ , hence increasing the LIB effect with pressure (decrease of the TNP curve). This complex interplay between SRS and LIB makes the TNP focal length dependance difficult to predict (fig. 8): below 5 atm pressure the shortest cell ( $f=25$  cm) is the most transparent, whereas at first approximation the reverse would be true due to the tighter focusing. At higher pressures ( $> 5$  atm) the  $f=25$  cm cell becomes the most opaque, but the  $f=75$  cell is still less transparent than the  $f=50$  cm cell.



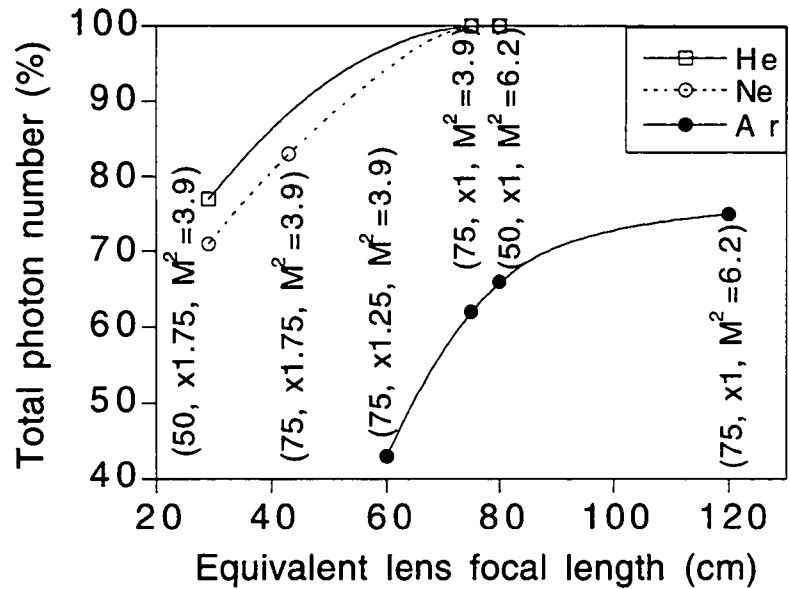
**Fig. 9.** Steady-state stimulated Raman scattering (SRS) and laser-induced breakdown (LIB) thresholds in hydrogen at 266 nm and 300 K.  $G=30$  has been taken as the definition of the SRS threshold, along with a Rayleigh range of 2.8 mm. For the LIB threshold a  $1/p_a$  dependence is considered,  $p_a$  the hydrogen pressure, and adjusted to the experimental data of Alcock et al.<sup>40</sup>.

Fig. 10 shows the LIB occurring in the cell when filled only with buffer gas. The measurements have been taken with various input pump beam sizes  $\omega_L$ , obtained with different beam expanders. At first approximation the waist size is inversely proportional to  $\omega_L$ , whereas it is proportional to  $f$ . Therefore different beam expansion configurations are compared by defining an equivalent lens focal length  $f_{eq}$  calculated as  $f$  divided by the beam expansion factor. The waist size is proportional to  $M^2$ , and similarly  $f$  was divided by  $M^2(\text{Su}) / M^2(\text{Po}) = 6.2/3.9 = 1.6$  for the Su laser in order to yield a comparable focusing capability with the Po laser. For the three gases investigated the LIB decreases with  $f_{eq}$ , as expected from the  $1 / f_{eq}^2$



Section 4: Experimental investigation

proportionality of the intensity at the waist. The ionization energy of He, Ne and Ar equals respectively 23.6, 21.6 and 15.8 eV<sup>41</sup>, and accordingly the transmittance is the highest for He, followed by Ne and Ar.



**Fig. 10.** Total number of photons in one pulse at cell exit, normalized to its maximum value (i.e. when the cell is filled with 1 atm of air), as a function of the equivalent lens focal length, at 20 atm pressure. The points are labelled with the lens focal length in cm, the number of times the pump beam has been expanded before entering the cell, and the  $M^2$  of the input pump (3.9 and 6.2 resp. for the Po and Su laser). The equivalent lens focal length is calculated as the focal length divided by the beam expansion factor, and multiplied by  $6.2/3.9=1.6$  for the Su laser.

Fig. 11 shows the effect on the photon transmittance of adding argon to 10 atm of hydrogen or deuterium. At this pressure of Raman-active gas ( $p_a$ ) and lens focal length (75 cm), the TNP is on the decrease with  $p_a$  trend that occurs at high pressure (fig. 8). The addition of buffer gas reduces the Raman gain. It has therefore a similar effect than reducing the active gas pressure, hence increasing the TNP in this pressure regime. But because the argon is highly absorbive due to LIB (30% reduction in TNP at 20 atm pure argon, in this configuration), increasing its pressure eventually leads to a decrease in the photon transmittance.

Deuterium shows a higher transmittance than hydrogen (fig. 12,  $f=75$  cm), attributed to the lower Raman gain. Methane highly absorbs at low pressure (35% photon loss at 1 atm), which may not be solely explained by the ionization energy (12.5, 15.5 eV resp. for CH<sub>4</sub> and H<sub>2</sub>).

Section 4: Experimental investigation

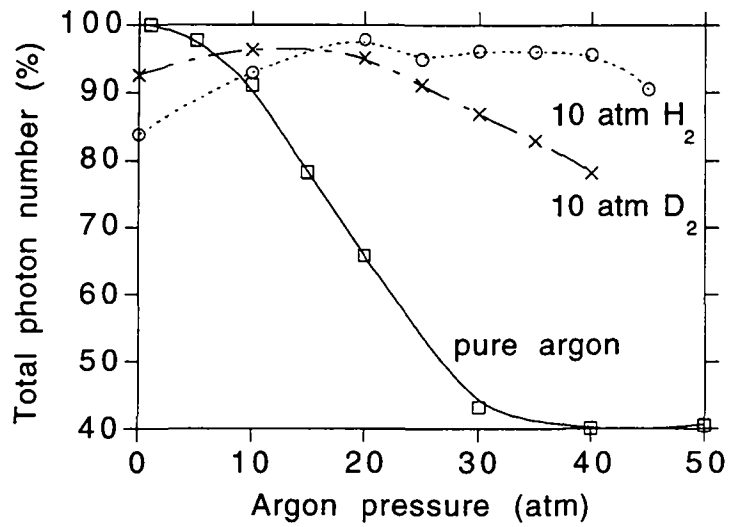


**Fig. 11.** Total number of photons in one pulse at cell exit, normalized to its maximum value (i.e. when the cell is filled with 1 atm of air), as a function of argon pressure, for pure argon (squares) and a mixing of 10 atm hydrogen (circles) or deuterium (crosses) with argon. Po laser, 75 cm focal length lens.

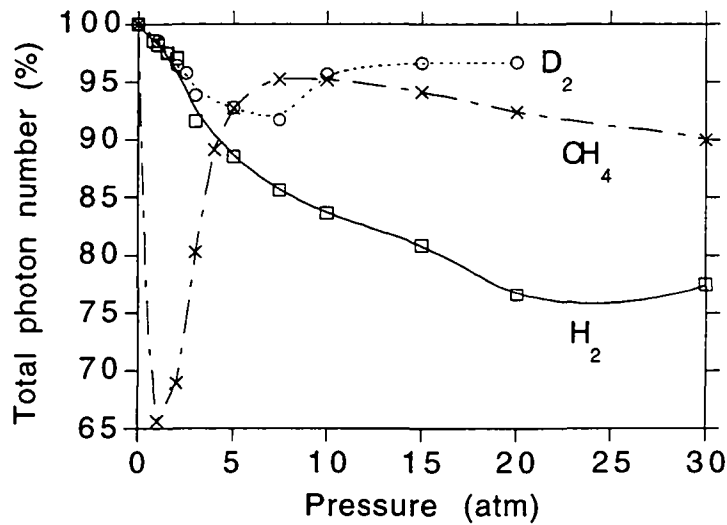


**Fig. 12.** Total number of photons in one pulse at cell exit, normalized to its maximum value (i.e. when the cell is filled with 1 atm of air), as a function of pressure for H<sub>2</sub>, D<sub>2</sub> and CH<sub>4</sub>. Po laser, 75 cm focal length lens.

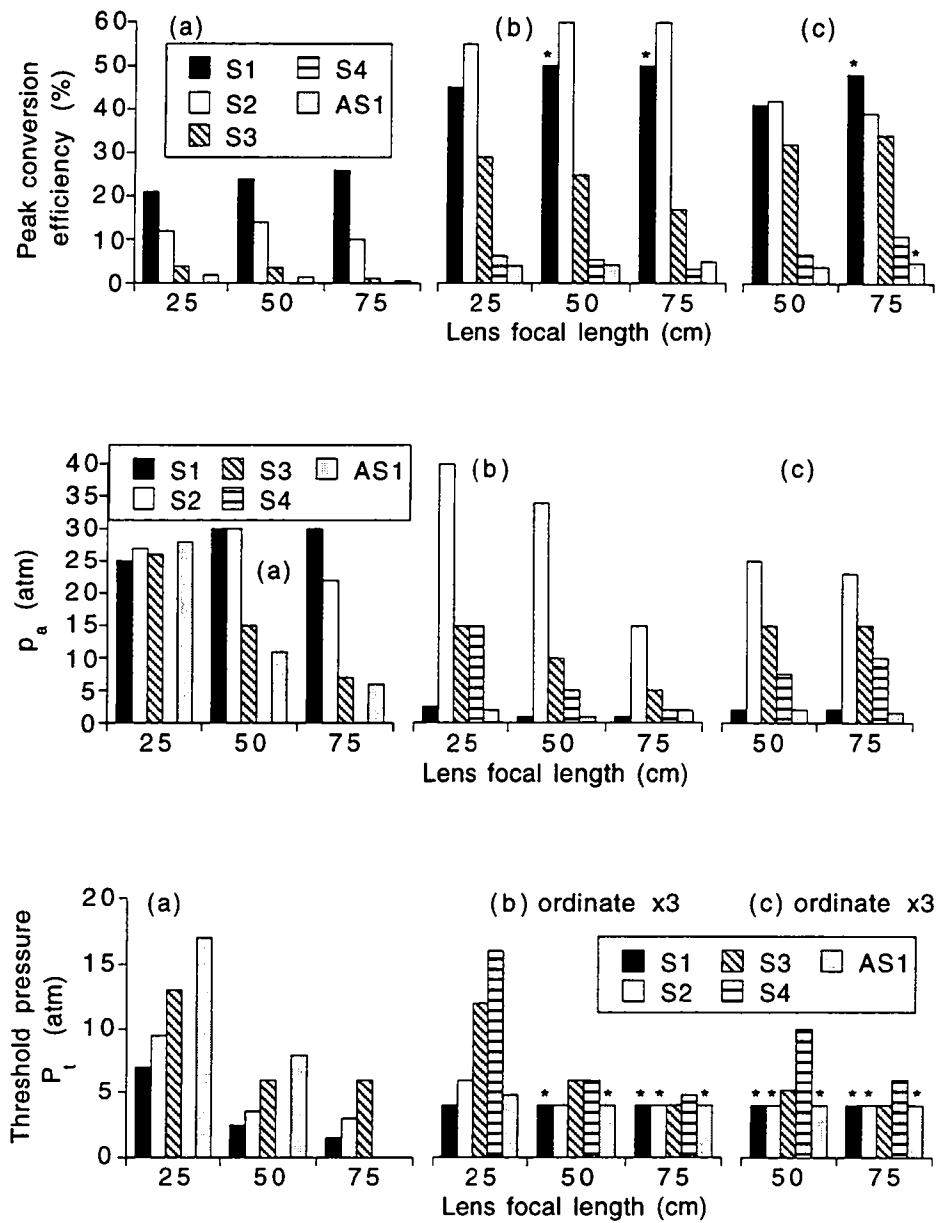
#### 4.4.1.2 Focusing geometry

Fig. 13-15 show that for the three lasers and gases investigated the threshold pressure ( $p_t$ ) decreases with increasing  $f$  for all the Stokes. It is also the case for  $\hat{p}_a$  concerning the higher Stokes ( $S_3, S_4$ ), and to a lesser extent for  $S_1, S_2$  and  $AS_1$ . Increasing  $f$  reduces the FWM, however the  $S_1$  threshold is independent of the FWM; its inverse proportionality with increasing  $f$  is best evidenced in our experimental configuration with the excimer laser (see also fig. 16 and 17). At first approximation the product of the intensity at the waist with the Rayleigh range (depth of focus) is independent of  $f$ . The  $p_t$  dependence with  $f$  can be explained by transient effects<sup>21</sup>: the gain reduction factor ( $R$ ) decreases with increasing pump intensity (through  $G$  in equ. (2)) which in turn decreases with increasing  $f$ . The  $p_t$  and  $\hat{p}_a$  decrease of  $AS_1, S_3$  and  $S_4$  with increasing  $f$  shows that the transient effects are stronger than the FWM since the latter would yield the reverse dependence.

For most of the cases investigated, similar trends for  $\hat{p}_a$  are observed between  $H_2, D_2$  and  $CH_4$  for the Nd:YAG pumping:  $S_2$  takes its maximum at high pressure (because of the downconversion of the higher Stokes at high pressure), and  $\hat{p}_a(S_2) > \hat{p}_a(S_3) > \hat{p}_a(S_4)$  showing that the higher the Stokes index the more it is produced by FWM (and hence is more reduced when the pressure is increased). Deviations from these trends are noticed for  $D_2$  and  $CH_4$  at  $f=25$  cm, attributed to the higher cascading at this lens focal length ( $S_5$  and  $S_6$  not shown in this figure). For  $H_2$  and  $D_2$   $\hat{p}_a(S_1)$  and  $\hat{p}_a(AS_1)$  are seen to be roughly equal (which suggests that  $AS_1$  is mainly produced by the  $(\mathcal{E}^P)^2 \mathcal{E}_1^{s*}$  FWM process), but it is not the case for  $CH_4$  (attributed to the higher wave-vector-mismatch).

The peak conversion efficiency ( $\hat{\eta}$ ) of the lower Stokes (excimer:  $S_1$ , Nd:YAG:  $S_1, S_2$ ) increases whereas that of the higher Stokes (excimer:  $S_2, S_3$ , Nd:YAG:  $S_3, S_4$ ) and the anti-Stokes decreases with increasing  $f$ . The lower gain of the excimer configuration, limiting the Stokes cascade, explains the difference with the Nd:YAGs. For the Surelite,  $AS_1$  is seen to increase with increasing  $f$  due to the occurrence of an anti-Stokes cascading (it is  $\hat{\eta}$  of  $AS_2$  which decreases with increasing  $f$  - not displayed in the figures). The reduced FWM with increasing  $f$  explains the dependence of  $\hat{\eta}$  with increasing  $f$ , and is most clearly evidenced with the excimer laser (fig. 13, 16).  $\hat{\eta}(S_1)$  with the excimer increases regularly with increasing  $f$  (fig. 16), whereas there is no clear dependence for the Nd:YAG lasers for that Stokes (fig. 17). It is attributed to the reduced FWM (see below) and LIB with this excimer. Fig. 18 illustrates the decrease of  $\hat{p}_a(S_3)$  and  $\hat{\eta}(S_3)$  with increasing  $f$  which occurs for the higher Stokes, as well as the decrease of  $p_t$  with increasing  $f$  noticed for all the beams.

Section 4: Experimental investigation



**Fig. 13.** Peak conversion efficiency (upper panel), pressure at which the latter occurs ( $\hat{p}_a$ , middle panel) and threshold pressure (bottom panel), in hydrogen. Ex (a), Su (b) and Po laser (c). Pressures were not measured below 1 atm, so that when  $p_t$  or  $\hat{p}_a$  occur below this limit they are marked by a star (\*) and are displayed in the figure as equal to 1 atm; correspondingly the peak conversion efficiency displayed is the value at 1 atm and is also marked by a star.

Section 4: Experimental investigation

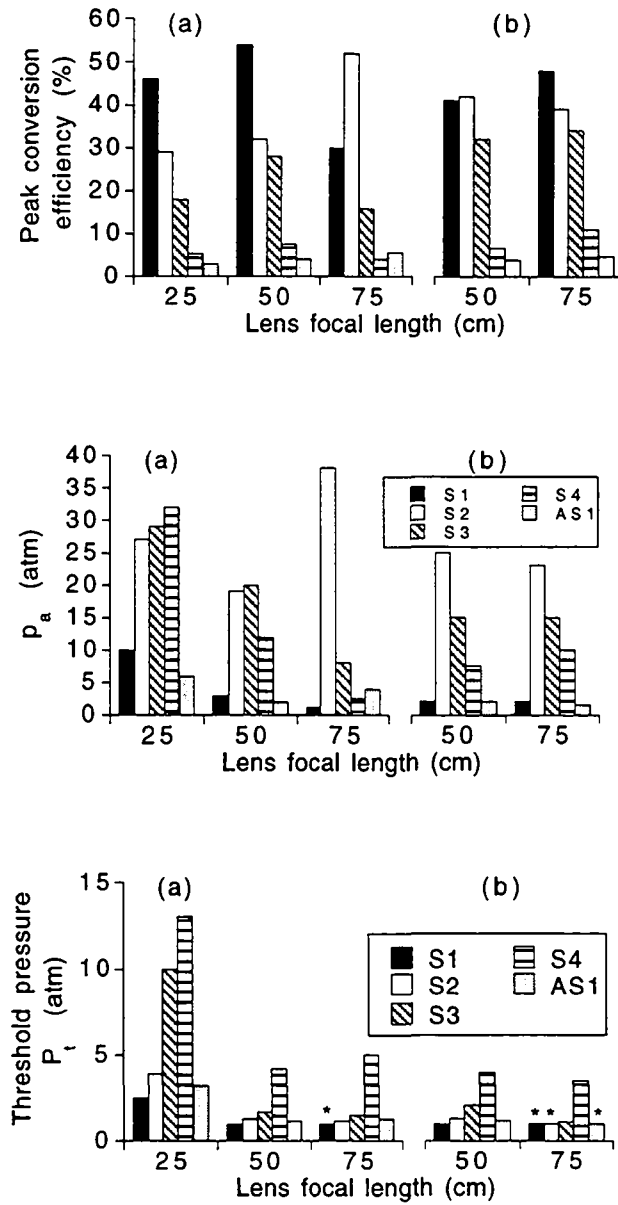


**Fig. 14.** Same as fig. 13, but in deuterium. Peak conversion efficiency (upper panel), pressure at which the latter occurs ( $\hat{p}_a$ , middle panel) and threshold pressure (bottom panel), in deuterium. Su (a) and Po (b) laser. Pressures were not measured below 1 atm, so that when  $p_t$  or  $\hat{p}_a$  occur below this limit they are marked by a star (\*) and are displayed in the figure as equal to 1 atm; correspondingly the peak conversion efficiency displayed is the value at 1 atm and is also marked by a star.

Section 4: Experimental investigation

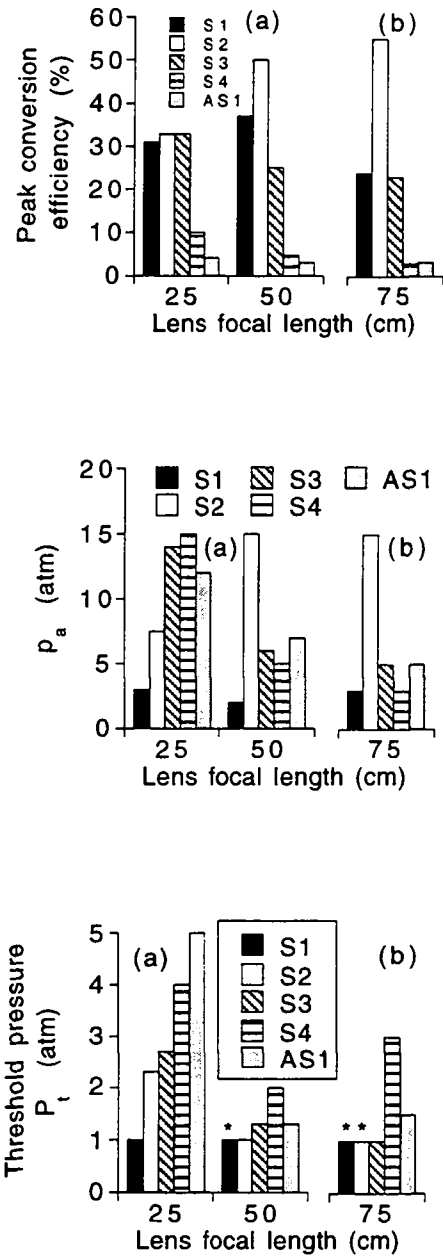


**Fig. 15.** Same as fig. 13, but in methane. Peak conversion efficiency (upper panel), pressure at which the latter occurs ( $\hat{p}_a$ , middle panel) and threshold pressure (bottom panel), in deuterium. Su (a) and Po (b) laser. Pressures were not measured below 1 atm, so that when  $p_t$  or  $\hat{p}_a$  occur below this limit they are marked by a star (\*) and are displayed in the figure as equal to 1 atm; correspondingly the peak conversion efficiency displayed is the value at 1 atm and is also marked by a star.

Section 4: Experimental investigation

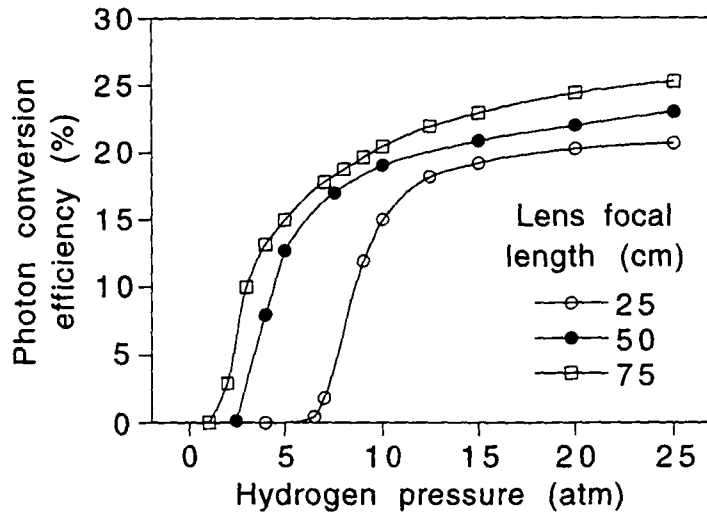


Fig. 16. S<sub>1</sub> photon conversion efficiency in hydrogen with the Ex laser

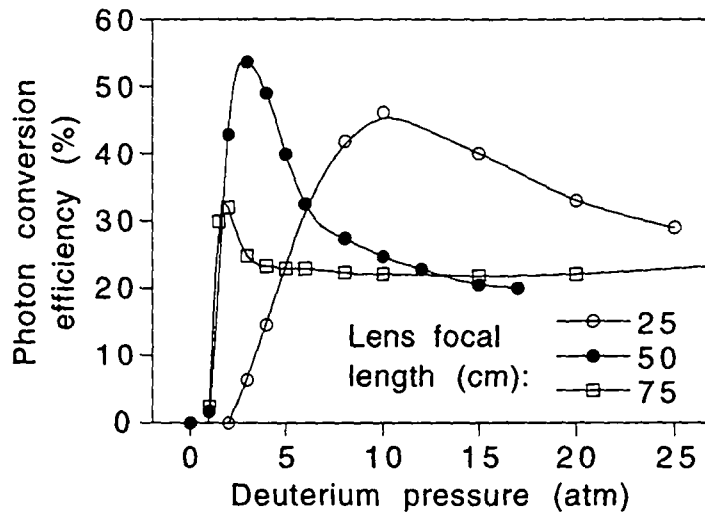


Fig. 17. S<sub>1</sub> photon conversion efficiency in deuterium with the Su laser.

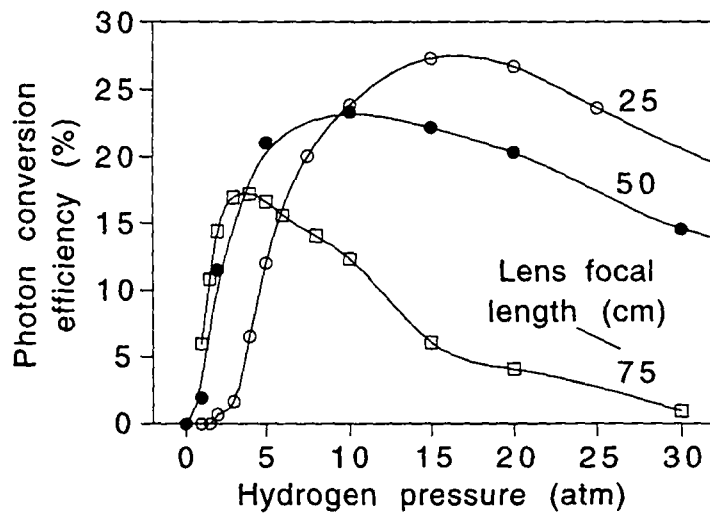
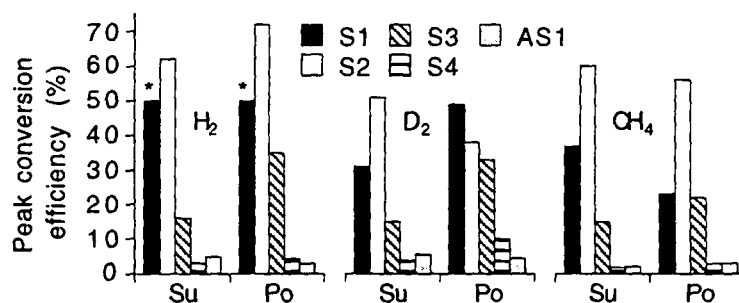


Fig. 18. S<sub>3</sub> photon conversion efficiency in hydrogen with the Su laser.

#### Section 4: Experimental investigation

For a given input pump beam size, the Rayleigh range and the waist size are proportional to the  $M^2$  parameter, whereas they are respectively proportional to  $f^2$  and  $f$ . It is therefore expected that increasing the  $M^2$  has similar effects as increasing the lens focal length. When comparing two lasers the pump beam size at the input lens and the pump pulse duration  $\tau$  must be taken into account since both determine the intensity at the waist. From the beam size measurements of §3 and with the formulas (7), the waist size of resp. the Po, Su and Ex is approximately in the proportion  $1 \times 1 : 1.5 \times 1.5 : 15 \times 4$ , and the Rayleigh range in the proportion  $1 \times 1 : 1.5 \times 1.5 : 4 \times 2.5$  (along the axis of bigger, resp. smaller, dimension of the excimer laser rectangular beam). The pulse duration of the Su, Po and Ex is in the proportion 1:1.5:3, so that the pulse energy was adjusted accordingly in order to yield a similar input power: 55 resp. 80 mJ for the comparison of the Su with the Po, and 40 resp. 80 mJ for the comparison of the Po with the Ex. Fig. 19 shows that  $S_3$  and  $S_4$  are systematically lower for the Su than for the Po laser. The same trend is exhibited by  $AS_1$  between the two Nd:YAGs, except the case of  $CH_4$ , while  $S_1$  and  $S_2$  do not show any clear trend. The conversion behaviour differs much more between the Po and the excimer (than between the two Nd:YAGs), attributed to the bigger difference in  $M^2$  (fig. 20).  $\hat{\eta}$  of  $S_2$ ,  $S_3$  and  $S_4$  are in the ratio 20:11:1 for the Po and 450:55:1 for the Ex.  $\hat{\eta}(S_1)$  occurs below 1 atm for the Po, and thus only a lower bound (determined at 1 atm) was measured, but even if  $\hat{\eta}(S_1)=100\%$ ,  $S_1$  and  $S_2$  would be in the ratio 1.5:1 for the Po whereas they are in the ratio 2.9:1 for the Ex. This comparison between the two pairs of lasers suggests that the higher the  $M^2$  of the pump, the less the FWM, and therefore there is proportionally more conversion in the two first Stokes. A similar reduction in FWM was noticed when increasing the lens focal length.

With argon as a buffer gas the  $S_1$  peak photon conversion efficiency is found to be 71% for the Surelite (10 atm  $H_2$ , 35 atm Ar) and 54% for the Powerlite (8 atm  $H_2$ , 30 atm Ar). This effect is also similar as increasing  $f$  (§4.1.4). There must exist nevertheless an optimal geometry of focusing (determined by  $M^2$  or  $f$ ) since when focusing looser and looser  $\hat{\eta}$  eventually decreases, as it is the case for the excimer for which  $\hat{\eta}$  of  $S_1$  is two to three times smaller than for the Nd:YAGs. Nevertheless KrF lasers are capable to produce pulse energies several times that of the quadrupled Nd:YAG, and can thus possibly yield  $S_1$  and  $S_2$  pulse energies higher than with the Nd:YAG, even though the conversion efficiency is lower. The dependence of  $\hat{\eta}$  with the pump energy has not been investigated. An alternative way of focusing tightly yet limiting the FWM and LIB is to use cylindrical lenses<sup>42</sup>.



**Fig. 19.** Peak photon conversion efficiency in hydrogen, 75 cm focal length lens. Input pulse energy of 55 mJ and 80 mJ for the Su and Po laser resp., which yields an approximately equal input power (13 MW) for both lasers.



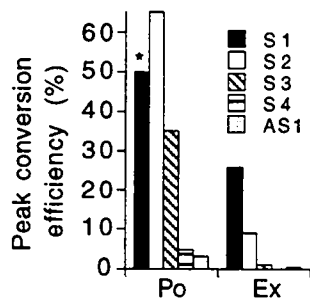


**Fig. 20.** Peak photon conversion efficiency in hydrogen, 75 cm focal length lens. Input pulse energy of 40 mJ and 80 mJ for the Po and Ex laser resp., which yields an approximately equal input power (6.7 MW) for both lasers.

#### 4.4.1.3 Buffer gases

The active and buffer gas pressure (resp. noted  $p_a$  and  $p_b$ ) were varied in order to determine those which maximize the first Stokes conversion efficiency ( $\hat{\eta}$ ), respectively noted  $\hat{p}_a$  and  $\hat{p}_b$ , shown in table 4.

**Table 4.** Mixture of active and buffer gas which maximizes the first Stokes photon conversion efficiency ( $\hat{\eta}$ ).

Laser	Lens focal length (cm)	Active gas	Active gas pressure (atm)	Buffer gas	Buffer gas pressure (atm)	$\hat{\eta}$ (%)	
Su	25	H <sub>2</sub>	5	Ar	20	31	
		D <sub>2</sub>	10	Ar	20	35	
	50	H <sub>2</sub>	10	Ar	55	56	
		D <sub>2</sub>	10	Ar	30	47	
	75	H <sub>2</sub>	10	Ar	40	64	
		D <sub>2</sub>	10	Ar	40	47	
	Po	50	H <sub>2</sub>	10	Ar	25	41
			D <sub>2</sub>	12	Ar	15	30
75		H <sub>2</sub>	1.5	He	10	35	
			3.0	Ne	8.0	32	
			10	Ar	33	61	
		D <sub>2</sub>	2.0	He	2.5	39	
			3.0	Ne	6.0	37	
			10	Ar	35	33	
CH <sub>4</sub>	10	Ar	45	52			

The three buffer gases were tested at a fixed lens focal length ( $f=75$  cm, Po laser).  $\hat{p}_a$  is seen to increase with the buffer gas molecular mass ( $M_b$ ), for both active gases (table 4), which follows from the dependence of the Raman gain with  $M_b$  (fig. 3).  $\hat{p}_b$  for Ar ( $> 30$  atm) is much bigger than for He and Ne ( $< 10$  atm). For the former the optimum is found when the Raman gain dependence with  $p_b$  is in the asymptotic regime and hence it is the wave-vector mismatch which is predominant, while for the latter it is mainly the gain reduction which controls the optimum.

Section 4: Experimental investigation

The level of  $\hat{\eta}$  reached with the addition of buffer gas depends on the gain reduction, the FWM wave-vector mismatch, and the LIB which eventually worsens with increasing  $p_b$ . In fig. 11, the net effect of adding argon to high-pressure hydrogen or deuterium (> 5 atm, say) is to increase the power of the lower Stokes ( $S_1, S_2$ ) by reducing the LIB and the FWM, but it eventually leads to a power decrease due to the increasing LIB in the buffer gas and the Raman gain reduction. The FWM and the LIB depend on the focusing geometry ( $f$  and the input pump  $M^2$ ). The highest  $\hat{\eta}$  in  $H_2$  is obtained by adding Ar, which is also found for the Su laser (not shown in table 4) and in a previous experiment making use of another type of Nd:YAG laser<sup>9</sup>.  $\hat{\eta}$  for  $D_2$  is similar for the three buffer gases, whereas for the Su laser  $\hat{\eta}$  is found 20% higher with Ar than with He and Ne (not shown in table 4), as seen in fig. 21 and 22.  $\hat{\eta}(S_2)$  in  $H_2$  is seen to attain similar levels as for  $S_1$ , and in  $D_2$  the addition of buffer gas is profitable to  $\hat{\eta}(S_2)$  only with Ar (Po laser). In both active gases  $S_3$  and  $S_4$  show no optimum when adding buffer gas.

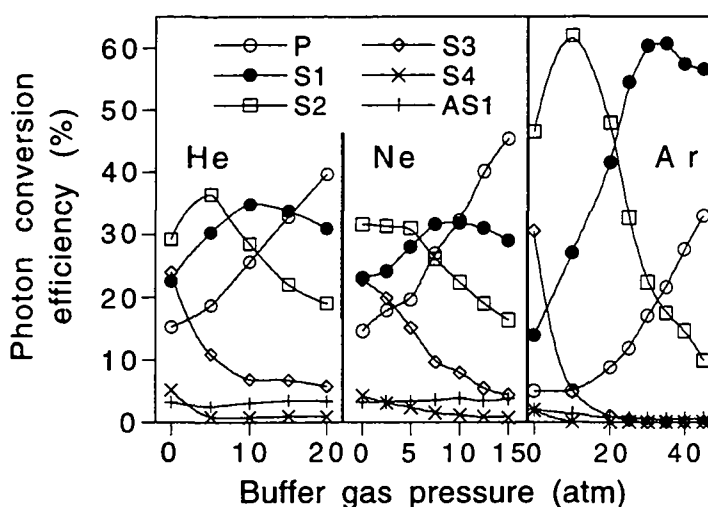


Fig. 21. Photon conversion efficiency in hydrogen when adding helium (to 1.5 atm  $H_2$ ), neon (to 3 atm  $H_2$ ) and argon (to 10 atm  $H_2$ ). Po laser, 75 cm focal length lens.

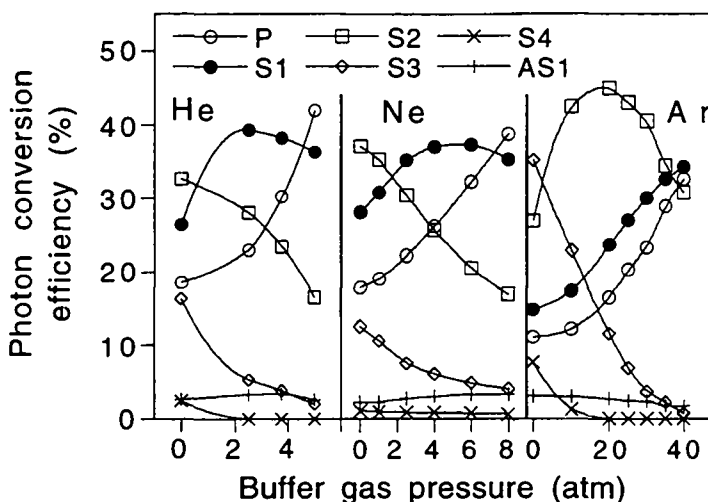
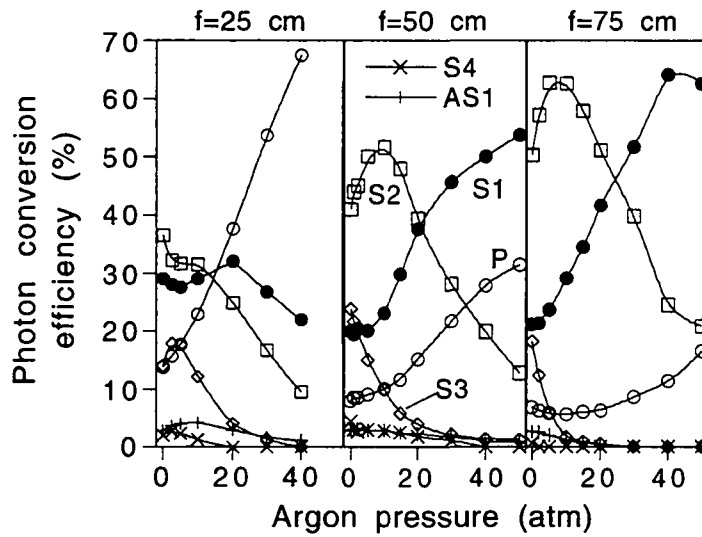


Fig. 22. Photon conversion efficiency in deuterium when adding helium (to 2 atm  $D_2$ ), neon (to 3 atm  $D_2$ ) and argon (to 10 atm  $D_2$ ). Po laser, 75 cm focal length lens.

Section 4: Experimental investigation

The lens focal length was varied for the argon buffer case (Su laser, table 4). As for the pure active gases (§4.1.2) the peak conversion efficiency increases with  $f$ , the effect being the strongest in  $H_2$ . Fig. 23 and 24 show that this dependence of  $\hat{\eta}$  with  $f$  is due to the reduction in FWM, evidenced by the reduced energy sharing among the Stokes when  $f$  increases. Moreover, LIB is a limiting factor when focusing tightly ( $f=25$  cm) since less than 50% photon transmission (TNP) was measured for an argon pressure above 20 atm, in either  $H_2$  or  $D_2$ .

The peak conversion efficiency in  $CH_4:Ar$  could be optimized ca. 50% higher than in  $D_2:Ar$  (Po laser). This effect is attributed to the higher gain (fig. 1,2) and FWM wave-vector mismatch (fig. 1) with respect to  $D_2$ . Fig. 25 shows that in  $CH_4$ , argon acts very efficiently since the  $S_1$  conversion efficiency more than doubles between 0 and 40 atm of Ar, while  $S_2$ ,  $S_3$  and  $S_4$  all decrease with Ar pressure. No etching of the optics was noticed at this methane pressure (10 atm) and these Ar pressures even after hours of operation.



**Fig. 23.** Photon conversion efficiency with the Su laser in hydrogen when adding argon, as a function of the lens focal length ( $f$ ). The  $H_2$  pressure is 5, 10, 10 atm for  $f=25$ , 50 and 75 cm respectively.

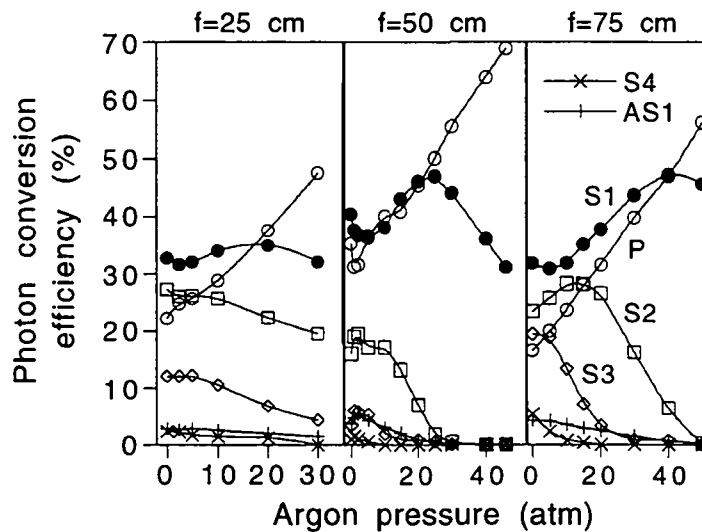


**Fig. 24.** Photon conversion efficiency with the Su laser in deuterium when adding argon, as a function of the lens focal length ( $f$ ). The  $D_2$  pressure is 10 atm for all the cases of  $f$  displayed.

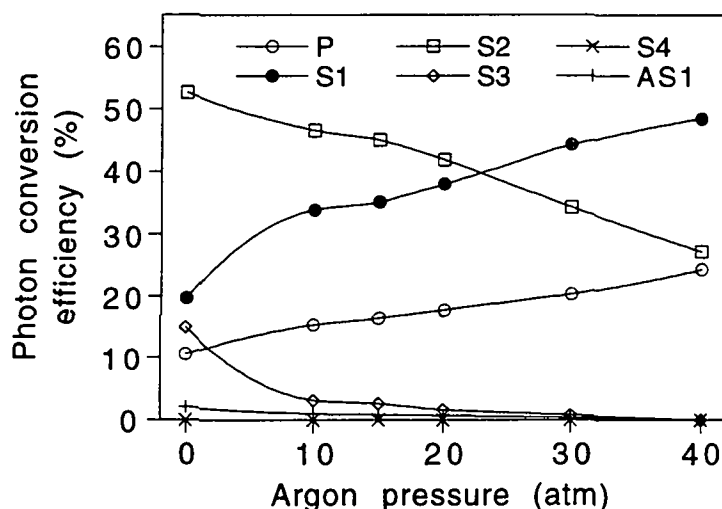


Fig. 25. Photon conversion efficiency when adding argon to 10 atm methane. Po laser, 75 cm focal length lens.

#### 4.4.2 Stokes beam quality

The quality of the output pump beam when the cell is filled with air at atmospheric pressure was measured and compared with the beam quality at input: the  $M^2$  is unchanged (within 5%) for the excimer, and is multiplied by a factor 2.0 for the two Nd:YAGs (yielding respectively an  $M^2$  of 7.8 and 12.4 for the Po and Su). At 80 mJ pulse energy the beam profile of the two latter shows a number of hot spots (at 266 nm) which induced stress on the anti-reflection coatings and the fused silica substrates, hence degrading the beam quality. Such problems were not encountered with the excimer.

The output pump beam quality of the excimer when the cell is filled with 25 atm argon was measured to be unchanged ( $M^2$  within 5%) compared to when it is filled with air at atmospheric pressure, whereas for the Po and the Su it is respectively multiplied by a factor 1.8 (to  $M^2=14.0$ ) and 1.3 (to  $M^2=16.1$ ). In these measurements  $f=50$  cm for the Ex and Su, and  $f=75$  cm for the Po. For the Ex the TNP at the exit of the cell was measured to vary less than 3% when adding argon (up to 30 atm), indicating at most a weak LIB. The TNP at 25 atm argon for the Po and Su was measured to be resp. 46 and 29% lower than when the cell is filled with air at atmospheric pressure (see also fig. 11). Therefore the beam degradation of the Nd:YAG lasers when adding argon is attributed to LIB.

In table 5, the  $M^2$  parameter of the Stokes beam is normalized with the  $M^2$  of the output pump when the cell is filled with 25 atm of argon, namely:  $273 \times 27.6$  for the excimer, 16.1 for the Su and 14.0 for the Po. The normalized  $M^2$  is noted  $\tilde{M}^2$ . The  $M^2$  parameter defined in this way avoids only to some extent the effect of the LIB on the beam quality, however it helps interpreting the sole SRS-FWM effects.

Section 4: Experimental investigation

**Table 5.** Beam quality measured at the output of the Raman cell. The cell lens focal length is 50 cm (Su and Ex laser) and 75 cm (Po laser). For the Ex laser, the knife-edge measurement was performed along the biggest (x) and lowest (y) dimension of the rectangular beam, whilst for the Nd:YAGs the  $M^2$  parameter along two perpendicular axes was measured to be within 10% of each other and is presented as the average in the table. The  $M^2$  parameter is normalized with the  $M^2$  of the output pump beam when the cell is filled with 25 atm of argon, namely: 273 (x) and 27.6 (y) for the Ex, 16.1 for the Su, 14.0 for the Po laser. The normalized  $M^2$  is noted  $\tilde{M}^2$ . The uncertainties on  $M^2$  are calculated from the dispersion of the measurement points around the model curve, equ. (6). “P” in the “beam” column refers to the residual output pump.

Laser	Active gas	Active gas pressure (atm)	Buffer gas	Buffer gas pressure (atm)	x / y (excimer)	Beam	$\tilde{M}^2$ parameter
Ex	H <sub>2</sub>	8.5	-		x	P	1.0 ± 0.1
						S1	0.48 ± 0.04
						S2	0.51 ± 0.1
		y	P	1.6 ± 0.1			
			S1	0.66 ± 0.06			
			S2	0.48 ± 0.09			
	H <sub>2</sub>	26	-		x	P	1.1 ± 0.1
						S1	0.57 ± 0.09
						S2	0.37 ± 0.04
		y	P	1.6 ± 0.1			
			S1	0.94 ± 0.08			
			S2	0.57 ± 0.06			
H <sub>2</sub>	15	He	7.5	x	P	1.0 ± 0.1	
					S1	0.41 ± 0.1	
					S2	0.23 ± 0.05	
	y	P	1.2 ± 0.1				
		S1	0.68 ± 0.08				
		S2	0.45 ± 0.07				
Su	H <sub>2</sub>	5	Ar	25		S1	1.2 ± 0.1
		2	-			S1	0.73 ± 0.06
Po	H <sub>2</sub>	10	-			P	3.3 ± 0.3
						S1	3.4 ± 0.4
						S2	12.5 ± 1.5
	D <sub>2</sub>	2.5	-			P	1.2 ± 0.1
						S1	1.1 ± 0.2
						S1	1.4 ± 0.2
					P	1.1 ± 0.1	
					S1	0.52 ± 0.04	

For the excimer there is a clear improvement ( $\tilde{M}^2 < 1$ ) between the quality of the input pump beam and that of S<sub>1</sub>, as well as between S<sub>1</sub> and S<sub>2</sub> (table 5). This beam cleanup effect is weakly dependent on the Raman gain, as noticed between 8.5 and 26 atm of H<sub>2</sub> (except for S<sub>1</sub> in the y direction). Adding He buffer slightly improves the beam quality. Similar results were obtained with a  $f=25$  cm and a  $f=75$  cm lens. Different features characterize the Nd:YAGs. At low amplification (2 atm H<sub>2</sub> or 2.5 atm D<sub>2</sub>, Po laser) the Stokes beam quality is measured to be the same as that of the input beam, or better. At higher amplification (10 atm H<sub>2</sub>, Po laser) the Stokes beam is very much degraded ( $\tilde{M}^2=3.4$  and 12.5 for S<sub>1</sub> and S<sub>2</sub> respectively), which can hardly be explained by the sole LIB. Adding 25 atm argon to 10 atm hydrogen improves the  $M^2$  of S<sub>1</sub> by more than a factor 3. Adding 10 atm He improves the  $M^2$  of S<sub>1</sub> by a factor 2.5 (its conversion efficiency is modified by 20%). A similar S<sub>1</sub> beam quality in the presence of argon buffer is obtained with both Nd:YAG lasers. These results are consistent with previous

## Section 4: Experimental investigation

measurements of the beam divergence<sup>9,16,17</sup>, with the difference that in this work the  $M^2$  parameter is measured which is independent on the beam diameter.

The  $S_1$  and  $S_2$  beam profile with the excimer (measured with a pinhole instead of the knife-edge scanned in the beam, fig. 4) replicate the beam profile of the input pump, while those with the Nd:YAGs showed annular structure at high pressure (attributed to FWM), which tends to disappear when adding buffer gas or decreasing the pressure of the active gas. Off-axis lobes were previously noticed by Cheng and Kobayashi<sup>17</sup>, which disappeared when increasing  $f$ .

The expressions of “beam cleanup” and “beam degradation” are used when the  $M^2$  parameter of the output Stokes is respectively lower and higher than the  $M^2$  of the input pump. The beam quality measurements are consistent with a numerical model<sup>21</sup>, which showed that there is beam cleanup at low amplification (i.e. before the  $S_1$  conversion efficiency becomes less than that of  $S_2$ ), and beam degradation at high amplification. The beam degradation is partly caused by the depletion at the beam center due to the conversion to higher Stokes, but mainly by the FWM which adds off-axis lobes to the beam profile (corresponding to the angle of phase-matching of the FWM). This effect of the FWM is evidenced by the fact that adding buffer gas improves the Stokes beam quality.

### 4.5. Mixture of two Raman-active gases

#### 4.5.1 Hydrogen and deuterium

At a given lens focal length the optimization process depends on four parameters: the input pump energy, the partial pressure of  $H_2$ ,  $D_2$ , and of the buffer gas (Ar in this study). In order to facilitate the optimization, the dependence of the partial pressure of  $H_2$ ,  $D_2$  and Ar such that the steady-state Raman gain in  $H_2$  equals that in  $D_2$  is plotted in fig. 26. We notice that these “optimum” pressures are quite sensitive to the pressure of  $H_2$ , as expected from its higher gain (5 times the gain of  $D_2$  at 266 nm and 10 atm active gas pressure). For example, increasing the  $H_2$  pressure from 4 to 5 atm, the  $D_2$  pressure has to be increased respectively from 12 to 16.5 atm while keeping the Ar pressure at 5 atm, or the Ar pressure has to be decreased resp. from 7 to 3 atm while keeping the  $D_2$  pressure at 15 atm. On the same figure are shown the  $H_2$  and  $D_2$  pressures at which equal energy in  $S_1(D_2)$  and  $S_1(H_2)$  could be experimentally obtained by varying the Ar pressure up to 30 atm, which are also found in table 6. The agreement between the measurements and the theoretical curves is reasonable, taking into account that such comparison is not direct since not only the Raman gain is significant but also the FWM wave-vector mismatch. We notice that either theoretically or experimentally the dependence of the  $D_2$  pressure on the  $H_2$  pressure is almost linear, so that as a rough guide the  $H_2$  pressure has to be multiplied by a factor between 2.5 and 3.5 to yield the  $D_2$  pressure in order that equal energies in  $S_1(D_2)$  and  $S_1(H_2)$  can be achieved by varying the Ar pressure.

A similar dependence of the Stokes efficiencies with argon pressure ( $p_b$ ) is noticed in all cases studied (fig. 27 (Surelite) and fig. 28 (Powerlite)). The sum of the second Stokes of  $H_2$  and  $D_2$  decreases with  $p_b$ , which shows that these beams are not substantially further converted (otherwise it would first increase and then decrease with  $p_b$ ).  $S_1(D_2)$  increases with  $p_b$  (sometimes after a short decrease), indicating that energy is backconverted from  $S_2(D_2)$  when argon is added.  $S_1(H_2)$  first increases and then decreases with  $p_b$ , showing that it is less further converted than  $S_1(D_2)$ . This effect is attributed to a higher cascading in  $D_2$ , as it was noticed with the individual active gases (§ 4.1). The residual pump increases with  $p_b$ , as it is also the case with a single active gas. Fig. 29 shows that the pulse energy of the residual pump and of the first Stokes is weakly sensitive to the input pulse energy. Even if the gas partial pressures do not yield in this case equal power in  $S_1(D_2)$  and  $S_1(H_2)$ , we notice that the ratio of the  $S_1(D_2)$  to  $S_1(H_2)$  pulse energy is approximately constant with respect to the input pump beam energy.

Section 4: Experimental investigation

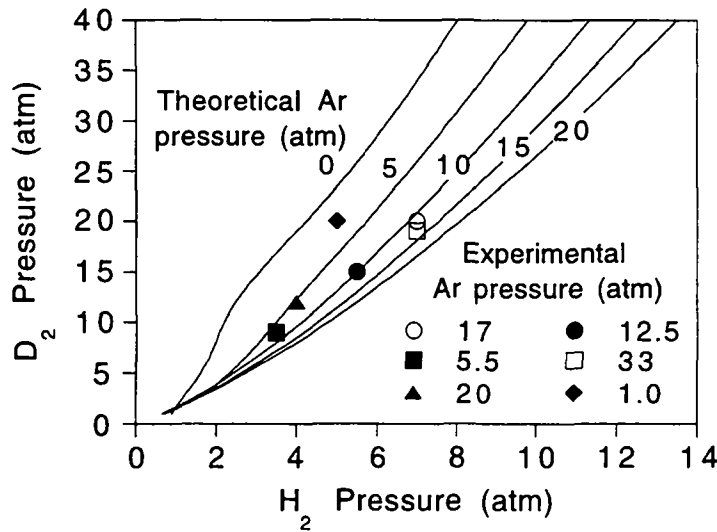


**Fig. 26.** The curves yield the dependence of the partial pressures of H<sub>2</sub>, D<sub>2</sub> and Ar in such a way that the steady-state Raman gain of H<sub>2</sub> equals that of D<sub>2</sub> in a mixing of the three gases. The dots are experimental results for which the pressure of Ar could be adjusted so that the energy in the first Stokes of D<sub>2</sub> equals the energy in the first Stokes of H<sub>2</sub>.

**Table 6.** Experimental partial pressures in a mixture of H<sub>2</sub>, D<sub>2</sub> and Ar which yield equal pulse energy in the first Stokes of deuterium and hydrogen. A lower bound in the Ar pressure column, and correspondingly a “-” in the S<sub>1</sub> energy column, means that in the indicated pressure range equal energy in both first Stokes could not be reached. 75 cm focal length lens.

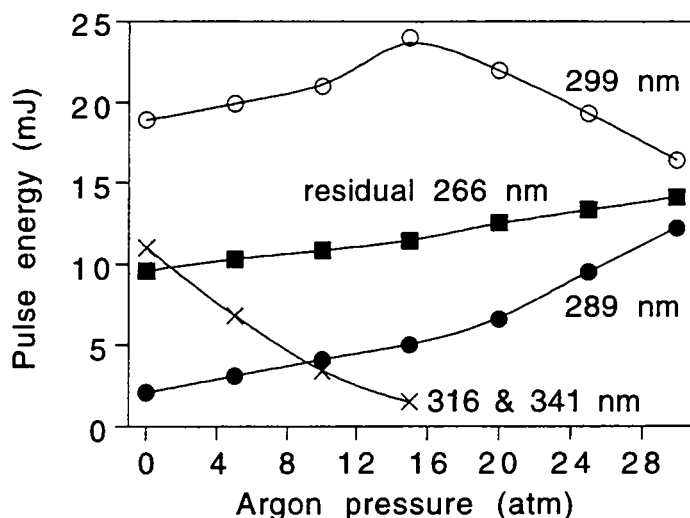
Laser	H <sub>2</sub> pressure (atm)	D <sub>2</sub> pressure (atm)	Ar pressure (atm)	Input pump pulse energy (mJ)	S <sub>1</sub> pulse energy (mJ)
Su	5.0	20	1.0	50	10
	7.0	19	33	50	14
	10	15	> 20	50	-
Po	3.5	9.0	5.5	70	7.0
	4.0	12	20	70	9.0
	5.0	10	> 20	70	-
	5.5	15	12	70	9.0
	7.0	20	17	55	7.0

Table 6 gathers the results about the search of equal energy in S<sub>1</sub>(D<sub>2</sub>) and S<sub>1</sub>(H<sub>2</sub>). Up to 9 and 14 mJ were obtained with the Po and Su laser respectively (the pump input power was approximately equal between the two lasers). The higher efficiency of the Su is attributed to the lower numerical aperture with respect to the Po (higher M<sup>2</sup>). This argument yields a high sensitivity to the geometry of focusing that indicates the predominance of FWM, which can be explained in the case of mixing of two active gases by the bigger number of possible FWM processes compared with a single active gas configuration.

The M<sup>2</sup> parameter is normalized with the M<sup>2</sup> of the output pump when the cell is filled with 25 atm Ar, in the same way as in § 4.2. The beam quality was measured for the Su laser at 7 atm H<sub>2</sub>, 19 atm D<sub>2</sub>, 33 atm Ar, f=75 cm and 50 mJ input pump pulse energy (yielding 14 mJ in S<sub>1</sub>(H<sub>2</sub>) and S<sub>1</sub>(D<sub>2</sub>), table 6). The  $\bar{M}^2$  of the residual pump, S<sub>1</sub>(D<sub>2</sub>) and S<sub>1</sub>(H<sub>2</sub>) was found respectively to be 2.1 ± 0.2, 1.2 ± 0.1 and 1.1 ± 0.1. The beam quality of both first Stokes is

#### Section 4: Experimental investigation

similar to what is measured with a single active gas, whereas that of the residual pump is ca. two times worse. The full-angle divergence (at 86% power) of the recollimated beams, at some fixed position of the output lens, was found to be  $0.50 \pm 0.02$ ,  $0.42 \pm 0.02$ ,  $0.85 \pm 0.03$  mrad for  $S_1(D_2)$ ,  $S_1(H_2)$  and the residual pump respectively. The worse divergence of the residual pump beam is due to the worse beam quality, which represents an intrinsic limitation of the Raman cell rather than a matter of the optical set-up after the cell.



**Fig. 27.** Residual pump,  $S_1$  of  $D_2$ ,  $S_1$  of  $H_2$ ,  $S_2$  of  $D_2$  plus  $S_2$  of  $H_2$ , as a function of argon pressure, in a mixture of  $H_2$ ,  $D_2$  and Ar. The parameters are: 50 mJ at cell input, Su laser, 7.0 atm  $H_2$ , 19 atm  $D_2$ , 75 cm focal length lens.

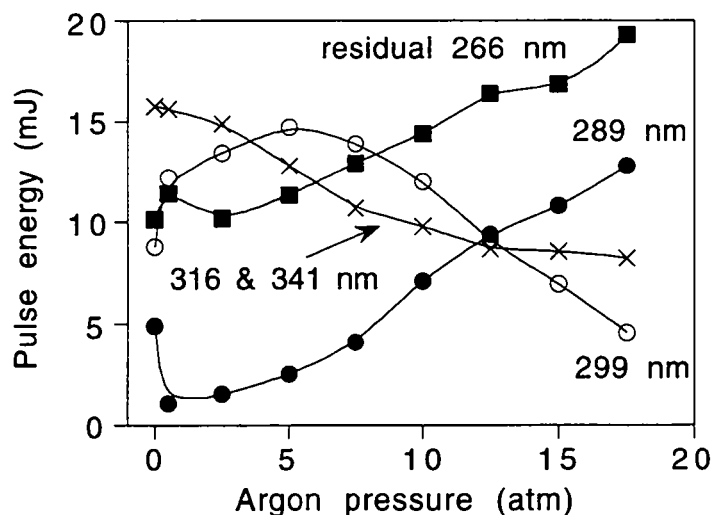


**Fig. 28.** Residual pump,  $S_1$  of  $D_2$ ,  $S_1$  of  $H_2$ ,  $S_2$  of  $D_2$  plus  $S_2$  of  $H_2$ , as a function of argon pressure, in a mixture of  $H_2$ ,  $D_2$  and Ar. The parameters are: 70 mJ at cell input, Po laser, 5.5 atm  $H_2$ , 15 atm  $D_2$ , 75 cm focal length lens.

The spectrum of the cell output radiation was investigated by removing the prism at cell output (fig. 4), taking the reflection of the radiation on a fused silica surface, dispersing it with a grating, and measuring the distance between the lines on a flat panel located at 2m of the grating. Nineteen spectral components were found (table 7) which were identified to be composed of only Stokes or anti-Stokes of either single  $H_2$ , single  $D_2$ , or the Raman-shifted frequencies in  $D_2$  of the single  $H_2$  lines, or the Raman-shifted frequencies in  $H_2$  of the single



*Section 4: Experimental investigation*

D<sub>2</sub> lines. The closest wavelength to S<sub>1</sub>(D<sub>2</sub>) (289 nm) and S<sub>1</sub>(H<sub>2</sub>) (299 nm) is seen to lie 5 nm apart (284 nm).

**Table 7.** Spectrum at output of a Raman cell filled with a mixture of H<sub>2</sub>, D<sub>2</sub> and Ar, as dispersed by a grating. The lines are identified with the following notation: for example S<sub>1</sub>(D<sub>2</sub> - 299.0) means the first Stokes in D<sub>2</sub> of the 299.0 nm beam, which is the first Stokes in H<sub>2</sub> of the 266.0 nm input pump. The parameters are: 70 mJ at cell input, Po laser, 5.5 atm H<sub>2</sub>, 15 atm D<sub>2</sub>, 12.5 atm Ar, and 75 cm focal length lens.

Wavelength (nm)	Identification
239.5	AS <sub>1</sub> (H <sub>2</sub> - 266.0)
246.4	AS <sub>1</sub> (D <sub>2</sub> - 266.0)
258.0	AS <sub>1</sub> (H <sub>2</sub> - 289.0)
266.0	pump
274.4	AS <sub>1</sub> (D <sub>2</sub> - 299.0)
279.6	AS <sub>1</sub> (H <sub>2</sub> - 316.3)
283.6	AS <sub>2</sub> (D <sub>2</sub> - 341.5)
289.0	S <sub>1</sub> (D <sub>2</sub> - 266.0)
299.0	S <sub>1</sub> (H <sub>2</sub> - 299.0)
309.8	AS <sub>1</sub> (D <sub>2</sub> - 341.5)
316.3	S <sub>2</sub> (D <sub>2</sub> - 266.0)
328.4	S <sub>1</sub> (D <sub>2</sub> - 299.0) S <sub>1</sub> (H <sub>2</sub> - 289.0)
341.5	S <sub>2</sub> (H <sub>2</sub> - 266.0)
349.3	S <sub>3</sub> (D <sub>2</sub> - 266.0)
364.2	S <sub>2</sub> (D <sub>2</sub> - 299.0) S <sub>1</sub> (H <sub>2</sub> - 316.3)
380.3	S <sub>2</sub> (H <sub>2</sub> - 289.0) S <sub>1</sub> (D <sub>2</sub> - 341.5)
390.2	S <sub>4</sub> (D <sub>2</sub> - 266.0)
397.9	S <sub>3</sub> (H <sub>2</sub> - 266.0)
408.7	S <sub>3</sub> (D <sub>2</sub> - 299.0) S <sub>1</sub> (H <sub>2</sub> - 349.3)

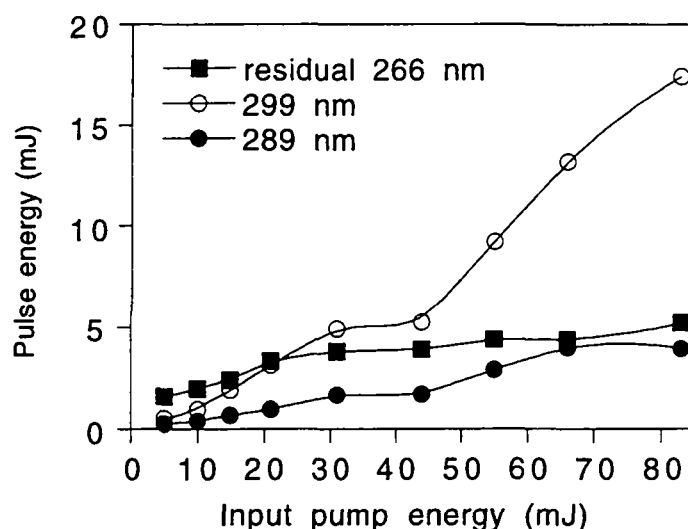


**Fig. 29.** Residual pump,  $S_1$  of  $D_2$ ,  $S_1$  of  $H_2$ , as a function of the input pump energy, in a mixture of  $H_2$ ,  $D_2$  and Ar. The parameters are:  $P_o$  laser, 7.5 atm  $H_2$ , 18.5 atm  $D_2$ , 16.5 atm Ar, 75 cm focal length lens.

#### 4.5.2 Other gas fillings

A mixture of  $H_2$ ,  $CH_4$  and Ar was also investigated. The conversion efficiency to  $S_1(H_2)$  and  $S_1(CH_4)$  is seen to be lower than with the ( $H_2$ ,  $D_2$ ) mixture (more energy is observed to be converted to the higher Stokes beams). With 15 atm  $H_2$ , 10 atm  $CH_4$ , 20 atm Ar,  $f=75$  cm and 70 mJ input pump pulse energy ( $P_o$  laser), respectively 6, 8 and 8 mJ were measured in the residual pump,  $S_1(CH_4)$  and  $S_1(H_2)$ . At this pressure of methane no etching of the optics was observed.

Ethane ( $C_2H_6$ ) was tried in an attempt to obtain two wavelength-shifted beams from its two principal vibrational modes (C-C and C-H stretching which yield respectively 273 and 289 nm from the 266 nm pumping radiation). It proved to be very unsatisfactory for the following reasons. First LIB has a much lower threshold than in  $H_2$ ,  $D_2$  or  $CH_4$ : intense sparks were visible at 1 bar of  $C_2H_6$  with corresponding cell photon transmission of ca. 30% (the ionization potential of ethane equals  $11.5 \text{ eV}^{41}$ ). Second, ethane becomes liquid at room temperature for pressures above 10 atm, which limits its applicability. Third, the Raman gain at low pressure ( $< 10$  atm) is too low for high power applications: at most 5 mJ at 273 nm and 1 mJ at 289 nm were obtained at 7.5 atm pressure.

#### 4.6. Conclusion

In single-pass UV Raman cells there exists a complex interplay between the stimulated Raman scattering (SRS), the four-wave-mixing (FWM), transient effects and the laser-induced breakdown (LIB). All these effects complicate the interpretation of conversion efficiency and beam quality measurements. One aim of the present work is to unravel some simplified rules that allow an easier interpretation of the measurements, and hence possibly a better optimization of the cell performance. A model of the SRS, FWM and the transient effects<sup>21</sup> helps to further explain several of the features observed (Stokes threshold, effect of the FWM, dependence on the lens focal length, Stokes beam quality).

Transient effects and LIB are shown to be important aspects in the interpretation of single-pass high-energy Raman cell measurements. No clear focal length dependence of the LIB was found, due to the interplay between LIB, SRS and FWM. Hydrogen and deuterium show a similar LIB behaviour, whereas it is stronger in methane. LIB degrades the Stokes beam quality (by roughly a factor of two in our setup).

The addition of Ar to H<sub>2</sub> brings higher conversion efficiencies than with He or Ne, while for D<sub>2</sub> the three types of buffer gases are equivalent. Methane leads to higher efficiencies than D<sub>2</sub>, but above 15 atm it etched the anti-reflection coatings and the fused silica substrate. There is a strong dependence of the conversion efficiencies on the lens focal length ( $f$ ). Increasing  $f$  reduces the threshold of all the Stokes and increases the first Stokes conversion efficiency. The former feature is attributed to transient effects. The input pump beam quality ( $M^2$  parameter) affects the conversion process through the geometry of focusing. Increasing the pump  $M^2$  is similar to increasing the lens focal length. A difference in conversion efficiencies of ca. 20-50% (the higher Stokes showing a larger difference) is found between the two Nd:YAG lasers, which are characterized by an  $M^2$  of 3.9 and 6.2 (at the fourth harmonic). Cylindrical lenses are foreseen to yield a higher first Stokes conversion efficiency than with spherical lenses, since it would limit the LIB and the FWM.

Concerning the Stokes beam quality two regimes are identified: low and high amplification, the limit between the two occurring when the second Stokes becomes of equal energy with the first Stokes (onset of the intensity-averaging regime). At low amplification there is beam cleanup (the  $M^2$  of the Stokes is lower than that of the input pump), whereas at high amplification the beam quality degrades (the  $M^2$  of the Stokes is higher) due to the predominance of FWM. The addition of buffer gas improves the Stokes  $M^2$  considerably, by reducing the FWM. A factor of three improvement in the first Stokes  $M^2$  parameter was measured when adding 10 atm of He or Ar.

Between 10 to 15 mJ in the first Stokes of D<sub>2</sub> and H<sub>2</sub> (pumped by the Nd:YAG fourth harmonic) can be obtained from a single Raman cell filled with the appropriate mixture of D<sub>2</sub>, H<sub>2</sub>, and Ar. The beam quality of the Stokes is comparable with the one obtained with a single active gas, while the quality of the residual pump beam is ca. two times worse. With the collimating lens positioned such as to make a compromise between the divergence of the two first Stokes and the residual pump, the full-angle divergence (at 86% power) of the two former is measured to be less than 0.5 mrad, while for the latter it is approximately 0.9 mrad. These divergences make the beam appropriate e.g. for the measurement of ozone by differential absorption lidar.

#### Acknowledgements

This work was supported by the Swiss Federal Office for Education and Science, grant n° Eureka-BBW(94)3. The author would like to thank P.-A. Biemann and D. Jeker for their technical assistance.

## References

1. D. A. Haner, I. S. McDermid, "Stimulated Raman shifting of the Nd:YAG fourth harmonic (266 nm) in H<sub>2</sub>, HD, and D<sub>2</sub>", *IEEE J. Quant. Electron.*, **26**, 1292-1298 (1990).
2. W. B. Grant, E. V. Browell, N. S. Higdon, S. Ismail, "Raman shifting of KrF laser radiation for tropospheric ozone measurements", *Appl. Opt.*, **30**, 2628-2633 (1991).
3. J. A. Sunesson, A. Apituley, D. P. J. Swart, "Differential absorption lidar system for routine monitoring of tropospheric ozone", *Appl. Opt.*, **33**, 7045-7058 (1994).
4. S. E. Bisson, "Parametric study of an excimer-pumped, nitrogen Raman shifter for lidar applications", *Appl. Opt.*, **34**, 3406-3412 (1995).
5. Z. Chu, U. N. Singh, T. D. Wilkerson, "Multiple Stokes wavelength generation in H<sub>2</sub>, D<sub>2</sub> and CH<sub>4</sub> for lidar aerosol measurements", *Appl. Opt.*, **30**, 4350-4357 (1991).
6. C. Higgs, J. A. Russell, D. W. Trainor, T. Roberts, E. D. Ariel, B. E. Player, B. W. Nicholson, M. J. Smith, L. C. Bradley, "Adaptive-optics compensation in a Raman amplifier configuration", *IEEE J. Quant. Electron.*, **26**, 934-941 (1990).
7. B. W. Nicholson, J. A. Russell, D. W. Trainor, T. Roberts, C. Higgs, "Phasefront preservation in high-gain Raman amplification", *IEEE J. Quant. Electron.*, **26**, 1285-1291 (1990).
8. D. W. Trainor, "Military excimer-laser technology seeks real-world uses", *Laser Focus World*, PennWell Publishing, June 1993.
9. Final report to the project EUROTRAC/TESLAS, "Tropospheric Environmental Studies by Laser Sounding", Jens Bösenberg Ed. (Max-Planck Institut für Meteorologie, Hamburg, Germany), Commission of the European Communities, in press.
10. K. Sentrayan, A. Michael, V. Kushawaha, "Design of a compact blue-green stimulated hydrogen Raman shifter", *Appl. Phys. B*, **62**, 479-483 (1996).
11. D. W. Trainor, H. A. Hyman, R. M. Heinrichs, "Stimulated Raman scattering of XeF\* laser radiation in H<sub>2</sub>", *IEEE J. Quant. Electron.*, **18**, 1929-1934 (1982).
12. A. Luches, V. Nassisi, M. R. Perrone, "Improved conversion efficiency of XeCl radiation to the first Stokes at high pump energy", *Appl. Phys.*, **B47**, 101-105 (1988).
13. J. A. Sunesson, A. Apituley, "RIVM tropospheric ozone lidar, report II: system description and first results", report n° 222201006, RIVM, Dutch National Institute of Public Health and Environmental Protection (1991).
14. U. Kempfer, W. Carnuth, R. Lotz, T. Trickl, "A wide-range UV lidar system for tropospheric ozone measurements: development and application", *Rev. Sci. Instrum.*, **65**, 3145-3164 (1994).
15. J. C. van den Heuvel, F. J. M. van Putten, R. J. L. Lerou, "Quality of the Stokes beam in stimulated Raman scattering", *IEEE J. Quant. Electron.*, **30**, 2211-2219 (1994).
16. D. Diebel, M. Bristow, R. Zimmermann, "Stokes shifted laser lines in KrF-pumped hydrogen: reduction of beam divergence by addition of helium", *Appl. Opt.*, **30**, 626-628 (1991).

Section 4: Experimental investigation

17. Xusan Cheng, Takayoshi Kobayashi, "Raman wave front of higher-order Stokes and four-wave-mixing processes", *J. Opt. Soc. Am. B*, **5**, 2363-2367 (1988).
18. Xusan Cheng, Runwen Wang, Qihong Lou, Zhijiang Wang, "Investigation of the Raman wavefront of higher-order gaussian-hermite modes", *Opt. Comm.*, **64**, 67-71 (1987).
19. See e.g. J. Reintjes, R. H. Lehmborg, R. S. F. Chang, M. T. Duignan, G. Calame, "Beam cleanup with stimulated Raman scattering in the intensity-averaging regime", *J. Opt. Soc. Am. B*, **3**, 1408-1427 (1986).
20. L. Schoulepnikoff, V. Mitev, "Numerical method for the modelling of high-gain single-pass cascade stimulated Raman scattering in gases", *J. Opt. Soc. Am. B*, in press.
21. L. Schoulepnikoff, V. Mitev, "High-gain single-pass stimulated Raman scattering and four-wave-mixing in a focused beam geometry: numerical study", *Pure and Applied Optics*, in press.
22. T. Yagi, Y. S. Huo, "Laser-induced breakdown in H<sub>2</sub> gas at 248 nm", *Appl. Opt.*, **35**, 3183-3184 (1996). Also: Dorothee Diebel, Michael Bristow, Rainer Zimmermann, "UV DIAL for simultaneous measurement of tropospheric O<sub>3</sub> and SO<sub>2</sub>: optimization of the transmitter section", *Proc. 15th International Laser Radar Conference (Tomsk, USSR, 1990)*.
23. D. C. Hanna, M. A. Yuratich, D. Cotter, *Nonlinear optics of free atoms and molecules* (Springer, Berlin, 1979).
24. W. K. Bischel, M. J. Dyer, "Wavelength dependence of the absolute Raman gain coefficient for the Q(1) transition in H<sub>2</sub>", *J. Opt. Soc. Am. B*, **3**, 677-682 (1986).
25. D. A. Russel, W. B. Roh, "High-resolution CARS measurement of Raman linewidths of deuterium", *J. Mol. Spectrosc.*, **124**, 240-242 (1987).
26. Y. Taira, K. Ide, H. Takuma, "Accurate measurement of the pressure broadening of the  $\nu_1$  Raman line of CH<sub>4</sub> in the 1-50 atm region by inverse Raman spectroscopy", *Chem Phys. Lett.*, **91**, 299-302 (1982).
27. W. K. Bischel, G. Black, "Wavelength dependence of the Raman scattering cross section from 200-600 nm", in *Excimer Lasers - 1983*, C. K. Rhodes, H. Egger, H. Pummer, Eds. (American Institute of Physics, New-York, 1983).
28. C.-S. Wang, "Theory of stimulated Raman scattering", *Phys. Rev.*, **182**, 482-494 (1969).
29. R. J. Heeman, H. P. Godfried, "Gain reduction measurements in transient stimulated Raman scattering", *IEEE J. Quant. Electron.*, **31**, 358-364 (1995).
30. D. Cotter, D. C. Hanna, R. Wyatt, "Infrared stimulated Raman generation effects of gain focusing on threshold and tuning behaviour", *Appl. Phys.*, **8**, 333-340 (1975).
31. Gary C. Bjorklund, "Effects of focusing on third-order nonlinear processes in isotropic media", *IEEE J. Quant. Electron.*, **11**, 287-296 (1975).
32. J. Bartels, H. Borchers, H. Hausen, K.-H. Hellwege, K. L. Schafer, E. Schmidt, *Landolt-Börnstein Zahlenwerte und funktionen* (Springer-Verlag, Berlin, 1962), pp. 6.871-6.885.

Section 4: Experimental investigation

33. *International critical tables of numerical data, physics, chemistry and technology*, vol. VII, E. W. Washburn Ed. (McGraw-Hill, New-York, 1930), pp.1-11.
34. G. Herzberg, *Molecular spectra and molecular structure*, second edition (Krieger, Malabar, Florida, 1989), volume 1, chapter VII.
35. D. Robert, J. Bonamy, F. Marsault-Herail, G. Levi, J.-P. Marsault, "Evidence for vibrational broadening of Raman lines in H<sub>2</sub>-rare gas mixtures", *Chem. Phys. Lett.*, **74**, 467-471 (1980).
36. G. E. Hahne, C. Chackerian, Jr., "Vibration-rotation line shifts for  $^1\Sigma_g^+ \text{H}_2(\nu, J) - ^1S_0 \text{He}$  computed via cloe coupling: temperature dependence", *J. Chem. Phys.*, **73**, 3223-3231 (1980).
37. K. C. Smyth, G. J. Rosasco, W. S. Hurst, "Measurement and rate law analysis of D<sub>2</sub> Q-branch line broadening coefficients for collision with D<sub>2</sub>, He, Ar, H<sub>2</sub> and CH<sub>4</sub>", *J. Chem. Phys.*, **87**, 1001-1011 (1987).
38. A. E. Siegman, M. W. Sasnett, T. F. Johnston, "Choice of clip levels for beam width measurements using knife-edge techniques", *IEEE J. Quant. Electron.*, **27**, 1098-1104 (1991).
39. C. G. Morgan, "Laser-induced electrical breakdown of gases", in "Electrical breakdown of gases", J. M. Meek, J. D. Craggs Eds. (Wiley, New-York, 1978).
40. A. J. Alcock, K. Kato, M. C. Richardson, *Optics Commun.*, **6**, 342 (1972).
41. *CRC handbook of chemistry and Physics*, 74th edition, D. R. Lide Ed. (CRC Press, Boca Raton, 1993).
42. J. C. van den Heuvel, F. J. M. van Putten, R. J. L. Lerou, "Experimental and numerical study of stimulated Raman scattering in an astigmatic focus", *IEEE J. Quant. Electron.*, **29**, 2267-2272 (1993).

## **Section 5**

# **Experimental optimization of hydrogen and deuterium Raman cells pumped by the fourth harmonic of a Continuum Powerlite 8010 Nd:YAG laser**

### **Abstract**

The optimization of the Raman cells proceeds by a parametric study. The parameters varied are: the pulse energy at input of the cell, the cell lens focal length, the type and pressure of the Raman active gas ( $H_2$ ,  $D_2$ ,  $CH_4$ ), the type and pressure of the buffer gas (He, Ne, Ar). Sets of parameters which optimize the first Stokes conversion efficiency and beam quality ( $M^2$  parameter) are determined. The results obtained with the Powerlite laser agree with those of another group, which make use of a Spectra Physics DCR 3D laser of the same specifications. However, the poor beam quality of the Powerlite at 266 nm (hot spots) does not allow to operate at full power, and hence the operational efficiency of the Powerlite system is less (ca. 25%) than the DCR 3D. The optimized pulse energies of the Powerlite at 60 mJ pump are: 25, 20, 15 mJ in the first Stokes of  $H_2$ , the first Stokes of  $D_2$ , and the residual pump respectively. Energy fluctuations of the output beams of the same level as those of the input pump is achievable, at the optimized conversion efficiency, in pure active gas. In a mixing with buffer gas, the energy fluctuations become ca. two times those of the input pump at the optimized conversion efficiency.

## 5.1 Introduction

The "Raman cells" project had the goal to upgrade the tropospheric ozone lidar (DIAL ozone) of the Laboratory of Air and Soil Pollution (LPAS) of EPFL with the addition of single-pass high-conversion Raman cells. It has been conducted jointly between the lidar groups of the Observatory of Neuchâtel (ON) and LPAS, as part of the european EUROTRAC research frame, TESLAS subproject<sup>1</sup>. TESLAS (Tropospheric Environmental Studies by Laser Spunding) main objective is the development of reliable DIAL systems for the routine measurement of tropospheric ozone.

Raman cells were designed, machined, assembled and eventually optimized. The design is modular: a removable flange can be adapted to tubes of different lengths, thus allowing to vary the cell lens focal length. The position of the input and output cell lenses can be adjusted along the optical axis. The optimization procedure consists in a parametric study, with the conversion efficiency and quality ( $M^2$  parameter) of the shifted beams measured. The parameters varied are: the pulse energy at input of the cell, the cell lens focal length, the type and pressure of the Raman active gas ( $H_2$ ,  $D_2$ ,  $CH_4$ ), the type and pressure of the buffer gas (He, Ne, Ar). The setup of the optimization experiment is described in §4.3.

The first Nd:YAG lasers delivered by Continuum to the LPAS were two pieces of model Surelite III (single oscillator configuration). Both showed severe setbacks: the Pockels cells leaked, the flashlamp cladding was not waterproof, the beam at 266 nm showed hot spots which burnt the laser 266 nm dichroic mirrors, and these were optimized at a different angle than specified. Continuum replaced the Surelites by two pieces of model Powerlite 8010 (oscillator - amplifier). The Powerlites also exhibit hot spots at 266 nm. The optimization of the Raman cells pumped by the Surelites has been carried out by Biemann<sup>2</sup>. This section reports on the optimization of the Raman cells pumped by the Powerlites.

## 5.2 Optimization procedure

The energy conversion is first optimized, via the parametric variation. At the optimum Raman cell configurations found regarding energy conversion, the beam quality ( $M^2$  parameter) is checked. The  $M^2$  is measured with the knife-edge technique (§ 4.3). The computer-controlled system developed by Jeker<sup>3</sup> is used (the computer commands a stepping motor which moves the knife-edge, and simultaneously acquires the energies measured by the energy meter). Due to lack of time, the optimization reported in this section has been carried out for the powerlite 8010 S/N 2772 only, and not for the second model which has been delivered after this optimization process.

The lidar group of the Dutch National Institute of Public Health and Environmental Protection (RIVM) have also developed Raman cells pumped by quadrupled Nd:YAG lasers<sup>4</sup>. They dispose of two Spectra Physics lasers (model DCR-3D) in an oscillator-amplifier configuration, operating at 10 Hz and delivering up to 100 mJ at 266 nm; these specifications are very similar to those of the Continuum Powerlite 8010. The RIVM group obtains with 85 mJ pump pulse energy: 35 mJ of first Stokes in hydrogen, 25 mJ of first Stokes in deuterium, and 15 mJ of residual pump, all with a divergence of  $0.5 \pm 0.1$  mrad. the objective here is to obtain the same, or better, Raman cell specifications as those of RIVM.



## Section 5: Raman cell experimental optimization

### 5.3 Pump beam characterization (at 266 nm)

The standard deviation of the energy fluctuations is measured to be ca. 5% (266 nm), on a 1000 pulses statistics. The mean energy, once the doubling crystal are energy optimized, shows typically a drift of 3% per hour.

The Powerlite beam at 266 nm is characterized by an annular shape above 60 mJ pulse energy, as can be seen on a photosensitive paper (e.g. Kodak “linagraph”). The same pattern has been reported<sup>5</sup> with a Powerlite 9030 (oscillator with two amplification stages, 30 Hz) above 100 mJ. The dip at the beam center is due to self-absorption of the 266 nm radiation in the KDP doubling crystal, and is a intrinsic limitation of such crystals. The  $M^2$  was measured to be  $3.9 \pm 0.2$  and  $4.1 \pm 0.2$  in the horizontal and vertical direction respectively (c.f. §4.3).

Burns in the bulk of the fused silica of the cell windows, lenses and prisms, are noticed for an energy above 70 mJ (which corresponds to 1.30 kV flashlamp voltage, without apodizer in the laser cavity). These burns consist of fine “needles” located on the “donut” part of the beam, and are attributed to self-focusing. They arise after a few hours of operation. Similar burns were experienced with the two Surelites<sup>2</sup> and with a Powerlite 9030<sup>5</sup>. An apodizer (plate with one rough surface) between the oscillator and the amplifier worsens the hot spot problems. It is recommended not to increase the high voltage above 1.28 kV in order to keep the pulse energy under 70 mJ; hours of operation at 1.26 kV (60 mJ pulse energy) led to no noticeable damage and is hence recommended. There are only few users of high energy lasers operating at 266 nm; the Continuum lasers are not optimized for that purpose<sup>6</sup>. Continuum has the “top hat beam profile philosophy”, which is well suited for operation at other wavelengths than 266 nm e.g. to pump OPOs. Top-hat profile beams seem to lead to hot spots after quadrupling to 266 nm.

### 5.4 Beam expansion before focusing

A beam expander composed of one planoconvex and one planoconcave lens is inserted in the pump beam before focusing. With a *1.75 beam expander* no optical damage in the fused silica windows, lenses and prisms is noticed, when operating at 90 mJ at laser output. On the other hand the conversion efficiency of the cell is seen to be significantly lower than without expansion: no more than 20 mJ of first Stokes in H<sub>2</sub> and 15 mJ of first Stokes in D<sub>2</sub> can be achieved (ca. 25% less than without expansion). This effect is mainly caused by laser induced breakdown (LIB) due to the tighter focusing (the waist size is inversely proportional to the beam size at lens), and also to the stronger four-wave-mixing (FWM) which is a consequence of the higher numerical aperture (see section 4). Fig. 1 illustrates the effect of the beam expansion on the LIB (see also fig. 10 of section 4).

With a *1.25 beam expander* (BE), the conversion efficiency is very much the same than without expansion. Nevertheless, uncoated optics were used for the BE, so that the high voltage had to be increased (to 1.34 kV, without apodizer) in order to keep to ca. 85 mJ at the entrance of the cell. It is seen that increasing the high voltage above ca. 1.30 kV, the beam quality at 266 nm quickly degrades (in particular the beam gets more and more annular). the result is that the intensity decrease due to the expansion is compensated by the local intensity increase on the beam ring (plus more hot spots), leading to no net advantage with this beam expander. However, at reduced energy (< 70 mJ) the efficiency is still very much the same than without expansion, hence making the 1.25 beam expander attractive.

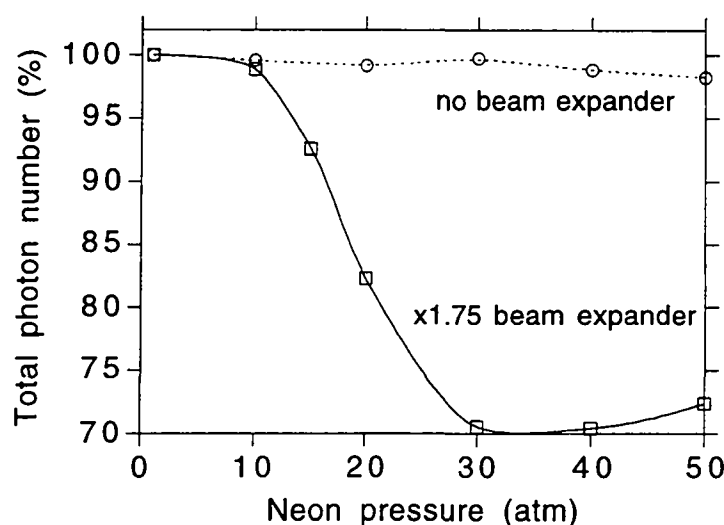


**Fig. 1.** Total number of photons in one pulse at cell exit, in neon, normalized to its maximum value (i.e. when the cell is filled with 1 atm of air). A times 1.75 beam expander has been optionally inserted in the pump beam before focusing.

### 5.5 Energy conversion without beam expansion

The conversion efficiencies were clearly the highest with the longest cell available (1.3 m length, 75 cm focal length lens), due to less four-wave-mixing and optical breakdown (see section 4). The results presented below were obtained with this cell.

As shown in section 4 (fig. 21 and 22), argon is the most efficient buffer gas in H<sub>2</sub>, while Ar, Ne and He have comparable effect in D<sub>2</sub>. The peak conversion efficiency ( $\hat{\eta}$ ) in pure H<sub>2</sub> is very sharp (FWHM of ca. 1 atm) and occurs at or below 1 atm, which makes it impractical. The addition of argon to H<sub>2</sub> brings higher conversion efficiency than in pure H<sub>2</sub>, with a broad peak (FWHM of ca. 20 atm), and is thus preferred. The addition of buffer gas in D<sub>2</sub> does not bring any significant improvement of  $\hat{\eta}$  with respect to pure D<sub>2</sub>.  $\hat{\eta}$  in pure D<sub>2</sub> occurs at about 2-3 atm, with a FWHM of ca. 4 atm, and therefore for simplicity it is the configuration adopted.

For a single active gas, the conversion efficiencies do not depend strongly on the input pump energy, whereas the dependence is stronger in case of a mixture of H<sub>2</sub> and D<sub>2</sub>.

Section 5: Raman cell experimental optimization

Flashes high voltage (kV)	Pulse energy at laser output (mJ)	H <sub>2</sub> pressure (atm)	D <sub>2</sub> pressure (atm)	Ar pressure (atm)	Residual pump energy (mJ)	H <sub>2</sub> first Stokes energy (mJ)	D <sub>2</sub> first Stokes energy (mJ)
1.30	85	1			15	25	
		10		35	15	35	
			1.5		20		25
			5	15	18		15
			10	35	15		15
		4	12	19	20	10	10
		5.5	15	12.5	17	10	10
1.28	75	1.25			15	20	
		10		25	12	28	
			2		20		20
1.26	65	2			13	20	
		10		25	14	24	
			2.5		15		20
		7	20	15	6	5	5

**Table 1.** Pressures of H<sub>2</sub>, D<sub>2</sub> and Ar which maximize first Stokes conversion efficiency, as a function of the input pump pulse energy.

Table 1 shows the optimal cell configurations for H<sub>2</sub> and D<sub>2</sub>, as a function of the pump pulse energy. We notice that the Powerlite 8010 yields the same conversion efficiencies than the Spectra Physics DCR-3D of the RIVM group. However, the beam quality shortcomings force to operate at a lower energy level (<70 mJ) than with the DCR-3D laser (100 mJ). With the latter, optical damage when operating at 90 mJ is noticed after a few months of operation<sup>7</sup>, which is clearly a better performance than with the Powerlite. The beam quality weakness of the Powerlite makes the Raman cell system less efficient than with the DCR-3D laser.

### 5.6 Beam quality

The Stokes beam quality measurements are summarized in table 5 of section 4. At the pressures optimizing the conversion efficiency in H<sub>2</sub> (10 atm H<sub>2</sub> with 25 atm Ar) and D<sub>2</sub> (2.5 atm D<sub>2</sub>), the divergence is measured to be  $0.5 \pm 0.1$  mrad for all three beams (H<sub>2</sub> first Stokes, D<sub>2</sub> first Stokes and residual pump), which agrees with the RIVM results. The beam quality for a mixture of H<sub>2</sub> and D<sub>2</sub>, with the Powerlite pump, has not been measured.

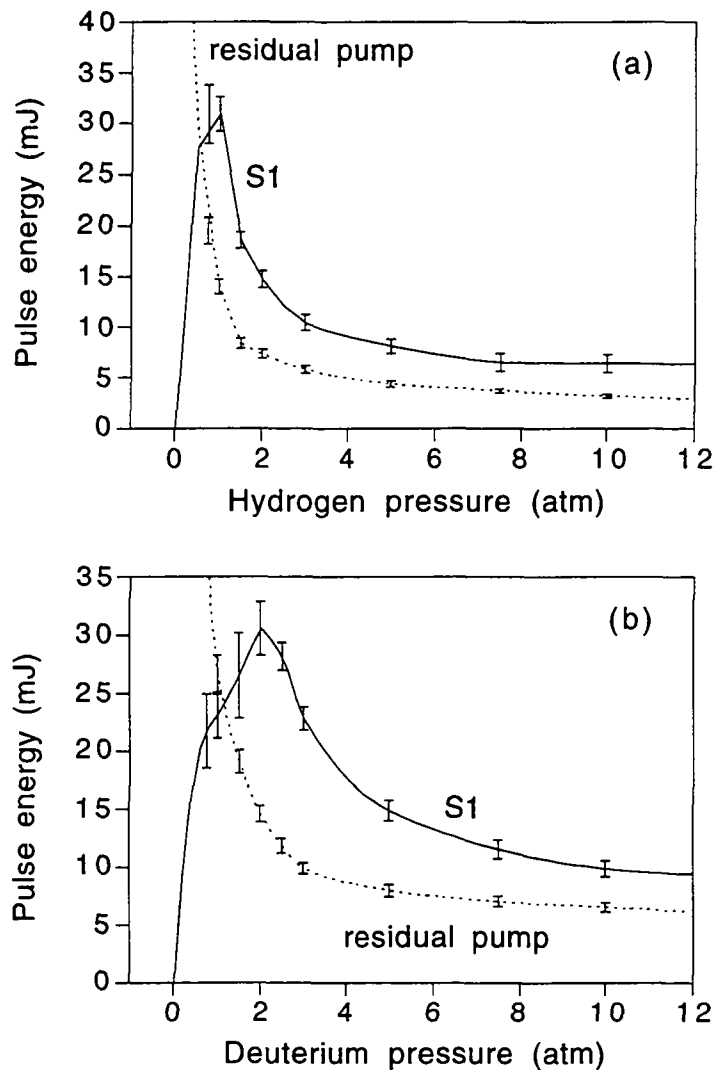
It has to be mentioned that for all the optimum conditions of energy conversion listed in table 1, rotational Stokes (SRRS) were noticed in the first Stokes and the residual pump. SRRS was evidenced either directly with a white sheet of paper after separation by a prism (most clearly seen after >10 m free propagation), or by converging one of the output beams with a lens (at focus the vibrational Stokes are separated from the rotational Stokes and can be selected by a pinhole of typically 1 mm diameter). For example, at 10 bar H<sub>2</sub> no rotational Stokes was seen whereas there were observable after adding 20 bar of helium or argon. SRRS is weaker in D<sub>2</sub> than in H<sub>2</sub>, probably due to the lower Raman gain. SRRS occurs when the pump has a circular polarization component. The latter can be provoked by imperfect optics.

The beam quality measurements reported at the beginning of this chapter were performed with the SRRS components blocked by a pinhole, transmitting the vibrational Stokes only. The beam quality of the combination "vibrational + rotational Stokes" at the optimal gas pressures is measured to be ca. two times the one of the sole vibrational Stokes:  $0.9 \pm 0.1$  mrad for the first Stokes in H<sub>2</sub> and D<sub>2</sub>,  $1.2 \pm 0.2$  mrad for the residual pump.

### 5.7 Stokes energy fluctuations

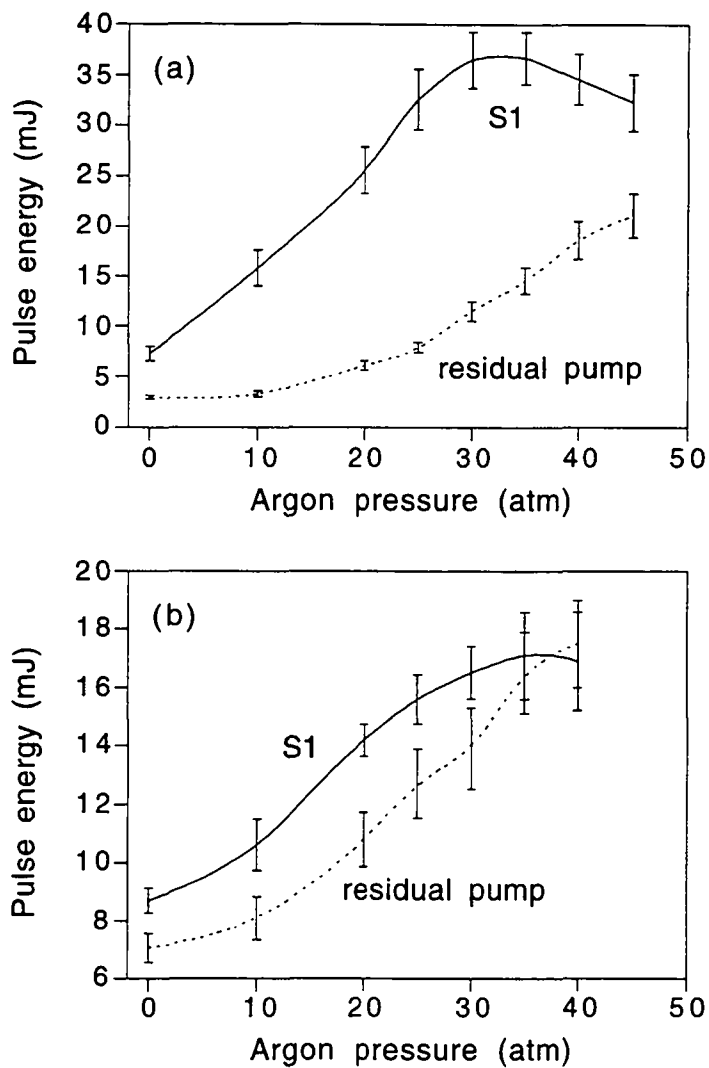
The energy fluctuations of the transmitted beams has to be minimized, which is an important aspect of the DIAL measurement of ozone. Fig. 2 and 3 show the pulse energy at the output of the Raman cell. The error bars correspond to the pulse energy standard deviation ( $\sigma$ ), calculated on a 100 shots basis. It was verified that increasing the number of shots in the average did not change significantly the measured statistics of the fluctuations.

Fig. 2 shows that at pressures below the one which yields the peak conversion efficiency ( $\hat{p}_a$ ),  $\sigma$  of the first Stokes is of the order of 10%. When the pressure is increased above  $\hat{p}_a$ ,  $\sigma$  quickly drops to about 5%, which is the standard deviation of the input pump. The standard deviation of the residual pump equals ca. 5%, irrespective of the pressure. When adding argon, the standard deviation of the first Stokes ( $S_1$ ) and the residual pump rises from about 5% with no argon to 10% at the peak  $S_1$  conversion efficiency (fig. 3). The same results are obtained with helium and neon.



**Fig. 2.** Pulse energy at the output of the Raman cell in hydrogen (a) and deuterium (b). The error bars correspond to the standard deviation calculated on a 100 shots basis. 75 cm lens, 85 mJ input pulse (1.30 kV flashlamp voltage, S/N 2772).

Section 5: Raman cell experimental optimization



**Fig. 3.** Pulse energy at the output of the Raman cell, when adding argon to 10 atm hydrogen (a) and deuterium (b). The error bars correspond to the standard deviation calculated on a 100 shots basis. 75 cm lens, 85 mJ input pulse (1.30 kV flashlamp voltage, S/N 2772).

### 5.8 Recommended Raman cell configuration

To summarize, a pump pulse energy of 60 mJ (high voltage of 1.26 kV, S/N 2772) is a reasonable compromise between energy and probability of optical damage. The highest efficiencies in D<sub>2</sub> were found when operating without buffer gas. In H<sub>2</sub> the conversion efficiency maximum that occurs at low pressure is very sharp which makes it not very practical; it is therefore preferred to work at high pressure with Ar buffer. The longest cell available (1.3 m, with 75 cm focal length lens) is the safest regarding optical damage and was seen to yield the highest conversion efficiencies. The recommended parameters, out of table 1, are listed in table 2. At this pump energy the conversion efficiencies for a single active gas are substantially higher than those of a mixture of H<sub>2</sub> and D<sub>2</sub>.

In pure active gas, the energy fluctuations of the first Stokes (S<sub>1</sub>) and the residual pump (P) were observed to replicate that of the input pump for pressures above the one ( $\hat{p}_a$ ) which yields the peak S<sub>1</sub> conversion efficiency ( $\hat{\eta}$ ). It is therefore recommended to operate at a pressure slightly above  $\hat{p}_a$  (of about 0.5-1 atm). In a mixing with buffer gas, the standard deviation of P and S<sub>1</sub> is ca. two times the one of the input pump.

Flashes high voltage (kV)	Pulse energy at laser output (mJ)	H <sub>2</sub> pressure (atm)	D <sub>2</sub> pressure (atm)	Ar pressure (atm)	Residual pump energy (mJ)	H <sub>2</sub> first Stokes energy (mJ)	D <sub>2</sub> first Stokes energy (mJ)
1.26	60	10		25	14	24	
			2.5		15		20
		7	20	15	6	5	5

**Table 2.** Recommended optimal pressures of H<sub>2</sub>, D<sub>2</sub> and Ar.

### Acknowledgements

This work was supported by the Swiss Federal Office for Education and Science, grant n° EUREKA-BBW(94)3.

### References

1. Final report to the project EUROTRAC/TESLAS, "Tropospheric Environmental Studies by Laser Sounding", Jens Bösenberg Ed. (Max-Planck Institut für Meteorologie, Hamburg, Germany), Commission of the European Communities, in press.
2. P.-A. Biemann, "Optimisation numérique et expérimentale de la partie émission du lidar du LPAS", MSc thesis, Swiss Federal Institute of Technology Lausanne, Rural Engineering Department, Laboratory for Air and Soil Pollution (1996).
3. Dominique P. Jeker, "Optimization of the EPFL lidar for the Geneva COST-CITAIR campaign", MSc thesis, Swiss Federal Institute of Technology Lausanne, Rural Engineering Department, Laboratory for Air and Soil Pollution (1996).
4. J. A. Sunesson, A. Apituley, "RIVM tropospheric ozone lidar. Report II: system description and first results", report n°222201006, National Institute of Public Health and Environmental Protection (RIVM), Bilthoven, The Netherlands.
5. T. Trickl, private communication.
6. Pay Chiu (Continuum Santa Clara), private communication.
7. A. Apituley, private communication.

## **Section 6**

# **Numerical optimization of multiwavelength differential absorption lidar (DIAL) for pollution modelling**

### **Abstract**

A computer code has been developed which simulates the lidar (transmitter, receiver) together with the propagation of the laser beams in the atmosphere and the interaction with its constituents. The best compromises in relation with the needs of the pollution airshed modelling undertaken at the LPAS have been determined. Namely, at least three wavelengths are needed in order to comply with the LPAS photochemical model grid and to variable atmospheric conditions (ozone loading, visibility). Alternative correction schemes were investigated in view of minimizing the interference of aerosol gradients, which frequently occur in polluted environments: the dual-DIAL and Raman DIAL methods. They require the detection of more than two wavelengths, but are shown to decrease substantially the interference of the aerosols in polluted conditions. The simultaneous lidar measurement of ozone and water vapor is shown to be feasible by adding a Raman water vapor channel to the DIAL ozone instrument.

## 6.1. Introduction

Single-pass Raman cells in the ultraviolet combine a high conversion efficiency with a simple set-up. KrF excimer or quadrupled Nd:YAG lasers are generally used as the pump laser<sup>1-4</sup>. The lack of continuous tunability does not constitute a drawback for ozone DIAL since the Hartley absorption band extent is larger than the separation between adjacent Raman-shifted wavelengths. The question is rather of which DIAL wavelength pair to choose in the shifted spectrum. Two criteria are generally adopted to constrain the wavelength choice, namely the minimization of both the statistical error  $E_1$  (shot-noise of the detector) and the systematic error  $E_2$  (which takes its origin mainly in the interference from aerosols and other absorbing species).

Several former studies addressed the question of the wavelength choice<sup>1-4</sup>. In particular, Papayannis et al.<sup>1</sup> concluded that firstly three elastic wavelengths are needed for measurements up to 15 km height, which define one pair for the planetary boundary layer (PBL) and one pair for the free troposphere, and secondly standard two-wavelength aerosol correction schemes<sup>5,6</sup> are insufficient in case of high aerosol loading. These studies considered a zenith or nadir line-of-sight with a fixed range resolution (100m in the PBL, 1 km in the free troposphere). The need to comply to photochemical airshed modellings<sup>7,8</sup> requires a variable line-of-sight zenith angle. Moreover these modellings make use of a computational grid of variable vertical cell size (fig.1), and hence the DIAL ozone retrieval should be accurate at various range resolutions. The measurement sampling time has also to be taken into account in order to comply to the time-step of the airshed modelling. It is the objective of this study to determine which and how many wavelengths are the most suited specifically to the airshed modelling.

The question of the necessity of more channels than the required minimal two-elastic-wavelength configuration is partly addressed here. More channels possibly allow to reduce both  $E_1$  and  $E_2$ . Polluted environments contain generally strong aerosol loadings and gradients, which interference can be the major source of error in the ozone DIAL<sup>4</sup>. One additional Raman channel ( $N_2$  or  $O_2$ ) allows to reduce the aerosol interference to an error ( $E_2$ ) estimated less than 10%<sup>1</sup> in good conditions. The drawback of the one-channel Raman technique is that the return signals are weak (the Raman backscattering cross section is 1000 times smaller than the Rayleigh backscattering cross section), and it requires to know the lidar calibration constant and the extinction-to-backscatter ratio at one altitude. Two alternative aerosol correction schemes are simulated in this work. In the first one (so-called "DIAL-Raman"), the ozone is retrieved from two Raman returns ( $N_2$  or  $O_2$ ) in the same scheme as with two elastic returns. It allows a very good correction of the aerosol interference (only the extinction wavelength dependence has to be guessed), but the range of the measurement is limited by the weak returns, and this point is investigated here. The DIAL-Raman method has been applied to stratospheric ozone measurements in presence of high volcanic aerosol loading<sup>9</sup> (the operating wavelengths are different for the stratospheric and tropospheric DIAL ozone cases). The second one<sup>10,11</sup> (so-called "dual-DIAL") makes use of at least three elastic wavelengths in order to form two pairs, and performs a double-differentiation for the retrieval of ozone. When the wavelengths are suitably located, the aerosol interference is more reduced than the ozone differential absorption cross section, hence reducing the retrieved ozone relative error with respect to the single differentiation performed with one wavelength pair. This scheme has been applied to field measurements with a KrF-pumped Raman cell DIAL system<sup>10</sup>, and the error ( $E_2$ ) is estimated to be reduced by a factor of two, in case of high aerosol loading, compared to a two-wavelength configuration. The present study has been conducted in parallel to these works<sup>10,11</sup>.

Adding one channel recording the Raman water vapor return to an ozone DIAL possibly allows to profile simultaneously the ozone and the water vapor. The additional water vapor profile has potentialities for the airshed pollution modelling. The water vapor profile has been measured night-time with the Raman technique in the solar-blind wavelength region<sup>12,13</sup> (< 300 nm), with a range of 1-3 km, zenith probing. Attempts were made to perform measurements day-time in the spectral region of high solar background (> 300 nm) by using a narrowband transmission



Section 6: Numerical optimization of DIAL wavelengths

and detection<sup>14,15</sup>. These systems make use of a single wavelength emitted in the atmosphere. The ozone absorption is corrected by recording the N<sub>2</sub> and O<sub>2</sub> Raman returns. The latter are separated by only 5 nm (with 248 or 266 nm emitted wavelength), which limits the range of the ozone retrieval (Raman DIAL scheme) due to the small ozone differential absorption cross section; however the quality of the ozone profile is sufficient for the ozone absorption correction in the water vapor retrieval. The aim here is to study the feasibility of using the water vapor Raman technique with the two pumping wavelengths of an ozone elastic DIAL. An additional N<sub>2</sub> or O<sub>2</sub> Raman channel is required to compute the water vapor mixing ratio, but on the other hand it allows for the Raman aerosol correction of the ozone retrieval. The ozone absorption is this time corrected with the elastic DIAL measurement. It is therefore the configuration of two emitted wavelengths, two elastically recorded wavelengths and two recorded Raman wavelengths (one N<sub>2</sub> or O<sub>2</sub>, the other one H<sub>2</sub>O) which is investigated here.

This optimization study has been performed via a computer simulation of the DIAL instrument and of representative atmospheric situations. The principal parameters of the transmitter, receiving optics, detection acquisition, have been taken into account. The molecular atmosphere, clouds, aerosols, background solar radiance and gaseous pollutants have been modelled following the recommendations of the US Air Force Geophysical Laboratory<sup>16-18</sup> (AFGL). These models are flexible to some extent, according to the natural variability of the atmosphere. This variability is important regarding the lidar performances. Therefore two cases of ozone loadings have been considered (rural and urban), along with three cases of aerosol loadings (background, low visibility and a case of high loading at the top of the PBL). The minimization of  $E_1$  and  $E_2$  has been adopted as a criterion for the wavelength choice. The interference of other absorbing species has not been considered here. The SO<sub>2</sub> interference has been investigated by Weitkamp et al.<sup>19</sup>.

Such a computer simulation certainly does not take into account all the critical issues of a field DIAL O<sub>3</sub> measurement, but it intends to point out some general principles of importance when making the choice of the operating wavelengths.

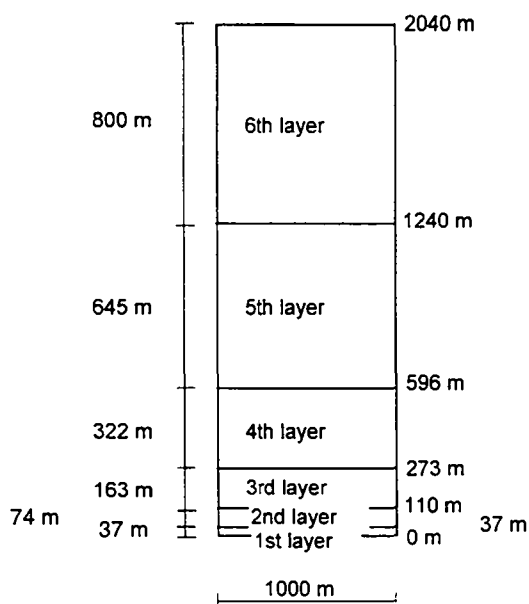


Fig. 1. Typical grid cell size of the CIT-EPFL photochemical airshed model.

### 6.2. Computer simulator of ozone DIAL

The simulated lidar instrumental parameters are gathered in table 1. The Stokes wavelength spectrum with either KrF excimer or quadrupled Nd:YAG pump laser is found in table 2. The feasibility of using D<sub>2</sub> and H<sub>2</sub> cells in series with KrF pump (generating the 302 nm beam in addition to the 248 nm shifted beams) has been assessed by Grant et al.<sup>20</sup>, and the (292,302) nm wavelength pair is considered in this study. S<sub>i</sub> refers to the i-th frequency downconverted beam.

<i>Fixed:</i>				
Telescope diameter		60 cm		
Telescope field-of-view		1 mrad		
Filter bandwidth		1 nm		
PMT quantum efficiency		20%		
Optical efficiency		30%		
Repetition rate	KrF: 50 Hz	YAG: 10 Hz		
Pulse energy		30 mJ		
<i>Unless otherwise specified:</i>				
Range resolution		100 m		
Number of shots		3000		
Probing angle rel. to zenith		70 deg		

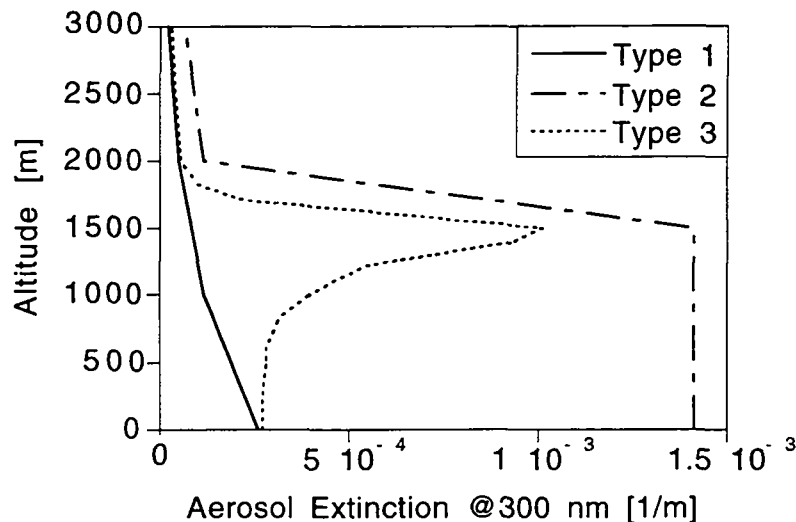
  

KrF		pump	248.4
	H <sub>2</sub>	S1	277.1
		S2	313.2
	D <sub>2</sub>	S1	268.4
S2		291.8	
Nd:YAG x 4		pump	266.0
	H <sub>2</sub>	S1	299.0
	D <sub>2</sub>	S1	289.0
		S2	316.2
KrF, cells in series		pump	248.4
	D <sub>2</sub>	S2(248.4)	291.8
	H <sub>2</sub>	S1(268.4)	302.1

**Table 1.** Lidar instrumental parameters considered in the ozone DIAL simulation

**Table 2.** Wavelength spectrum out of KrF- or Nd:YAGx4- pumped Raman cells, that is potentially useful for tropospheric O<sub>3</sub> DIAL.

The US76 molecular atmosphere (N<sub>2</sub> + O<sub>2</sub>) model profile is adopted<sup>16</sup>. Three types of aerosol extinction profile have been considered<sup>16</sup>: background (type 1), loaded (type 2) and an accumulation layer at top of the planetary boundary layer (PBL) (type 3), shown in fig. 2. Unless otherwise specified, the extinction-to-backscatter ratio has been taken equal to 40.



**Fig. 2.** Simulated aerosol profile extinction: background (type 1), loaded (type 2) and an accumulation layer at top of the planetary boundary layer (PBL) (type 3). The type 1, 2 and 3 aerosols correspond respectively to a visibility<sup>22</sup> of 25, 15 and 5 km.

Section 6: Numerical optimization of DIAL wavelengths

The ozone model is taken from the US76 model<sup>16</sup>, which corresponds to rural conditions (~30 ppb up to 4000 m). The situation of 100 ppb up to 4000 m was also considered as an urban case study. The simulated ozone profiles are shown in fig. 3.

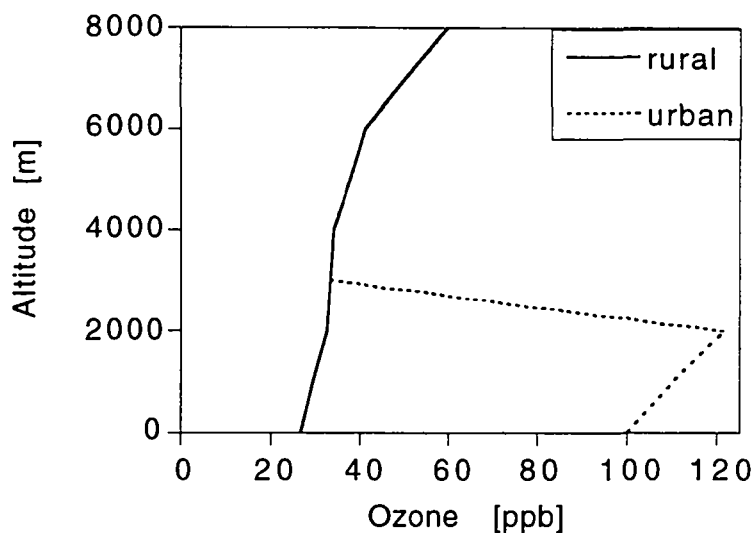
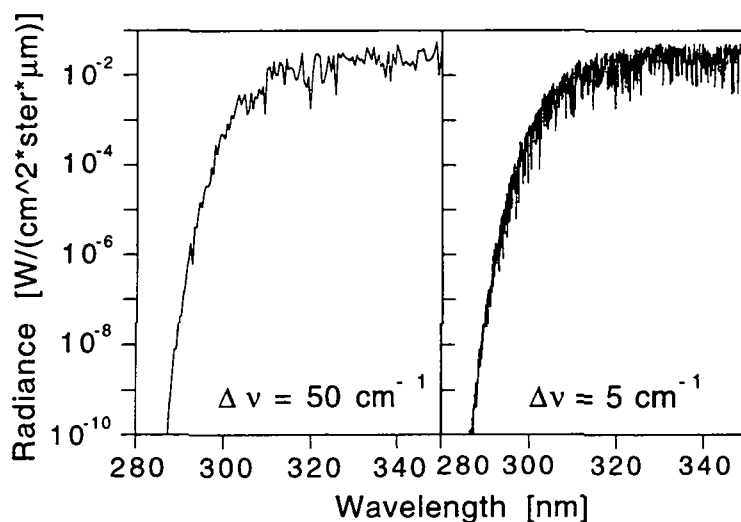


Fig. 3. Simulated ozone profiles.

The solar background radiance is taken from the Lowtran 7 model<sup>16</sup>; we considered unclouded daylight with an angle of 30° between the sun and the lidar path.

The solar background radiance has been calculated with the MODTRAN 3 code<sup>18</sup>, shown in fig. 4 to 8. The parameters varied are: the molecular atmosphere model (tropical, midlatitude summer, midlatitude winter, subarctic summer, subarctic winter, and US 76), the sun zenith angle ( $\theta_s$ ) for a given zenith line-of-sight angle ( $\theta_{los}$ ), and the azimuthal angle ( $\varphi$ ) for fixed  $\theta_s$  and  $\theta_{los}$  (respectively 35 and 60 degrees).

MODTRAN 3 has a maximum band resolution of 5 cm<sup>-1</sup> in the UV (1 cm<sup>-1</sup> above 500 nm). The spectral radiance has been calculated with two band resolutions (5 and 50 cm<sup>-1</sup>, fig. 4). The 50 cm<sup>-1</sup> resolution is seen to be sufficient for the needs of the lidar simulation.



**Fig. 4.** Spectral sky radiance calculated with MODTRAN 3, for a band resolution ( $\Delta v$ ) of 5 and  $50 \text{ cm}^{-1}$ . US 76 molecular atmosphere, zenith line-of-sight,  $5^\circ$  sun zenith angle.

The UV radiance cutoff show a weak dependence on the molecular atmosphere model (fig. 5). At the level of  $10^{-10} \text{ W}/(\text{cm}^2 \cdot \text{ster} \cdot \mu\text{m})$  radiance (8 orders-of-magnitude less than the rather constant value above 320 nm) there is one nm difference between all the models, except with the tropical one which is one more nm apart.

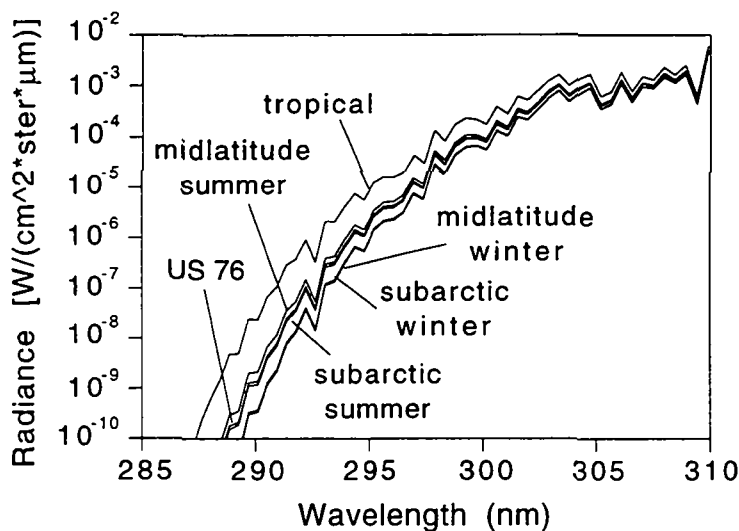


**Fig. 5.** Spectral sky radiance calculated with MODTRAN 3, for various molecular atmosphere models. Band resolution of  $50 \text{ cm}^{-1}$ , zenith line-of-sight,  $35^\circ$  sun zenith angle.

The radiance shows even less dependence on the azimuthal angle  $\phi$ , as shown in fig. 6. There is less than 0.5 nm difference between  $\phi=0^\circ$  and  $\phi=180^\circ$  at the level of  $10^{-10} \text{ W}/(\text{cm}^2 \cdot \text{ster} \cdot \mu\text{m})$  radiance.

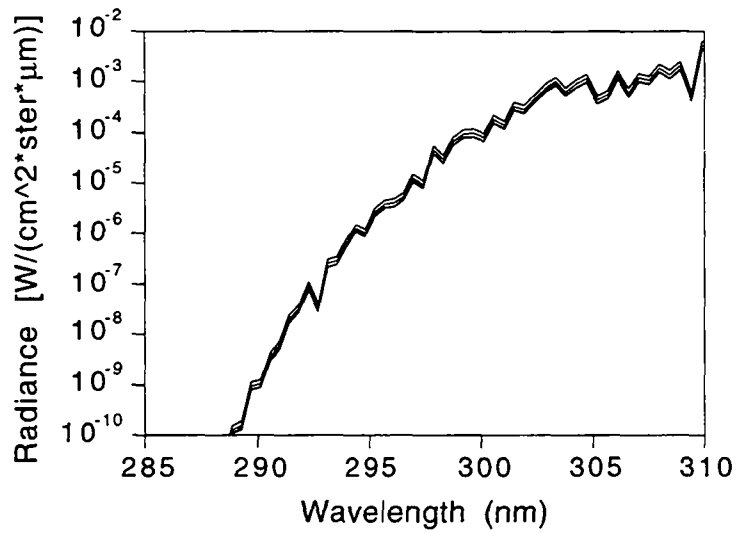


**Fig. 6.** Spectral sky radiance calculated with MODTRAN 3, for an azimuthal angle  $\phi$  of  $0^\circ$ ,  $45^\circ$ ,  $90^\circ$ ,  $135^\circ$ , and  $180^\circ$ . The curves corresponding to these values of  $\phi$  are almost undistinguishable on the plot. US 76 molecular atmosphere model, band resolution of  $50 \text{ cm}^{-1}$ ,  $60^\circ$  line-of-sight angle,  $35^\circ$  sun zenith angle.

The solar background radiance has its strongest parametric dependence with the sun zenith angle (and similarly with the line-of-sight zenith angle), as shown in fig. 7. The variation spans in a 8 nm interval between  $\theta_s=5^\circ$  and  $\theta_s=85^\circ$  at the  $10^{-10} \text{ W}/(\text{cm}^2 \cdot \text{ster} \cdot \mu\text{m})$  radiance level.

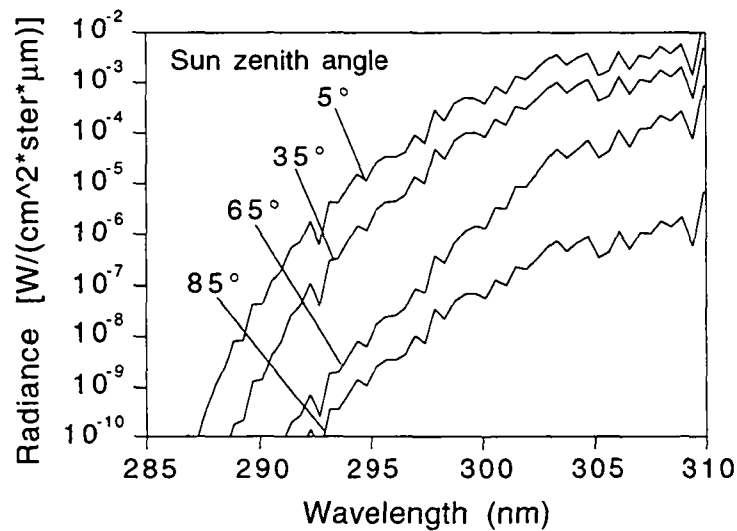


**Fig. 7.** Spectral sky radiance calculated with MODTRAN 3, for various sun zenith angles. US 76 molecular atmosphere model, band resolution of  $50 \text{ cm}^{-1}$ , zenith line-of-sight.

The model dependence on the sun zenith angle agrees well with experimental measurements<sup>3</sup> (fig. 8). The latter are performed by using the receiving section of a lidar system (transmitter turned off). For example there is less than 0.5 nm discrepancy between the model and the measurements at the  $10^{-10} \text{ W}/(\text{cm}^2 \cdot \text{ster} \cdot \mu\text{m})$  radiance level.

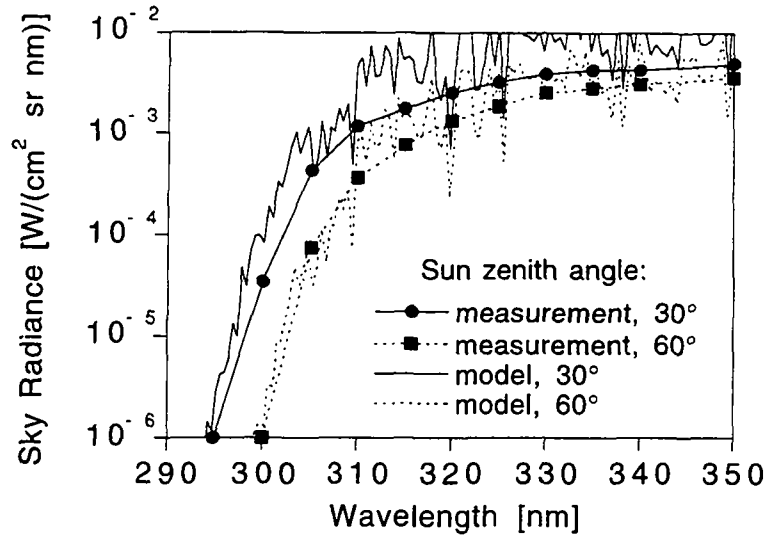


**Fig. 8.** Spectral sky radiance measured<sup>3</sup>, and calculated with MODTRAN 3. Zenith line-of-sight, midlatitude summer molecular atmosphere model. The measurements were taken in Japan. The radiances were not measured under the level of  $10^{-6}$  W/(cm<sup>2</sup>\*ster\* $\mu$ m) radiance.

In all the simulations that will follow, the sky background radiance is calculated assuming the US 76 molecular atmosphere model and a sun zenith angle of 30°. When the line-of-sight angle is different from zenith, the azimuthal angle  $\varphi$  is chosen to be 0°.

### 6.3. Theoretical background

#### 6.3.1 Random error $E_1$

The type 1 aerosol and the rural ozone profile (the latter is the most demanding relative to the instrumental sensitivity) were considered in the random error evaluation.

##### a) Two-wavelength DIAL

The absorbing specie concentration  $n$  is retrieved according to

$$n = \frac{1}{2 \Delta \sigma \Delta R} \ln \left( \frac{N_{22}^s N_{11}^s}{N_{12}^s N_{21}^s} \right) \quad (1)$$

with  $\Delta \sigma = \sigma(\lambda_1) - \sigma(\lambda_2)$  being the specie differential absorption cross section,  $N_{ij}^s$  the atmospheric backscattered photon counts at wavelength  $\lambda_i$  and at the discrete range  $R_j$ , and  $\Delta R$  the range bin.

The random error  $E_1$  is given by<sup>1</sup>

$$E_1 = \frac{1}{2 n \Delta \sigma \Delta R \sqrt{N}} \sqrt{\frac{2}{\text{SNR}_1^2} + \frac{2}{\text{SNR}_2^2}} \quad (2)$$

Section 6: Numerical optimization of DIAL wavelengths

with  $n$  being here the specie model profile,  $N$  is the number of laser shots,  $\text{SNR}_1$  and  $\text{SNR}_2$  are the signal-to-noise ratio at resp.  $\lambda_1$  and  $\lambda_2$ , at range  $R_j$ . Assuming Poisson shot-noise statistics, the signal-to-noise ratio is calculated as

$$\text{SNR} = \frac{N_s}{\sqrt{N_s + N_b + N_d}} \quad (3)$$

with  $N_s$ ,  $N_b$  and  $N_d$  being respectively the atmosphere backscattered photon counts, the sky radiance photon counts and the detector dark counts.

b) dual DIAL

The absorbing specie concentration is retrieved according to<sup>11</sup>

$$n = \frac{1}{2 \Delta\sigma \Delta R} \ln \left( \frac{N_{22}^s N_{32}^s N_{11}^s N_{41}^s}{N_{12}^s N_{42}^s N_{21}^s N_{31}^s} \right) \quad (4)$$

with  $\Delta\sigma = [\sigma(\lambda_1) - \sigma(\lambda_2)] - [\sigma(\lambda_3) - \sigma(\lambda_4)]$  being the specie differential absorption cross section,  $(\lambda_1, \lambda_2)$  is the first DIAL pair and  $(\lambda_3, \lambda_4)$  the second.

The random error  $E_1$  is given by

$$E_1 = \frac{1}{2 n \Delta\sigma \Delta R \sqrt{N}} \sqrt{\frac{2}{\text{SNR}_1^2} + \frac{2}{\text{SNR}_2^2} + \frac{2}{\text{SNR}_3^2} + \frac{2}{\text{SNR}_4^2}} \quad (5)$$

c) Water vapor Raman retrieval

The absorbing specie concentration is retrieved according to

$$\frac{n'(R)}{n_o(R)} = k \frac{\sigma_2^r}{\sigma_1^r} \frac{N_1^s(R)}{N_2^s(R)} \exp \left[ \int_0^R n(H) (\sigma_1 - \sigma_2) dH \right] \quad (6)$$

with  $n'$  and  $n_o$  resp. the water vapor and reference molecular ( $\text{N}_2$  or  $\text{O}_2$ ) concentration,  $\sigma_1^r$  and  $\sigma_2^r$  resp. the Raman backscattering cross section at  $\lambda_1$  and  $\lambda_2$ ,  $\lambda_1$  and  $\lambda_2$  corresponding resp. to the water vapor and reference molecular channel.  $n$  is here the ozone concentration, determined e.g. simultaneously by DIAL,  $\sigma_1$  and  $\sigma_2$  is resp. the ozone absorption cross section at  $\lambda_1$  and  $\lambda_2$ .  $k$  is a calibration constant (equal to the the ratio of the lidar calibration constant at  $\lambda_2$  and  $\lambda_1$ ).

The random error  $E'_1$  on the water vapor concentration is approximated as

$$E'_1 = \text{SNR}_1^2 + \text{SNR}_2^2 + 2(\Delta n \Delta\sigma \Delta R)^2 \quad (7)$$

with  $\Delta n = n E_1$  the random error standard deviation on the ozone profile, and  $\Delta\sigma = \sigma_1 - \sigma_2$ .

### 6.3.2 Systematic error $E_2$

The lidar simulator calculates the beam return signal with the lidar equation<sup>21,22</sup>, which is an average signal (i.e. without random fluctuations). The systematic error has been calculated by making the difference of the specie concentration retrieved from the lidar equation (equ. (1), (4), or (6)) with the specie concentration that is specified at the simulation input. It has been verified that  $E_2$  calculated this way equals the analytic formula for the the two-wavelength DIAL and the dual-DIAL cases. Namely

$$E_2 = \frac{1}{2 \Delta \sigma \Delta R} \ln \left( \frac{\beta_{12} \beta_{21}}{\beta_{22} \beta_{11}} \right) + \frac{1}{2 \Delta \sigma} (\alpha_{11} + \alpha_{12} - \alpha_{21} - \alpha_{22}) \quad (8)$$

for the two-wavelength DIAL case.  $\beta$  and  $\alpha$  denote respectively the aerosol backscattering and extinction coefficient, and follow the same subscript notation as  $N^s$ . For the dual-DIAL case  $E_2$  is given by

$$E_2 = \frac{1}{2 \Delta \sigma \Delta R} \ln \left( \frac{\beta_{12} \beta_{42} \beta_{21} \beta_{31}}{\beta_{22} \beta_{32} \beta_{11} \beta_{41}} \right) + \frac{1}{2 \Delta \sigma} \{ (\alpha_{11} + \alpha_{12} - \alpha_{21} - \alpha_{22}) - (\alpha_{31} + \alpha_{32} - \alpha_{41} - \alpha_{42}) \} \quad (9)$$

For the DIAL Raman case, the Raman return signal is differentiated to yield

$$\frac{dS'}{dR} = \frac{d\beta_r}{dR} + \frac{d\beta_m}{dR} - 2\alpha_a - 2\alpha_m - 2\alpha_{O_3} \quad (10)$$

where  $S' = \ln(R^2 N^s)$ ;  $\beta_r$  and  $\beta_m$  denote respectively the Raman and molecular ( $N_2 + O_2$ ) backscattering cross section,  $\alpha_a$ ,  $\alpha_m$  and  $\alpha_{O_3}$  denote resp. the aerosol, molecular and ozone extinction coefficient. In equ. (8) and (9), the backscattering and extinction coefficients relate to the aerosol, and no subscript was written for simplicity. The Angström parameter  $p$  is defined as the best fit of the relation  $k / \lambda^p$ ,  $k$  a constant, to the extinction coefficient wavelength dependence. When the extinction coefficient is assumed to satisfy such a relation, the two Raman returns of the Raman DIAL define each an equation of type (10), and hence there are three unknowns ( $\alpha_{O_3}$ ,  $\alpha_a$  at one wavelength, and  $p$ ) for two equations. The easiest parameter to guess is generally the Angström coefficient. In this process, the molecular concentration is assumed to be known from models or independent measurements.

In equ. (8) and (9),  $E_2$  is assumed to have its origin only in the aerosol interference. The type 3 aerosol is considered in the systematic error study (which is the worst concerning the aerosol interference due to the strong vertical gradient).



### 6.4. Two-wavelength ozone DIAL

#### 6.4.1 Measurement range (random error)

The random error ( $E_1$ ) is an increasing function of the range<sup>1,22</sup>. The “measurement range”  $\hat{R}$  corresponding to a given level of  $E_1$ , noted  $\hat{E}_1$ , is defined as the range which yields  $\hat{E}_1$ . For ranges below  $\hat{R}$ ;  $E_1$  is hence below  $\hat{E}_1$ . The precision required on the ozone profile is estimated as 5 ppb for climatic and trend studies, and 1-2 ppb for pollution and transport studies<sup>4</sup>. Considering background ozone concentrations of ca. 30 ppb, 5 ppb corresponds to 15% error, and this level was chosen for the simulations which follow. The case of 1 ppb precision has been outlined in ref. [22] and [23].

The dependence of the measurement range with respect to the probing angle is shown in fig. 9. It is seen that the wavelength choice weakly depends on the probing angle (the curves do not intersect).

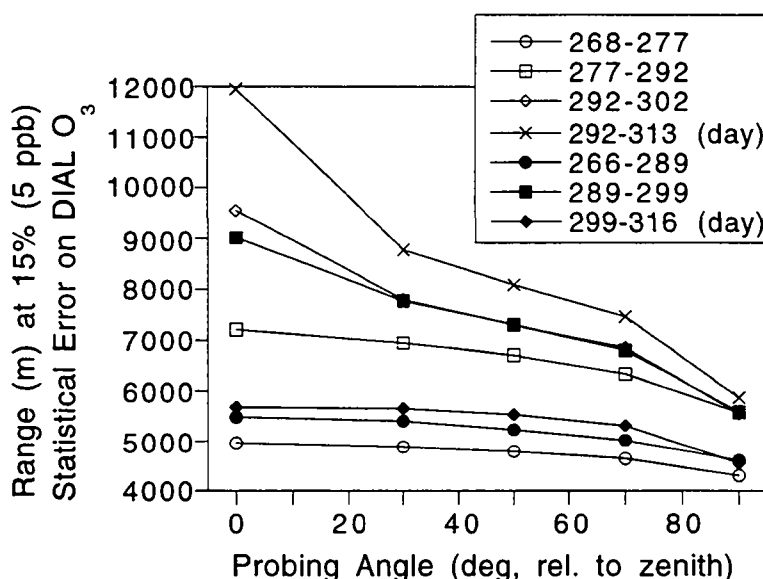


**Fig. 9.** Measurement range as a function of the probing angle relative to zenith. Type 1 aerosol, rural ozone profile, 100 m range bin, 3000 shots average.

The wavelength choice depends on the sampling time and the range bin, as shown in fig. 10 and 11 (the curves intersect). In the following, “shorter wavelengths” refer to the KrF pairs (268,277), (277,292), and the Nd:YAG pair (266,289), while “longer wavelengths” refer to the KrF pairs (292,302), (292,313) and the Nd:YAG pairs (289,299), (299,316). It is seen that the shorter wavelengths are superior for a small range bin and a short sampling time ( $\hat{R}$  higher than the longer wavelengths). Conversely the longer wavelengths are superior for large range bin and large sampling time. The wavelength pairs (292,313) and (299,316) are not shown on these figures, but were observed to be consistent with the (292,302) and (289,299) pairs.

Section 6: Numerical optimization of DIAL wavelengths

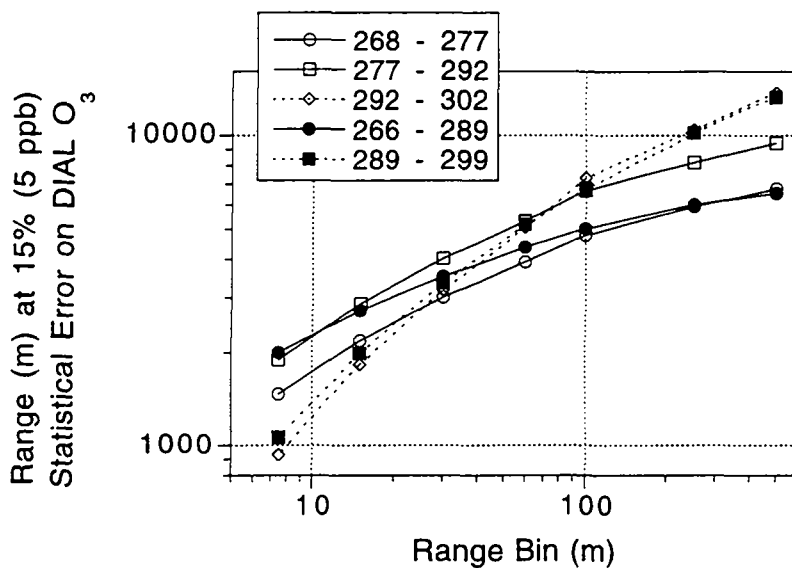


Fig. 10. Measurement range as a function of the range bin. Type 1 aerosol, rural ozone profile, 70° probing angle relative to zenith, 3000 shots average.

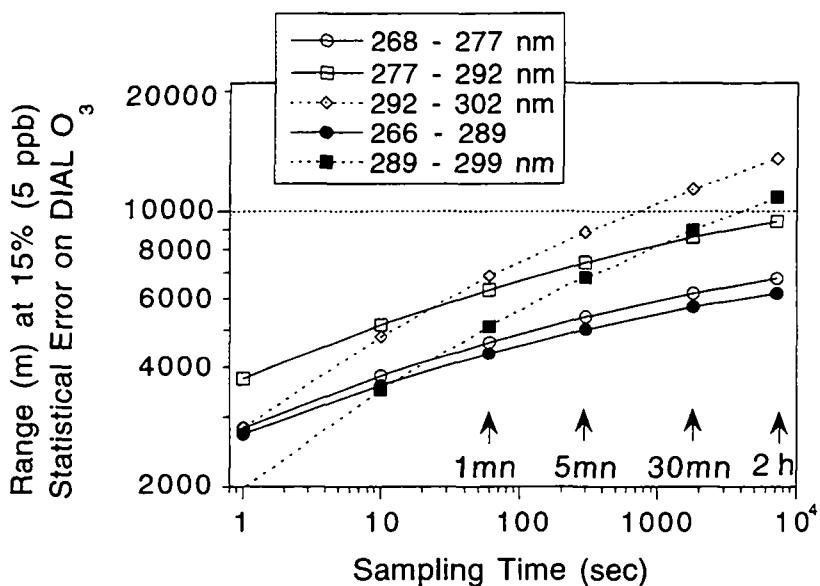


Fig. 11. Measurement range as a function of the sampling time. Type 1 aerosol, rural ozone profile, 70° probing angle relative to zenith, 100 m range bin. The repetition rate is taken as 50 and 10 Hz for the KrF and Nd:YAG system respectively.

Section 6: Numerical optimization of DIAL wavelengths

All wavelength pairs show a strong dependence on the aerosol loading (fig. 12). The shorter wavelengths are more sensitive to the ozone loading than the longer ones. This fact is explained by the bigger ozone differential absorption cross section of the shorter wavelengths (table 3).

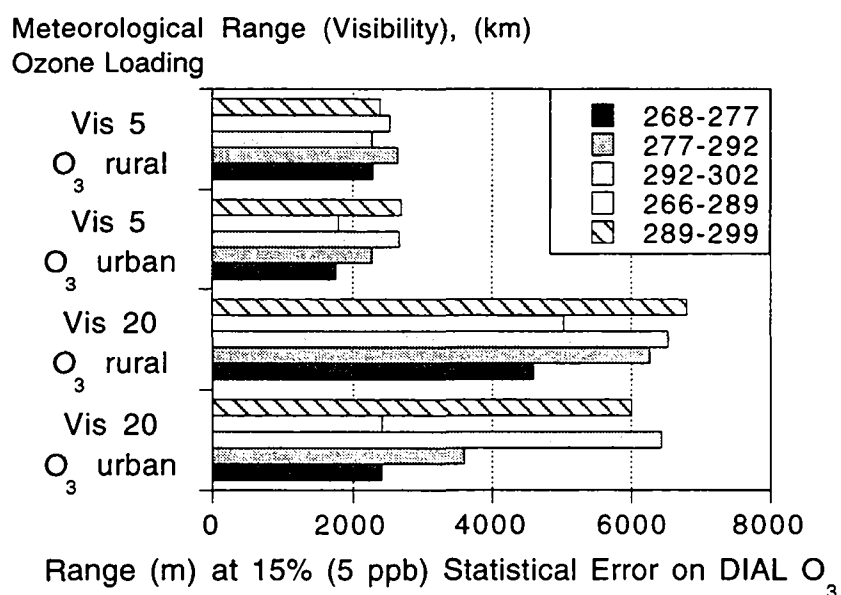


Fig. 12. Measurement range as a function of the aerosol and ozone loading (cf. fig. 2 and 3). 70° probing angle relative to zenith, 100 m range bin, 3000 shots average.

Laser	Wavelength pair (nm)	$\Delta\sigma$ at 298 K ( $10^{-20}$ cm <sup>2</sup> /mol.)
KrF	<i>(268,277)</i>	366
	<i>(277,292)</i>	398
	(292,302)	80.4
	(292,313)	104
Nd:YAG	<i>(266,289)</i>	790
	<i>(289,299)</i>	113
	<i>(299,316)</i>	40.7

Table 3. Ozone differential absorption cross section  $\Delta\sigma$  for the KrF and Nd:YAG Raman-shifted wavelength pairs in H<sub>2</sub> and D<sub>2</sub>. The wavelengths written in italic are the so-called “shorter wavelengths” (see text), while the other ones are the so-called “longer wavelengths”.

## Section 6: Numerical optimization of DIAL wavelengths

A horizontal probing has been simulated (fig. 13). In order to comply to the EPFL-CIT grid (fig. 1), a range bin of 1 km was considered. Configuring the DIAL instrument with such a range bin is probably not the best approach, and a smaller range bin with subsequent summation and smoothing between the bins would yield a better discretization of the derivative (which enters the DIAL ozone retrieval). The same conclusions as for fig. 12 apply for fig. 13, since both figures exhibit the same patterns.

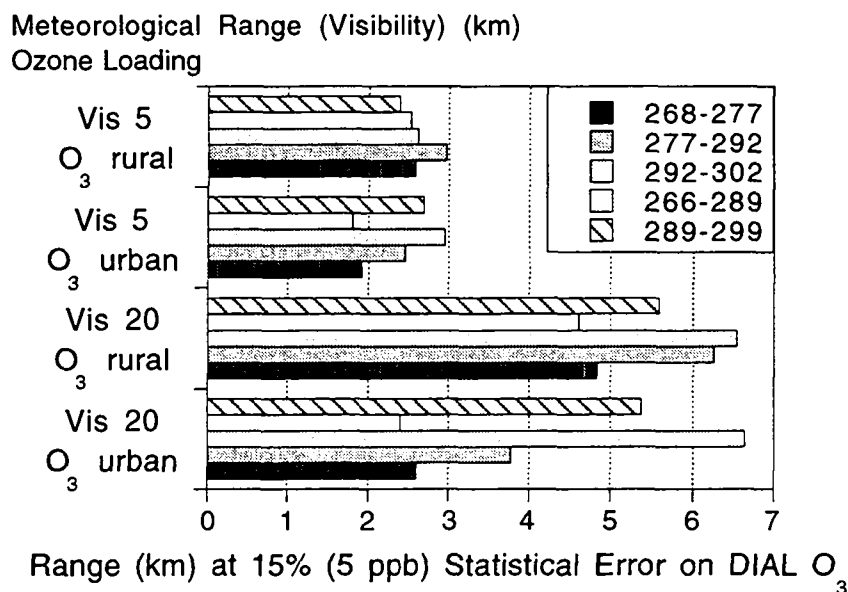


**Fig. 13.** Measurement range as a function of the aerosol and ozone loading (cf. fig. 2 and 3). Horizontal probing, 1 km range bin, 3000 shots average.

### 6.4.2 Aerosol interference (systematic error $E_2$ )

The Angström parameter ( $p$ ) and the extinction-to-backscatter ratio ( $s$ ) of the aerosol of type 3 (fig. 2) have been varied.

Fig. 14 and 15 show that the shorter wavelengths (§6.4.1) exhibit a lower aerosol interference than the longer wavelengths. This is due to the higher ozone differential absorption cross section of the shorter wavelengths (table 3 and equ. (8)). When uncorrected, the KrF pairs (268,277) and (277,292) yield  $E_2$  of the order of 30-50%, and the Nd:YAG pair (266,289) an  $E_2$  of the order of 20-40%.

The shorter wavelengths remain clearly superior to the longer ones when correcting the aerosol interference with the Klett-Browell scheme<sup>5,6</sup> (fig. 16). After correction, the pairs (268,277), (277,292) and (266,289) yield a systematic error of the order of 5-15%, which is a factor 2-3 improvement with respect to the uncorrected  $E_2$ .

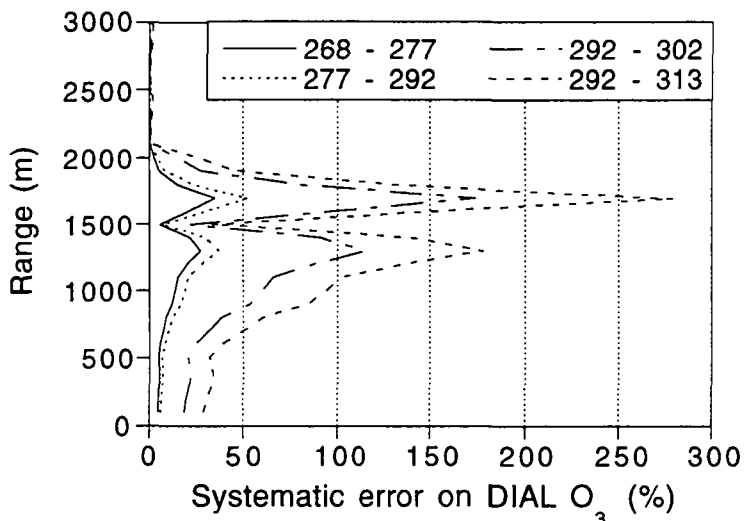


Fig. 14. Aerosol interference (systematic error) for the KrF Raman shifted wavelengths in H<sub>2</sub> and D<sub>2</sub>. Type 3 aerosol with Angström parameter  $p=1$  and extinction-to-backscatter ratio  $s=40$  sr, 100 m range bin, zenith probing.

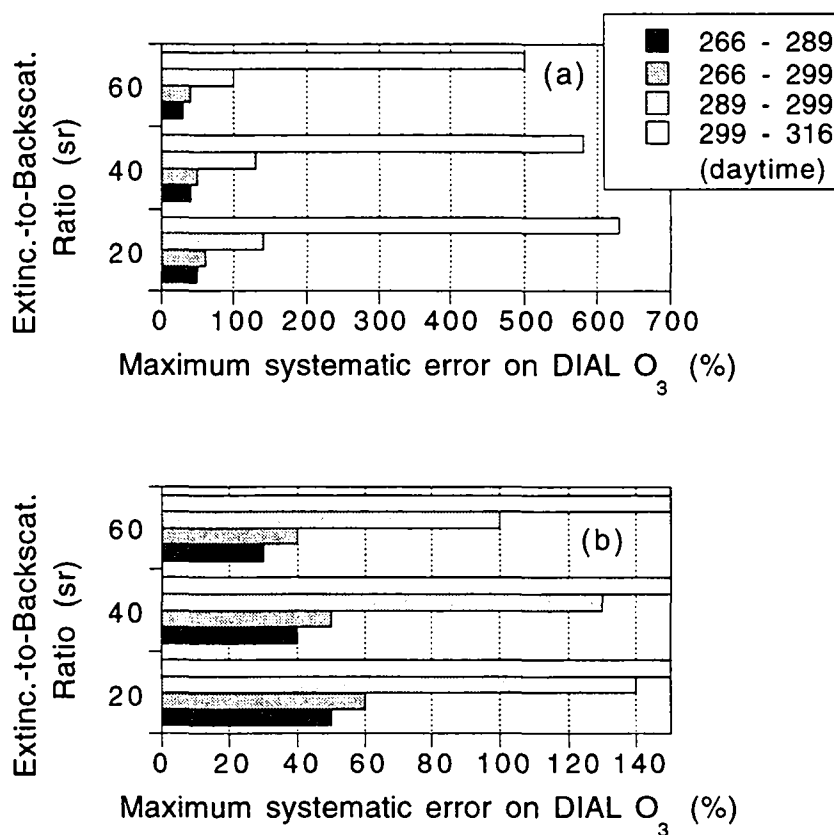
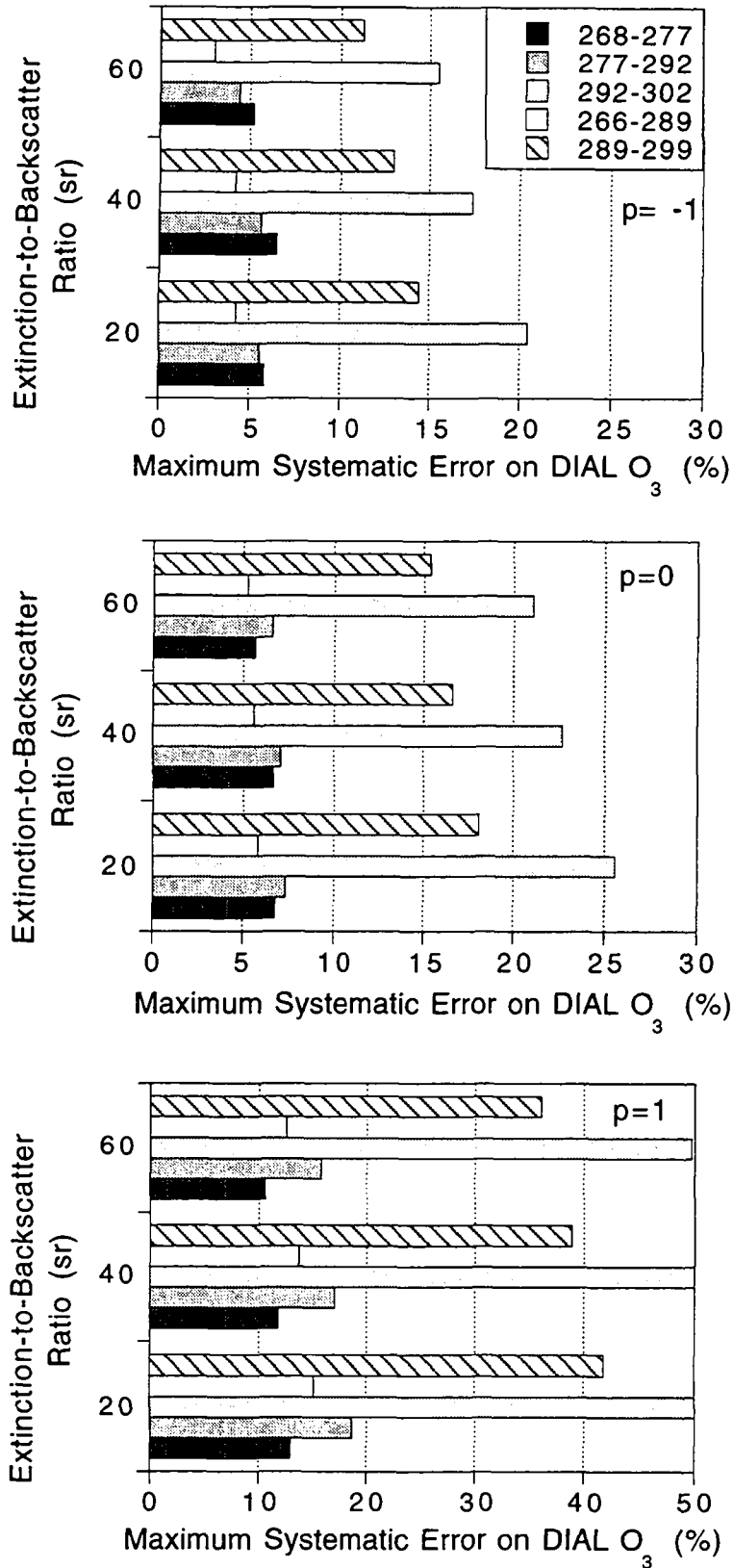


Fig. 15. Aerosol interference (systematic error) for the Nd:YAG Raman shifted wavelengths in H<sub>2</sub> and D<sub>2</sub>. The maximum error on the profile (0 - 3000 m) is plotted. Type 3 aerosol with Angström parameter  $p=1$ , 100 m range bin, zenith probing. (b) is a zoom of (a).

Section 6: Numerical optimization of DIAL wavelengths



**Fig. 16.** Aerosol interference (systematic error), as a function of the Angström parameter  $p$ . The maximum error on the profile (0 - 3000 m) is plotted. Type 3 aerosol, 100 m range bin, zenith probing. (b) is an enlargement of (a). 30% error has been added or subtracted to the Angström coefficient and the the extinction-to-backscatter ratio.

### 6.5 Dual-DIAL

The dual-DIAL scheme reduces the aerosol interference efficiently when first the wavelength separations  $\Delta\lambda = \lambda_2 - \lambda_1$  and  $\Delta\lambda' = \lambda_4 - \lambda_3$  of the two DIAL pairs  $(\lambda_1, \lambda_2)$  and  $(\lambda_3, \lambda_4)$  are approximately equal, and second when the separation between the two pairs  $(\lambda_3 - \lambda_2)$ , for  $\lambda_2 > \lambda_1$  and  $\lambda_4 > \lambda_3$  is small (equ. (9)). This principle is verified in fig. 17: the pairs that minimize  $E_2$  are (268,292)-(292,313), (266,289)-(299,316) and (266,289)-(289,316), for which  $\{\Delta\lambda, \Delta\lambda'\}$  equals respectively  $\{24,21\}$ ,  $\{23,17\}$  and  $\{23,27\}$  nm. The pairs which show an  $E_2$  clearly higher (ca. two times) are (266,299)-(299,316), (266,289)-(289,299) and (277,292)-(292,302), for which  $\{\Delta\lambda, \Delta\lambda'\}$  equals respectively  $\{33,17\}$ ,  $\{23,10\}$  and  $\{15,10\}$  nm. The (268,292)-(292,313) shows the least aerosol sensitivity with an  $E_2$  of the order of 10%. The (266,289)-(299,316) and (266,289)-(289,316) pairs are characterized by an  $E_2$  of the order of 10-20%. Further reduction in the aerosol interference is expected when applying the Klett-Browell correction scheme.

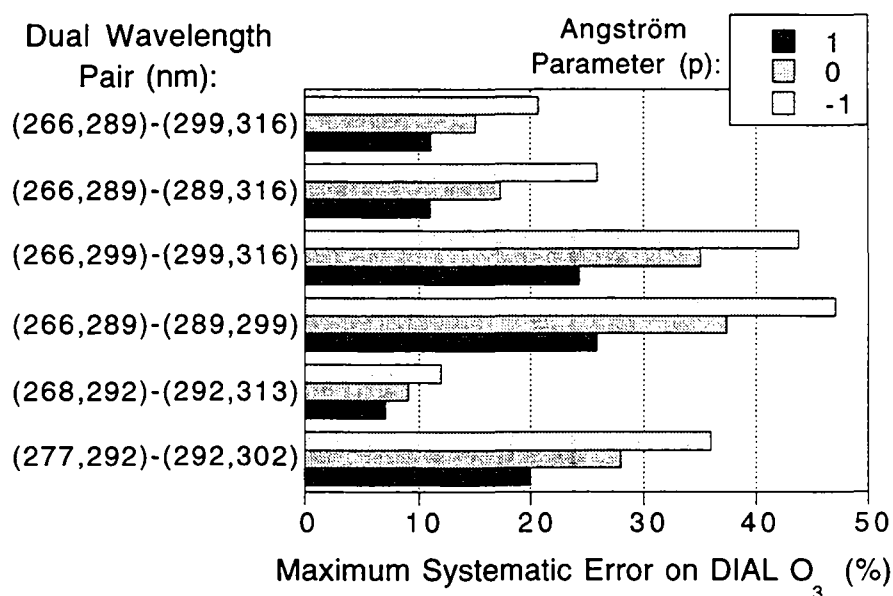


**Fig. 17.** Aerosol interference (systematic error) of the dual-DIAL scheme, as a function of the Angström parameter  $p$ . The maximum error on the profile (0 - 3000 m) is plotted. The wavelength pairs corresponding to other combinations of the KrF or Nd:YAG Raman-shifted wavelengths yield a higher error than those presented in this graph. Type 3 aerosol with extinction-to-backscatter ratio equal to 40 sr, 100 m range bin, zenith probing.

Section 6: Numerical optimization of DIAL wavelengths

Fig. 18 shows that it is feasible to reach the top of the PBL with the dual-DIAL scheme: a measurement range ( $\hat{R}$ ) higher than 2000 m is found for all the wavelength combinations in urban conditions of ozone loading.  $\hat{R}$  is weakly sensitive to the wavelength, which is explained by the similar differential absorption cross section ( $\Delta\sigma$ ) for all the wavelength combinations (table 4). Concerning  $\Delta\sigma$ , the dual-DIAL scheme is similar to the two-wavelength DIAL (table 4 and the shorter wavelengths of table 3), but the measurement range of the former depends on the signal-to-noise ratio of three or four channels (depending on the type of wavelength combination) instead of two for the latter.

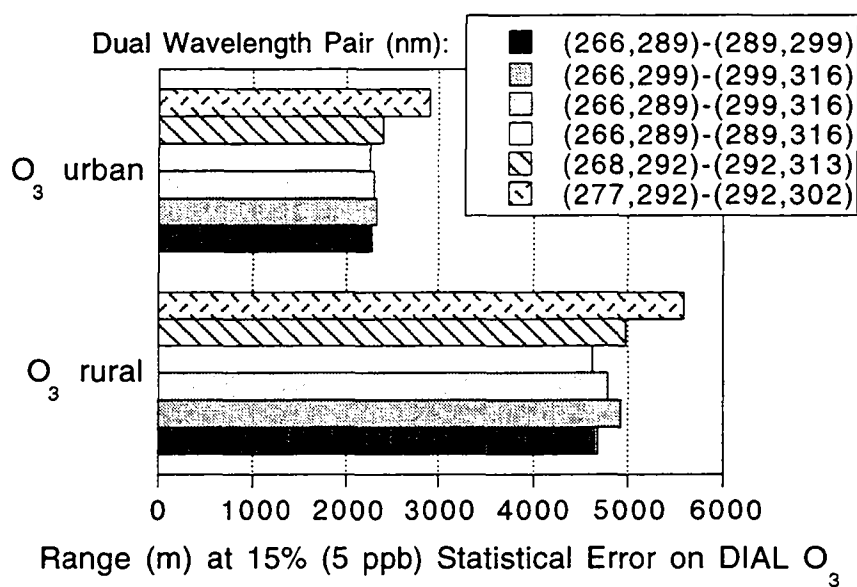


**Fig. 18.** Measurement range of the dual-DIAL scheme, as a function of the ozone loading, for the wavelength pairs displayed in fig. 17. Type 3 aerosol (15 km visibility), 100 m range bin, zenith probing, 5 min. measurement time (which corresponds to 3000 shots for the Nd:YAG and 15'000 shots for the KrF).

Laser	Dual wavelength pair (nm)	$\Delta\sigma$ at 298 K ( $10^{-20}$ cm <sup>2</sup> /mol.)
KrF	(268,292) - (292,313)	660
	(277,292) - (292,302)	318
Nd:YAG	(266,289) - (299,316)	749
	(266,289) - (289,316)	636
	(266,299) - (299,316)	862
	(266,289) - (289,299)	677

**Table 4.** Dual-DIAL ozone differential absorption cross section  $\Delta\sigma$ , equ. (4), for the KrF and Nd:YAG Raman-shifted wavelength pairs in H<sub>2</sub> and D<sub>2</sub>.



## 6.6 Raman DIAL

The Raman shift of O<sub>2</sub> and N<sub>2</sub> equals respectively to 1552 and 2332 cm<sup>-1</sup>. The O<sub>2</sub> and N<sub>2</sub> returns from 248 nm pumping (resp. 257.9 and 263.2 nm) are too much absorbed for an ozone retrieval to the top of the PBL. A pumping wavelength between 265 and 280 nm is preferable since the O<sub>2</sub> and N<sub>2</sub> Raman returns are less absorbed, yet still located in the solar-blind spectrum (< 300 nm). Table 5 summarizes the wavelength configurations which were tested.

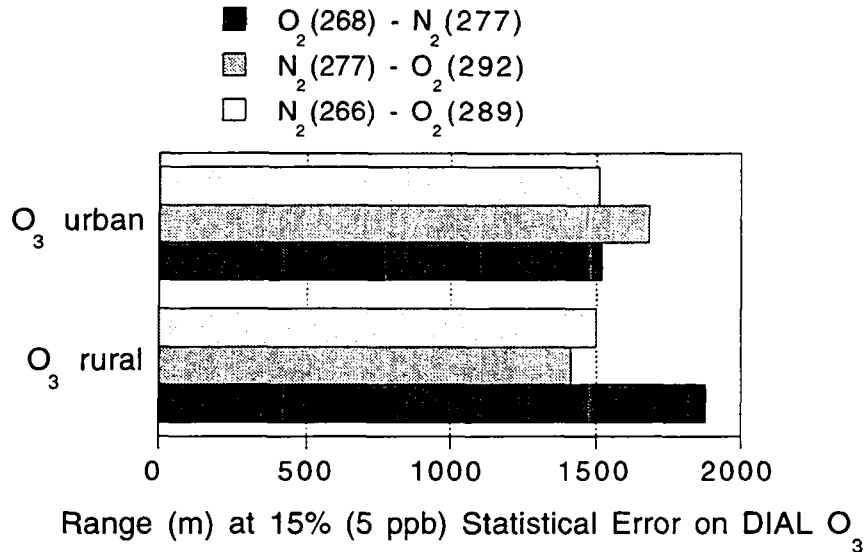
Pump 1			Pump 2			$\Delta\sigma$ at 298 K (10 <sup>-20</sup> cm <sup>2</sup> /mol.)
Wavelength (nm)	Pulse energy (mJ)	Raman wavelength (nm)	Wavelength (nm)	Pulse energy (mJ)	Raman wavelength (nm)	
268	30	O2 - 280	277	30	N2 - 296	699
277	30	N2 - 296	292	30	O2 - 306	448
266	100	O2 - 277	266	100	N2 - 283	207
266	30 or 100	N2 - 283	289	30	O2 - 302	1062
266	100	O2 - 277	289	30	N2 - 310	1289

**Table 4.** The Raman DIAL wavelength combinations which were simulated. The ozone differential absorption cross section is given by  $\Delta\sigma = (\sigma_1^p - \sigma_2^p) + (\sigma_1^r - \sigma_2^r)$ , where the superscripts “p” and “r” refer respectively to the pump and the Raman return.

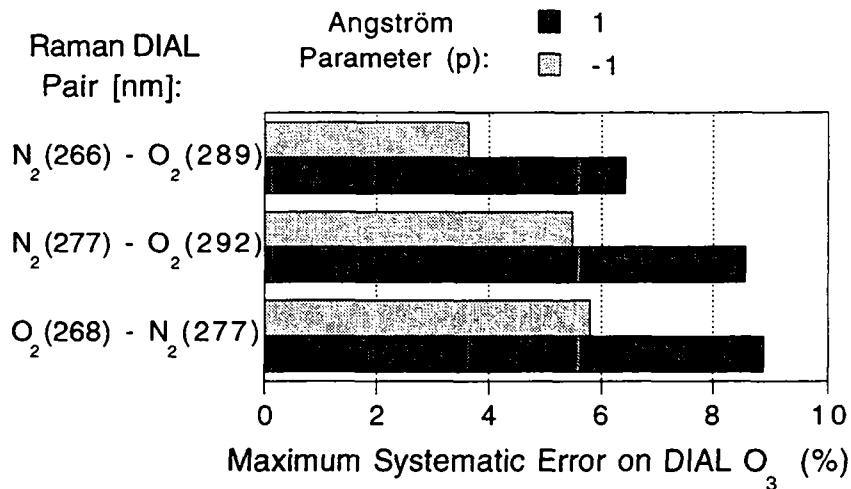
A configuration comprising only one pump laser is considered first, which yields ca. 30 mJ in the first or second Stokes and in the residual 266 nm. For 5 min. sampling time and 100 m range bin, the measurement range allows an ozone profiling up to the top of the PBL for a KrF or Nd:YAG system, fig. 19 ( $\hat{R} \approx 1500$  m). The systematic error, which results from the uncertainty on the guessed Angström coefficient, is below 10 % (fig. 20).

Fig. 21 shows the configuration comprising two Nd:YAG lasers, one which pumps a Raman cell (yielding an energy of ca. 30 mJ in the first Stokes), and the other one which is sent directly in the atmosphere (with an energy of ca. 100 mJ). The range bin in this case is set to 30 m, which is suitable for short range studies (e.g. the first cells of the airshed modelling grid, fig. 1). The case of the 266 nm beam pumping both the O<sub>2</sub> and N<sub>2</sub> Raman returns is seen to yield a measurement range ca. two times less than for the case in which one Raman return is pumped by a Stokes beam. This fact is explained by the discrepancy in the differential absorption cross section (factor of 5-6 between the two cases, table 4), which overcomes the discrepancy in pump pulse energy. A measurement range of 500 - 1000 m is achieved with the “case 2” configuration. This capability seems interesting as a short-range complement to an elastic backscatter instrument, the latter covering the longer range.

Section 6: Numerical optimization of DIAL wavelengths



**Fig. 19.** Measurement range of the Raman DIAL scheme. Type 3 aerosol (15 km visibility), 100 m range bin, zenith probing, 5 min. measurement time (which corresponds to 3000 shots for the Nd:YAG and 15'000 shots for the KrF), 30 mJ at the Nd:YAG fourth harmonic (266 nm). “O<sub>2</sub>(λ)” and “N<sub>2</sub>(λ)” refer respectively to the O<sub>2</sub> and N<sub>2</sub> Raman return of the pumping beam of wavelength λ.



**Fig. 20.** Aerosol interference (systematic error) of the Raman DIAL scheme, as a function of the Angström parameter *p*. The maximum error on the profile (0 - 3000 m) is plotted. Note that for *p*=0 the systematic error cancels. Type 3 aerosol with extinction-to-backscatter ratio equal to 40 sr, 100 m range bin, zenith probing. “O<sub>2</sub>(λ)” and “N<sub>2</sub>(λ)” refer respectively to the O<sub>2</sub> and N<sub>2</sub> Raman return of the pumping beam of wavelength λ.

Section 6: Numerical optimization of DIAL wavelengths

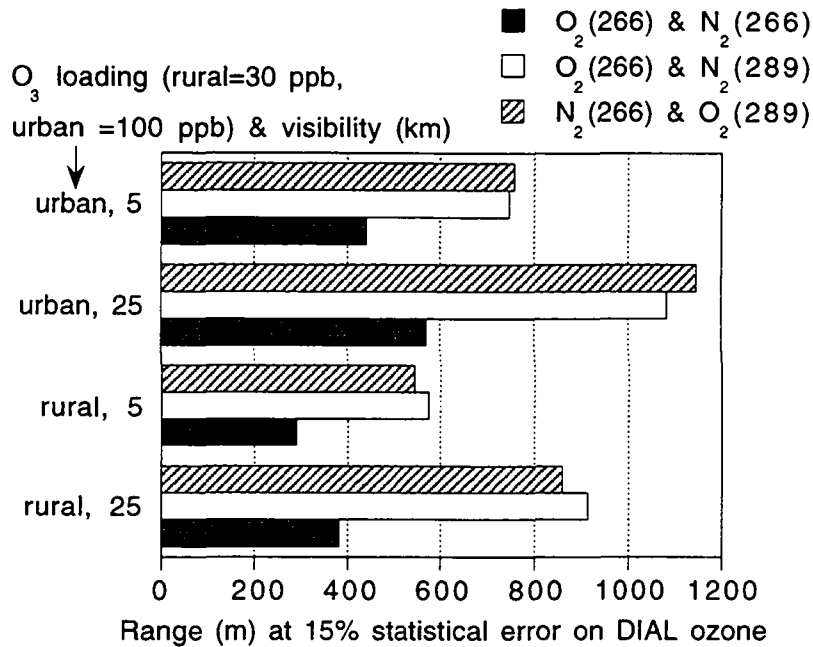


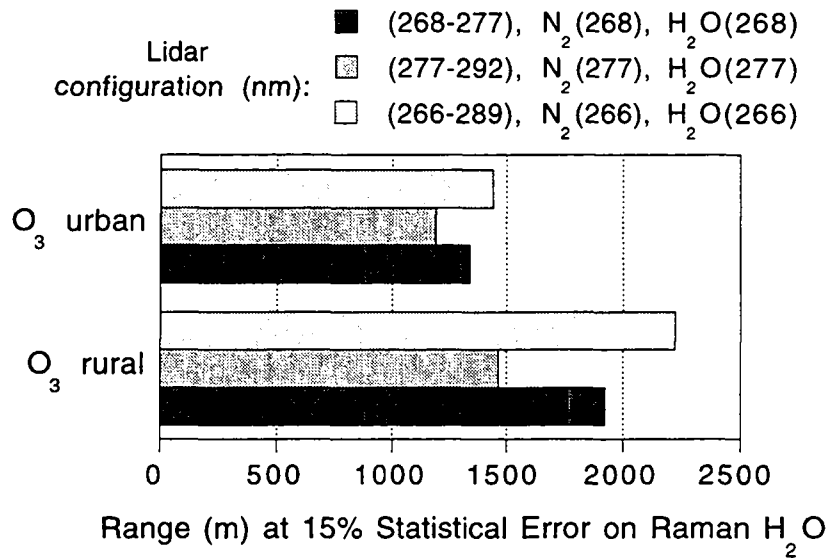
**Fig. 21.** Measurement range of the Raman DIAL scheme, Nd:YAG system. Type 3 aerosol (15 km visibility), 30 m range bin, zenith probing, 5 min. measurement time (which corresponds to 3000 shots), 100 mJ at the Nd:YAG fourth harmonic (266 nm). “O<sub>2</sub>(λ)” and “N<sub>2</sub>(λ)” refer respectively to the O<sub>2</sub> and N<sub>2</sub> Raman return of the pumping beam of wavelength λ.

**6.7 Simultaneous ozone and water vapor profiling**

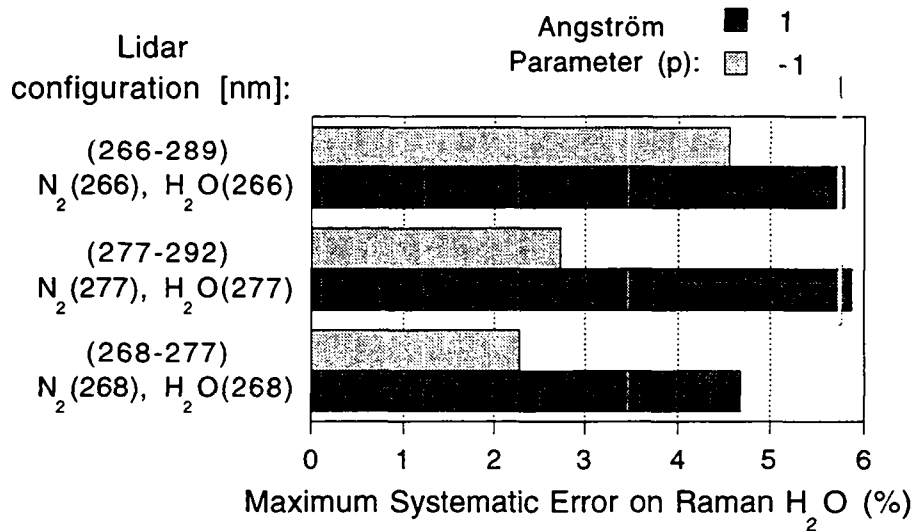
The instrument simulated is a two-wavelength ozone DIAL (elastic returns) which is added by one N<sub>2</sub> Raman channel, and one water vapor Raman channel. The N<sub>2</sub> channel serves to the calculation of the H<sub>2</sub>O mixing ratio, and possibly also for the aerosol correction of the ozone DIAL. Three configurations of ozone DIAL have been considered: the (268,277) and (277,292) nm pairs of the KrF system, and the (266,289) pair of the Nd:YAG system. The Raman returns are set to be pumped by the lower wavelength. The Raman shift of water vapor equals to 3652 cm<sup>-1</sup>, so that the return is in the solar-blind spectrum for 266 and 268 nm pumping (return at 295 and 297 nm resp.), and out of it for the 277 nm pumping (return at 308 nm).

Fig. 22 shows that ca. 1500 m range is achievable for a zenith probing, 100 m range bin, and 5 min. sampling time, which allows to reach the top of the PBL in some cases. Fig. 23 shows the peak systematic error on the Raman H<sub>2</sub>O. The Klett-Browell aerosol correction scheme<sup>5,6</sup>, with 30% error added on the Angström coefficient and the extinction-to-backscatter ratio, is applied to the DIAL ozone retrieval which is used to correct the ozone absorption at the Raman wavelength, equ. (10). It is the error in this correction which constitutes the systematic bias in the Raman H<sub>2</sub>O, plotted in fig. 23. It is seen that this correction is accurate on the percent level. Finally, fig. 22 and 23 show that both the KrF and Nd:YAG systems demonstrate equal performances.

Section 6: Numerical optimization of DIAL wavelengths



**Fig. 22.** Measurement range of the Raman water vapor retrieval. The ozone profile retrieved with an ozone DIAL (wavelength pair indicated in brackets) is used to correct for the ozone absorption of the Raman return. “N<sub>2</sub>(λ)” and “H<sub>2</sub>O(λ)” refer respectively to the N<sub>2</sub> and H<sub>2</sub>O Raman return of the pumping beam of wavelength λ, which is set as the lower wavelength of the DIAL pair. Type 3 aerosol (15 km visibility), 100 m range bin, zenith probing, 5 min. measurement time (which corresponds to 3000 shots for the Nd:YAG and 15’000 shots for the KrF), 30 mJ pulse energy in the emitted beams.



**Fig. 23.** Aerosol interference (systematic error) of the Raman water vapor retrieval, as a function of the Angström parameter  $p$ . The maximum error on the profile (0 - 3000 m) is plotted. The ozone profile retrieved with an ozone DIAL (wavelength pair indicated in brackets) is used to correct for the ozone absorption of the Raman return. The Klett-Browell aerosol correction scheme, with 30% error added on  $p$  and the extinction-to-backscatter ratio, is applied to the DIAL retrieval of ozone. “N<sub>2</sub>(λ)” and “H<sub>2</sub>O(λ)” refer respectively to the N<sub>2</sub> and H<sub>2</sub>O Raman return of the pumping beam of wavelength λ, which is set as the lower wavelength of the DIAL pair. Type 3 aerosol with extinction-to-backscatter ratio equal to 40 sr, 100 m range bin, zenith probing.

## 6.8 Conclusion

The airshed pollution modelling requires that the ozone measurement can be performed under variable conditions of probing angle, range bin, ozone and aerosol loading. The usual two-wavelength setup does not allow to comply to these requirements. The computer simulation points out a number of instrumental configurations which yield such a performance flexibility.

With three emitted wavelengths, the short wavelength pair is used for short range measurements (and small range bins), high sensitivity on the retrieved ozone, and in case of high aerosol loading (aerosol interference). The long wavelength pair is used to reach longer ranges. The KrF wavelengths (268,277,292) nm and Nd:YAG wavelengths (266,289,299) represent possible configurations. The longer wavelengths, KrF-313 and Nd:YAG-316 nm, offer good potentialities but are affected by the sky radiance, which is quite variable with respect to the sun zenith angle and the probing angle. The three channels allow to use the dual DIAL scheme which can be accurate in case of high aerosol interference. The aerosol sensitivity of this scheme depends critically on the wavelength configuration. The wavelength sets KrF-(268,292,313) and Nd:YAG-(266,289,316) nm perform well ( $E_2 < 20\%$ ). The wavelength sets KrF-(277,292,302) and Nd:YAG-(266,289,299) nm show worse performance ( $E_2 < 40\%$ ).

The addition of two ( $O_2$  or  $N_2$ ) Raman channels to a two-wavelength configuration is another solution to provide the necessary flexibility. The Raman DIAL retrieval of ozone is performed in case of high aerosol interference. The weaker Raman returns with respect to the elastically scattered returns lower the signal dynamic range and allow for short range measurements. Possible configurations are: KrF-(268,277) nm with the  $O_2$  Raman return of 268 and the  $N_2$  Raman return of 277; KrF-(277,292) nm with  $N_2(277)$  and  $O_2(292)$ ; Nd:YAG-(266,289) nm with  $N_2(266)$  and  $O_2(289)$ .

The configuration of a  $H_2O$  and a  $N_2$  (or  $O_2$ , although not tested) channel in addition to a two-wavelength ozone DIAL is interesting in two respects. First it allows the simultaneous profiling of the water vapor and ozone up to the top of the PBL. Second, the  $N_2$  Raman channel improves the aerosol correction of the ozone DIAL. Possible configurations are: KrF-(268,277) nm with the  $N_2$  and  $H_2O$  Raman return of 268; KrF-(277,292) nm with  $N_2(277)$  and  $H_2O(277)$ ; Nd:YAG-(266,289) nm with  $N_2(266)$  and  $H_2O(266)$ .

The most complete and efficient configuration consists in three emitted wavelengths, and the  $O_2$ ,  $N_2$ ,  $H_2O$  Raman channels. The three elastic returns yield the flexibility in range and atmospheric condition (ozone loading and visibility). Alternatively, the  $N_2$  and  $O_2$  Raman returns lower the signal dynamic for the short range. In case of high aerosol interference, the dual-DIAL and Raman DIAL schemes are used, which may show complementary to each other depending on the conditions. The simultaneous ozone and water vapor profiling can be performed. A number of wavelength combinations can be drawn, out of which the following were tested and shown to be feasible: KrF-(268,277,292) nm with the  $N_2$  Raman return of 268, the  $O_2$  Raman return of 277, and the  $H_2O$  Raman return of 268; KrF-(277,292,313) nm with  $N_2(277)$ ,  $O_2(292)$  and  $H_2O(277)$ ; Nd:YAG-(266,289,299) nm with  $N_2(266)$ ,  $O_2(289)$  and  $H_2O(266)$ . These configurations can be implemented with one or two Raman cells. With Nd:YAG pumping, it was demonstrated that the two 289 and 299 nm beams can be generated from a single cell (section 4). The beam of the second laser can thus be emitted with full power in the atmosphere, which is 3-4 times higher than the residual 266 nm out of a Raman cell. The single Raman cell setup has therefore more potentialities.

The computer simulation showed that these proposed ozone DIAL configurations are feasible in terms of measurement range ( $E_1$ ) and aerosol interference ( $E_2$ ). It does not, however, take into account the practical difficulties which arise in the field measurements.

## Acknowledgements

This work was supported by the Swiss Federal Office for Education and Science, grant n° EUREKA-BBW(94)3.

## References

1. A. Papayannis, G. Ancellet, J. Pelon, G. Mégie, "Multiwavelength lidar for ozone measurements in the troposphere and the lower stratosphere", *Appl. Opt.*, **29**, 467-476 (1990).
2. T. Shibata, T. Fukuda, T. Narikiyo, M. Maeda, "Evaluation of the solar-blind effect in the ultraviolet ozone lidar with Raman lasers", *Appl. Opt.*, **26**, 2604-2608 (1987).
3. M. Maeda, T. Sibata, H. Akiyoshi, "Optimum wavelengths in solar-blind UV ozone lidars", *Jap. Jou. Appl. Phys.*, **29**, 2843-2846 (1990).
4. Final report to the project EUROTRAC/TESLAS, "Tropospheric Environmental Studies by Laser Sounding", Jens Bösenberg Ed. (Max-Planck Institut für Meteorologie, Hamburg, Germany), Commission of the European Communities, in press.
5. J. D. Klett, "Lidar inversion with variable backscatter/extinction ratios", *Appl. Opt.*, **24**, 1638-1643 (1985).
6. E. V. Browell, S. Ismail, S. T. Shipley, "Ultraviolet DIAL measurements of ozone profiles in regions of spatially inhomogeneous aerosols", *Appl. Opt.*, **24**, 2827-2836 (1985).
7. G. J. McRae, A. G. Russel, R. A. Harley, "CIT photochemical airshed model, data preparation manual", Carnegie Mellon University, Pittsburgh, Pennsylvania 15213, and California Insitute of Technology, Pasadena, California 91125.
8. Qin Pang, "Etude de la qualité de l'air à Genève: approche de 'nesting one way' ", MSc thesis, Swiss Federal Institute of Technology Lausanne, Rural Engineering Department, Laboratory for Air and Soil Pollution (1996).
9. T. J. McGee, M. R. Gross, U. N. Singh, J. J. Butler, P. E. Kimvilakani, "Improved strotospheric ozone lidar", *Opt. Eng.*, **34**, 1421-1430 (1995). Also: U. N. Singh, T. J. McGee, M. Gross, W. S. Heaps, R. Ferrare, "A new Raman DIAL technique for measuring stratospheric ozone in the presence of volcanic aerosols", in *16th International Laser Radar Conference*, Cambridge, MA, paper B4 (1992).
10. V. Kovalev, M. Bristow, "Compensational three-wavelength DIAL technique for reducing the influence of differential scattering on ozone concentrations measurements", *Appl. Opt.*, in press.
11. Z. Wang, J. Zhou, H. Hu, Z. Gong, "Evaluation of dual differential absorption lidar based on Raman-shifted Nd:YAG or KrF laser for tropospheric ozone measurements", *Appl. Phys. B*, **62**, 143-147 (1996).
12. D. Renaut, R. Capitini, "Boundary-layer water vapor probing with a solar-blind Raman lidar: validations, meteorological observations and prospects", *J. Atm. Ocean. Tech.*, **5**, 585-601 (1988).
13. D. N. Whiteman, S. H. Melfi, R. A. Ferrare, "Raman lidar system for the measurement of water vapor and aerosols in the Earth's atmosphere", *Appl. Opt.*, **31**, 3068-3082 (1992).

*Section 6: Numerical optimization of DIAL wavelengths*

14. D. N. Whiteman, S. H. Melfi, R. A. Ferrare, K. D. Evans, "Daytime measurements of water vapor mixing ratio using Raman scattering - techniques and assessments", in *17th International Laser Radar Conference*, Sendai, Japan, paper 25PF2 (1994).
15. J. E. M. Goldsmith, S. E. Bisson, "Daytime Raman lidar profiling of atmospheric water vapor", in *17th International Laser Radar Conference*, Sendai, Japan, paper 26A3 (1994).
16. F. X. Kneizys et al., "Users guide to LOWTRAN 7", AFGL-TR-88-0177, environmental research paper n°1010, Air Force Geophysical Laboratory, Hanscom AFB, MA, (1988).
17. A. Berk, L. S. Bernstein, D. C. Robertson, "MODTRAN: a moderate resolution model for LOWTRAN 7", GL-TR-89-0122, Air Force Geophysical Laboratory, Hanscom AFB, MA, (1989).
18. The MODTRAN 3 v1.5 code is available on the FTP site 146.153.100.3, user anonymous, directory pub/chet/modtran3-v1.5 (status of June 1996).
19. C. Weitkamp, O. Thomsen, P. Bisling, "Signal and reference wavelengths for the elimination of SO<sub>2</sub> cross sensitivity in remote measurements of tropospheric ozone with lidar", *Laser und Optoelektronik*, **24**, 46-52 (1992).
20. W. B. Grant, E. V. Browell, N. S. Higdon, S. Ismail, "Raman shifting of KrF laser radiation for tropospheric ozone measurements", *Appl. Opt.*, **30**, 2628-2633 (1991).
21. R. M. Measures, "Laser remote sensing - fundamentals and applications" (Wiley, New-York, 1984).
22. P.-A. Biemann, "Optimisation numérique et expérimentale de la partie émission du lidar du LPAS", MSc thesis, Swiss Federal Institute of Technology Lausanne, Rural Engineering Department, Laboratory for Air and Soil Pollution (1996).
23. L. Schoulepnikoff, V. Mitev, Intermediate report to the "Raman cells" project, grant n° EUREKA-BBW(94)3, Swiss Federal Office for Education and Science (Bern, 1995).

## **Section 7**

### **Conclusions and perspectives**



## 7.1 Conclusions

The research conducted in the frame of this PhD can be divided in two contributions: first the Raman cell numerical and experimental characterization, and second the numerical optimization of the DIAL ozone wavelengths for pollution monitoring.

### *(a) Numerical method for the modelling of high-gain single-pass cascade stimulated Raman scattering in gases (section 2)*

The fundamental work on these specific Raman cells (high-gain, single-pass, focused pump beam geometry, ultraviolet spectral range) was motivated by the incomplete understanding of the collection of experimental results collected by various groups in different configurations. These results show commonalties and discrepancies which are only partially explained by the current models.

A first major difficulty encountered in the Raman cell modelling is the numerical method itself. The most usual standard methods (finite differences and finite elements) showed severe numerical artefacts in such a high amplification regime. The other method tested (spectral decomposition) has shown to be applicable, but only with a suited parametrization.

The discretization of physical equations involving continuous variables is often considered as a subtle problem, since the way the numerical scheme approximates the underlying physics is generally not apparent in the discretization formula. The behaviour of the three numerical methods investigated has been unravelled only after an analytical analysis of what physics they describe. In particular, numerical dispersion of the higher modes which arises from the high gain was shown to be one of the critical factors. Also critical is the numerical method which solves the set of differential equations describing the nonlinear coupling. This set of equations is stiff due to very different growing rates of the different orders of Stokes / anti-Stokes waves. Explicit schemes, which are routinely used to solve many physical problems, revealed to lead to exponential numerical instabilities. An implicit scheme had to be applied, which is more costly in terms of numerical computations.

As an overall conclusion, the numerical method suited for the description of such a high-gain device is very demanding computationally: the proper method with specific parameters has to be chosen, and requires powerful computing capabilities.

### *(b) Numerical modelling of high-gain single-pass Raman cells in the ultraviolet (section 3)*

The physical modelling of HG-SP Raman cells of practical importance is challenging since several effects superimpose as a consequence of the very strong amplification. Namely, at least the following effects were identified to be important: diffraction in the plane transverse to propagation (especially in the region of the waist), cascade Stokes and four-wave-mixing, optical breakdown of the Raman and buffer medium, transient effects. All the previous modellings either did not consider a specific HG-SP Raman cell configuration, or incorporated only partially these features, and are therefore of limited usefulness in interpreting experimental results of such Raman cells.

In our attempt to contribute to this subject, one major difficulty has been the computational requirements of the numerical method to describe high amplification, even with the powerful resources available (rated as one tenth computing capability with respect to the most powerful computers available at this time). A trade-off was unavoidable with these computing resources, and the only choice possible is to approximate the transient effects since the transverse diffraction is a key element in a focused geometry which could not be approximated. The approximation adopted is a gain reduction formalism in a steady-state description, based on former theoretical and experimental work.

## *Section 7: Perspectives*

The capability of this model has proven limited, however useful in explaining some qualitative trends of experimental results. Some experimental features of importance have been unravelled: the key importance of four-wave-mixing in any HG-SP Raman configuration, either concerning the conversion efficiency or the Stokes beam quality; the lens focal length dependence, which is explained by transient effects; the pressure regimes for which there is beam replication or cleanup, and those for which a dramatic beam degradation occurs; the importance of the pump beam characteristics (pulse duration and spatial shape,  $M^2$  parameter). On the other hand, this modelling could not achieve a close match with experimental results (such as e.g. to compare model and experimental results on the same graph). Conversely, on the purely modelling aspect, the still limited ability of the present model contributes to our understanding of HG-SP Raman cells: it points out that a complete characterization of the transient effects (i.e. solving for the time derivatives) is absolutely needed for a close agreement with the experiment. A complete input beam characterization is also a key element towards such an agreement, which is certainly not an easy task with respect to the quality of the beams delivered by high-power lasers in the UV (either excimer or quadrupled Nd:YAG).

The practical usefulness of this modelling effort stands in the trends that it successfully reproduces with respect to the experiment (see above). These trends, such as the focal length dependence or the beam quality relation to the gases partial pressure, give a theoretical basis to the experimental observations. As such, they give confidence in some design principles for future instrumentation (as, for example, to choose the longest cell possible, or to work either at low active gas pressure, or at high active gas pressure but with buffer gas).

### *c) Experimental study of high-gain single-pass Raman shifters in the ultraviolet (section 4)*

The experimental Raman cell investigation complemented the former studies in a number of topics: optical breakdown, focal length dependence, methane and ethane, beam quality, and the mixture of two active gases.

The “loss of photon” (of the total number of photons in the laser pulse, which has to be conserved by the Raman process) has been shown to arise from laser-induced breakdown (LIB). The pressure-dependence of the LIB has been investigated in the active and buffer gas. LIB brings practical limitations such as to prevent using a too high beam expansion factor of the input beam, since it brings a higher intensity at the waist. Short cells (<25 cm lens focal length) are not recommended for the same reason. LIB puts also limitations on the Stokes beam quality.

From the point-of-view of the Raman effect and the four-wave-mixing, short cells (<25 cm lens focal length) are to be avoided when high photon conversion efficiency (> 20%) and pump beam replication (or cleanup) is requested. This focal length dependence was best evidenced with the excimer laser, since LIB was quasi-nonexistent due to the low pump focusing capability.

Methane showed useful conversion efficiencies (>20%) and beam quality (input beam replication) at low pressure (< 15 atm), above which optical damages occur on the inner face of the entrance window, attributed to stimulated Brillouin scattering. At low pressure, methane is an alternative to deuterium since it has almost the same Raman shift and brings comparable conversion efficiencies.

The study of the effect of the input pump beam quality on the cell performance has been carried out by using different types of laser. A KrF excimer laser with poor beam quality (due to the stable resonator design), as well as two models of Nd:YAG lasers (with different  $M^2$  parameter). The input pump beam quality ( $M^2$  parameter) affects the conversion process through the geometry of focusing. Increasing the pump  $M^2$  was found similar to increasing the lens focal length. A difference in conversion efficiencies of 20-50% (the higher Stokes

## *Section 7: Perspectives*

showing a the largest difference) was measured between the two Nd:YAG lasers, which are characterized by an  $M^2$  of 3.9 and 6.2 (at the fourth harmonic). As a consequence, the importance of the pump beam quality has been recognized.

The pressure dependence of the Stokes beam quality ( $M^2$  parameter) has been characterized. The Stokes  $M^2$  parameter determines its divergence, which is an important parameter in lidar or laser ranging applications. Beam cleanup was observed unfeasible when the Raman cell is tuned to high conversion efficiencies. Rather, pump beam quality replication is the best achievable. Beam replication occurs either at low active gas pressure, or at higher active gas pressure with the presence of buffer gas (He, Ne or Ar tested). The addition of buffer gas is seen to have a stronger influence on the Stokes beam quality than on its conversion efficiency (as it is best evidenced with helium), which is confirmed by the modelling (effect of the four-wave-mixing). At high active gas pressure, a severe beam degradation occurs (Stokes  $M^2$  parameter more than ten times the input pump  $M^2$  were observed).

The mixture of two Raman-active gases has the interesting advantages over a dual single gas filling, of requiring a single laser and possibly to simplify the alignment procedures in some applications (e.g. the on- and off-resonance beams in a differential absorption lidar - DIAL). As required for instance in DIAL applications, a comparable energy in the first Stokes of  $D_2$  (289 nm) and  $H_2$  (299 nm) from quadrupled Nd:YAG pumping (266 nm) has been sought (they are the usual DIAL operating wavelengths of a tropospheric ozone DIAL). The first Stokes conversion efficiency was seen to be quite sensitive on the partial pressure of  $H_2$ ,  $D_2$  and Ar. As a rule of thumb, the pressure of  $D_2$  has to be taken between 2.5 and 3.5 times the pressure of  $H_2$  in order that equal energy in the 289 and 299 nm beams can be achieved by varying the Ar pressure (between 0 and 40 atm in this study). With the configuration tested of a single recollimating lens at the cell exit, the lens position has to be chosen so as to compromise the divergence of the two first Stokes beams. In our configuration, the trade-off revealed to be acceptable for DIAL applications, since the divergence of the two first Stokes was measured to be less than 0.5 mrad (full angle, at 86% power).

### *d) Numerical optimization of multiwavelength ozone DIAL for pollution modelling (section 6)*

The numerical simulation of the DIAL instrument and of representative atmospheric cases, revealed that in order to yield the flexibility required to comply to airshed photochemical models (in terms of the probing angle, range binning along the probing path, sampling time, and the atmospheric conditions - ozone and aerosol loading), a more complex instrument than the standard two-fixed-wavelength configuration is needed. The simulation points out a number of instrumental configurations which yield the required performance flexibility.

With three emitted wavelengths, the short wavelength pair is used for short range measurements (and small range bins), high sensitivity on the retrieved ozone, and in case of high aerosol loading (aerosol interference). The long wavelength pair is used to reach longer ranges. The three channels allow to use the dual DIAL scheme which can be accurate in case of high aerosol loading and/or gradients. The aerosol sensitivity of this scheme depends critically on the wavelength configuration.

The addition of two ( $O_2$  or  $N_2$ ) Raman channels to a two-wavelength configuration is another solution to provide the necessary flexibility. The Raman DIAL retrieval of ozone is performed in case of high aerosol interference. The weaker Raman returns with respect to the elastically scattered returns lower the signal dynamic range and allow for short range measurements.

The configuration of a  $H_2O$  and a  $N_2$  (or  $O_2$ , although not tested) channel in addition to a two-wavelength ozone DIAL is interesting in two respects. First it allows the simultaneous profiling of the water vapour and ozone up to the top of the PBL. Second, the  $N_2$  Raman channel improves the aerosol correction of the ozone DIAL.

## Section 7: Perspectives

The most complete and efficient configuration consists in three emitted wavelengths, and the O<sub>2</sub>, N<sub>2</sub>, H<sub>2</sub>O Raman channels, although the increased performance is traded-off by the added complexity of the instrument. The three elastic returns yield the flexibility in range and atmospheric condition (ozone loading and visibility). Alternatively, the N<sub>2</sub> and O<sub>2</sub> Raman returns lower the signal dynamic for the short range. In case of high aerosol interference, the dual-DIAL and Raman DIAL schemes are used, which may show complementary to each other depending on the conditions. The simultaneous ozone and water vapour profiling can be performed. This configuration can be implemented with one or two Raman cells. When a single Raman cell with a mixture of H<sub>2</sub> and D<sub>2</sub> is used, a single pump laser is needed. The beam of the second laser can thus be emitted with full power in the atmosphere, which is 3-4 times higher than the residual 266 nm out of a Raman cell. The single Raman cell setup has therefore more potentialities.

The computer simulation showed that these proposed ozone DIAL configurations are feasible in terms of measurement range (statistical error) and aerosol interference (systematic error). It does not, however, take into account the practical difficulties which arise in the field measurements.

### 7.2 Perspectives

The model of high-gain single-pass Raman cell in the ultraviolet has to be upgraded in order to fully reproduce the experiment. Three key improvements were identified: a full temporal description, a complete input beam characterization (intensity and spatial coherence) and the addition of multi-photon ionization. Such an upgraded model would require very high computing capabilities, due to the high amplification and the high number of variables in the set of partial differential equations (four variables).

A Raman cell with cylindrical lenses represents an interesting alternative to the conventional spherical lens design. Cylindrical lenses increase the depth of focus with respect to spherical lenses. As a consequence of the reduced intensity at the waist, four-wave-mixing, optical breakdown and ground-state depletion are less likely to occur than with spherical lenses. Raman cells with cylindrical lenses have been investigated numerically and experimentally by other authors<sup>1,2</sup>, at the Nd:YAG fundamental wavelength (1064 nm) only. The result of this study is that the cylindrical lenses bring a higher conversion efficiency than spherical lenses at high amplification. When extrapolated to the ultraviolet spectral range, which is characterized by a higher Raman gain than in the infrared, it shows that a cylindrical lens design is worth trying in the UV (at least with respect to the conversion efficiency).

Laser-induced breakdown (LIB) which occurs in the waist region has been evidenced in this study, but the type of breakdown (multiphoton ionization or the effect of impurities) has not been investigated. A former study addressed that LIB is due to multiphoton ionization<sup>3</sup> (EPA [ref]). It has been claimed in the EPA study that the gas purity in the cell has been carefully controlled. However, this experiment is worth repeating since the cell gas purity is a parameter which is difficult to control.

Optical damages were noticed on the inner side of the cell entrance window when using methane at more than 15 bar pressure (80 mJ input pump energy at 266 nm). This damage has been attributed to stimulated Brillouin scattering. This argument should have to be experimentally verified.

With the configuration of one Raman cell with a mixture of H<sub>2</sub> and D<sub>2</sub>, a pulse energy of 10-15 mJ in the first Stokes of H<sub>2</sub> and D<sub>2</sub> could be achieved with 70 mJ pumping. This configuration is interesting for the differential absorption lidar (DIAL) probing of tropospheric ozone, since only one Nd:YAG pump laser is needed, and the operating DIAL beams (respectively on- and off-resonance with respect to the ozone absorption) are collinear at the output of the Raman cell. One setback of this design when using a lens at the output of

## *Section 7: Perspectives*

the cell stands in the fact the lens position is to be compromised for the on and off wavelength so as to minimize the divergence of both beams (and possibly also of the remaining pump beam, should it be used in the DIAL instrument). A divergence (full angle, at 86% power) of 0.5 mrad at both 289 and 299 nm, and of 1 mrad at the remaining 266 nm, were found in this study which would be suitable to DIAL measurements. However, practical difficulties could arise in the beam steering and detection in DIAL applications. Therefore the practical implementation of this Raman cell H2 and D2 mixture design in a tropospheric ozone DIAL is interesting but its practical usefulness is to be demonstrated.

A certain number of improved tropospheric ozone DIAL configuration have been proposed in this study, by adding more wavelengths to the usual two-wavelength configuration. The practical feasibility of this more complex DIAL instrument has to be demonstrated. In particular, difficulties could arise in the alignment of the emitted beams, and the spectral separation and detection of the atmospheric returns. The simulation assumed representative idealized atmospheric situations. Ozone DIAL field tests are needed in order to verify that the claimed improvements (in range and aerosol interference) are attained in the diversity of a real situation.

In DIAL measurements there are more unknowns (the target specie concentration, the aerosol backscattering and extinction coefficients, and the lidar calibration constant) that measured quantities. This fact imposes a trade-off between the quantities which are guessed "a-priori" and those which are determined from the measurements. The tropospheric ozone DIAL simulation presented in section 6 allowed to investigate various trade-off possibilities, with the objective to minimize the aerosol interference. Numerous other possibilities exist, and further simulation work could bring interesting new ozone DIAL configurations.

### **Acknowledgements**

I am deeply indebted to the highly experienced professionals who supervised my research: Prof. H. van den Bergh, Prof. G. Busca, Dr. B. Calpini, Dr. V. Simeonov, and last but not least, Dr. V. Mitev. They taught me invaluable aspects of their experience.

I am grateful to Prof. H. van den Bergh for having made possible this thesis in his laboratory, as an “external” status.

The recommendations of the experts of the PhD commission have proven very relevant for the writing of the manuscript, and are therefore acknowledged. The author is grateful to Dr. Milton for his suggestion of stimulated Brillouin scattering being the cause of the optical damages when using methane at high pressure.

I appreciated a lot the excellent working atmosphere with my colleagues at ON and LPAS.

I have been supported nicely throughout this work by my beloved fiancée Laurence, my friends and my family.

### **References**

1. J. C. van den Heuvel, “Numerical modeling of stimulated Raman scattering in an astigmatic focus”, *IEEE J. Quant. Electron.*, **28**, 378-385 (1992).
2. J. C. van den Heuvel, F. J. M. van Putten, R. J. L. Lerou, "Experimental and numerical study of stimulated Raman scattering in an astigmatic focus", *IEEE J. Quant. Electron.*, **29**, 2267-2272 (1993).
3. Dorothee Diebel, Michael Bristow, Rainer Zimmermann, “UV DIAL for simultaneous measurement of tropospheric O<sub>3</sub> and SO<sub>2</sub>: optimization of the transmitter section”, *Proc. 15th International Laser Radar Conference (Tomsk, USSR, 1990)*.

# List of publications

## Articles in international journals

1. C. Flesia, A. Mugnai, L. Schoulepnikoff, L. Stefanutti, *Particle size characterization of polar stratospheric clouds by means of depolarization lidar measurements*, in "IRS '92: current problems in atmospheric radiation", S. Keevallik and O. Kaerner Editors, Deepak Publishing, Hampton VA, 1993.
2. C. Flesia, A. Mugnai, Y. Emery, S. Godin, L. Schoulepnikoff, V. Mitev, *Interpretation of lidar depolarization measurements of the Pinatubo stratospheric layer during EASOE*, *Geophysical Research Letters*, **21**, 1443-1446 (1994).
3. L. Schoulepnikoff, V. Mitev, *Numerical method for the modelling of high-gain high-conversion single-pass stimulated Raman scattering in gases*, *Journal of the Optical Society of America B*, in press.
4. L. Schoulepnikoff, V. Mitev, *High-gain single-pass stimulated Raman scattering and four-wave-mixing in a focused beam geometry: numerical study*, *Pure and Applied Optics* (journal of the European Optical Society), in press.
5. L. Schoulepnikoff, V. Mitev, V. Simeonov, B. Calpini, H. van den Bergh, *High-power single-pass Raman shifters in the ultraviolet*, submitted to *Applied Optics*.

## Contributions presented at international conferences

1. C. Flesia, A. Mugnai, L. Schoulepnikoff, L. Stefanutti, *Lidar depolarization by non-spherical particles: potential of combined depolarization/backscattering measurements for PSC's characterization*, 16th International Laser Radar Conference, NASA, Cambridge, Massachusetts, U.S.A., 1992.
2. C. Flesia, A. Mugnai, L. Schoulepnikoff, L. Stefanutti, *Particle size characterization of polar stratospheric clouds by means of depolarization lidar measurements*, International Radiation Symposium, Tallin, Estonia, 1992.
3. C. Flesia, A. Mugnai, L. Schoulepnikoff, L. Stefanutti, *Interpretation of lidar depolarization measurements for aerosol size characterization*, OSA Topical Meeting on Optical Remote Sensing of the Atmosphere, Salt Lake City, U.S.A., 1993.
4. L. Schoulepnikoff, B. Stein, P. Rairoux, *Determination of aerosol size distribution moments with multi-wavelength lidar*, 17th International Laser Radar Conference, Sendai, Japan, 1994.
5. L. Schoulepnikoff, H. van den Bergh, P.-A. Biemann, V. Mitev, V. Simeonov, B. Calpini, *Numerical optimization of multiwavelength UV differential absorption lidar (DIAL) for pollution modelling*, EUROTRAC symposium, Garmisch-Partenkirchen, Germany, 1996.

6. V. Mitev, R. Matthey, L. Schoulepnikoff, S. Pershin, A. Bukharin, *Comparative test of PRN-cw and micro-joule pulsed total backscatter lidars*, in "Advances in Remote sensing with Lidar", A. Ansmann, R. Neuber, P. Rairoux, U. Wandinger Eds., selected papers of the 18th International Laser radar Conference, Serlin, 22-26 July 1996 (Springer, Berlin, 1996).
7. L. Schoulepnikoff, H. van den Bergh, P.-A. Biemann, B. Calpini, V. Simeonov, V. Mitev, *Characterization of Raman cell-based transmitters for UV DIAL applications*, in "Advances in Remote sensing with Lidar", A. Ansmann, R. Neuber, P. Rairoux, U. Wandinger Eds., selected papers of the 18th International Laser radar Conference, Serlin, 22-26 July 1996 (Springer, Berlin, 1996).

### European Space Agency (ESA) reports

During the year 1991, L. de Schoulepnikoff was fully involved in an ESA contract, which resulted in the following report:

1. C. Flesia, L. Schoulepnikoff, M. Morandi, L. Stefanutti, *Technical assistance for the inversion of the lidar equation*, Final report, ESTEC contract No.XA/89/171/PK, 10-06-91.

He has since then participated in other contractual work the ON lidar group has with ESA. This was not his primary activity. As a result, he took part in the following reports delivered to ESA:

1. V. Mitev, R. Matthey, L. Schoulepnikoff, *Modellisation of pseudo-random noise (PRN) code modulation for spaceborne lidars*, Purchase Order No.131'174, 11-05-93.
2. V. Mitev, R. Matthey, L. Schoulepnikoff, *Breadboarding of a pseudo-random noise continuous-wave lidar*, Technical Note n°2, ESTEC contract No.9099/90/NL/PB, WO-7, 11-05-94.
3. V. Mitev, R. Matthey, D. Reusser, L. Schoulepnikoff, *Breadboarding of a pseudo-random noise continuous-wave lidar*, Technical Note n°3.1, ESTEC contract No.9099/90/NL/PB, WO-7, 22-08-94.
4. V. Mitev, R. Matthey, L. Schoulepnikoff, *Comparative performance test of diode-laser-based lidars*, Purchase Order No.150976, 28-03-95.



# Curriculum Vitae

## EDUCATION

- '86 High school degree ("maturité") in science. Entered the Swiss Federal Institute of Technology in Lausanne to study physics.
- '88 - '89 Third academic year at Laval University, Quebec, Canada, within the framework of a collaboration between EPFL and north American universities.
- '90 - '91 Master's thesis in nuclear engineering.
- '91 Master's degree in engineering physics.

## WORK EXPERIENCE

- '91 - '92 **Physicist at the Observatory of Neuchâtel**, Switzerland. Computer simulation of a LIDAR (laser radar), under contract of the European Space Agency.
- '92 - '94 Observatory of Neuchâtel, **European campaign EASOE**, aiming at the characterization of the physico-chemical processes of the ozone in the Arctic stratosphere. Analysis and interpretation of LIDAR measurements, which comprised of the development of novel computer tools.
- '94 - '96 **Ph.D. thesis** conducted in the scope of the "Raman Cell" project, a collaboration between the Observatory of Neuchâtel and the Laboratory of Air and Soil Pollution (LPAS) of EPFL.  
Ph.D. supervisor: Prof. H. van den Bergh, LPAS-EPFL.  
Conducted the computer simulation and the experimental optimization of the laser source. Computer modelling of the LPAS ozone LIDAR, with the goal to establish a better compatibility with the air pollution numerical codes of the LPAS. Supervised one master's thesis.
- '96 onwards Research and development of laser engraved rolls for the printing industry (flexography), within the company Praxair Surface Technologies (Geneva plant).

## INTERESTS AND EXTRA-PROFESSIONAL ACTIVITIES

- Project manager at INGECOM, a student-run company which develops technico-commercial products for industry ('90-'91).
- Member of the board of the student travel agency at Laval University, Quebec, Canada. Organized a forum which gathered professional travel advisors on the university campus ('88-'89).
- Member of the Swiss Alpine Club (since 1981). Numerous high-mountaineeing ascents in the Alps.
- Classical music enthusiast.